UNIVERSITÀ DEGLI STUDI DI PADOVA

Dipartimento di Fisica e Astronomia "Galileo Galilei"

Corso di Dottorato di Ricerca in Astronomia - ciclo XXXVIII

Ph.D. thesis

A multiwavelength perspective on extreme flares in narrow-line Seyfert 1 galaxies

---

Author:
Luca Crepaldi

Supervisor:
Prof. Stefano Ciroi

External Referees:
Prof. Chiara Mazzucchelli
Prof. Elina Lindfors

Co-Supervisors:
Dr. Marco Berton
Prof. Emilia Järvelä

A thesis submitted in fulfillment of the requirements for the degree of Doctor of Philosophy

Academic year
2024-2025

To my family, present and future, and to families all over the world.

Abstract

A few decades have passed since the identification of narrow-line Seyfert 1 (NLS1) galaxies as a subclass of active galactic nuclei (AGN). NLS1s show a Seyfert 1-like spectrum, but with permitted emission line widths comparable to those of Seyfert 2 spectra. These peculiar traits suggest a combination of factors, high accretion rates near the Eddington limit and low-mass black holes, which indicate an early stage in the AGN life cycle. Although few, jetted NLS1s have been discovered. Recently, seven sources with an inverted radio spectrum and extreme radio variability were identified by the Metsähovi Radio Observatory, among a sample of radio-quiet and radio-silent NLS1s. They show rapid flares at 37 GHz that increase their flux density up to 9000-fold (Jy level) with an *e*-folding time-scale of a few hours. During quiescence and at lower frequencies, they achieve only mJy levels. As the main cause, relativistic jets would have been the most likely, but no jet emission traits were detected. Until now, their radio spectra are the only common feature. To explain the flares' behavior, three main hypotheses have been suggested: jet-cloud/star interaction, relativistic jet and free-free absorption with moving clouds, and magnetic reconnection. In this thesis, I carried out three works to study the sample from different perspectives, with the goals of investigating the peculiarities of the sample and estimating the flares' properties. In the first work, I performed a multi-epoch analysis for different optical bands, in particular through a variability and periodicity Fourier-based analysis. I used publicly available data retrieved from the catalogs of All-Sky Automated Survey for Supernovae and Zwicky Transient Facility surveys. For the second work, I derived the main physical properties of the sources in the sample by means of an optical spectra analysis. Here I used proprietary data acquired with the long-slit spectrometer Optical System for Imaging and low-Intermediate-Resolution Integrated Spectroscopy mounted on the Gran Telescopio Canarias. Finally, in the third work, I moved on to the radio regime to estimate the main characteristics of the flare episodes using both single-dish and interferometer data at multiple frequencies. The results revealed no apparent connection between the flare episodes detected in radio and the optical behavior. From the spectra, one of the sources turned out to be an intermediate Seyfert galaxy, while the remaining six showed typical values for the NLS1 class. On the other hand, the radio analysis results on the flares, with *e*-folding time-scales down to a few tens of minutes and variability brightness temperatures $>10^{15}$ K, were much more extreme and unexpected. Considering the multi-wavelength results, the magnetic reconnection in the black hole magnetosphere seems to be the most likely driver in the flare production. In particular, considering the radio behavior, the magnetic reconnection might be coupled with an emission mechanism as either an inverse Compton catastrophe or a coherent emission. To disentangle between these two main scenarios, and to further investigate also less viable hypotheses, follow-up radio observations very close in time will be fundamental.

Abstract – Italiano

Alcuni decenni sono trascorsi dall'identificazione delle galassie narrow-line Seyfert 1 (NLS1) come sottoclasse di nuclei galattici attivi (AGN). Le NLS1s mostrano uno spettro simile a quello di galassie Seyfert 1, ma con larghezze delle righe di emissione permesse paragonabili a quelle degli spettri di Seyfert 2. Questi tratti peculiari suggeriscono una combinazione di fattori, alti tassi di accrescimento vicino al limite di Eddington e buchi neri di bassa massa, che indicano una fase iniziale del ciclo di vita dell'AGN. Sebbene poche, NLS1s con getti relativistici sono state scoperte. Di recente, l'Osservatorio radio di Metsähovi ha identificato sette sorgenti con spettro radio invertito ed estrema variabilità, in un campione di NLS1s cone emissione radio debole o totalmente assente. Questi oggetti mostrano rapidi brillamenti a 37 GHz che aumentano la loro densità di flusso fino a 9000 volte (livello del Jy) in una scala temporale di poche ore. Durante la quiescenza e a frequenze più basse, raggiungono invece solo livelli di mJy. Come causa principale, i getti relativistici sarebbero stati i più probabili, ma non sono stati rilevati in nessuna delle analisi condotte. Finora, i loro spettri radio erano l'unica caratteristica comune del campione. Per spiegare il comportamento dei brillamenti, sono state suggerite tre ipotesi principali: interazione del getto con nube/stella, getto relativistico e assorbimento free-free con nubi in movimento, e riconnessione magnetica. In questa tesi ho svolto tre lavori per studiare il campione da diverse prospettive, con l'obiettivo di indagare le peculiarità del campione e stimare le proprietà dei brillamenti. Nel primo lavoro ho eseguito un'analisi multiepoca in diverse bande ottiche, in particolare attraverso un'analisi (Fourier-based) sulla variabilità e sulla periodicità. Ho utilizzato dati pubblici presenti nei cataloghi delle surveys All-Sky Automated Survey for Supernovae e Zwicky Transient Facility. Nel secondo lavoro ho derivato le principali proprietà fisiche delle sorgenti nel campione mediante un'analisi degli spettri ottici. Qui ho utilizzato dati proprietari acquisiti con lo spettrometro long-slit OSIRIS montato al Gran Telescopio Canarias. Infine, nel terzo lavoro, sono passato al radio per stimare le caratteristiche principali degli episodi di brillamento utilizzando sia dati single-dish che dati interferometrici a frequenze multiple. I risultati non hanno rivelato alcuna connessione apparente tra gli episodi di brillamento rilevati via radio e il comportamento ottico. Dagli spettri, una delle sorgenti si è rivelata essere una galassia di Seyfert intermedia, mentre le restanti sei hanno mostrato valori tipici per la classe NLS1. D'altro parte, i risultati dell'analisi radio sui brillamenti, con tempi scala fino a poche decine di minuti e temperature di luminosità $>10^{15}$ K, sono stati molto più estremi e inaspettati. Considerando i risultati ottenuti a più lunghezze d'onda, la riconnessione magnetica nella magnetosfera del buco nero sembra essere il fattore più probabile per la produzione dei brillamento. In particolare, considerando il comportamento radio, la riconnessione magnetica potrebbe essere associata a un meccanismo di emissione come una catastrofe Compton inversa o un'emissione coerente. Per distinguere tra questi due scenari principali e per indagare ulteriormente anche ipotesi meno probabili, saranno fondamentali osservazioni radio di follow-up molto ravvicinate nel tempo.

Contents

Abstract v

List of figures xv

List of tables xvii

Acronyms xix

Symbols xxiii

1 Active Galactic Nuclei 1
- 1.1 Introduction . . . 1
- 1.2 Structure of AGN . . . 2
  - 1.2.1 Sizes in an AGN . . . 8
- 1.3 Taxonomy and unification . . . 9
- 1.4 Observational properties . . . 12
  - 1.4.1 Spectral Energy Distribution . . . 13

2 Multiwavelength properties of narrow-line Seyfert 1 galaxies 17
- 2.1 Optical spectrum . . . 19
  - 2.1.1 Black hole mass estimation . . . 23
  - 2.1.2 Eddington ratio . . . 25
- 2.2 Radio properties . . . 26
- 2.3 A sample of extremely variable NLS1s . . . 28

3 Time-series analysis 31
- 3.1 Light curves properties . . . 35
- 3.2 Analysis methods . . . 37
- 3.3 Light curves simulation . . . 43

4 Optical time-series analysis on flaring NLS1s 47
- 4.1 Introduction . . . 47
- 4.2 Sample and data . . . 48
  - 4.2.1 All-Sky Automated Survey for Supernovae . . . 48
  - 4.2.2 Zwicky Transient Facility . . . 49
- 4.3 Optical light curves analysis . . . 49
  - 4.3.1 Variability test . . . 51
  - 4.3.2 PSD slope estimation . . . 52
- 4.4 Periodicity searching . . . 53
  - 4.4.1 Generalized Lomb-Scargle periodogram . . . 54
  - 4.4.2 weighted wavelet Z-transform . . . 54
  - 4.4.3 Significance levels estimation . . . 55
- 4.5 Results . . . 55
  - 4.5.1 Radio-optical LCs comparison . . . 55

4.5.2 Variability . . . 56
4.5.3 GLS and WWZ . . . 56
4.6 Discussion and conclusions . . . 57

5 An optical perspective on early-stage AGN with extreme radio flares 69
5.1 Introduction . . . 69
5.2 Sample . . . 70
5.3 Observations and data reduction . . . 70
5.4 Spectral analysis . . . 71
5.4.1 Line profiles . . . 71
5.4.2 BLR radius estimation . . . 74
5.4.3 Black hole mass . . . 75
5.4.4 Eddington ratio . . . 76
5.5 Results . . . 77
5.5.1 SDSS J102906.69+555625.2 . . . 77
5.5.2 SDSS J122844.81+501751.2 . . . 77
5.5.3 SDSS J123220.11+495721.8 . . . 78
5.5.4 SDSS J150916.18+613716.7 . . . 80
5.5.5 SDSS J151020.06+554722.0 . . . 80
5.5.6 SDSS J152205.41+393441.3 . . . 80
5.5.7 SDSS J164100.10+345452.7 . . . 81
5.6 Discussion . . . 81
5.6.1 Black hole mass comparison . . . 82
5.6.2 Eddington ratio comparison . . . 84
5.6.3 *R*4570-Eddington ratio discrepancy . . . 85
5.6.4 SDSS-GTC spectral continuum comparison . . . 86
5.6.5 Comparison of the NLS1s properties . . . 87
5.7 Conclusions . . . 88
5.8 Appendix: tables, spectra and line profiles . . . 89

6 Investigation on the fastest radio variability in AGN 99
6.1 Introduction . . . 99
6.2 Sample and data reduction . . . 100
6.2.1 Metsähovi Radio Observatory . . . 100
6.2.2 Owens Valley Radio Observatory . . . 100
6.2.3 Effelsberg 100-m telescope . . . 101
6.2.4 Institut de Radioastronomie Millimétrique . . . 101
6.2.5 Karl G. Jansky Very Large Array . . . 101
6.3 Analysis and results . . . 102
6.3.1 MRO-JVLA quasi-simultaneous observations . . . 104
6.3.2 MRO-OVRO quasi-simultaneous observations . . . 105
6.3.3 J1029+5556 . . . 106
6.3.4 J1228+5017 . . . 106
6.3.5 J1232+4957 . . . 106
6.3.6 J1509+6137 . . . 107
6.3.7 J1510+5547 . . . 107
6.3.8 J1522+3934 . . . 107
6.3.9 J1641+3454 . . . 109
6.4 Discussion . . . 109
6.5 Conclusions . . . 110
6.6 Appendix: lists and light curves of observations . . . 112

7 Conclusions **121**

References **123**

List of Figures

1.1 Schematic representation of the structure of an AGN. 3
1.2 Representation of a multi-color blackbody as a result of the superposition of blackbody curves, derived from different rings at increasing temperature in the accretion disk. 4
1.3 AGN unification model (Thorne et al., 2022). 10
1.4 Schematic representation of an AGN SED. The black solid curve represents the total SED and the colored curves represent the individual components (Padovani et al., 2017, adapted from Harrison et al., 2014). 13

2.1 Optical spectrum of an NLS1 between 4000Å and 7000Å. The spectrum was obtained with the OSIRIS instrument mounted at the Gran Telescopio Canarias. 20
2.2 UV-optical composite spectrum of an NLS1. The spectrum was obtained with the FOS, GHRS, and STIS instruments mounted in the Hubble Space Telescope (Constantin and Shields, 2003). 22

3.1 Right: AGN LC in the radio band at 15 GHz. Left: PDF related to the LC. The histogram represents the data, the black dashed line a single Gaussian fit, and the red solid line a log-normal fit (Liodakis et al., 2017). 35
3.2 Top: NLS1 LC in the optical band in g-filter. Bottom: PSD related to the LC. The black solid line is the PSD calculated from the observed LC, while the colored lines show the average PSD power-law models for spectral indices between 0.2 and 3. 38
3.3 Representation scheme of the aliasing effect. The red points are the observed points of the time-series. The blue solid line and the green dashed line are, respectively, the real and the fake periodic signal. . . . 39
3.4 GLS periodogram calculated adopting a Hann window function of the LC in the top box of Fig. 3.2. The blue line represents the GLS periodogram, while the orange, green, and red lines are respectively the 1, 2, and 3σ significance levels. 42
3.5 WWZ of the LC in the top box of Fig. 3.2. The color scale represents the absolute power of the wavelet transform, where higher values indicate stronger periodicity. 43

4.1 Radio and optical LCs of J1232. 51
4.2 Fitting of the χ^2_{obs} calculated in the PSRESP method version of Kiehlmann (2015). The minimum χ^2_{min} corresponds to the most realistic intrinsic β. 54
4.3 GLS with significance levels of the selected LCs. 58
4.3 *continued* 59
4.4 WWZ of the selected LCs. 60
4.4 *continued* 61
4.5 MRO and optical LCs of J1029. 64
4.6 MRO and optical LCs of J1228. 65

4.7 MRO and optical LCs of J1509. 65
4.8 MRO and optical LCs of J1510. 66
4.9 MRO and optical LCs of J1522. 66
4.10 MRO and optical LCs of J1641. 67

5.1 [O III]$\lambda\lambda$4959,5007 emission lines of J1641. The light gray shadows represent the ranges where the χ^2 is assessed. 72
5.2 [O III]$\lambda\lambda$4959,5007 line profiles of J1228. 78
5.3 Hα+[N II]$\lambda\lambda$6548,6583 lines profile of J1232. The cyan dashed line represents the [N II] line profiles, which are much fainter than the Hα emission. 79
5.4 [O III]$\lambda\lambda$4959,5007 line profiles of J1232, which show wing components stronger than the core components. 79
5.5 Hβ line profile of J1641. The broad and narrow components have a FWHM of 4050 km s^{-1} and 493 km s^{-1} , respectively. 81
5.6 Eddington ratios calculated using the measured continuum luminosity at 5100Å (blue dots), and the derived continuum luminosity (red dots). The not visible error bars, due to their small values, are inside the size of the dots. 87
5.7 Spectrum of J1029. 90
5.8 Hβ and [O III]$\lambda\lambda$4959,5007 line profiles of J1029. 90
5.9 Spectrum of J1228. 93
5.10 Hβ, Hα+[N II]$\lambda\lambda$6548,6583 and [S II]$\lambda\lambda$6716,6731 line profiles of J1228. 93
5.11 Spectrum of J1232. 94
5.12 Hβ and [S II]$\lambda\lambda$6716,6731 line profiles of J1232. 94
5.13 Spectrum of J1509. 95
5.14 Hβ, [O III]$\lambda\lambda$4959,5007, Hα+[N II]$\lambda\lambda$6548,6583 and [S II]$\lambda\lambda$6716,6731 line profiles of J1509. 95
5.15 Spectrum of J1510. 96
5.16 Hβ, [O III]$\lambda\lambda$4959,5007, Hα+[N II]$\lambda\lambda$6548,6583 and [S II]$\lambda\lambda$6716,6731 line profiles of J1510. 96
5.17 Spectrum of J1522. 97
5.18 Hβ, [O III]$\lambda\lambda$4959,5007, Hα+[N II]$\lambda\lambda$6548,6583 and line profiles of J1522. 97
5.19 Spectrum of J1641. 98
5.20 [O III]$\lambda\lambda$4959,5007, Hα+[N II]$\lambda\lambda$6548,6583 and line profiles of J1641. . 98

6.1 Quasi-simultaneous radio spectrum of J1522+3934. Note the very steep rise between 22 GHz and 37 GHz with $\alpha \simeq 16$. This is unphysical and indicates that the source varied between these two measurements, so they cannot be treated as simultaneous for the purposes of spectral analysis. 105
6.2 IRAM radio map at 260 GHz of J1509+6137. The contours are related to the uncatalogued source, while the red symbol is located in the actual position of J1509+6137. 108
6.3 MRO light curves of the sample between June 2022 and January 2024. The blue dots are detections, with the relative flux densities and errors. The orange triangles are the upper limits of non-detections. The green line is related to the date of Effelsberg epoch 3 observations, with an arbitrary flux. 113

6.4 OVRO light curves of the sample between June 2022 and October 2024. The blue dots are detections, with the relative flux densities and errors, while the orange triangles are the upper limits of non-detections. The error bars that are not visible, due to their small values, are within the size of the dots. 114
6.5 J1522+3934 light curve of JVLA X-band observations. 115
6.6 J1522+3934 light curve of JVLA K-band observations. The dots at the bottom are related to non-detections. 115
6.7 10-22 GHz spectral index for the J1522+3934 JVLA observations. The grey dashed line represents the mean value. 115

List of Tables

4.1 Number of data points in the sources LCs. . . . 50
4.2 Starting-ending time of the sources LCs. . . . 50
4.3 Selected gap for the PSD slope estimation algorithm 53
4.4 Variability test. . . . 56
4.5 Fractional variability. . . . 56
4.6 PSD slope. . . . 57

5.1 Properties of the sample. . . . 71
5.2 Observational parameters derived from the optical spectra. . . . 77
5.3 Black hole mass and Eddington ratio results. . . . 82
5.4 Pearson correlation coefficients. . . . 86
5.5 Observational and physical parameters derived from the optical spectra. 89
5.6 [O III]$\lambda\lambda$4959,5007 model parameters. . . . 91
5.7 Hβ model parameters. . . . 91
5.8 Hα+[N II]$\lambda\lambda$6548,6583 and [S II]$\lambda\lambda$6716,6731 model parameters. . . . 92

6.1 MRO 37 GHz detections. . . . 102
6.2 Flare properties at 37 GHz from the MRO detection. . . . 103
6.3 Flare properties at 15 GHz from the MRO-OVRO quasi-simultaneous observations of J1228+5017. . . . 106
6.4 J1522+3934 JVLA observations. . . . 112
6.5 OVRO detections. . . . 116
6.6 Effelsberg observations. . . . 117
6.7 Effelsberg observations - *continued* 118
6.8 Effelsberg observations - *continued* 119

List of Abbreviations

ADAF ..... Advection-dominated accretion flow

AGN ..... Active galactic nuclei

ASAS-SN ..... All-Sky Automated Survey for Supernovae

AU ..... Astronomical unit

BBH ..... Binary black hole

BL Lac ..... BL Lacertae object

BLS1 ..... Broad-line Seyfert 1 galaxy

BLR ..... Broad-line region

CSS ..... Catalina Sky Survey

DFT ..... Discrete Fourier transform

DR ..... Data release

DRW ..... Damped random walk

EC ..... External inverse Compton

EMP ..... Emmanoulopoulos method

ENLR ..... Extended narrow-line region

FAP ..... False-alarm probability

FIRST ..... Faint Images of the Radio Sky at Twenty-Centimeters survey

FFA ..... Free-free absorption

FSRQ ..... Flat-Spectrum Radio Quasar

FWHM ..... Full width at half maximum

GLS ..... Generalized Lomb-Scargle

GTC ..... Gran Telescopio Canarias

HERG ..... High-excitation radio galaxy

IC ..... Inverse Compton

IDFT ..... Inverse discrete Fourier transform

INOV ..... Intra-night optical variability

IRAF ..... Image Reduction and Analysis Facility

IRAM ..... Institut de Radioastronomie Millimétrique

ISCO ..... Innermost stable circular orbit

ISM ..... Inter-stellar medium

JVLA ..... Karl G. Jansky Very Large Array

KWS ..... Kamogata/Kiso/Kyoto wide-field Survey

LC ..... Light curve

LERG ..... Low-excitation radio galaxy

LINER ..... Low Ionization Nuclear Emission Region

LOFAR ..... Low Frequency ARray

LoTSS ..... LOFAR Two-metre Sky Survey

MAD ..... Magnetically arrested disk

MJD ..... Modified Julian day

MRO ..... Metsähovi Radio Observatory

NIR ..... Near-infrared

NLS1 ..... Narrow-line Seyfert 1 galaxy

NLR ..... Narrow-line region

NRAO NVSS .. National Radio Astronomy Observatory Very Large Array Sky Survey

NIKA2 ..... New IRAM KID Array 2

OSIRIS ..... Optical System for Imaging and low-Intermediate-Resolution Integrated Spectroscopy

OVRO ..... Owens Valley Radio Observatory

PCA ..... Principal Component Analysis

PDF ..... Probability density function

PSRESP ..... Power spectral response method

PSD ..... Power spectral density

QPO ..... Quasi-periodic oscillation

QSO ..... Quasi-Stellar Objects

rms ..... Root mean squared

SANE ..... Standard and normal evolution

SED ..... Spectral energy distribution

SMBH ..... Supermassive black hole

SSA ..... Synchrotron-self absorption

SSC ..... Synchrotron self-Compton

TESS ..... Transiting Exoplanet Survey Satellite

TK ..... Timmer & König method

VLA ..... Very Large Array

VLA Sky Survey VLA Sky Survey

WWZ ..... Weighted wavelet Z-transform

ZTF ..... Zwicky Transient Facility

List of Symbols

pc ..... Parsec

Å ..... Angstrom

kpc ..... Kiloparsec

Mpc ..... Megaparsec

T ..... Temperature

μ**m** ..... Micrometer

R_S ..... Schwarzschild radius

$\mathscr{R}$ ..... Radio-loudness parameter

M_{BH} ..... Black hole mass

G ..... Gravitational constant

c ..... Speed of light

η ..... Energy efficiency

$\dot{M}$ ..... Mass accretion rate

L_{bol} ..... Bolometric luminosity

L_{Edd} ..... Eddington luminosity

m_p ..... Proton mass

$\dot{M}_{Edd}$ ..... Eddington limit

σ_T ..... Thomson scattering cross section

ϵ ..... Eddington ratio

λ ..... Wavelength

ν ..... Frequency

Hz ..... Hertz

MHz ..... Megahertz

eV ..... ElettronVolt

keV ..... Kiloelettronvolt

TeV ..... Teraelettronvolt

S ..... Flux density

α ..... Power-law index

γ ..... Lorentz factor

β ..... Velocity in units of c

M_B ..... B-band absolute magnitude

$\mathbf{M}_{\odot}$ ..... Solar mass

Jy ..... Jansky

mJy ..... MilliJansky

η ..... von Neumann ratio

χ^2 ..... Chi-square test

ν_{Nyq} ..... Nyquist frequency

μ ..... LC mean amplitude

β_{PSD} ..... Power-law index for the PSD model

σ^2 ..... Variance

A ..... Amplitude

ϕ ..... Phase

P ..... Peak period in the PSD

$\mathscr{P}$ ..... Peak power in the PSD

p ..... p-value

m ..... Apparent magnitude

σ^2_{NXV} ..... Normalized excess variance

S/N ..... signal-to-noise ratio

k_{bol} ..... Bolometric correction factor

Chapter 1

Active Galactic Nuclei

1.1 Introduction

In modern astrophysics, the most common example of compact objects is represented by black holes. Such objects can be roughly divided into two main categories: stellar black holes, and massive and supermassive black holes. The former reside in the outskirts of active and non-active galaxies, while the latter are located at the center of active galaxies, also called active galactic nuclei (AGN). According to our current knowledge, $\sim$10% of the whole amount of galaxies in the local Universe are active galaxies. They can be easily distinguished from the non-active galaxies, since an AGN is much brighter and generates radiation over the whole electromagnetic spectrum, from radio frequencies up to γ-ray.

A century ago, the understanding of what a galaxy is was just at the very beginning. Fath (1909) performed an optical spectra study of NGC 1068, the first ever AGN spectrum obtained, not really convinced about the extragalactic origin of such a source, then called a nebula. The idea of nebulae outside our Galaxy was first brought forward by Slipher (1917), via redshifted line measurements, lately confirmed by Curtis (1918). Nevertheless, it was the famous work of Hubble (1926), establishing a system of classifying galaxies, permanently abandoning the term nebula, which definitely drew attention to extragalactic astronomy. Even though the idea of the existence of galaxies similar to the Milky Way was being constantly consolidating, we had to wait until 1943 to see the first classification of AGN as a separate class of objects (Seyfert, 1943). Carl Seyfert came to this conclusion by analyzing the spectra of six galaxies with a strong emitting component in the center, noticing that some of them showed narrow emission lines, while others exhibited broader ones. The first distinction between broad and narrow emission line objects led, thirty years later, to the first classification into Seyfert 1 and Seyfert 2 galaxies (Khachikian and Weedman, 1974).

In the same years, the birth of radio astronomy opened a new window on extragalactic research from a different perspective. The radio-engineer Grote Reber made the first radio detection of an AGN at 160 MHz, Cygnus A, using his self-made radio telescope (Reber, 1944). The junction between optical and radio astronomy allowed for growing interest in the AGN research field. The well-known radio calibrator 3C 273 was first detected in 1959 by the third Cambridge survey at 159 MHz (Edge et al., 1959). A subsequent optical study by Maarten Schmidt recognized strongly redshifted Balmer lines, which suggested a redshift of z=0.158. Moreover, due to such a great distance, 3C 273 was estimated to be a hundred times more luminous compared to a normal bright spiral galaxy (Schmidt, 1963). Due to the distance of objects similar to 3C 273, they appear as point-like sources in optical. For this reason, they were named Quasi-Stellar Radio Sources (i.e., quasars) (Chiu, 1964). The quasars class was generalized to Quasi-Stellar Objects (QSO) in those cases where

the sources showed a quasar-like optical spectrum but without radio emission. In the following years, the distinction between quasars and Seyfert galaxies became ever more subtle, understanding that they are two manifestations of the same phenomenon.

Besides the characterization of these new kinds of objects, there were attempts to explain the driver of the emission. Several theories were proposed, spanning from thermal emission by interstellar dust in the optical wavelength (Whipple and Greenstein, 1937), to free-free emission by the ionized gas in the interstellar medium (Reber, 1944), and synchrotron emission in the radio band (Alfvén and Herlofson, 1950). Woltjer (1959) pointed out the necessity of a mass of a few 10^8 $M_\odot$ located in the central regions to explain optical luminosities of 10^{40}-10^{48} erg s^{-1} . In a few years, the idea of a hypermassive star has been replaced with that of a supermassive black hole (SMBH), which emits mainly by accretion processes of gas available in the surrounding disk (Hoyle and Fowler, 1963; Salpeter, 1964; Zel'dovich and Novikov, 1964).

With the advent of new telescopes, AGN were, and are, among the top places as the most interesting sources, since for each answer accomplished, several new questions are raised. Therefore, the complete understanding of the complex puzzle of AGN is far from being reached.

1.2 Structure of AGN

To date, thanks to the never-ending increase of the observational power of ground-based and space observatories, we can distinguish several kinds of AGN (see Sec. 1.3 for a full description). Even though they can show characteristics which can sometimes also be very different, the general structure is considered to be fairly similar for all (Fig. 1.1).

In the central position resides an SMBH, which is the engine of the system, with a mass usually between $\sim 10^5$ $M_\odot$ and 10^{10} $M_\odot$ (Woo and Urry, 2002; Chen et al., 2018). To define its boundary, the event horizon is used, which by definition is the limit beyond which not even light can escape. For a non-rotating black hole, such a boundary is given by the Schwarzschild radius

$$R_S = \frac{2M_{BH}G}{c^2}, \tag{1.1}$$

where M_{BH} is the black hole mass, G is the gravitational constant and c the speed of light. The black hole provides most of the power to the system, but it is obviously invisible by definition since it does not emit any kind of radiation[1]. In the more realistic case of a rotating black hole, the main responsible of the high brightness is the accretion of gas in an accretion disk, which occurs around the black hole up to several R_S. The extremely intense gravitational field of the central compact object efficiently converts the gravitational potential energy into thermal energy, with the resulting radiation production. The disk temperature (T $\sim$ 10^5-10^7 K) is due to viscous friction between layers of gas at different radii. Each gas particle makes a spiraling motion toward the event horizon, which can be, in first approximation, described as the inward motion of rings with different angular momentum. Then inner rings have higher rotational speed, resulting in an increase of the friction and higher

[1]The only radiation which has been theorized to be emitted by a black hole is the Hawking radiation (Hawking, 1974). However, this radiation is extremely faint and therefore negligible for general astrophysical studies.

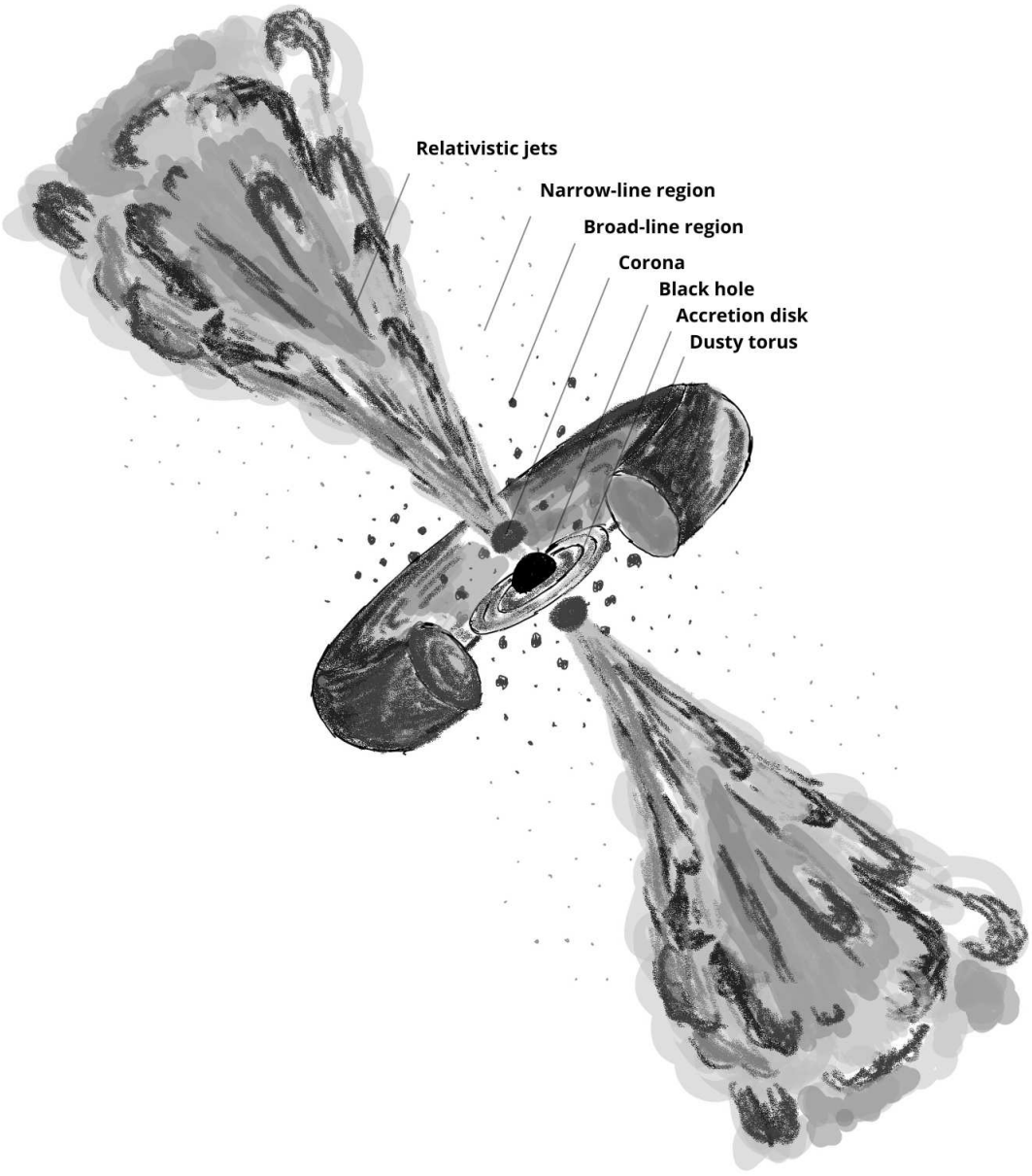

Figure 1.1: Schematic representation of the structure of an AGN.

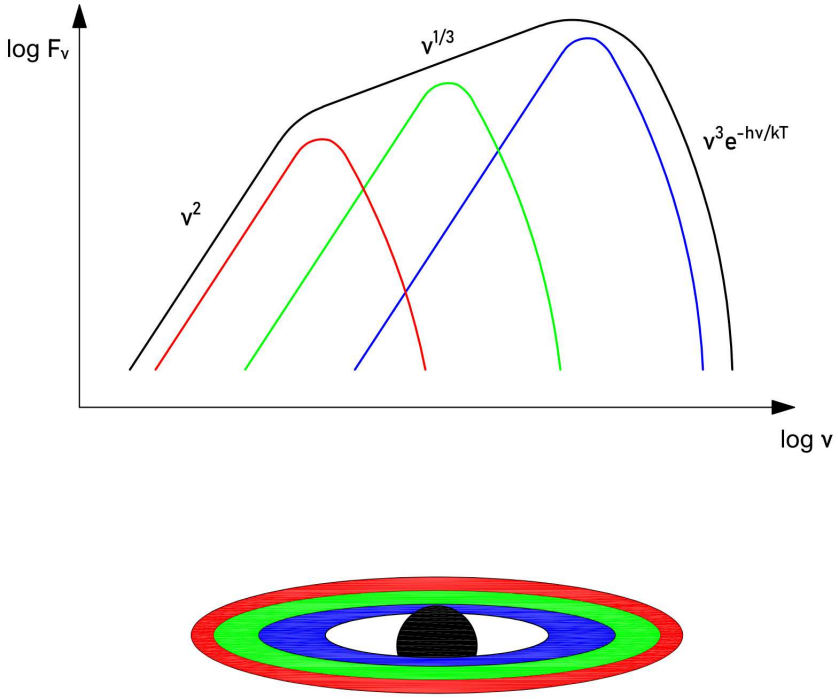

Figure 1.2: Representation of a multi-color blackbody as a result of the superposition of blackbody curves, derived from different rings at increasing temperature in the accretion disk.

temperatures with respect to the farthest ones ($T \propto R^{-3/4}$, Beckmann and Shrader, 2012). This produces a gradient in the disk, along the radial direction, producing a well-defined shape for the optical continuum emission. It is well known that an object with a uniform temperature has a blackbody spectrum. If we consider a temperature gradient for different layers of the accretion disk, we obtain a superposition of blackbody emission profiles. The result is a *multi-color blackbody* (Fig. 1.2), which is a composition of three different blackbody approximations. In the low-energy range the Rayleigh-Jeans spectrum is dominant with a slope of ν^2, in the high energy one the Wien tail that has an exponential cut-off like $\nu^3 e^{-\frac{h\nu}{kT}}$ is present, and in the middle range of energy there is a trend typical of multi-color spectrum which follows $\nu^{1/3}$. In general, the thermal emission of the accretion disk ranges from optical to soft X-ray, with a peak at ultraviolet frequencies often defined as the *Big Blue Bump*.

The bolometric luminosity can be derived as

$$L_{bol} = \eta \dot{M} c^2, \tag{1.2}$$

where η is the energy efficiency, $\dot{M}$ is the mass accretion rate and c the speed of light. If we take a generic particle which is at rest at infinity, and starts from there its motion towards the black hole, considering the energy lost by the particle, η is $\sim 6\%$ (Fabian and Lasenby, 2019). Such an efficiency is more than ten times that of the nuclear burning efficiency in stars.

Such a huge amount of energy irradiated by the disk produces a powerful radiation pressure against the infalling gas particles, mostly interacting via Thomson scattering. For a spheroidal system, the critical value called Eddington luminosity (Eddington, 1926) is reached when the radiation pressure equals the gravitational force

$$L_{Edd} = \frac{4\pi G m_p c M_{\rm BH}}{\sigma_T} \simeq 1.26 \times 10^{46} \frac{M_{\rm BH}}{10^8 M_\odot} \ [\rm erg\ s^{-1}], \tag{1.3}$$

where m_p is the mass of the proton and σ_T the Thomson cross section. The Eddington limit can be derived equaling Eq. 1.2 and 1.3

$$\dot{M}_{Edd} = \frac{4\pi G m_p M_{\rm BH}}{c\sigma_T \eta} \simeq 2.3 \frac{M_{\rm BH}}{10^8 M_\odot} \left(\frac{\eta}{0.1}\right)^{-1} \ \rm M_\odot\ yr^{-1}, \tag{1.4}$$

Such a value is a physical limit because if $\dot{M} > \dot{M}_{Edd}$ the radiation pressure blows away part of the infalling gas, reducing the accretion rate at a level below the Eddington limit. In terms of luminosity, it can be expressed as the Eddington ratio

$$\epsilon = \frac{L_{bol}}{L_{Edd}} \tag{1.5}$$

As mentioned, all the cited equations are derived for accretion in spheroidal geometry. Since the accretion has a disk shape in AGN, these limits can be used as references. For this reason, a super-Eddington accretion can be maintained. There are three main models used to describe the physical properties and radiative processes of the accretion disk. The optically thick, geometrically thin accretion disk model, also known as the Shakura-Sunyaev model (Shakura and Sunyaev, 1973), is widely adopted for AGN with $\epsilon \sim 0.01$ to 0.3. The radiatively inefficient advection-dominated accretion flow (ADAF) model (Ichimaru, 1977; Narayan and Yi, 1995) is found in low-luminosity AGN with $\epsilon < 0.01$, which indicates a geometrically thick and optically thin accretion. Finally, the slim disk model (Abramowicz et al., 1988; Szuszkiewicz, Malkan, and Abramowicz, 1996; Mineshige et al., 2000) presents a thin disk-like geometry but with considerable advection, and it is suitable for luminous quasars with high accretion rates ($\epsilon > 0.3$) like narrow-line Seyfert 1 (NLS1) galaxies.

Beyond the accretion disk lies a toroidal region composed of molecular gas and warm dust clouds (T $\sim$ 100-1500 K). The torus absorbs part of the radiation coming from the central engine, re-emitting it at infrared wavelengths. Part of the torus could be formed by gas from the outer layers of the accretion disk, and the inner radius is set by the dust sublimation temperature (Netzer, 2015). Even though in general approximation this region can be represented as a torus, recent studies are pointing more toward a region composed of an equatorial dusty disk and a polar dusty wind, launched by radiation pressure (Drewes et al., 2025). As it is described in Sec. 1.3, the dusty torus is one of the elements used by some classification schemes.

Above and below the SMBH, a corona made of hot plasma (T $\sim 10^8$-10^9 K) (Liang, 1979) is thought to be present. Its existence is still widely debated, but the majority believe that it is the region where most of the X-ray emission originates (Sunyaev and Titarchuk, 1980). In this case, there are two main models theorized to describe the corona geometry. The two-phase model (Liang, 1979; Haardt and Maraschi, 1991; Haardt and Maraschi, 1993) relies on two coupled elements: an optically thin hot X-ray corona and an optically thick cold UV-emitting accretion disk. Here, the soft emission from the disk undergoes an inverse Compton scattering in a plane-parallel corona, producing a hard emission some of which comes back to the thick disk by heating it. The resulting emission is made of polarized hard and soft X-rays, with a polarization degree dependent on the optical thickness and geometry of the corona (Marinucci et al., 2022; Di Gesu et al., 2023). In particular, the soft X-ray emission can superimpose the typical AGN X-ray power-law continuum, producing a soft X-ray

excess. The Lamp-Post model instead assumes a point-like source located on the rotation axis above the SMBH (Matt, Perola, and Piro, 1991; Martocchia and Matt, 1996; Henri and Petrucci, 1997; Petrucci and Henri, 1997; Martocchia, Karas, and Matt, 2000; Miniutti and Fabian, 2004). In this scenario, part of the coronal emission is reflected by the accretion disk. Therefore, the observer sees the primary radiation from the corona and the reflected one from the disk.

Moving away perpendicularly to the plane of rotation, there are two regions responsible for the crowding of emission lines in the spectrum: the broad-line region (BLR) and the narrow-line region (NLR). The BLR is an extremely dense region with an electron density of 10^9-10^{11} cm^{-3}. Here prominent permitted lines are produced, such as hydrogen Balmer lines (e.g. Hα λ6563, Hβ λ4861 and Hγ λ4340), Lyα λ1216, Mg II λ2798, He II λ4686, He I λ5876 and others. Recombination emission lines are formed thanks to the ionizing photons that come from the nearby accretion disk. Moreover, Fe II multiplets are generated in the wavelength range between 4000 and 5500 Å and in the UV band, for instance. The average temperature is estimated to be $\sim 10^4$ K, which produces a broadening of a few km s^{-1} . The main broadening which characterizes the emission lines in this region, which can be of several thousands km s^{-1} , is the Doppler broadening, which is due to the rapid motion of the gas because of the proximity to the black hole. Some insights suggest that the BLR is composed of clouds, and not of a uniform distribution of gas (Ferland and Mushotzky, 1982; Nenkova et al., 2008a; Nenkova et al., 2008b). The wide-scale geometry, however, is difficult to analyze. Recent spatially resolved spectro-astrometry data for a few high-mass AGN claimed a flattened geometry for fast-rotating BLR, while a more spherical geometry for slower BLR (GRAVITY Collaboration et al., 2018; GRAVITY Collaboration et al., 2020; GRAVITY Collaboration et al., 2021; GRAVITY Collaboration et al., 2024). Each cloud is in photoionization equilibrium, namely, the photoionization rate due to the ionizing photons coming from the accretion disk is equal to the recombination rate. Since the BLR is positioned all above and below the accretion disk, the inner part of the clouds that faces the central engine has a higher ionization degree compared to the back side. This suggests the emission of high ionization lines in the inner part, while the low ionization lines would be consequently produced in the back of the clouds.

The NLR is the most extended region of the structure of an AGN, and the farthest away from the center. As it is clear from the name, it is the place where the narrow emission lines are emitted. Among the most frequently visible narrow lines in spectra, there are [O III]$\lambda\lambda$4959,5007, [O II]λ3727, [O I]λ6300, [N II]$\lambda\lambda$6548,6583, [S II]$\lambda\lambda$6716,6731, and C III]λ1909. All the cited emission lines are forbidden or semi-forbidden lines. This is due to a low density of the region around 10^3-10^5 cm^{-3}. In addition, several other permitted emission lines are produced. Also, the orbital velocity of the gas is much lower compared to the BLR gas velocity, that is, from 300 to 1000 km s^{-1} , resulting in narrower lines. However, the dynamics of the region is not influenced only by the central compact object, but also by the gravitational field of the stars (Nelson and Whittle, 1996), especially at large distances from the nucleus. Other elements which can modify the width and the shape of the lines in the NLR are the outflows and the relativistic jets (Peterson, 1997; Komossa et al., 2008; Berton et al., 2016c). The geometry is axisymmetric and, similar to the BLR, the gas is divided into clouds. In some cases, we can find an extended narrow-line region (ENLR; Cracco et al., 2011; Harrison et al., 2014; Congiu et al., 2017) that can reach up to several kiloparsecs.

The last element that shapes the structure of AGN is the relativistic jet. Due to its nature and the strong connection with the black hole, the available knowledge about

its composition, evolution, and emission mechanisms is still limited. When present, it is actually composed of two almost identical jets, one along the northern semi-axis of the black hole, and one along the southern (Fig. 1.1). Not all AGN host relativistic jets, only about 10% of sources host them (Padovani, 2017). As a matter of fact, the expulsion of material by an AGN ranges from non-collimated outflows to collimated relativistic jets. The main theory for the jets production claims that part of the ionized matter, during its travel toward the black hole, interacts with the strong magnetic field generated by the accretion disk. The accretion disks most favorable to the jets production are usually those described by the ADAF and slim disk models (Foschini, 2017). Because of the black hole spin, the latest beliefs show that the magnetic field lines start from the plane of the accretion disk and are developed along both rotation semi-axes, with a spiral shape. Therefore, the ionized particles follow such magnetic field lines, being accelerated by Fermi acceleration, generating a bi-conical shape typical of jets (Blandford and Znajek, 1977; Blandford, Meier, and Readhead, 2019). The spin of the black hole, as well as the magnetic field strength, and the accretion disk characteristics, are just a few of the factors that set the jets characteristics. As a result, the relativistic jets emission spans along the entire electromagnetic spectrum, from radio to γ-ray, and sometimes even beyond. The main emission mechanism is the non-thermal synchrotron radiation. The accreting gas is ionized, then the free electrons perform a spiral motion around the magnetic field lines, which causes a constant acceleration. This leads to the emission of radiation by the electrons with a well-defined spectral shape, defined as

$$S_\nu = \nu^\alpha \tag{1.6}$$

where S_ν is the emitted flux density, ν is the frequency of emission, and α the power-law index. In the case of an optically thin medium, α is around -0.7 (Condon and Ransom, 2016), and typical values seen for relativistic jets are $\alpha > -0.7$. Synchrotron emission is dominant at radio frequencies, but it extends to the optical/UV, and also up to X-ray in some specific types of AGN. In an optically thick medium, below a critical frequency, part of the emitted photons are reabsorbed by the charged particles that emitted them. The lower the energy of the photons, the higher the probability for them to be absorbed. Such a phenomenon is called synchrotron self-absorption (SSA). At higher frequencies, the main radiative process is the inverse Compton (IC) scattering, which produces a peak in γ-ray. Here, the scattering between relativistic electrons and seed photons gives the photons energy. Such seed photons can come either from the region around the jets, undergoing the external inverse Compton (EC), or from the jets, experiencing the mechanism called synchrotron self-Compton (SSC).

Relativistic jets are all but a uniform expulsion of gas. Their internal structure constantly changes and evolves according to how matter is injected from the accretion disk. There are substructures like moving blobs of matter and shocks which produce hot spots (Marscher and Gear, 1985; Türler, 2011). In particular, the shocks are formed when minor disturbances propagate along the jets. They are one of the main sources of flux density variability in jetted AGN (Hughes, Aller, and Aller, 1985; Hughes, Aller, and Aller, 1989). Besides a relatively small amplitude variability, a strong increase with a consequently rapid damping of the flux density is sometimes observed during AGN flare episodes. The variability of AGN will be further discussed in Sec. 3.

Due to the high velocities, the jets are among the most interesting natural laboratories for special and general relativity. Indeed, several relativistic effects occur as

the relativistic beaming, the Doppler boosting, and the relativistic aberration, among the most relevant. The relativistic beaming becomes more and more dominant as the jet is pointing closer to the line of sight of the observer. In such a condition, due to the time dilation of a relativistic emitter, the delay between two consecutive photons is larger in the observer's rest frame compared to the emitter's rest frame. This causes superluminal motion, namely an apparent velocity of the emitting particles greater than c, and a boost on the observed flux density (Rees, 1966). One of the main relativistic factors is the Lorentz factor, defined as

$$\gamma = \frac{1}{\sqrt{1-\beta^2}} \tag{1.7}$$

in which β is the velocity of a particle in units of c. As described before, jetted AGN emit a jet along the northern semi-axis of the black hole and one along the southern semi-axis. Except for the limit case of an edge-on view, there is always a jet approaching and the other receding from the observer. The radiation of the former is therefore enhanced, while the radiation of the latter is diminished due to the relativistic Doppler boosting effect. The incoming flux density can even increase by several thousand times (Lähteenmäki and Valtaoja, 1999). Also, the relativistic aberration produces an increase in the flux density. The emitted radiation is beamed in a narrow cone pointing towards the direction of motion in the co-moving rest frame of the source. The increasing velocity of the source narrows the cone aperture ($\propto 1/\gamma$ for $\gamma \gg 1$), increasing the observed flux density. Considering all the cited relativistic effects, the observed enhanced flux density is dependent on the Lorentz factor, the angle between the jet and the line of sight of the observer, the intrinsic spectral index of the jet power-law, and, of course, on the emitted flux density in the co-moving frame of the jet.

1.2.1 Sizes in an AGN

Measuring the size of elements in extragalactic sources is a challenge. Obviously, the main limitation is given by the technology, since the angular resolution that allows for spatially resolving the astronomical object's components is directly proportional to the size of the telescopes. In the last thirty years, the interferometry technique has developed a lot, in radio and also in optical, preciously helping in the acquisition of images with increasing resolution. Nevertheless, direct measurements are not always possible, since not everything is visible. The most striking case is represented by the black hole, invisible by definition. As stated in Sec. 1.2, the dimension of a black hole is commonly set by the Schwarzschild radius (Eq. 1.1), in which the unknown parameter is the black hole mass. There are several ways to estimate the $M_{\rm BH}$, through either the kinematics of nearby objects or the dynamics of the system, then obtaining an approximate size for the $R_{\rm S}$ of around 0.01-10 astronomical units (AU). For the accretion disk, the inner and outer boundaries are calculated in different ways. The inner part is set by the black hole influence, called the innermost stable circular orbit (ISCO). The radius of the ISCO varies if the black hole is rotating or not (Kerr or Schwarzschild solution, respectively), and if the accretion disk is co- or counter-rotating with respect to the black hole spin. Accounting for all of this, the $R_{\rm ISCO}$ can vary between 1.2-6 $R_{\rm S}$, and its physical size becomes $R_{\rm ISCO} \sim$ 0.01-60 AU. For the estimation of the outer radius, there are direct methods, through either gravitational microlensing (Kochanek, 2004; Morgan et al., 2006) or continuum reverberation mapping (Collier et al., 1999; Cackett, Horne, and Winkler, 2007), or even relying on scaling laws (e.g. Morgan et al., 2010). An approximate value is

between 1 and 1000 AU. Usually, the dust sublimation radius is used as a reference for the dusty torus dimension (Elitzur, 2008; Foschini et al., 2019). However, recent interferometric data directly measured a size for such a torus around 40 pc (Drewes et al., 2025). On average, dimensions of ∼1-50 pc can be claimed. The size of the corona is still a very debated topic. The most recent literature states that the corona likely resides within a few to tens of R_S (Hancock, Young, and Chainakun, 2023; Chan et al., 2025).

The BLR usually extends from 0.01 pc to 1 pc. For its size measurements, the usage of the emission lines' delay by the reverberation mapping technique is one of the most reliable methods (Blandford and McKee, 1982; Peterson, 1993; Peterson et al., 2004). Unfortunately, it is as effective as time-consuming, since long timescale observations are necessary. For this reason, if not enough data are available, scaling laws are widely used (see Sec. 5). The NLR starts right after the BLR, even though the two regions are not physically separated, but instead the boundary is more of a smooth transition from one region to the other. In any case, the size attributed to the NLR goes from 1-10 pc for the inner layer, up to 10^5 pc for the farthest. A standard dimension for the relativistic jets cannot be defined. Because it depends on the type and evolution of the AGN, and also on the internal environment of the source, which could help or hinder the jets' propagation. For small-scale jets, models and simulations suggest sizes also of AU-scale. On the other hand, Mpc-scale jets (∼10% of the total jetted AGN) can be easily measured by radio interferometers.

1.3 Taxonomy and unification

One of the fundamental questions in AGN research, but recurrent in every field of observational astrophysics, is whether all the different types of sources can be classified with a unique common model. The key element is to identify if there is one or more parameters that drive the behaviors of the objects. However, from an observational point of view, two sources may appear different even if they are physically identical. In fact, an observational classification does not usually match a more physical taxonomy. From the point of view of observations, two main broad classification schemes for AGN were developed, considering the radio emission and optical/UV spectra.

In the first case, the distinction is made according to the radio-loudness parameter $\mathscr{R}$ (sometimes also called Kellerman parameter, from Kellermann et al., 1989), defined as the ratio between the radio flux density at 5 GHz and the optical flux density in the B-band. In this way it is possible to divide radio-loud ($\mathscr{R} > 10$), radio-quiet ($\mathscr{R} < 10$), and radio-silent ($\mathscr{R} = 0$) AGN. Old ideas claim that radio-loud sources are those capable of launching and maintaining relativistic jets, while radio-quiet sources do not (Hutchings, Janson, and Neff, 1989; Wilson and Colbert, 1995). Although used for several years, and not completely set aside even nowadays, it has been proven that the radio-loudness parameter is not reliable to predict the presence of relativistic jets. For this reason, a distinction between jetted and non-jetted AGN must be preferred (Padovani, 2017; Järvelä et al., 2017; Lähteenmäki et al., 2018; Berton and Järvelä, 2021b).

In the second case, the optical/UV emission lines are used to distinguish between Type I and Type II AGN, which is thought to be due to obscuration effects. The former have spectra with broad emission lines (full width at half maximum (FWHM) > 3000 km s^{-1}), besides narrower emission lines, therefore, they are completely unobscured sources. On the other hand, the latter only shows narrow emission lines,

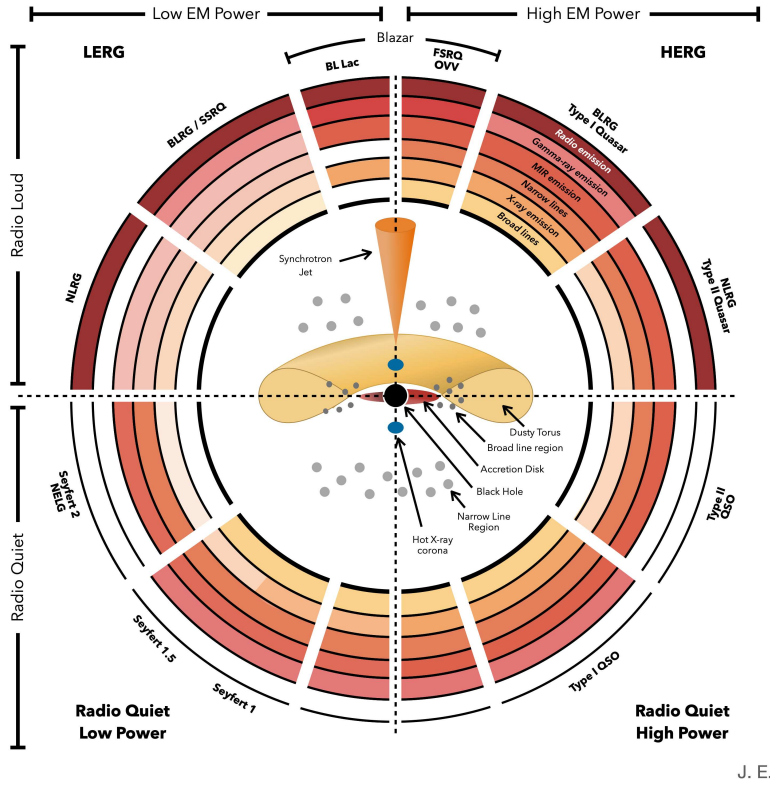

Figure 1.3: AGN unification model (Thorne et al., 2022).

since the BLR is obscured. In addition to the main distinction, are usually defined Type 0 AGN those sources in which any strong emission or absorption feature in the optical spectrum is missing, and intermediate AGN which have the broad lines being weaker compared to Type I and the narrow lines being stronger than in Type II.

The two described classifications set general constraints on the plethora of AGN. Using them, the AGN zoo can be identified (Fig. 1.3) which is made of several families of sources with the same intrinsic nature, briefly described below.

- **Seyfert galaxies:** Classified for the first time by Carl Seyfert (Seyfert, 1943) as a distinct class of AGN. On average they show $10^{40} < L_{bol} < 10^{46}$ erg s^{-1} and a B-band absolute magnitude $M_B > -23$. Seyfert galaxies are radio-quiet sources, with strong emission lines in the optical spectra. They are mainly divided into Seyfert 1 (Type I) and Seyfert 2 (Type II) galaxies. However, there are two more subclasses: the intermediate Seyfert (intermediate between Type I and Type II) and the NLS1 (Type I, Sec. 2). Their host galaxy is usually an early-type spiral (Xanthopoulos, 1996), namely with a more elliptical-like morphology. The continuum level of the spectrum of Seyfert 1 is brighter compared to the one of its host galaxy. Instead, the continuum in Seyfert 2 galaxies tends to have a brightness similar to that of their host galaxy.

- **Quasi-Stellar Objects:** Also QSOs are radio-quiet sources, and they can be Type I or Type II. Their radio-loud counterpart are the quasars, with similar features but with a stronger radio emission. QSOs have similar spectra to Seyfert galaxies, but they are more powerful ($L_{bol} > 10^{46}$ erg s^{-1} and $M_B < -23$).

- **LINERs:** Low Ionization Nuclear Emission Regions properties are very similar to Seyfert 2 galaxies, but they do have stronger forbidden lines and fainter ionization lines. With luminosities of $L_{bol} \lesssim 10^{40}$ erg s^{-1} , they are supposed to be the connection between Seyfert galaxies and non-active galaxies (Beckmann and Shrader, 2012). They are radio-quiet AGN with usually early-type spiral host galaxies.

- **Blazars:** They are jetted sources seen face-on, with the line of sight inside the jet, and are divided into two main classes: BL Lacertae Objects (BL Lac) and Flat-Spectrum Radio Quasars (FSRQ) (Urry and Padovani, 1995). They are radio-loud AGN with rapid optical variability and highly polarized emission. FSRQs are efficient accretors, producing strong emission lines in their optical spectrum. BL Lacs instead have inefficient accretion mechanisms and subsequent lower luminosities, with a featureless optical spectrum (Strittmatter et al., 1972). They constitute the largest population of γ-ray sources.

- **Radio galaxies:** Radio galaxies are thought to be the parent population of blazars seen at large angles, since they show similar features in the optical spectra. They can be both Type I and Type II, and they frequently show relativistic jets and resolved radio structures. Radio galaxies usually reside in giant elliptical galaxies (Capetti, Massaro, and Baldi, 2017a; Capetti, Massaro, and Baldi, 2017b).

The most famous orientation-based model introduced with the aim of finding a common AGN scheme is, without a doubt, the Unified Model, proposed by Antonucci (1993). Antonucci and Miller (1985) discovered that the distinction between Seyfert 1 and Seyfert 2 galaxies was an obscuration effect. Since the main obscuring element is the dusty torus, the Unified model discriminates between the different types of AGN according to the inclination of the symmetry axis of the AGN relative to the line of sight of the observer. When a source is seen at low inclination angles, face-on, all the central emitting regions, as the BLR, are visible from the observer's point of view. In this case, the optical spectrum shows both broad and narrow emission lines (i.e., Type I sources). Increasing the inclination angle, till the limit case of an edge-on view, the dusty torus partially or fully shadows the innermost region, hiding, for instance, the broad emission line components in the spectrum (i.e,. Type II and intermediate sources). Coupling the Unified Model with $\mathscr{R}$, and other spectral features, the different kinds of sources can be divided as in Fig. 1.3. More specific models have been proposed, as the 4D Eigenvector 1 AGN parameter space for Type I AGN, for instance (Marziani, Dultzin-Hacyan, and Sulentic, 2006; Sulentic, Dultzin-Hacyan, and Marziani, 2007).

From a physical point of view, AGN can be divided into jetted and non-jetted as we already described. Similarly, Heckman and Best (2014) divided AGN into two distinct populations, which are radiative-mode and jet-mode AGN, performing a low-redshift large survey of the Universe. The former are associated with slightly less massive black holes growing in high-density pseudo-bulges, accreting at around 1% of the Eddington limit. The circumnuclear environment contains high-density cold gas, which is associated with the ongoing star formation. In the latter, most of the energy extracted from the accretion process is expelled by the relativistic jets. This population is associated with the more massive black holes, which usually reside in massive elliptical galaxies. Such black holes are probably fueled by the accretion of slowly cooling hot gas, with a very low efficiency accretion mechanism. Star formation in jet-mode AGN is either missing or very inefficient. In some cases,

radiative-mode AGN can also harbor relativistic jets. A similar distinction dedicated to jetted AGN, focused on the optical spectrum, defines high-excitation radio galaxies (HERGs), the sources that show strong narrow emission lines and sometimes also broad emission lines, and low-excitation radio galaxies (LERGs), the AGN with only weak or no emission lines in their spectra. Probably even in this case, the difference seems to correspond to two different accretion mechanisms (Hardcastle, Evans, and Croston, 2006). HERGs are similar to radiative-mode AGN, and on the other hand, LERGs are thought to accrete as jet-mode AGN.

As stated in Sec. 1.2, the knowledge we have on the physics of relativistic jets, especially on their formation, is very limited. For this reason, it is not easy to understand which types of AGN are more prone to host relativistic jets. For several years, as described, $\mathscr{R}$ was thought to be the key component able to identify jetted sources. As a consequence, only radio-loud AGN residing in massive elliptical galaxies, with massive black holes, were believed to be the perfect environment for the production of relativistic jets (McLure et al., 1999; Laor, 2000). Indeed, AGN with late-type host galaxies are more likely radio-quiet sources (Bahcall et al., 1997). Nowadays, it is confirmed that $\mathscr{R}$ is not a reliable proxy in the distinction between jetted and non-jetted AGN, at least in general, since numerous AGN with relatively low-mass black holes, residing in spiral galaxies, have been found to emit powerful relativistic jets (Järvelä, Lähteenmäki, and Berton, 2018; Varglund et al., 2022; Varglund et al., 2023). A debated role in the jets production is that of mergers. It seems that major mergers have a key role in this context. Nevertheless, a common understanding has not been reached yet, because there are still many conflicting opinions (Kaviraj et al., 2015; Hota et al., 2011; Bagchi et al., 2014; Singh et al., 2015; Tadhunter, 2016). The black hole spin was proposed as another essential ingredient in jetted sources. Some theories state that powerful relativistic jets can be launched only by fast-rotating black holes, coupled with an ADAF accretion at low ϵ (Tchekhovskoy, Narayan, and McKinney, 2010; Bagchi et al., 2014). Such conditions can be reached in case of either prolonged non-isotropic gas accretion or ideal mergers conditions (Volonteri et al., 2005; Dotti et al., 2013) for less massive black holes in late-type galaxies ($M_{\rm BH} < 10^8$ $M_\odot$; Kinney et al., 2000; Schmitt et al., 2001; Capetti et al., 1999; Kharb et al., 2006), even though they are more easily reached by heavier black holes in early-type galaxies (Sob'yanin, 2018). Two scenarios explaining the capabilities of an AGN to launch relativistic jets, through the interplay between the accretion disk and the magnetic field, have a growing consensus. The first is the magnetically arrested disk (MAD; Bisnovatyi-Kogan and Ruzmaikin, 1974; Narayan, Igumenshchev, and Abramowicz, 2003; Tchekhovskoy, Narayan, and McKinney, 2011; McKinney, Tchekhovskoy, and Blandford, 2012), and the second is the standard and normal evolution (SANE; Narayan et al., 2012). In particular, in the MAD scenario, recent simulations confirmed the theory (Chamani et al., 2021; Ricci et al., 2022; McKinney et al., 2017; Liska et al., 2022).

1.4 Observational properties

The observational behaviors of AGN are incredibly peculiar among all astrophysical sources. In particular, extendedness, intensity, and variability of the emission over the whole electromagnetic spectrum are the main ones. Briefly, AGN show a very broad band emission, from MHz frequencies in the radio domain all the way up to the TeV energy range, by both emission lines and continuum emission. They are extremely bright, with luminosities $L_{bol} \gg 10^{40}$ erg s^{-1} , which can sometimes exceed

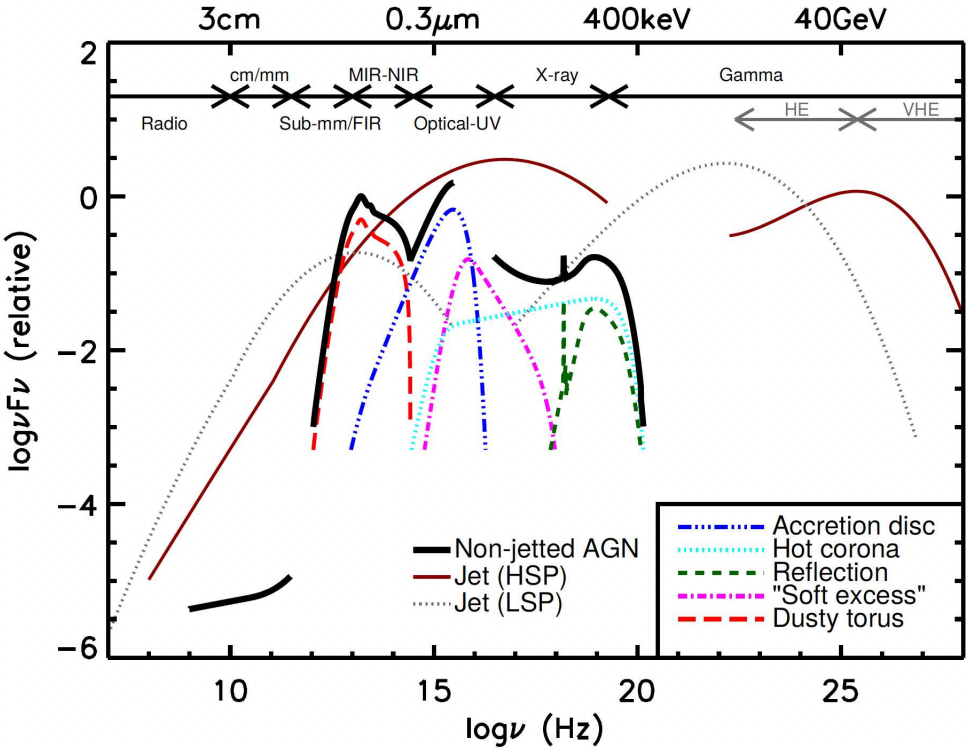

Figure 1.4: Schematic representation of an AGN SED. The black solid curve represents the total SED and the colored curves represent the individual components (Padovani et al., 2017, adapted from Harrison et al., 2014).

the total luminosity of their host galaxy. Finally, their emission exhibits stochastic variability and rarely also presents a periodic pattern (e.g., in the case of binary black holes).

1.4.1 Spectral Energy Distribution

All physical processes taking place in an AGN (partially described in Sec. 1.2), both thermal and non-thermal, compose the spectral energy distribution (SED). The emission from each region is the result of several processes. Even though every source has its own SED, the general shape is quite standard, dividing blazars and other AGN. With the jet seen pole-on, blazars' SED is dominated by the jet emission. Indeed, it is typically characterized by two bumps. The lower frequency bump is due to synchrotron radiation by the jet, while the higher frequency one originates from IC scattering.

Fig. 1.4 shows a schematic representation of SEDs, which can be divided into four main emission bands: radio, infrared, optical/UV, and high energies, that, omitting the jet component for a moment, can be described as follows.

- **Radio:** As described in Sec. 1.3, an AGN can be either radio-quiet, with weak radio emission, or radio-loud, showing a much powerful radio continuum. The radio emission can consist of extended and compact components. The dominant component at this wavelength, for jetted sources, is composed of the synchrotron emission with the typical power law trend (Eq. 1.6; Jones, O'Dell, and Stein, 1974). In this case, the extended emission arises from large-scale jet lobes, while the compact emission is believed to be coincident with a position

close to the central black hole, called the core or the jet base. In the case of non-jetted AGN, the radio spectrum comes from different elements, such as supernova remnants, free-free emission from ionized gas, AGN-driven winds, low-power jets, outflows, and coronal activity (Condon et al., 1998a; Panessa et al., 2019; Chen et al., 2023).

- **Infrared:** At wavelengths between 1 and 300 μm, an important contribution to the bolometric luminosity comes from the infrared emission (red dashed line in Fig. 1.4). Its origin can be thermal or non-thermal. For jetted sources, the infrared band is composed of synchrotron emission and emission coming from synchrotron photons produced in the radio band upscattered by SSC (Beckmann and Shrader, 2012; Fernández-Ontiveros et al., 2013). Nevertheless, a thermal origin has been recently proposed (Collinson et al., 2017). In particular, there are three sources of thermal infrared emission. The first is the re-emission by the dusty torus of the absorbed optical/UV continuum produced in the accretion disk. The wavelength range of such radiation is $\sim$10-20 μm, which corresponds to a typical temperature value for the dust grains of $\sim$1000-2000 K, which is a reasonable temperature for the dusty torus region. This first idea is supported by the time delay between the variability of the optical/UV continuum and the infrared continuum, agreeing with the travel time required by the photons emitted in the accretion disk to reach the dusty torus (Hönig and Kishimoto, 2011; Cackett, Bentz, and Kara, 2021). The second is the thermal dust continuum associated with star formation and starburst activity. Finally, the third is the emission lines production from molecules and atoms, investigated thanks to the Spitzer space telescope (Netzer et al., 2007; Soifer, Helou, and Werner, 2008).

- **Optical/UV:** The spectral shape in the optical and UV bands is defined by the thermal multi-color blackbody, emitted by the accretion disk (see Sec. 1.2 and Fig. 1.2). In the SED, there is a peak in the UV corresponding to the Big Blue Bump (bump in the blue dash-dot line in Fig. 1.4), which for highly accreting AGN is supposed to be emitted by the outer layers of the accretion disk (Jin et al., 2017). According to the Unified model, Type I and Type II sources show different values of continuum since the higher the inclination, the smaller the visible central region. At these wavelengths, several broad and narrow emission lines crowd the spectrum. They can be produced in the broad- or the narrow-line region, and are still one of the most used elements for AGN classification. Another component in the optical/UV is the host galaxy spectrum. Even if less dominant compared to the AGN optical spectrum, it shows a continuum emission with a few faint absorption lines.

- **High energies:** X-ray emission is next after the UV band. Its origin is thought to come from the innermost part of the accretion disk and the debated corona (Haardt and Maraschi, 1991). In any case, the vicinity to the black hole is necessary to produce X-ray photons (Green, McHardy, and Lehto, 1993), since the main idea is that such photons are optical and UV photons which have undergone an IC scattering (Fabian, 1989; Haardt and Maraschi, 1993). In first approximation the spectrum in this band is described by a power-law (with an index $\sim$2, Piconcelli et al., 2005), with an increasing flux toward shorter wavelengths until a cutoff ($\sim$200-300 keV), called Compton edge, which likely corresponds to the cut-off in the electron energy distribution involved in the scattering process (Fabian et al., 2017). The same photons that produce the main X-ray

spectrum illuminate the neutral and ionized material in the accretion disk and the dusty torus. This generates a characteristic reflection spectrum that is the result of both Compton scattering and photoelectric absorption, generating either Auger de-excitation or fluorescent emission lines (Guilbert and Rees, 1988; Matt, Perola, and Piro, 1991). As a result, in the spectrum there is a Compton hump, at $\sim$20-30 keV, and an Iron Kα line. Arnaud et al. (1985) firstly identified an extra emission peaked at around 0.5 keV, subsequently found in many AGN. It is known as X-ray soft-excess and its origin is still almost totally unknown (Bianchi et al., 2009). The three described components are represented in Fig. 1.4 by the dotted cyan, dashed green, and dash-dot magenta lines, respectively. γ-ray emission and beyond must be produced by IC by electrons with relativistic velocities. The most likely place where such scattering can occur is within the jets, since these are almost the only environment where relativistic effects can take place (Zhang and Cheng, 1997).

Chapter 2

Multiwavelength properties of narrow-line Seyfert 1 galaxies

The first official classification of NLS1s as a separate class of AGN was provided by Osterbrock and Pogge (1985). However, the insight that these sources had something different compared to the other Seyfert galaxies dates back to a few years before (Davidson and Kinman, 1978). Investigating the optical spectrum of Mrk 359, they found narrow emission lines in a clear Type I AGN. The main optical features with which NLS1 galaxies are uniquely identified are a FWHM of the Hβ line $<$ 2000 km s^{-1} (Goodrich, 1989), a flux ratio between the [O III]λ5007 emission line and the broad component Hβ line $<$ 3, and a strong Fe II multiplets emission always compared to the Hβ (Boroson and Green, 1992; Osterbrock and Pogge, 1985). This confirms their Type I nature, since an unobscured nucleus is necessary to detect the Fe II emission and a prominent Hβ. The optical spectrum features are described in detail in Sec. 2.1.

Using several measurement methods (see Sec. 2.1.1 for an overview), the black hole mass was found to be $\sim$10^6-10^8 M$_\odot$, lower compared to the Seyfert class (Peterson, 2011; Komossa, 2018). Such a low mass explains the narrowness of the permitted lines, since a lower gravitational force leads to a lower rotational velocity of the clouds, like the BLR. This reduces the Doppler broadening, which is the main source of broadening for the emission lines (Peterson, 2011). Coupling relatively low black hole masses with luminosities of $10^{40} < L_{bol} < 10^{46}$ erg s^{-1} , comparable to the Broad-line Seyfert 1 (BLS1) galaxies' luminosities, from Eq. 1.5, the result is a high accretion rate, usually with ϵ between 0.1 and 1, but sometimes even higher (Boroson and Green, 1992; Marziani et al., 2018a; Tortosa et al., 2022). The high accretion rate suggests a slim disk model for the geometry of the accretion disk (Mineshige et al., 2000).

One of the most interesting points, which makes the study of NLS1s so puzzling, is their capability to launch powerful relativistic jets. As described in Sec. 1.2, the jets are one of the main sources of radiation in the radio band. Originally, NLS1s were classified as radio-quiet without any doubt, since no radio detections occurred. Remillard et al. (1986) detected for the first time a radio-loud NLS1, and Komossa et al., 2006 found that roughly 7% of this population is composed of radio-loud sources. However, radio emission from an AGN does not necessarily mean that such a source hosts relativistic jets. The confirmation arrived in 2009 with the γ-ray detection of an NLS1 (PMN J0948+0022) by the *Fermi Gamma-ray Space Telescope* (Abdo et al., 2009a; Abdo et al., 2009b; Foschini, 2011b). This important discovery, succeeded by many other detections, confirmed NLS1s as a new population of jetted AGN, besides blazars and radio-galaxies (Abdo et al., 2009b; Foschini et al., 2010). Thanks to this, there was an improvement in AGN understanding. NLS1s have a different environment compared to the other jetted AGN, like blazars, especially in terms of

black hole mass and host galaxy morphology, but in any case, they are capable of launching fully developed relativistic jets with blazar-like powers (Foschini et al., 2015). So far, ∼20 γ-NLS1s are known (Lähteenmäki et al., 2018; Romano et al., 2018; Paliya et al., 2019; Romano et al., 2023), and several new possible candidates have been selected (Foschini et al., 2021; Foschini et al., 2022). Even though the total number is quite small, it is important to remember that γ-ray detections occur only when these sources are in a flaring state (Foschini, 2011a). Other roughly 50 jetted NLS1s have been confirmed through radio imaging (Richards and Lister, 2015; Lister et al., 2016; Berton et al., 2018; Chen et al., 2018; Chen et al., 2020; Chen et al., 2022). Usually, but not exclusively, γ-NLS1 galaxies show a considerable radio emission with flat radio spectra (Abdo et al., 2009a; Foschini et al., 2015; Schulz et al., 2016). Radio properties will be further discussed in Sec. 2.2.

In the X-ray band, they show steeper spectra than regular Seyfert galaxies (Boller, 2000; Grünwald et al., 2023), also strongly variable (Boller, Brandt, and Fink, 1996). The spectrum in this band is rather complex, showing a partial covering, with a column density of $n_H \sim 10^{22}$ cm^{-2}. The spectral shape and the X-ray brightness can be due to an intense Compton cooling of the corona, a further indicator of intense accretion activity (Pounds, Done, and Osborne, 1995; Kara et al., 2017). A super-Eddington accretion can also produce strong outflows, e.g., outflowing disk winds, due to the intense radiation pressure (Vignali et al., 2015; Lanzuisi et al., 2016). Disk winds, coupled with advection in the disk, can carry away a significant amount of disc energy, thereby reducing the energy radiated (Jin et al., 2017). Moreover, highly accreting AGN frequently show a strong soft X-ray excess, which has also been seen in some NLS1s (Komossa and Meerschweinchen, 2000).

For several types of AGN, the characteristic timescale of the X-ray variability seems to correlate with the black hole mass and anti-correlate with the accretion rate (Uttley and McHardy, 2005). Because of their low mass black holes, NLS1s present a short timescale variability in the range 2-10 keV (Ponti et al., 2012). Sometimes high amplitude flux changes have also been observed (Gallo, 2006). In those cases, the spectrum presents absorption features and a sharp drop at 2.5-10 keV, which could be due to highly relativistic ionized reflections on the inner layers of the disk (Fabian et al., 2013), or from absorptions by material in the winds (Turner, 2007; Miller, Turner, and Reeves, 2008; Tatum et al., 2012; Gardner and Done, 2015; Hagino et al., 2016). NLS1s show a γ-ray spectral slope comparable to that visible in FSRQs (Foschini et al., 2015; Paliya et al., 2018). The γ-ray luminosity is on average of 10^{44}-10^{46} erg s^{-1} , with a few cases that reach 10^{47} erg s^{-1} (Paliya et al., 2018; Yang et al., 2018), similar to the observed luminosity of BL Lacs.

These similarities, together with the capabilities of launching relativistic jets, suggest a connection with blazars. However, as described, black hole masses, Eddington ratios, and host galaxies prove that NLS1s are part of an independent class. From another point of view, the frequently observed barred disk-like host galaxies with pseudobulges (Crenshaw, Kraemer, and Gabel, 2003; Mathur et al., 2012; Järvelä et al., 2017; Olguín-Iglesias, Kotilainen, and Chavushyan, 2020; Varglund et al., 2022; Varglund et al., 2023) and an enhanced circumnuclear star formation (Deo, Crenshaw, and Kraemer, 2006; Sani et al., 2010; Winkel et al., 2023), might be an indicator of secular evolution (Orban de Xivry et al., 2011). Indeed, pseudobulges usually form when galaxy merging events are absent, and the galaxy evolution is only driven by the evolution of stellar populations. It is possible that NLS1s are young objects, gas-rich, highly accreting, and not interacting with the surrounding environment, representing the first evolutionary phase of a Seyfert galaxy (Grupe, 2000; Mathur, 2000). Other hypotheses claimed that, in particular, the low black hole masses may

be due to an inclination effect. In the presence of a flattened disk-shaped BLR, when seen face-on, the lack of Doppler broadening along the line of sight would produce narrow permitted lines, making a BLS1 galaxy appear as an NLS1 (Decarli et al., 2008; Pozo Nuñez et al., 2013; Calderone et al., 2013).

Krongold, Dultzin-Hacyan, and Marziani (2001) performed an investigation of the local environment of a sample of NLS1 galaxies, comparing them with a non-active galaxy control sample. They found that NLS1s have fewer companions residing farther away from them, supporting the scenario of non-merging galaxies previously cited. The only attempt to study the NLS1s' large-scale environment, and how it impacts their properties, was done by Järvelä et al. (2017). In this work, they pointed out that NLS1 galaxies are a heterogeneous class of objects whose radio properties are affected by the large-scale environment density. In particular, radio-loud and jetted NLS1s preferably reside in denser regions compared to radio-quiet or non-jetted NLS1 sources, which prefers a low-density environment in the cosmic web, such as voids and filaments.

By means of automated data processing, more than ten thousand sources have been identified and classified as NLS1s in Rakshit et al. (2017) and almost twenty-three thousand in Paliya et al. (2024). However, a detailed study showed that automated identification methods can lead to spurious results (Berton et al., 2020b), finding that only $\sim$36% of the selected sources are NLS1s with a high probability (Rakshit et al., 2017). In any case, nowadays the amount of NLS1s is thought to be $\lesssim$1% of the total of AGN. Regardless of the absolute number of detected sources, or those that are still wrongly classified as another kind of AGN, the diversity of properties they show suggests how they might be important to bring answers to dilemmas in astrophysics that are still unresolved today.

2.1 Optical spectrum

Osterbrock and Pogge (1985) proposed a robust classification for NLS1s from an optical point of view, as cited before. Although the narrow Hβ and the weak [O III]λ5007 compared to the Hβ emission are characteristics always visible, the intense Fe II multiplets are not. The Fe II components vary a lot, from basically nonexistent to very strong (Järvelä et al., 2017; Marziani et al., 2018b). Indeed, a lower threshold for the strength of the Fe II compared to the Hβ emission of 0.5 has been proposed to define whether or not an AGN belongs to the NLS1 class (Véron-Cetty, Véron, and Gonçalves, 2001). Nevertheless, sources with lower values that share all the traits of NLS1s are not uncommon (Cracco et al., 2016). A couple of spectra as an example are shown in Fig. 2.1 and Fig. 2.2.

One of the most peculiar traits that makes these types of sources so interesting is definitely the narrowness of the permitted emission lines. It is straightforward to notice in Fig. 2.1, especially looking at Hα and Hβ. The broadening of the lines can be due to very different mechanisms, and it is different for atoms and molecules. In the BLR, the principal source of broadening is the Doppler broadening, due to the circular motion of the region around the black hole. For this reason, the shape of the BLR emission lines can be used to draw information about the central compact object, as its mass (Sec. 2.1.1). In the case of NLS1s, the exact cause of the narrow emission lines produced in the BLR is often debated. As briefly introduced before, some studies proposed an orientation effect (Decarli et al., 2008; Shen and Ho, 2014). According to these studies, assuming the rotational velocity as the main source of

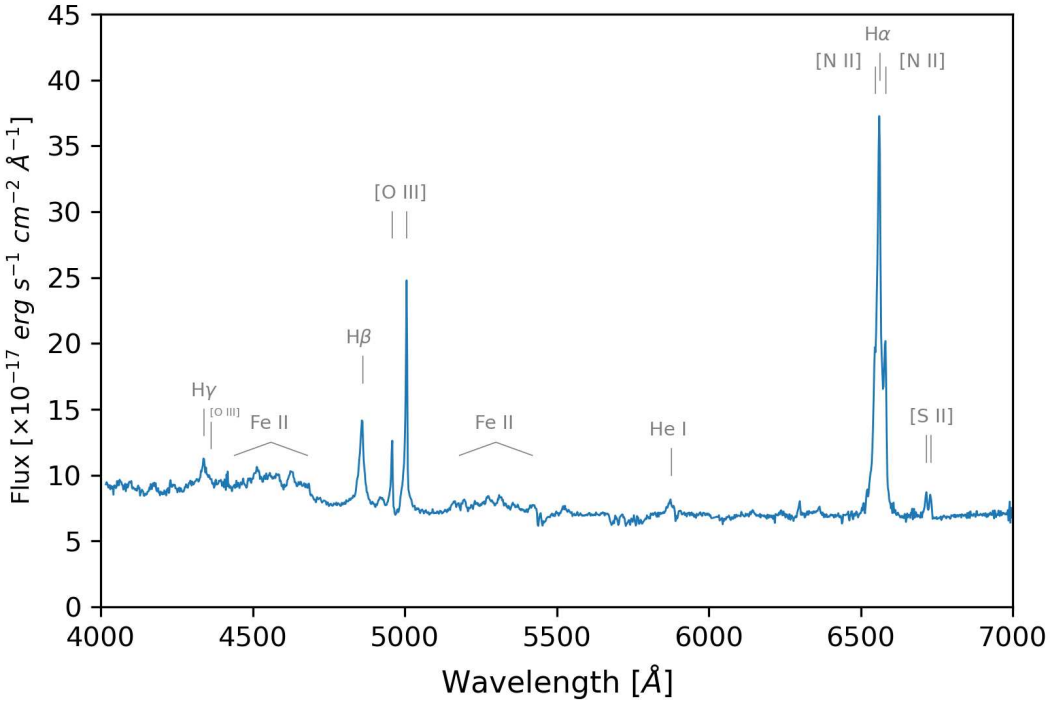

Figure 2.1: Optical spectrum of an NLS1 between 4000Å and 7000Å. The spectrum was obtained with the OSIRIS instrument mounted at the Gran Telescopio Canarias.

broadening, in the presence of a flat BLR and a face-on view of the object, the emission lines appear narrower than they actually are. However, the more diffuse idea claims that the emission lines are intrinsically narrow due to the low black hole mass, which induces a low rotational velocity of the virialized BLR.

In general, different regions can be composed by the same atomic species. Therefore, the resulting emission line is the sum of the emission from multiple regions of the AGN. Studying the line profile means getting insights into the emitting regions. For instance, Balmer lines are usually composed of a "relatively" broad component and a narrow component, which obviously come from the BLR and the NLR, respectively. For NLS1s, and for type 1 AGN in general, usually the main intense permitted lines have a much stronger emission from the BLR than from the NLR. For this reason, the narrow component is easily dominated by the broad one. In particular, Hβ can be considered as a proxy for the BLR properties. In NLS1s, its line profile can be frequently modeled, even if not always as will be explained in Sec. 5, with a single Lorentzian function (Cracco et al., 2016; Berton et al., 2020b). A Lorentzian shape is thought to be due to turbulent motions of the BLR clouds (Kollatschny and Zetzl, 2013a). Berton et al. (2020b) performed an investigation on how a specific line profile, either Lorentzian or Gaussian, is connected to the properties of the NLS1s. They found that, from Lorentzian to Gaussian sources, the black hole mass increases, the Eddington ratio decreases, the Fe II strength decreases, and the [O III] luminosity increases. According to their claims, it can be framed in an evolutionary scenario, following the black hole growth: NLS1s could be born showing a Lorentzian line profile, later evolving into a Gaussian line profile. Physically, a Lorentzian profile suggests that the shape of the line is a result of turbulent motion in the BLR.

The ensemble of close energetic levels of an Fe II atom can produce several emission lines, partially blended together. In the optical such emission is between 4000 Å and 5500 Å, especially on the blue side of Hβ, between Hβ and [O III]λ4959, and beyond [O III]λ5007 (Fig. 2.1 and bottom panel in Fig. 2.2). The origin of the Fe II emission is largely unknown. Possible theories are an overabundance of iron atoms, collisional excitation, the photoionization model (shock hypothesis), and fluorescence, similar to the Fe lines visible in the X-ray spectrum. But none of them can properly describe the strength and how the Fe II is related to the source characteristics (Kovačević, Popović, and Dimitrijević, 2010; Cracco et al., 2016; Marziani et al., 2021). The region where the Fe II is emitted is also highly debated. Marinello et al. (2016) found a positive correlation between the Fe II and the Lyα fluorescence, suggesting that the emitting clouds are located in the outer part of the BLR or between the BLR and the NLR. Contrary, Cracco et al. (2016) and Hu et al. (2015) identified the same emitting region for both Fe II and Hβ, supporting the hypothesis of the inverse-Baldwin effect suggested by Zhou et al. (2006), who found a correlation between an increase of the continuum luminosity and an increase of the equivalent widths of Fe II and Hβ. A widely used parameter to measure the relative iron strength is R4570, defined as the integrated Fe II emission in the range 4434-4684 Å in units of Hβ emission. The importance of this parameter is also noticeable since it is one of the main parameters of the 4D Eigenvector 1, at the basis of the quasar main sequence (Marziani, Dultzin-Hacyan, and Sulentic, 2006; Sulentic, Dultzin-Hacyan, and Marziani, 2007). Earlier, roughly 5% of AGN were found to have an R4570 higher than one, and less than 1% with a value higher than 2 (Lawrence et al., 1988). In NLS1 galaxies, higher values are more common compared to Type I AGN (Marziani et al., 2018b), indeed, R4570 even higher than three have been measured (Paliya et al., 2024). It is important to stress that even though large R4570 parameters are not so uncommon in NLS1s, cases with completely absent Fe II emission have been observed. For this reason, the exclusive use of the Fe II strength for the classification of an NLS1-type source should be avoided.

The information from emission lines I described, and the spatially resolved images available for a few AGN, drastically increased the knowledge about the BLR composition. Nevertheless, there is no clear and widely accepted model able to describe the kinematic of this region yet. Two are the kinds of permitted ionization lines formed in the BLR: low-ionization lines, such as Hβ, Mg II λ2800 and Fe II, and high-ionization lines, such as C IV λ1549 and He II λ1640 for example. The high-ionization lines are believed to originate in lower-density optically thin clouds, with a spherical geometry. These lines usually have blue asymmetries and larger FWHM than low-ionization lines. A Gaussian line profile would suggest a Keplerian motion of the emitting region. But, as described before, NLS1 galaxies frequently show Lorentzian emission lines (Berton et al., 2020b).

Besides permitted lines, NLS1s spectra include several forbidden lines, produced from the very low-density gas in the NLR. Among all the forbidden lines, the [O III] $\lambda\lambda$4959,5007 are definitely the most studied. Since the NLR is photoionized, the line strength of the [O III] doublet is thought to be proportional to the luminosity of the central engine and the entire AGN (Heckman and Best, 2014; Berton et al., 2015). The electron density and the ionization parameter of the emitting gas directly impact the [O III] intensity. But Baskin and Laor (2005) claims that the main driver is the covering factor of the NLR clouds. Indeed, some studies proposed a scenario in which high Eddington ratio sources might have strong winds and outflows that increase the covering factor, then decreasing the [O III] intensity and increasing the Fe II emission (Shen and Ho, 2014). Contradicting studies do exist (Baskin and Laor,

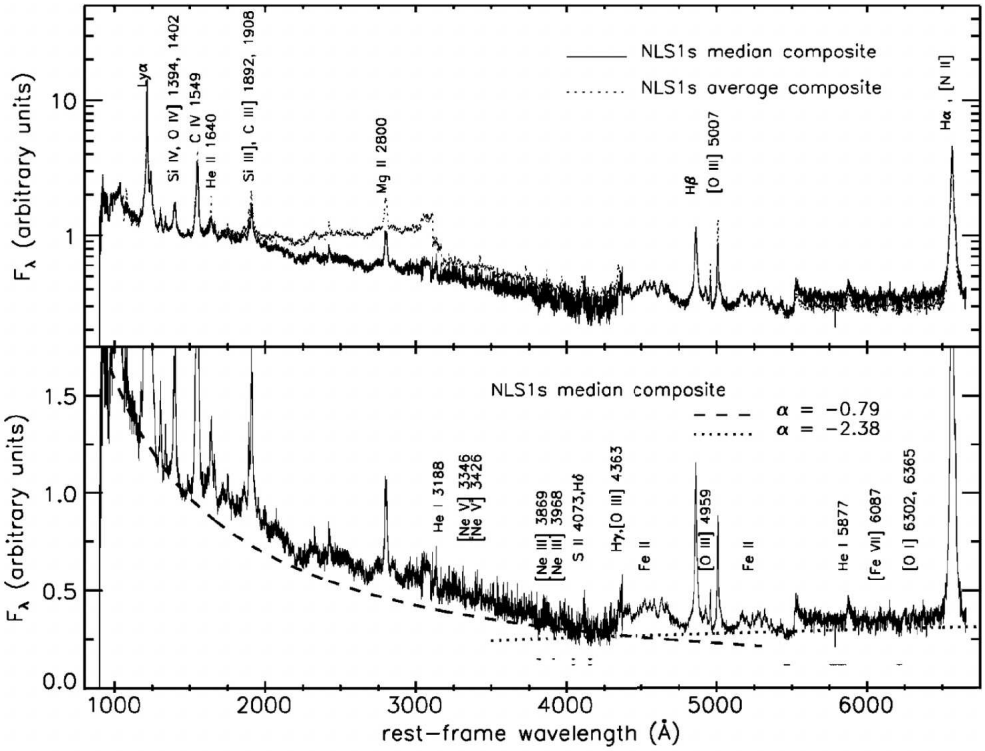

Figure 2.2: UV-optical composite spectrum of an NLS1. The spectrum was obtained with the FOS, GHRS, and STIS instruments mounted in the Hubble Space Telescope (Constantin and Shields, 2003).

2005). For jetted NLS1s, it has been suggested that the [O III] covering factor is reduced due to the interaction of the jets and the shielding gas (Berton et al., 2016b; Dalla Barba et al., 2025).

Frequently, the [O III] line profiles in NLS1s show asymmetries toward blue wavelengths. In particular, the profile is composed of a narrow component, called core component, with a FWHM$<$500 km s^{-1} centered at the [O III] rest-frame wavelength, and a broad component, called wing component, with a FWHM$\sim$500-1000 km s^{-1} often blueshifted. The blueshift of the wing component is thought to originate in powerful gas outflows caused by a high radiation pressure in the central region due to the high Eddington ratio (Proga, Stone, and Kallman, 2000; Cracco et al., 2016). Sometimes interestingly the whole emission line is blueshifted, and when the shift is $>$150 km s^{-1} the source is classified as blue outlier (Zamanov et al., 2002; Marziani et al., 2003; Komossa et al., 2008). This means that there is a bulk motion of the [O III] emitting gas toward the observer, which can be due to the interaction between the jet and the NLR gas (Tadhunter et al., 2001; Komossa et al., 2008) or outflows associated with the disk wind in a pc-scale NLR (Zamanov et al., 2002). Blue outliers are frequently found in sources with significant radio emission (Berton et al., 2016c), as well as in sources with increasing continuum luminosity and Eddington ratio (Cracco et al., 2016). Alternative explanations were proposed as the scattering of photons by the inflowing gas (Gaskell and Goosmann, 2013), or just an orientation effect (Boroson, 2011). The latter claims that the [O III] lines appear blueshifted when the source is seen pole-on, since the shift originates from polar flows, and appear at the rest-frame wavelength under large-angle views. Such a theory was disproved by (Berton and Järvelä, 2021a), showing that a relation between the jet orientation and

the blueshift of the [O III] lines is not present. Probably thanks to the high Eddington ratios, several NLS1 galaxies were found to be blue outliers (Berton et al., 2016b). Such blueshifts are frequently visible, but not exclusively, seen in [O III] lines, but it is also possible to find blueshifted line profiles in the high-ionization emission lines (Zamanov et al., 2002; Boroson, 2005; Komossa et al., 2008).

Another element of an NLS1 spectrum is the continuum emission. The whole continuum is actually made of two components, namely the AGN continuum and the host galaxy continuum. Dividing them is not an easy task. The AGN continuum is dominant especially in the UV band, indeed it has a steeper negative spectral index as visible in the bottom panel of Fig. 2.2. But when the host galaxy component is comparable to the AGN one, a proper removal of the host galaxy continuum is fundamental, since several scaling laws exploit the AGN continuum luminosity, as will be described in Sec. 2.1.1 and Sec. 2.2.

2.1.1 Black hole mass estimation

At this point it is clear how the black hole, especially its mass, is one of the main conductors of the whole AGN. What is the color or the temperature for stellar astrophysics, is represented by the black hole mass for AGN astrophysics. There are both direct and indirect methods for measuring the black hole mass. As for all astrophysical sources, the most reliable direct way to determine the mass of black holes is through dynamical methods. The virial theorem is one of the most used, since the dynamics of the surrounding gas or close stars are directly influenced by the gravitational field of the black hole (Ferrarese and Ford, 2005). Obviously, direct dynamical measurements can be performed only when the black hole surroundings are spatially resolved, then only for nearby sources (Macchetto et al., 1997; Gebhardt et al., 2000; GRAVITY+ Collaboration et al., 2025). For unobscured Type I AGN the reverberation mapping technique is another very powerful and reliable direct method (Blandford and McKee, 1982; Peterson et al., 2004). It relies on the time delay between continuum and emission-line variations, measuring the size of the line-emitting region, namely the BLR, for a particular emission line, usually a Balmer line. By means of the measured time delay (τ) and the emission line width (ΔV), the virial mass can be expressed as

$$M_{\rm BH} = f\frac{c\tau\ \Delta V^2}{G} \tag{2.1}$$

where f is the scaling factor which depends on the structure, kinematics, and orientation of the BLR, usually of the order of unity. Unfortunately, this method is very resource and time consuming, and can only be employed in AGN with broad lines that vary in a reasonably short timescale, even though large scales studies are ongoing (Almeida et al., 2023). In the case of obscured Type II AGN, the possibilities of a direct black hole mass measurement are very limited. By definition, the regions surrounding the black hole are partially or fully obscured, preventing their direct observation, especially in optical wavelengths. Only a few valuable results have been obtained by means of the water masers (Greenhill et al., 2003; Kuo et al., 2011; Tarchi et al., 2011).

Due to the difficulties necessary for the application of direct methods, which are mainly related to the need for resources and time, the indirect methods are far more common, especially for large samples. In the case of partially obscured and broad-line AGN, near infrared emission lines have been recently used to constrain the BLR

size with the hard X-ray luminosity (Ricci et al., 2017; Onori et al., 2017). For unobscured sources, like NLS1 galaxies, several relations between the BLR radius and some observables, frequently retrieved from the optical spectrum, have been found through correlation tests. Since the information can be derived only using a single-epoch spectrum, this method is also called single-epoch technique. This is a fairly common approach: since the BLR is gravitationally bound to the black hole, exploiting the emission lines produced in the BLR to retrieve the velocity information, the gas dynamics around the main compact object can be inferred. Therefore, combining with the BLR dimension, by means of the virial theorem used in dynamical methods the black hole mass can be measured

$$M_{\rm BH} = f\frac{R_{\rm BLR}v^2}{G}\,, \tag{2.2}$$

also in this case f represents the scaling factor, and R_{BLR} and v^2 are the dimension and the rotational velocity of the BLR, respectively. Some of the most widely used scaling laws tie the radius of the BLR with either Hβ luminosity (Greene et al., 2010) or continuum luminosity at 5100 Å, with or without using in addition the Fe II emission (Kaspi et al., 2000; Bentz et al., 2009; Bentz et al., 2013; Du and Wang, 2019; Paliya et al., 2024). Moreover, continuum luminosity at 5100 Å has been found to correlate with Hβ luminosity (Ilić et al., 2017; Dalla Bontà et al., 2020), and with [O III] luminosity (Berton et al., 2015).

Pure indirect methods do exist, connecting the black hole mass with observables. An example is the relation found by Mejía-Restrepo et al. (2022), which connects the black hole mass with Hα FWHM and luminosity. $M_{\rm BH}$-$\sigma_\star$ is another famous relation that exploits the properties of the galaxy bulge (Gebhardt et al., 2003; Kormendy and Ho, 2013), as well as the $M_{\rm BH}$-L_{bulge} which uses the bulge luminosity (Macchetto et al., 1997; Ferrarese and Ford, 2005). The fundamental plane of black hole activity involves X-ray luminosity, radio luminosity, and $M_{\rm BH}$, and it has been independently proposed both by Merloni, Heinz, and di Matteo (2003) and Falcke, Körding, and Markoff (2004). These last three represent quite weak correlations, and they are used in the absence of more reliable methods (see Williams et al., 2023 for a detailed discussion). X-ray-based methods, as the X-ray scaling method (Shaposhnikov and Titarchuk, 2009; Gliozzi et al., 2011) and the X-ray variability method (Papadakis, 2004; Ponti et al., 2012; Akylas, Papadakis, and Georgakakis, 2022), seem to be more reliable (Williams et al., 2023). An in-depth comparison has been carried out by Gliozzi et al. (2024). Also, the quasi-periodic oscillations (QPOs), which will be described in Sec. 3, have been found to show a relation between the frequencies of the periodic oscillations and the black hole mass and spin (Abramowicz et al., 2004; Remillard and McClintock, 2006; Zhou et al., 2015). Even though this relation showed promising results, it can be applied in a very few cases, namely, only for AGN showing QPOs in the X-ray LC. In the first approximation, the host galaxy can also be used as an estimator for the black hole mass. It is possible because the host galaxy morphology is linked to the properties of the central engine, since it co-evolves with the nuclear region (Ferrarese and Merritt, 2000; Morganti, 2017).

The low black hole masses measured for NLS1 galaxies are sometimes not widely accepted. They were found especially using indirect scaling laws combined with the virial method (Xu et al., 2012; Järvelä, Lähteenmäki, and León-Tavares, 2015; Rakshit et al., 2017; Berton et al., 2018; Paliya et al., 2024), but sometimes they were attributed to a face-on orientation and a flattened BLR geometry (Shen and Ho, 2014), which again would bring to narrow emission lines (Decarli et al., 2008). This would also explain the high Eddington ratios, suggesting a typical Seyfert 1 origin (Decarli et

al., 2008; Liu et al., 2016; Rakshit et al., 2017). Nevertheless, reverberation mapping confirms a black hole mass range of 10^6-10^8 $M_\odot$ (Wang et al., 2016; Du et al., 2018), proving the reliability of the virial method as a black hole mass estimator for NLS1s. Impey et al. (2011) pointed out that the frequently used relation between the BLR radius and the continuum luminosity is not always valid for both high and low Eddington ratio sources. Berton et al. (2021) proved that jetted NLS1 galaxies do not generally host high-mass black holes, performing different tests and uncertainty estimations. Moreover they confirmed this through the nonlinear relation between the jet power and the black hole mass, based on Foschini et al., 2015 comparison of the jet power of NLS1s, FSRQs, and BL Lacs. In particular, they pointed out that if NLS1s had high-mass black holes, they would have a low jet power in a high-density environment, indicating the unphysical condition in which the relativistic electrons of their jets are not cooling despite the photon-rich environment (Foschini, 2017).

There are also other studies, using different methods, claiming that NLS1s host higher black hole masses. A mass of $\gtrsim 10^8$ $M_\odot$ have been estimated using the M_{BH}-L_{bulge} relation (Ryan et al., 2007) and by means of spectro-polarimetric observations (Baldi et al., 2016). Such values have also been obtained using Eq. 1.1, Eq. 1.2, and the peak frequency generated by a Shakura-Sunyaev disk spectrum using optical and UV data (Calderone et al., 2013; Viswanath et al., 2019). However, as described at the beginning of the section a Shakura-Sunyaev disk model is likely not a good model to describe NLS1s accretion disks, which are better described by a slim disk model. Performing a wide study on the NLS1s properties (Foschini et al., 2015) supported the reliability of the low masses estimated using line dispersion of the broad component of Hβ line. Given the multiple scenarios in favor of low mass black holes (see Foschini, 2020 for a review), as reverberation mapping results, host galaxy morphology, evolutionary stage, and emission line profiles, this is likely the closest to reality hypothesis.

2.1.2 Eddington ratio

As it is clear from Eq. 1.3 and Eq. 1.5, fixing the bolometric luminosity, a lower black hole mass yields a higher Eddington ratio. Coupling the observed high luminosities with a M_{BH} $\sim 10^6$-10^8 $M_\odot$, as described in the previous section, NLS1 galaxies appear to be high accreting sources (Boroson and Green, 1992; Marziani et al., 2018b; Tortosa et al., 2022). Other evidences however confirm such high accretion. The most evident is the capability of NLS1s to produce relativistic jets. (Foschini, 2017) stated that the most favorable accretion disks, which are able to produce jets, are those described by the ADAF and the slim disk models. For a Shakura-Sunyaev disk, the viscous heating is balanced by the radiative cooling. If a source is experiencing high levels of accretion, the disk does not have enough time to cool down only by radiation losses, therefore an advective cooling is established, forming precisely a slim structure (Abramowicz and Fragile, 2013). A strong Fe II emission is another proxy for the high Eddington ratio. (Gaskell et al., 2022) suggested that the Fe II in AGN is produced by photoionization. From observations, only high Eddington AGN show soft X-ray radiation. But it is this radiation that breaks down the dust grains in the outer part of the BLR, consequently releasing the iron that then gets photoionized by the photons coming from the accretion disk. Strong Fe II is frequently seen in NLS1s, placing these AGN in the tail of the quasar main sequence (Marziani et al., 2018b), as well as the soft X-ray presence (Tortosa et al., 2022). The quasar main sequence has the aim to subdivide all the AGN, exploiting correlations between source properties,

through a Principal Component Analysis (PCA), resulting in the so-called eigenvectors, which represent each correlation. Over the years it has been introduced the 4-dimensions eigenvector 1 (Sulentic, Calvani, and Marziani, 2001; Marziani, Dultzin-Hacyan, and Sulentic, 2006; Sulentic and Marziani, 2015), that uses the following four parameters:

1. Full width half maximum of low-ionization (broad) lines (e.g. FWHM(Hβ)). Hβ is the most used because it is reasonably strong and visible also at high redshift ($z \sim 1$).
2. R4570
3. FWHM centroid velocity shift of the high-ionization lines CIVλ1549 ($C(1/2)_{CIV}$).
4. Soft X-ray photon index, which is used to measure the thermal emission in $0.1 - 2.4$ keV range.

It is important to notice that not all NLS1s, at least at first glance, seem to be high Eddington sources. An example will be described in Sec. 5.

2.2 Radio properties

From a radio point of view, only 15% of NLS1 galaxies have been detected at these frequencies (Komossa et al., 2006; Järvelä, Lähteenmäki, and León-Tavares, 2015), even though a recent work found a lower value of ∼8% (Varglund et al. submitted). Among these 1/3 are classified as radio-quiet and 2/3 as radio-loud. Historically, the radio loudness parameter described in Sec. 1.3 has been used as a proxy for the nuclear activity in AGN, by attributing to the radio-loud sources the only ones capable of launching relativistic jets. Now we know that this is not true, but already over twenty years ago Ho and Peng (2001) stated that most Seyfert 1 galaxies would be classified as radio-loud if only the optical and radio flux densities of the nuclear region were compared. Several other recent works sustain the more modern view of a continuous distinction of the AGN population instead of a two-fold one (Padovani, 2017; Järvelä et al., 2017; Lähteenmäki et al., 2018; Berton and Järvelä, 2021b; Wang et al., 2025). The variable nature of AGN strongly supports this view. The radio-loudness parameter relies on radio and optical flux density measurements taken non-simultaneously, ignoring that they can change in time. As described in Sec. 3 the luminosity variability influences the whole electromagnetic spectrum. For this reason, $\mathscr{R}$ can change for the same source according to the activity state in which it is observed, and therefore it cannot be tied to physical properties that are more stable in time. NLS1s with extreme flux density variability will be the focus of the next chapters.

Most of the NLS1s have a radio flux density around a few mJy, with a minority showing tens of mJy flux densities and rarely above one hundred mJy. The distribution of such emission in the radio spectrum can vary significantly. Assuming that the emission can be described with a power-law as in Eq. 1.6, the spectral shape can be divided in steep ($\alpha < -0.5$), flat ($\alpha > -0.5$), and inverted ($\alpha > 0$). Several factors and mechanisms shape the radio spectrum. Diffuse ionized gas, star-forming regions, radio core, outflows, and relativistic jets are just a few of them. For instance, in star forming regions the supernova remnants produce via synchrotron emission a spectrum with $\alpha \simeq -0.8$, while free-free radiation from ionized gas has an $\alpha \simeq -0.1$ (Condon et al., 1998a). The resulting spectrum in this case has a spectral index ~ -0.7. Usually NLS1 galaxies have a steep spectrum (Berton et al., 2018;

Järvelä et al., 2022), but exceptions with extremely inverted spectra do exist. In particular, if a relativistic jet is present, its emission variability can cause notable variability also in the spectral shape, especially during flaring episodes (Angelakis et al., 2015; Järvelä et al., 2024). Strong inverted spectra are usually thought to be connected with free-free absorption (FFA) and SSA mechanisms (Järvelä et al., 2024). Typically, SSA can reach $\alpha \sim 2.5$, usually in relativistic jets, while higher values need an external contribution by FFA. A spectral index this high usually does not have a clear physical interpretation. It can come from intense variability phenomena, but in this case, non-simultaneous observations can lead to very misleading results. More typical steep spectra can have different origins, from star-forming regions, to pure synchrotron emission in optically thin clouds, or again to a relic emission (Congiu et al., 2017). In these cases, the investigation of the radio morphology, through spectral index maps, for instance, can be very helpful.

NLS1 galaxies jets have usually a total power range between 10^{42} and 10^{45} erg s^{-1}, but they can reach also 10^{48} erg s^{-1} (Donato, 2010; Foschini et al., 2010; Foschini et al., 2011; Foschini, 2011a; Foschini, 2012). With a direct comparison, weaker BL Lac objects have similar jet powers as NLS1s, whereas FSRQs have much powerful jets. Nevertheless, for jetted NLS1s, if the lower black hole mass is considered, the jet power becomes comparable to that of FSRQs, suggesting similarities with blazar populations (Heinz and Sunyaev, 2003; Foschini, 2014; Foschini et al., 2015), and these sources are thought to be the low-mass and low-luminosity tail of the FSRQ distribution (Berton et al., 2016a).

Two of the most important public surveys covering NLS1 galaxies are the Very Large Array (VLA) Faint Images of the Radio Sky at Twenty-Centimeters[1] (FIRST) and the National Radio Astronomy Observatory (NRAO) VLA Sky Survey[2] (NVSS), both at 1.4 GHz, with a detection threshold of 1 mJy and 2.5 mJy, respectively. There are also more sensitive recent surveys as the VLA Sky Survey[3] and the LOw Frequency ARray (LOFAR) Two-metre Sky Survey[4] (LoTSS), both able to detect sub-mJy sources at 3 GHz and 144 MHz, respectively. Future radio telescope projects include the Square Kilometre Array Observatory[5] (SKAO) and the next-generation VLA[6] (ngVLA). An important dedicated JVLA radio investigation has been carried out by Berton et al. (2018), Chen et al. (2020), Chen et al. (2022), and Järvelä et al. (2022). Another long-term monitoring program dedicated to NLS1s has been carried out by the Metsähovi Radio Observatory (MRO) since 2012 (Lähteenmäki et al., 2017). This program monitors more than 250 NLS1 galaxies, and nowadays it is the largest monitoring campaign dedicated to these sources.

At this point, it is clear that the flares are not uncommon in the radio band. When a flare occurs, it is usually first seen at high energies, often accompanied, with a short lag, by an increase in the optical/UV emission. Even if this is not always the case, since sometimes it is the optical that leads to γ-ray flares. Usually, after a few months, with a large variability in the delay, the flare is visible at radio frequencies, propagating from high frequencies toward the lowest (Berton et al., 2018; Lisakov et al., 2017). During these episodes, the peaks' frequencies in the SED are shifted to higher frequencies, besides the amplitude increasing. Such a 'wave' effect suggests the common nature of the flare visible at different wavelengths. However, isolated

[1] https://sundog.stsci.edu/
[2] https://www.cv.nrao.edu/nvss/
[3] https://public.nrao.edu/vlass/
[4] https://lofar-surveys.org/surveys.html
[5] https://skao.int/
[6] https://ngvla.nrao.edu/

flares are not rare. In those cases, a variation of the emission at a specific wavelength does not necessarily lead to a similar effect somewhere else in the spectrum. The variability can even come from variations of the energy distribution of the emitter, or from the changes in the size or location of the emitting region (Collmar et al., 2010; Ghisellini et al., 2013). Nowadays, it is generally accepted that most of the radio flares are produced by shocks propagating in the relativistic jets (Blandford and Rees, 1978). In this model, called *shock model*, minor instabilities propagate along the jet until they encounter a pressure gradient. A pressure gradient forms when there is a slight change in the pressure of the jet flow. The interaction between the instability and the pressure gradient zone generates the shock, with a consequent variation of the Lorentz factor. The result is a strong increase in the emission, followed by a decrease. The shock model is theoretically described in Marscher and Gear (1985) and Valtaoja et al. (1992), and an observational point of view is presented in Türler, Courvoisier, and Paltani (2000) and Hovatta et al. (2008).

2.3 A sample of extremely variable NLS1s

The analyses carried out in this thesis are focused on a sample of 7 NLS1s, which showed unprecedented radio behaviors. They are part of a monitoring campaign at the MRO started in 2012. The aim of this campaign was to shed light on the very diverse radio properties of NLS1s. Two samples mainly composed of radio-quiet and radio-silent sources were selected according to two distinct criteria. The first sample consists of 45 sources selected from Foschini (2011b) and Komossa et al. (2006), residing in very dense large-scale environments (Järvelä, Lähteenmäki, and Lietzen, 2017). By means of luminosity-density fields, Järvelä, Lähteenmäki, and Lietzen (2017) studied the Mpc-scale environment of a sample of NLS1s. They found that in general NLS1s tend to reside in low-density regions. However, comparing this result with the influence of the environment on galaxy evolution, it was hypothesized that NLS1s in denser environments might be ahead in the evolution compared to their counterparts residing in low-density regions, likely hosting relativistic jets. The second sample includes 33 sources mostly selected from Järvelä, Lähteenmäki, and León-Tavares (2015) and Foschini (2011b), exhibiting SED that seemed favorable for 37 GHz observations. Four sources from each sample, eight in total, were detected, showing hundreds of mJy of flux density levels (Lähteenmäki et al., 2018). Among these, seven NLS1s have been detected several times, sometimes even at Jy-levels and with a time-scale of days to weeks, confirming the reliability of the detections. Previously, only two sources were detected in radio at 1.4 GHz in the FIRST (Becker, White, and Helfand, 1995; Helfand, White, and Becker, 2015) and the NRAO VLA sky survey (Condon et al., 1998b), and only at mJy-levels.

To untangle the situation, several follow-up radio observations have been carried out. In 2019, the sample was observed with the JVLA in A configuration at 1.6, 5.2, and 9.0 GHz (Berton et al., 2020a; Järvelä, Berton, and Crepaldi, 2021). Again in 2022, it was observed with the JVLA in A configuration at 10, 15, 22, 33, and 45 GHz and with the Very Long Baseline Array at 15 GHz (Järvelä et al., 2024). In the meantime, single-dish monitoring has been ongoing. Besides the MRO monitoring, the sources are part of the Owens Valley Radio Observatory (OVRO) 40 m radio telescope AGN monitoring program at 15 GHz (Järvelä et al., 2024). All the data acquired showed steep spectra up to 45 GHz, or no detection at all, especially at high radio frequencies. Although previous cases of such a high-frequency excess are known in the literature (Antonucci and Barvainis, 1988), the variability observed, combined with

the Jy-level flux densities, are rarely, if ever, seen in AGN. Because the observations are not simultaneous, the different beam sizes have to be considered, especially comparing single-dish with interferometric observations, with resolved-out structures in the latter. Although a minor difference can be present, resolved-out emission cannot explain such a huge difference in the flux density (Järvelä et al., 2024). Moreover, contamination by close sources has been ruled out (Lähteenmäki et al., 2018; Järvelä et al., 2024). Even though these recent data helped to discard some interpretations, they did not provide a unique and clear answer. Järvelä et al. (2024) discussed several hypotheses aimed at identifying the nature of this phenomenon. One of the possibilities is that these NLS1s could harbor small-scale (likely a few parsecs) relativistic beamed jets, whose low-frequency radio emission is SSA or FFA by ionized gas. The origin of the ionization is unclear, but it could either be due to the abundant star formation often observed in NLS1s (Sani et al., 2010), or by collision between the jet and the inter-stellar medium (ISM) surrounding the AGN, which produces via shocks a cocoon of ionized gas at the jet head (Bicknell, Dopita, and O'Dea, 1997). A detailed study of the radio spectral index maps of these sources revealed that the latter is actually the most likely mechanism to account for this unique behavior (Järvelä, Berton, and Crepaldi, 2021). Jets-in-jets magnetic reconnection or magnetic reconnection in the black hole magnetosphere are not ruled out either. The latter is particularly interesting since it does not require the presence of relativistic jets (see Sec. 6.4 for more details).

Chapter 3

Time-series analysis

Since their discovery, it was clear that AGN, NLS1s included, present variability that influences their whole spectrum (Matthews and Sandage, 1963; Ulrich, Maraschi, and Urry, 1997; Gaskell and Klimek, 2003). This is not unexpected considering the complexity of their structure. The origin of the variability is, however, not easy to address. Indeed, at each wavelength, it can also be very different, since different mechanisms and emitting regions are involved. It can be connected between different bands or not, and the time-scales are extremely variable: from less than an hour up to hundreds of thousands of years. The short-term variability is related to the physical processes, which mostly occur during the accretion and the ejection of matter. Especially for the accretion, the related variability is random and stochastic, even though possible consequent variability in the connected regions can sometimes be predicted. By means of monitoring campaigns with a high cadence in the observations, several models have been investigated with the aim of understanding the origin of variability. On the other hand, long-term variability is due to the general evolution and long-term changes of the source, involving morphological changes. Therefore, many more variables can play a crucial role in the fluctuations of the emission compared to short-term variability, and long-term monitoring is necessary for its study.

At radio frequencies, the variability usually presents the longest time-scales, besides possible short-time-scale flares (but see Sec. 2.2 and Sec. 6), and the time delays between different frequencies can be of the order of several months or years (Tornikoski et al., 1994; Soldi et al., 2008; MAGIC Collaboration et al., 2023). As described before, the main emission mechanism in this band is synchrotron emission, whose variations are likely responsible for the observed radio variability. Since the synchrotron emission is strongly tied to the relativistic jets when present, the radio variability has a different origin for blazars and the rest of the AGN. In both cases, it is probably due to variations of either the energetic distribution of the electrons involved in the synchrotron mechanism or the strength of the magnetic field, but for jetted sources it likely occurs within shocks along the jets (Stevens et al., 1994; Hovatta et al., 2008).

The synchrotron mechanism also extends in the millimeter and infrared wavelengths (for blazars, it is represented by the brown solid line and gray dashed line of the lower frequency bump in Fig. 1.4). Multi-wavelength variability studies found that the infrared band shows variability with an amplitude of about half that measured in optical, and time-scales less than a year (Edelson, 1987; Impey and Neugebauer, 1988; Mingaliev et al., 2015). Moreover, this variability is tied to longer wavelength variability. For non-jetted sources, the near-infrared (NIR) emission is partially produced by the reprocessed thermal optical radiation in the molecular torus. NIR variability can then be the mirror of the optical variability (Campitiello et al.,

2021). Also, some of the infrared emission may come directly from the accretion disk.

There are two main scenarios able to describe the origin of the optical and UV variability. The first suggests a thermal origin with propagation of instabilities through the accretion disk and possible changes in the accretion rate (Hameury, Viallet, and Lasota, 2009; Burke et al., 2021; Neustadt and Kochanek, 2022). This scenario assumes a standard disk with a temperature gradient and luminosity fluctuations toward the central regions. Such changes in luminosity produce axisymmetric temperature perturbations in the closest layers to the black hole, which act as a lamppost, consequently producing lower amplitude temperature fluctuations moving outwards at the speed of light. As a sort of wave, the temperature fluctuations drive the observed flux variability. Shorter wavelengths vary first, being those emitted in the inner layers of the accretion disk. The flux variability propagates toward longer wavelengths according to the travel time of the temperature fluctuations.

The second scenario favors the idea of optical variability due to X-ray reprocessing (Kammoun et al., 2021; Panagiotou et al., 2022). Here, part of the primary X-ray emission travels directly to the observer, and the other part irradiates the accretion disk. In the latter, a fraction of the incident light will be reprocessed and re-emitted in the X-ray (George and Fabian, 1991; Matt, Fabian, and Ross, 1993). The other fraction instead is absorbed by the accretion disk, increasing its temperature, and subsequently emitted as UV/optical radiation. In the case of a variable primary X-ray radiation, the generated UV/optical flux will be variable as well. Such a mechanism is called disk thermal reverberation (Cackett, Horne, and Winkler, 2007). There have been studies that argue against both of the described models. In the first case, the lamppost model, intrinsic thermal fluctuations in the disk instead of fluctuations induced by luminosity changes have been proposed as the origin of the variability (Kelly, Bechtold, and Siemiginowska, 2009; Burke et al., 2021). On the other hand, there is evidence that the X-rays vary after the UV/optical or show uncorrelated structures (Berkley, Kazanas, and Ozik, 2000; Kazanas and Nayakshin, 2001; Dexter et al., 2019; Edelson et al., 2019).

Also, the spectral properties, mainly in the optical, can undergo variations. The line profiles of the emission lines in the BLR and NLR are strongly connected to the central continuum emission (Ilić et al., 2015). Here, the time lag depends on the position of the region where the emission lines are formed, namely, on the travel time necessary for the photons to reach such a region. The variation of the optical spectrum leads to changes in the sources frequently called changing-look AGN (Penston and Perez, 1984; LaMassa et al., 2015; Yang et al., 2017; Xu et al., 2024).

As described in Sec. 1.4.1, the X-ray emission consists of multiple components. From observations, the most variable is the X-ray soft-excess (Boller et al., 1997; Middei et al., 2017). Sometimes it shows an order of magnitude increase in the flux density over a few days. Such a short time-scale confirms that the emission must come from a very small region, such as the corona. Variability at higher frequencies is also seen, and can be explained as a combination of variable effects in the corona emission and accretion disk reflection. The real mechanisms related to X-ray variability are widely unknown (Komossa et al., 2024), but some proposed explanations include blurred reflection by the accretion disk (Nardini et al., 2011) or an additional Comptonization component (Lohfink et al., 2013; Boissay, Ricci, and Paltani, 2016).

It is important to notice that the variability effects described for non-jetted sources are also present in jetted ones. However, the jet emission usually overshines any other effect. The emission states of a jetted AGN can often be divided into high and

low emission states. In the low-emission state, the variability described for the non-jetted sources can be distinguished in the SED. In the high-emission state, instead, the increasing flux density can be associated with the ejection of new components inside the jet.

Considering the variability time-scales, of course, an upper limit cannot be found, since a light curve (LC) of an infinite duration would be needed. As a lower limit, even though new AGN with lower variability time-scales could always be discovered, by means of radio and optical high-cadence observations, extremely fast variability has been measured. In the radio, extremely fast flares have been detected (Lähteenmäki et al., 2018; Järvelä et al., 2024), and will be discussed in Sec. 6. Short-term optical changes occurring on time-scales from minutes to hours represent the intra-night optical variability (INOV), also known as micro-variability (Gopal-Krishna, Sagar, and Wiita, 1995; Stalin et al., 2004). BL Lac objects seem to exhibit stronger INOV compared to non-jetted AGN (Yang, Ma, and Chen, 2024), and it is thought to be connected to the jet activity (Goyal et al., 2012; Webb et al., 2021). In quasars, instead, it may arise from weak jets or flare events near the accretion disk (Zhang and Bao, 1991; Chakrabarti and Wiita, 1993; Gopal-Krishna et al., 2003).

Identifying a variable object is not always an easy task. The errors in the measurement of the luminosity allow only the identification of a large amplitude variability. There are three common approaches in the literature for identifying variable objects: direct image comparison (*transient detection*), LC analysis using variability indices, and search for periodicity. The transient detection method seeks to detect variability by subtracting two aligned images pixel by pixel, taken in two different epochs. It is the strategy adopted by the Pan-STARRS survey, for instance (Rest et al., 2014). Using only two epochs is quite limiting, since two observations might measure the same luminosity just because at those epochs a variable source is emitting the same amount of radiation, or because the source is in a temporary quiescent state, or again because of contaminants or artifacts affecting one of the two images.

To bypass the problem, multiple epochs of observations are necessary, namely, producing an LC. In this way, it is possible not only to discover whether a source is variable, but also to investigate the average amplitude of the variability, even in the case of a low amplitude. Such methodology is robust also against systematics, because systematic errors would affect the whole LC in the same way, so they do not influence the amplitude of the fluctuations but only the absolute values of the LC. To quantify the variability under these conditions, there are several variability indexes used in the literature for different applications, which characterize the overall scatter of measurements in a light curve and/or the degree of correlation between consecutive flux measurements (Munari et al., 2014; Javadi et al., 2015; Yao et al., 2015). Sokolovsky et al. (2017) performed a detailed reliability comparison of nineteen different variability indexes, analyzing the degree of variability that each one measures for a test sample of sources. He divided the test into scatter-based indices and correlation-based indices. The former considers only the distribution of measured magnitudes, ignoring the time information available in the LC, considering or not the uncertainties. The latter also relies on the order in which the measurements are taken, and some indices also take into account the time difference between measurements. This makes correlation-based indices more sensitive to low-amplitude variability, but on the downside, they are insensitive to variability on time-scales shorter than the sampling time of the LC (Kim et al., 2011). Overall, the two best indexes turned out to be the Interquartile range (Kim et al., 2014) and the reciprocal of the von Neumann ratio ($1/\eta$, Neumann, 1941; Neumann, 1942), as scatter-based index and correlation-based index, respectively.

The last method exploits the fact that a periodic LC must be, first of all, a variable LC. Therefore, a periodic source implies a variable source. Periodicities in AGN are not as common as variabilities for two main reasons. The first is that nowadays the longest available LCs are quite short, of the order of decades, and often not even well sampled, especially for the oldest epochs. The second is that well-specific conditions must occur in AGN to produce periodic signals. Indeed, only a handful of phenomena show a periodicity (see Ackermann et al. (2015) for an overview). One of the most studied is that of binary black holes (BBHs, Begelman, Blandford, and Rees, 1980; Barnes and Hernquist, 1992, in particular the source OJ287 (Sillanpaa et al., 1988). Periodicities from AGN hosting BBHs are usually detected in optical with time-scales ranging from 1 to 25 years (Komossa et al., 2006; Rieger, 2007) and in γ-ray. In particular, the γ-ray variability is due to jet nutation expected from the misalignment of the rotating SMBH spins or the gravitational torque on the disk exerted by the companion (Katz, 1997; Romero et al., 2000; Caproni, Abraham, and Monteiro, 2013; Graham et al., 2015). BBHs existence can also be investigated from the gravitational waves' point of view. A periodic signal can even be produced by the jet itself, and not only induced in the jet as in the case of a BBH. In a jet wrapped by a sufficiently strong magnetic field, changes in the viewing angle can occur because of jet precession (Romero et al., 2000; Stirling et al., 2003; Caproni, Abraham, and Monteiro, 2013), rotation (Camenzind and Krockenberger, 1992; Vlahakis and Tsinganos, 1998; Hardee and Rosen, 1999), or a helical structure (Conway and Murphy, 1993; Roland, Teyssier, and Roos, 1994; Villata and Raiteri, 1999; Mohan and Mangalam, 2015). The variation of the emitted flux is due to the changes in the Doppler magnification factor.

Some sources show QPOs in the X-ray LC, first detected in stellar black hole X-ray binaries (McHardy, 2010; González-Martín and Vaughan, 2012; Markoff et al., 2015; Scaringi et al., 2015). They are divided into two types: high-frequency and low-frequency QPOs (Remillard and McClintock, 2006). The former present two periodicities with a constant frequency ratio of 3:2, and the latter show constant periodicity time-scales despite significant variations in fluxes (Remillard et al., 2002). The first AGN which showed QPOs was RE J1034+396, an NLS1 galaxy, and so far just a few others have been discovered (Gierliński et al., 2008; Alston et al., 2014; Hu et al., 2014). At least a few other NLS1s showed a QPO (Pan et al., 2016; Ren, Sun, and Zhang, 2024), and this kind of AGN seems to be particularly suitable for hosting such periodicity, likely due to their high accretion rate. A QPO has a time-scale on the order of hours, and it is thought to be a transient phenomenon that is produced by instabilities in the corona located at the inner edge of the accretion disk. Especially in NLS1 galaxies, the accretion disk can have an important role in the production of periodic signals. ADAF and slim disks are environments where accretion flow instabilities can occur. This leads to the production of rotating hot spots in the accretion disk inflow, with time-scales of different lengths, according to the black hole spin (McKinney, Tchekhovskoy, and Blandford, 2012). A similar phenomena happen for the tidal disruption event (TDEs) of a star, even though in this case the time-scale ranges from a few months to years (Bade, Komossa, and Dahlem, 1996; Komossa and Bade, 1999; Gezari et al., 2006; Gezari et al., 2008; van Velzen et al., 2011; van Velzen et al., 2019).

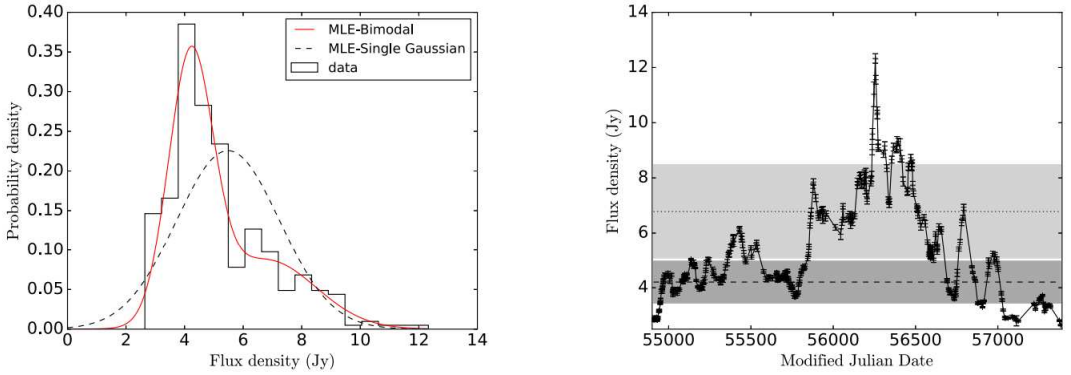

Figure 3.1: Right: AGN LC in the radio band at 15 GHz. Left: PDF related to the LC. The histogram represents the data, the black dashed line a single Gaussian fit, and the red solid line a log-normal fit (Liodakis et al., 2017).

3.1 Light curves properties

All the described sources of variability and periodicity produce different features in the LC. A QPO has a behavior which is completely different compared to an instability in the accretion disk, or again a TDE (e.g., Lyubarskii, 1997; Hogg and Reynolds, 2016; Phillipson, Boyd, and Smale, 2018; Sinha et al., 2018; Dobrotka, Negoro, and Mineshige, 2019; Bhatta and Dhital, 2020; Scargle, 2020 and references therein). Such differences translate into a specific shape of the LC, and exploiting them to extract physical information is the primary goal of a time-series analysis. One of the main limitations that frequently prevents the achievement of the goal is the limited observational power. Even if having a telescope fully dedicated to the observation of only one source, the "perfect" LC would never be reached. Indeed, a certain integration time is necessary to have a good enough S/N, but this means averaging all the variability inside that time period. Therefore, an LC is always made of a discrete distribution of points, sometimes well sampled and sometimes not, and never of a continuous signal. Moreover, a source can never be constantly observed by a telescope. Depending on the telescope location and the source coordinates, there are possible seasonal gaps in which the source is not visible in the sky. An optical telescope has to take into account the weather conditions, as well as the night and day duration. A radio telescope does not care about day and night, but it is still weather-sensitive. Moving into space, depending on the orbit of the spacecraft, the observations are interrupted whenever the Earth, the Sun, or other celestial bodies cross the line of sight. Everything described reduces the quality of the LC, but unlike spectroscopic and photometric observations, which can usually be repeated, a missing point on the LC cannot be recovered. Indeed, one of the most important applications of time-series analysis is for transient events, which are unique by definition.

At this point, it is clear that the quality of an LC cannot be defined in advance. Once the LC is available, there are several methodologies to investigate its properties. The first is the probability density function (PDF). The PDF characterizes the flux density distribution of the data points, namely, which is the probability that a certain point has a specific flux density (Fig. 3.1). Its shape is the most interesting property. A stochastic process produces a Gaussian PDF, centered on the mean flux density and with a standard deviation related to the amplitude of the variability. From a geometrical point of view, the *skewness* and the *Kurtosis* parameters are

frequently used to describe the deviations from a perfect Gaussian PDF, also in non-astronomical fields. The skewness measures the symmetry of the distribution, and it is equal to zero for a perfectly symmetric bell shape. Basically, it defines the way in which the data are spread around the mean. If there is an asymmetry, with a tail toward higher values, the distribution is positively skewed, and it is negatively skewed the other way around. If the data are more concentrated around the mean, compared to a normal distribution, the Kurtosis parameter is positive. On the other hand, if in the x-axis the data are more sparse, the Kurtosis is negative. The AGN PDFs usually have a positive skewness and Kurtosis. In particular, such a shape is frequently fitted using a log-normal distribution, even though the specific shape depends on the observational band (Max-Moerbeck et al., 2014; Liodakis et al., 2017). It is important to notice, as discussed in detail in Scargle (2020), that the PDF is the result of all the multiple processes that take part in the variability of the AGN. Therefore, the PDF shape cannot be perfectly represented by either a single Gaussian or a single log-normal function.

The PDF helps in the identification of the process causing the variability, but it does not provide further information on the process itself. To estimate the contribution of different time-scales to the total variability, as well as eventual periodicities, the most powerful tool adopted is the Fourier analysis. The Fourier transform of a general signal produces in the frequency domain the so-called power spectrum, in which the time-scale of a periodic pattern appears as a peak. Since the astronomical LCs are uneven and discrete distributions of points, the discrete Fourier transform (DFT) is necessary. Precisely, the power spectrum in this case is named power spectral density (PSD), which is the modulus squared of the DFT defined as

$$|F_N(\nu)|^2 = \Big(\sum_{i=1}^{N} f(t_i)\, cos(2\pi\nu t_i) \Big)^2 + \Big(\sum_{i=1}^{N} f(t_i)\, sin(2\pi\nu t_i) \Big)^2, \tag{3.1}$$

where t is the time of each observation, $f(t_i)$ is the flux density value at the time t_i, N is the number of data points in the LC, $\nu = k/T$ is the sampled frequency, and

$$k = \begin{cases} 1, ..., N/2 & \text{for } N \text{ even} \\ 1, ..., (N-1)/2 & \text{for } N \text{ odd} \end{cases} \tag{3.2}$$

$$T = \frac{N}{N-1}(t_N - t_1)\,. \tag{3.3}$$

Then the PSD is calculated from the lowest frequency $\nu_{min} = 1/T$ and the Nyquist frequency $\nu_{Nyq} = N/2T$. Frequently, the periodogram is used as an estimator of the true PSD of an LC, since it reduces the scatter (e.g. Uttley, McHardy, and Papadakis, 2002). It is calculated by applying a normalization of Eq. 3.1 (Deeming, 1975) as

$$P(\nu) = \frac{2T}{\mu^2 N^2} |F_N(\nu)|^2, \tag{3.4}$$

where μ is the mean amplitude of the LC. The normalization allows the calculation of the fractional root mean squared (rms) variability, which is given by the square root of the integral of the power spectrum across all measured frequencies. Moreover, it is necessary to compare different power spectra, as those derived from simulated LCs, for instance. This is the basis of the method to estimate the real PSD trend in Uttley, McHardy, and Papadakis (2002) as will be described in Sec. 3.2. The periodogram approaches the true PSD as the T increases, even though the variance in the former is systematically higher than in the latter. For a source, a similar PSD in different

observational bands means that the involved variable mechanisms are the same. For AGN, the PSD has on average a negative power-law trend $\propto \nu^{-\beta_{PSD}}$, with $\beta_{PSD} \gtrsim 1-2$ (Fig. 3.2). This is the typical PSD slope of red noise, produced for example by a Brownian motion (see Vaughan et al. (2003) and Kankkunen, Tornikoski, and Hovatta (2025) for details).

Another important property of an LC, necessary especially for simulations, is whether it is stationary or not. Stationarity means that an emission process is still stochastic, but that its LC mean and variance do not change over time. Practically, it translates into a constant PSD shape regardless of the interval of time selected for the calculation. Generally, the assumption of stationarity is in conflict with the sporadic flaring activity that AGN typically exhibit over the spectrum. Usually, flaring and non-flaring epochs are too short to reliably estimate the underlying PSD shape. Therefore, data sets as long as possible, containing both flaring and non-flaring states, would be necessary for a representative average PSD. For this reason, determining stationarity in the context of AGN LCs is always a difficult task (see Vaughan et al. (2003) for a discussion).

3.2 Analysis methods

Because of its importance, at this point it is clear that the usual first approach of an LC analysis is its PSD analysis. As described in the previous section, astronomical LCs are uneven and discrete distributions of points, and the related PSDs can be obtained through Eq. 3.1. The uneven and discrete distribution, coupled with the finite duration of the LC, can create some artifacts that affect the real PSD slope. For example, if T is the total duration of the LC, the minimum frequency of a power that can be spotted within the PSD is $\nu_{min} = 1/T$. Moreover, an LC can be represented as the sum of sine signals, each one with a specific amplitude, frequency, and shift. In all those cases where there is a pattern with a frequency $\nu < \nu_{min}$, or even only one of the signals with a number of periods that is not an integer number in the duration T, some powers leak into higher frequencies in the PSD, flattening it. This effect is known as *red-noise leakage*. It occurs because the Fourier transform of the rectangular observing window in the time domain is a sinc function in the frequency domain. For the cited conditions, this causes the powers to be spread toward higher frequencies in the case of PSDs with a red-noise shape, since in this case, high frequencies have lower powers, especially for slopes $\beta_{PSD} > 2$. There are some methods to reduce the impact of the red-noise leakage. Simulations of a longer LC with the same characteristics as the original one help to reduce the power leak effect. The LCs simulation will be further described in the next section. Another method is the windowing, namely the use of a window function. A window function is directly convolved to the time-series, performing a smoothing of the ends following a shape related to the function used (see VanderPlas (2018) for a mathematical description). Max-Moerbeck et al. (2014) showed that the windowing is very efficient against the red-noise leakage. This method is only applicable for evenly sampled data, and therefore, a resampling must be done in the case of uneven sampling. When relevant patterns are located at the ends of the LC, the windowing must be carefully avoided, since it smears this information out. Another artifact that impacts the PSD slope estimation is the *aliasing*. It occurs only for discrete data sampling, especially for evenly sampled data (Deeming, 1975), and it is due to the undersampling of the signal. A scheme of the aliasing effect is reported in Fig. 3.3. In the image, the yellow

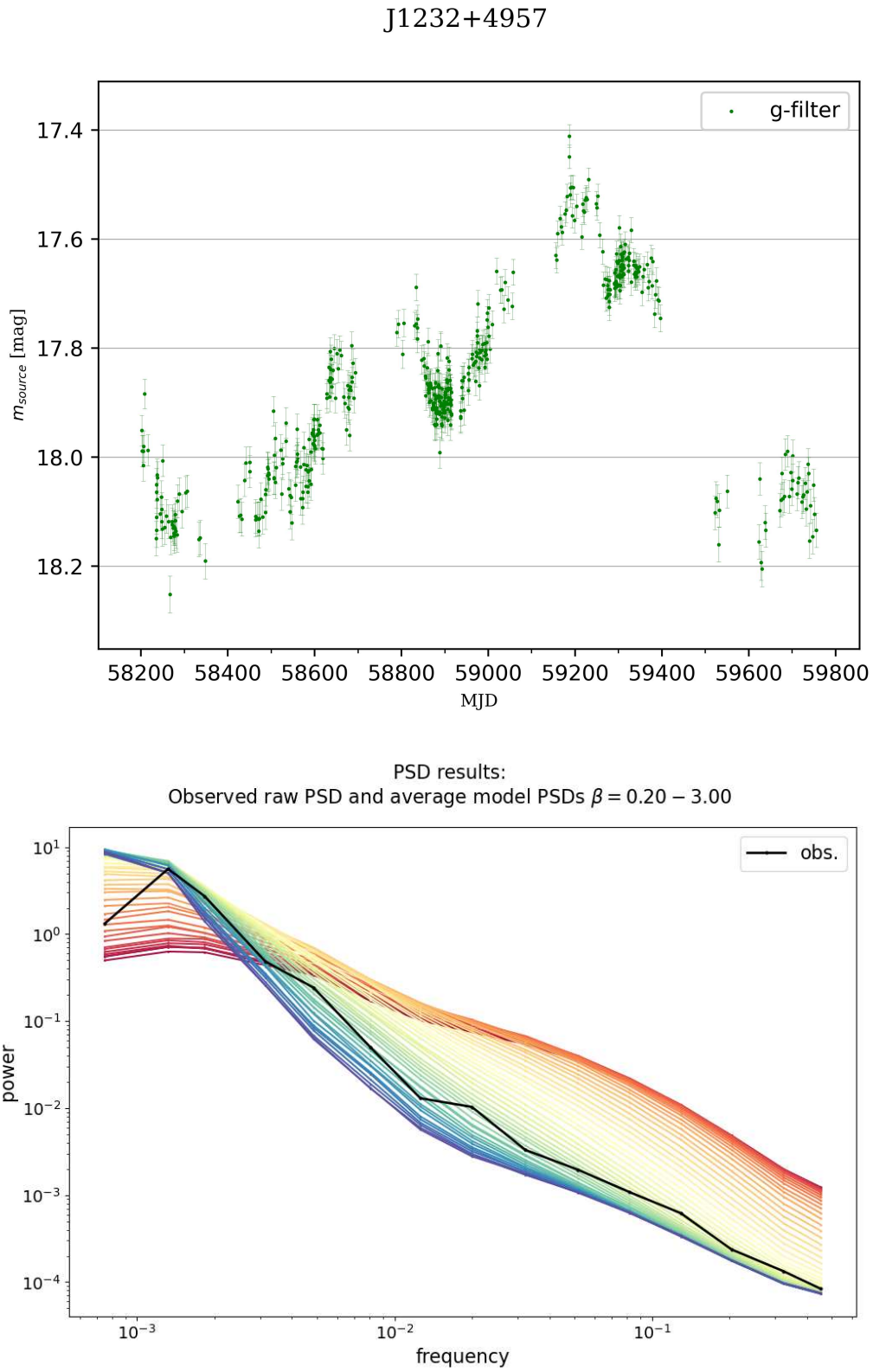

Figure 3.2: Top: NLS1 LC in the optical band in g-filter. Bottom: PSD related to the LC. The black solid line is the PSD calculated from the observed LC, while the colored lines show the average PSD power-law models for spectral indices between 0.2 and 3.

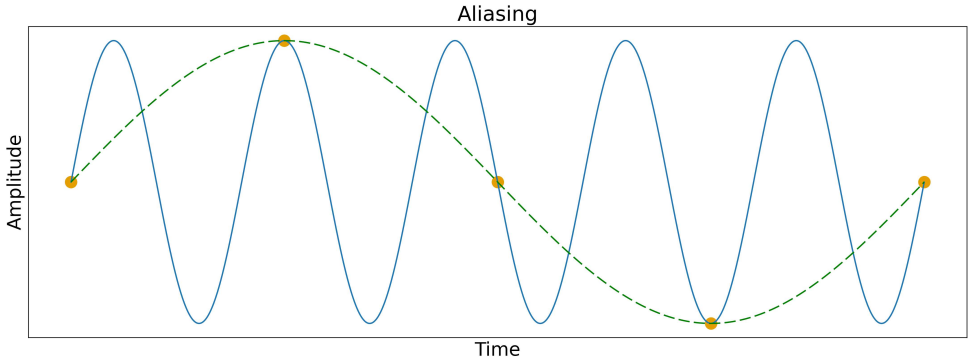

Figure 3.3: Representation scheme of the aliasing effect. The red points are the observed points of the time-series. The blue solid line and the green dashed line are, respectively, the real and the fake periodic signal.

points are the observed points that compose the LC. Even if they are the single observations of an emission mechanism, which has a periodic trend represented by the blue solid line, the same points could also arise from a different periodic emission, as the green dashed line, for instance. Without a proper sampling, and according to the total LC duration, the power related to the blue line may fall at $\nu > \nu_{Nyq}$, while its alias, the power generated by the green line, contributes on the shaping of the PSD. Aliasing mostly affects PSD with slopes $\beta_{PSD} < 1.5$, and due to its nature, it cannot be eliminated from the data. The only way to reduce it is a rebinning with a shorter sampling, even though this means introducing artificial data to the LC. The resulting PSD from Eq. 3.1 is the raw power spectrum, which is different from the intrinsic power spectrum that is the one free from any artifacts.

These and any other distortions prevent the actual slope measurement of the intrinsic PSD. For this reason, for astronomical LCs the pure application of the DFT does not provide reliable insights on the intrinsic PSD. As described before, every source has its own specific PSD shape, as a result of all variable emission mechanisms. Nowadays, several sky surveys have as their main goal the acquisition of an enormous quantity of sources' LCs for variability studies. If the analysis methods do not manage to disentangle between different sources and emission mechanisms, because of PSD artifacts, they may lead to misleading results. For this reason, many efforts have been made in the last thirty years to improve both the calculation of the intrinsic PSD and the analysis methods. The first step is obviously obtaining the intrinsic PSD, namely the power spectrum not affected by aliasing and red-noise leakage. The *response* method was first implemented by Done et al. (1992) and Green, McHardy, and Done (1999), and further deeply developed and generalized by Uttley, McHardy, and Papadakis (2002) and Max-Moerbeck et al. (2014), changing the name to *power spectral response* (PSRESP) method. I will discuss in the following the general outline of the PSRESP method, but refer to Uttley, McHardy, and Papadakis (2002) and Max-Moerbeck et al. (2014) for all the details. The basic concept is to use the sampling of the original LC and apply it to simulated LCs with a known PSD shape, to mimic artifacts and distortions that affect the PSD slope. The first step consists of measuring the raw periodogram of the observed LC, $P_{obs}(\nu)$, using Eq. 3.4, rebinning it in frequency to reduce the scatter, after the resampling onto an even-sampled time-series and the multiplication with a proper window function to reduce the red-noise leakage. After this, a PSD model must be chosen to test against the data. As described in the previous section, the typical model for AGN power

spectra is a power-law, but any function can be tested. For the given model, a large number M of LCs are simulated with an even distribution and different power-law indices. The simulations are performed using the method introduced by Timmer and König (1995), which will be further discussed in Sec. 3.3, which randomizes both the amplitude and phase of the Fourier transform coefficients consistent with the statistical properties of the periodogram model. Each simulated LC is resampled with the sampling of the original LC, the observational noise is added, and then they are interpolated to the same even grid. Therefore using the periodograms derived from the M simulated LCs, with the same binning of the original periodogram, it is calculated the mean periodogram $\overline{P_{sim}}(\nu)$, and the related associated error $\Delta\overline{P_{sim}}(\nu)$, equal to the rms spread in each frequency bin. At this point, a χ^2-like test is applied, defined by

$$\chi^2_{obs} = \sum_{\nu=\nu_{min}}^{\nu_{Nyq}} \frac{[\overline{P_{sim}}(\nu) - P_{obs}(\nu)]^2}{\Delta\overline{P_{sim}}(\nu)^2}, \tag{3.5}$$

calculating the χ^2_{obs} that is the χ^2 of the observed LC compared to the simulations for a given PSD model. For each simulated LC, the $\chi^2_{sim,i}$ is calculated, by replacing $P_{obs}(\nu)$ with $P_{sim,i}(\nu)$ in Eq. 3.5. The fraction of the distribution for which $\chi^2_{sim,i} > \chi^2_{obs}$ represents the p-value, namely the significance level at which the tested PSD model can be rejected. Thus, the higher the p-value, the better the PSD model chosen is.

A process widely used to mathematically model AGN optical LCs and their relative PSD shape is the damped random walk (DRW, also called the Ornstein-Uhlenbeck process from Uhlenbeck and Ornstein, 1930). The DRW process can be described as a Brownian motion but with a finite variance in time, therefore, it is stationary by definition. It is expressed as an exponential covariance function

$$S_{DRW}(\Delta t) = \sigma e^{-\left|\frac{\Delta t}{\tau}\right|} \tag{3.6}$$

where σ is the amplitude and τ the characteristic time-scale. Several studies found that the DRW is a good model in the case of LCs with a months-to-years time-scale, which shows a power-law PSD shape (Kelly, Bechtold, and Siemiginowska, 2009; Kozłowski et al., 2010; MacLeod et al., 2010). However, it seems that it is not able to represent faster variability well. The physical explanation is attributed to thermal fluctuations that are driven by an underlying stochastic process, such as a turbulent magnetic field (Kelly, Bechtold, and Siemiginowska, 2009). Nevertheless, as for most of the stochastic variability in AGN, a complete understanding is still far away. Because of the great capability of the DRW in the statistical description of AGN variability, it is also efficiently used for the selection of quasars from other variable sources in large surveys.

In addition to the investigation of the PSD shape on the whole, there are other analysis methods mainly focused on the identification of periodic patterns. The most famous is the Lomb-Scargle periodogram (Lomb, 1976; Scargle, 1982), a modification of the periodogram in Eq. 3.4, defined as

$$P_{LS}(\nu) = \frac{1}{2}\left[\frac{\left(\sum_{i=1}^{N} f(t_i)\, cos(2\pi\nu[t_i-\tau])\right)^2}{\sum_{i=1}^{N} cos^2(2\pi\nu[t_i-\tau])} + \frac{\left(\sum_{i=1}^{N} f(t_i)\, sin(2\pi\nu[t_i-\tau])\right)^2}{\sum_{i=1}^{N} sin^2(2\pi\nu[t_i-\tau])}\right], \tag{3.7}$$

where τ is specified for each ν as

$$\tau = \frac{1}{4\pi\nu} tan^{-1} \left(\frac{\sum_{i=1}^{N} sin(4\pi\nu t_i)}{\sum_{i=1}^{N} cos(4\pi\nu t_i)} \right). \tag{3.8}$$

This new periodogram form in Eq. 3.7 introduced by Scargle (1982), ensures time-shift invariance thanks to τ in Eq. 3.8.[1] Therefore it is applicable for both even and uneven time-series, since for the former it boils down to the classic periodogram equation, suitable for astrophysics applications. Moreover, compared to the classic DFT, it is not just a Fourier method, but it can also be viewed as a least-squares method, it can be derived from the principles of Bayesian probability theory, and it is closely related to phase-folded techniques (Swingler, 1989; VanderPlas, 2018). A weighted form of this method does exist, taking into account the uncertainties of the points in the LC. It is done adding to Eq. 3.7 a multiplicative weight $1/\sigma_i$ within each of the summations, being σ_i the errors of the i-th point of the LC (Gilliland and Baliunas, 1987; Irwin et al., 1989; Scargle, 1989; Zechmeister and Kürster, 2009). This also goes directly into the χ^2 calculation, which is the reason why the Lomb-Scargle periodogram can be seen as an extension of a least-squares method. A further modification of the Lomb-Scargle periodogram is named Generalized Lomb-Scargle method (GLS, Zechmeister and Kürster, 2009), also called floating-mean periodogram (Fig. 3.4). The standard Lomb-Scargle method assumes that all the points of the time-series are pre-centered around the mean value of the signal. In the case of LCs with a duration shorter than a period, or whenever there are missing points in some portion of the phase, a full phase coverage cannot always be reached, leading to the suppression of the peak's power in the periodogram related to the real periodicity. Using the GLS in which the mean can vary, the true period can be easily identified. Obviously, this method is not free from weaknesses. First of all, it is a global method, which means that the LC is treated as a single entity. In a source, a periodicity can also be variable. It can last for a few epochs, as for a TDE or a few repeated flares, and not for the full LC duration. This turns into a decrease in the peak power in the periodogram. The only solution is to analyze single epochs separately, albeit this emphasizes the distortions described before. Distortions that do not have a dedicated treatment in the Lomb-Scargle, more than what has already been described as general mitigation strategies, like the windowing. Moreover, as it is evident from Eq. 3.7, it adopts only sinusoidal functions for the time-series interpretation. If the LCs are not well represented by sinusoids, as is the case for AGN, spurious time-scales can be easily produced. Testing the overall reliability of the peaks is more of a challenge than a weakness of this method. A typical approach to quantify the significance of a peak is the false-alarm probability (FAP), which measures the probability that a time-series with no signal would lead to a peak in the periodogram, due to a coincidental alignment among the random errors of the data. A more computational method is the bootstrap. This method consists of the repeated computation of the periodogram on many random re-samplings of the data in order to approximate the distribution of that statistic (Ivezić et al., 2019). Another approach exploits simulated LC, with the same characteristics as the original LC, for the significance level estimation. Further details on this will be treated in the next section. For a detailed overview of the Lomb-Scargle periodogram strengths and weaknesses, see VanderPlas (2018).

[1] It is important to notice that the τ of Eq. 3.6 is not the same τ of Eq. 3.7 and 3.8.

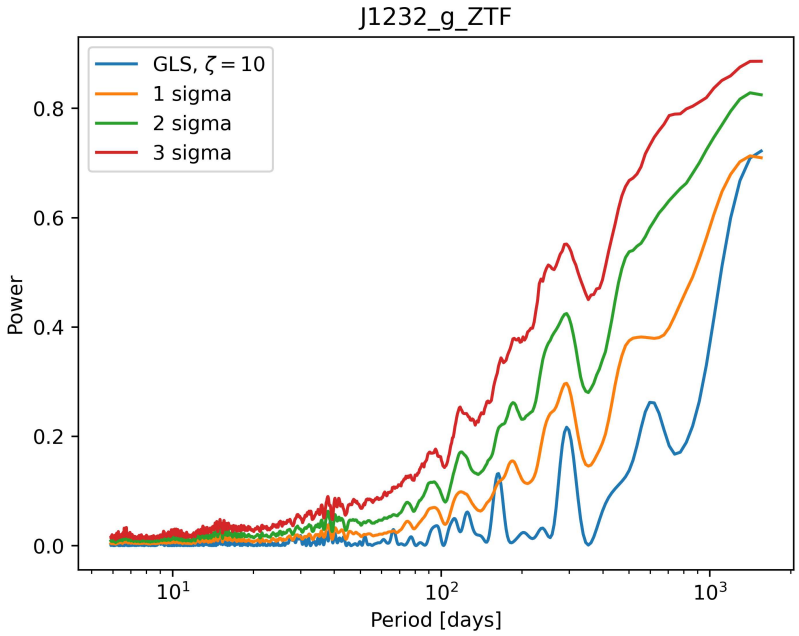

Figure 3.4: GLS periodogram calculated adopting a Hann window function of the LC in the top box of Fig. 3.2. The blue line represents the GLS periodogram, while the orange, green, and red lines are respectively the 1, 2, and 3σ significance levels.

Periodicities in astrophysical sources are rarely constant and permanent, but instead are often intermittent. Therefore, a local analysis of the single epochs of an LC is much more efficient. Treating separately all the time epochs, transient periodic fluctuations which last for a duration even much shorter than the total LC duration can be easily identified. Moreover, with a similar approach, gaps and outlier data points do not affect the analysis as much as in the global methods like the Lomb-Scargle periodogram. This can be done exploiting a wavelet transform (Grossmann, Kronland-Martinet, and Morlet, 1989; Foster, 1996b; Priestley, 1997; Scargle, 1997), a Fourier-based analysis for uneven time-series whose main difference is the possibility of using also non-sinusoidal functions as principal function (see Foster (1996b) for the full mathematical description). The principal function is called wavelet kernel (or mother wavelet), which, for a Fourier transform, is expressed as

$$f(z) = e^{iz} = e^{i\nu(t-\tau)}, \tag{3.9}$$

where ν is the frequency and τ is the characteristic time-scale as in Eq. 3.6. In astrophysics, the most used wavelet kernel for the wavelet transform is the Fourier wavelet with a Gaussian decay profile, called Morlet wavelet (Grossmann and Morlet, 1984), defined as

$$f(z) = e^{bz^2}(e^{iz} - e^{-1/4b}) = e^{b\nu^2(t-\tau)^2}(e^{i\nu(t-\tau)} - e^{-1/4b}), \tag{3.10}$$

where b is a constant value, and $e^{-1/4b}$ is inserted so that the average value of the wavelet is equal to zero. The actual implementation of the wavelet transform is the weighted wavelet Z-transform (WWZ, Fig. 3.5), which includes a weighted estimated variance and a Z-statistic that takes into account how the window function changes with frequency (Foster, 1996a). Because of its capabilities of local periodicity analysis, it can investigate time-scales both in the time and in the frequency

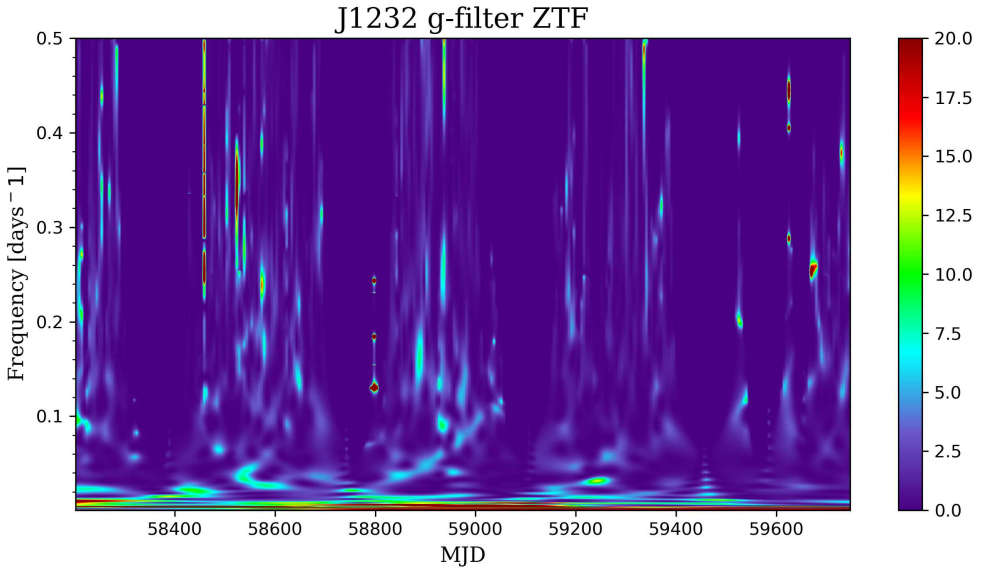

Figure 3.5: WWZ of the LC in the top box of Fig. 3.2. The color scale represents the absolute power of the wavelet transform, where higher values indicate stronger periodicity.

domain. Even though the WWZ is very efficient for transient periodicities, it is not as powerful as the global methods in the case of long-lasting periodicities. Moreover, the computational power necessary in the case of long and crowded LCs must be carefully considered.

I would like to point out an important consideration. As stated in the section, each of the analysis methods described has its pros and cons. Some of them are objectively more powerful than others, but the most effective method is not necessarily the most suitable for a specific case. High-quality single-epoch observations are not easy to obtain, and quality multi-epoch observations are even harder. Therefore, the main problem is often the quality of the data more than the adopted method. For this reason, even if a specific analysis method has its own limitations, it must not be excluded in advance, but it has to be assessed on a case-by-case basis.

3.3 Light curves simulation

There are several applications in which simulated LCs can be used. Among the best known, there are the estimation of the real PSD slope, as described for the PSRESP method in Sec. 3.2, the calculation of significance levels necessary to test the reliability in periodicity searching methods like the GLS, and the creation of artificial time-series with a well-known underlying distribution for the testing of new analysis methods. The first two are the ones that are interesting in my case, and therefore those described here. In the last thirty years, two methods have been used for the LCs simulation: the Timmer & König method (TK method, Timmer and König, 1995) and the Emmanoulopoulos method (EMP method, Emmanoulopoulos, McHardy, and Papadakis, 2013).

The Timmer & König method has been widely used since its algorithm realization (Timmer and König, 1995). It is able to simulate LCs, randomizing both the phase and the amplitude starting from the underlying PSD shape of the data according to their stochastic nature. Basically, it relies on the PSD shape, but it assumes a Gaussian PDF by default, namely preserving only the mean value and the variance

of the original time-series, ignoring higher-order statistical moments, such as skewness and Kurtosis, for instance. The operative steps of the algorithm are as follows:

1. Choose a model for the PSD $F_N(\nu)$, usually a power-law, but sometimes even a broken power-law or a knee-model.
2. For each of the Fourier frequencies ν_i with $i = 1(= \nu_{min}), ..., N(= \nu_{Nyq})$, which define the ΔT and T of the simulated LC, draw two Gaussian distributed random numbers. These last are the real and imaginary parts of the Fourier coefficients. If N is even, the Fourier coefficient related to ν_{Nyq} has to be real.
3. To obtain a real valued LC, the Fourier coefficient of the negative Fourier frequency is given by the complex conjugate of the respective positive frequency coefficient.
4. Each Fourier component is scaled by a factor $\sqrt{\frac{1}{2}F_N(\nu)}$ to match the simulated PSD and the PSD of the original LC.
5. The evenly sampled simulated LC in the time-domain is given by the (real-valued) inverse DFT (IDFT) of the calculated Fourier coefficients.
6. Resample by interpolation the simulated LC to the eventual uneven grid of the original LC.

To account for the contaminants described at the beginning of the previous section, which definitely influence the PSD slope of the original LC, the algorithm considers frequencies $\nu < \nu_{min}$ and $\nu > \nu_{Nyq}$. In particular, the time step is usually chosen as one-tenth of the median time step of the original time series. The LC duration is typically set to ten times the duration of the original LC and then divided into ten separate LCs, each with a total duration equal to T. These values are a compromise that allows a good enough resampling and at the same time reduces the computational time. The TK method, however, does not consider the variance of the original time-series, since it does not take into account the underlying PDF. This step is particularly useful in the PSRESP method described in Sec. 3.2. Max-Moerbeck et al. (2014) suggests scaling the LC variance directly in the time domain. They expressed the total variance of the observed LC σ^2_{data} as

$$\sigma^2_{data} = \sigma^2_{signal} + \sigma^2_{noise} \,, \tag{3.11}$$

where σ^2_{signal} is the intrinsic variance of the observed LC and σ^2_{noise} is the mean 1σ observational uncertainty. Finally, the scaling factor a is derived as

$$a^2 = \frac{\sigma^2_{data} - \sigma^2_{noise}}{\sigma^2_{sim}} \,, \tag{3.12}$$

where the σ^2_{sim} is the variance of the simulated LC before the rescaling.

To attribute an error to each point in the simulated LC, there are three possible ways. The first is adopted in Uttley, McHardy, and Papadakis (2002) and adds the same constant value to all the points, derived from the real noise in the original LC. Max-Moerbeck et al. (2014) instead derive the error as a random number from either a Gaussian or a Poisson distribution, which has zero as mean value and sigma equal to 1σ of the uncertainties distribution of the original LC. Since the error estimation is done after the resampling, the simulated and the original LCs have the same number

of points. Therefore, for the third possibility, the observational uncertainties of each point can be directly applied as errors.

The EMP algorithm has been introduced by Emmanoulopoulos, McHardy, and Papadakis (2013), and it is an implementation of the TK algorithm. The main difference is that it also considers the PDF of the original LC, not only the PSD shape. This is fundamental in my case since, as seen in Sec. 3.1 and in Fig. 3.1, the PDF of AGN is usually not Gaussian. The operative steps of the algorithm are as follows:

1. A Gaussian distributed time-series of N data points using the PSD model of the original LC is created using the TK algorithm. The DFT of this time-series is calculated for $\nu_i \in [\nu_{min}, \nu_{Nyq}]$ deriving for each frequency the amplitude, $A_{norm}(\nu_i)$, and the phase, $\phi_{norm}(\nu_i)$.

2. N pseudo-random numbers are drawn from a PDF model (usually a log-normal distribution), forming a white noise data set, and also in this case, the DFT is calculated deriving amplitudes, $A_{sim}(\nu_i)$, and phases, $\phi_{sim}(\nu_i)$.

3. *Spectral adjustment:* For each ν_i the amplitude $A_{sim}(\nu_i)$ is replaced with the amplitude $A_{norm}(\nu_i)$, keeping the phases $\phi_{sim}(\nu_i)$ unaltered. Performing an IDFT, the result is an LC with the desired PSD but with an altered PDF.

4. *Amplitude adjustment:* In the time-domain, the highest value, $x_{sim.adjust,1}(t_i)$, at the time t_i is replaced with the highest value of the time-series created in (2), $x_{sim,1}(t_i)$. After this, the two second-highest values from the two distributions are replaced, as well as all the N values of the time-series. At this point, the artificial LC has the same PDF as the original LC, but with an altered PSD.

5. Steps (2), (3), and (4) are repeated iteratively k-times until convergence (i.e. $x_{sim,k+1}(t_i) \equiv x_{sim,k}(t_i)$), finally obtaining an LC with the desired PSD and PDF shapes.

In this case, it is not necessary to correct the variance of the simulated LC, since the original PDF is already involved during the simulation phases.

Although the EMP method is more sophisticated than the TK method, it is not trivial to know which one is better suited for a specific case. For the estimation of the intrinsic PSD slope, done using the PSRESP method, Kiehlmann (2015) tested the performances of the TK and EMP algorithms. The tested LCs have power-law PSDs with spectral indices from 0 to 5, coupled with a Gaussian and a log-normal PDF, respectively, for the TK and EMP algorithms. He found that, while using the TK method, the spectral index is kept equal to the original one fairly well, the EMP algorithm does not preserve the spectral index for values $\gtrsim 1.8$. His interpretation is that the EMP algorithm works only for realistic combinations of PSD and PDF, since these last two are not fully independent from each other. This result suggests that the TK method must be preferred for the PSD slope estimation. However, the application in AGN LCs can be problematic, since, as stated before, their PDF distribution is not Gaussian. A global solution has not been found yet, it must therefore be assessed on a case-by-case basis, especially in steep PSD conditions.

As anticipated in the previous section, simulated LCs can be used for estimating the significance levels of the PSD. This can be done since simulated LCs share the characteristics, i.e., the PSD slope, with the original LC as described so far, but they do not necessarily have the same periodicity time-scales, which would lead to the exact same peaks in the PSD. Especially for AGN with a red-noise PSD, the significance levels are fundamental to avoid the detection of false positive periodicities due to the

noise. To estimate the significance levels, the p-values of the original LC peak, p_{peak}, and the simulated LC peak, p_{sim}, are necessary. Calculating the significance levels in a GLS periodogram, a periodicity produces a peak in the periodogram with a period P_{peak} and a power $\mathscr{P}_{peak}$. At the frequency related to P_{peak}, the GLS periodogram from the simulated LCs that have a $P_{sim} \geq P_{peak}$ are used to calculate the *single period p-value*, p_{peak}, and are averaged to obtain the significance level. The single period p-value is the probability of finding a periodic signal at a certain frequency with the same or greater power, under the null hypothesis that the signal is the result of a red-noise process with the same PSD, PDF, sampling, and observational noise as the original LC. O'Neill et al. (2022) claimed that the single period p-value is not reliable for the estimation of the significance levels, since it does not take into account the fact that spurious periodicities from a red-noise process could arise at any period, and suggested that the *global period p-value* must be used instead. To do so, they calculated the GLS periodogram for all the simulated LCs and measured the period, P_{sim}, and power, $\mathscr{P}_{sim}$, of the strongest peak. At each P_{sim} they calculated the p-value p_{sim}. Then they counted the number of simulated LCs for which $p_{sim} \leq p_{peak}$ to estimate the global p-value. They finally used only these simulated LCs to derive the significance levels. Both the methods I described in this section have been developed as Python algorithms in Kiehlmann (2015)[2].

[2]https://github.com/skiehl

Chapter 4

Optical time-series analysis on flaring NLS1s

Foreword: Sources of variability in AGN are frequently an intriguing mystery in astrophysics. Especially when this variability is extremely fast and detected only in a very specific band. This is the case of the radio flares at 37 GHz that the MRO constantly detects from seven sources since 2012. To investigate a possible connection with the optical band, I performed a variability and a periodicity analysis of optical LCs. I used public data from the All-Sky Automated Survey for Supernovae and Zwicky Transient Facility archives. The results show that there is no apparent connection between the extreme radio flares and the optical variability. I found a periodic pattern in the optical emission in only one source for a limited period of time. However, also in this case, the optical periodicity does not seem to be correlated with the radio flares. The lack of connection with the optical wavelengths does not preclude a relation between the radio and possible phenomena at different wavelengths which have not been analyzed yet. Therefore, the analysis performed in this case can be applied at different wavelengths, investigating other possible scenarios.

Based on: Crepaldi et al. in prep.

4.1 Introduction

Any kind of AGN shows stochastic luminosity variations along the whole electromagnetic spectrum (see Ulrich, Maraschi, and Urry (1997) for a review), and frequently this peculiarity is exploited in the identification of new sources. As I described in Sec. 3 there are several phenomena able to explain the variability of the AGN emission. Although all the theoretical scenarios are viable, the physical nature of the variability remains almost totally unclear. Different mechanisms can take place at the same time, producing unique as well as similar observational appearances when compared to other sources, increasing the difficulty of the analysis. This is exactly what MRO has found itself facing since 2012. The last thirteen years, they have monitored seven NLS1s which show non-periodic rapid Jy-level radio flares at 37 GHz (Lähteenmäki et al., 2017; Lähteenmäki et al., 2018).

Some viable interpretations for this phenomenon were extensively discussed in Järvelä et al. (2024). One of the possibilities is that these NLS1s could harbor small-scale (likely a few parsecs) relativistic beamed jets, whose low-frequency radio emission is SSA or FFA by ionized gas. The origin of the ionization is unclear, but it could either be due to the abundant star formation often observed in NLS1s (Sani et al., 2010), or by collision between the jet and the inter-stellar medium (ISM) surrounding the AGN, which produces via shocks a cocoon of ionized gas surrounding the jet head (Bicknell, Dopita, and O'Dea, 1997). A detailed study of the radio spectral

index maps of these sources revealed that the latter is actually the most likely mechanism to account for this unique behavior (Järvelä, Berton, and Crepaldi, 2021). As described before, jets-in-jets magnetic reconnection or magnetic reconnection in the black hole magnetosphere are also viable interpretations. The latter is particularly interesting since it does not require the presence of relativistic jets (see Sec. 6.4 for more details).

The goal of this work is to check if the radio flares had an optical counterpart, and investigate the similarities between the sources in the sample, through a variability and a periodicity analysis, from an optical time-series point of view. This Chapter is organized as follows. In Sec. 4.2 I outline the data used in the analysis, in Sec. 4.3 I describe the variability analysis and in Sec. 4.4 the periodicity searching, in Sec. 4.5 I report the results of the work, and finally, in Sec. 4.6 I discuss the results and provide a conclusion. Throughout this work, I adopt a standard ΛCDM cosmology, with a Hubble constant $H_0 = 72$ km s^{-1} Mpc^{-1}, and $\Omega_\Lambda = 0.73$.

4.2 Sample and data

The analyzed sample is described in Sec. 2.3 (see also Tab. 5.1 for details). The first idea that may have explained the origin of the radio flares was that of undetected relativistic jets. For this reason, for several years all the efforts have been spent on the analysis of the sample in the radio band, since this band, and the γ-ray, is the best place to investigate the relativistic jets' behavior. Several programs dedicated to the radio monitoring of the sources in the sample started in different observatories. However, the acquisition of optical LCs is harder to make compared to radio monitoring. The main reason is obviously the lower amount of time available for observations. Luckily, there are several dedicated sky surveys that monitor large areas in the sky every night. In particular I searched for data related to the sample in the catalogs of All-Sky Automated Survey for Supernovae survey (ASAS-SN), Zwicky Transient Facility survey (ZTF), Catalina Sky Survey DR2 (CSS, Larson et al., 2003), Kamogata/Kiso/Kyoto wide-field Survey (KWS, Maehara, 2014), Transiting Exoplanet Survey Satellite (TESS, Ricker et al., 2014), Kepler/K2 survey (Borucki et al., 2010; Howell et al., 2014), SuperWASP survey (Pollacco et al., 2006), and Pan-STARRS DR2 (Chambers et al., 2016). Among the surveys that had the sources in their catalogs, I excluded LCs with less than 10 points and with large or missing error bars. Since one of the goals is the direct comparison of the radio and optical LCs, I have also excluded those data that were acquired before the start of radio monitoring. The data that respect these constraints are the ASAS-SN and ZTF LCs. The LCs analyzed have a starting point according to the time at which the specific survey became operative, and an ending point around mid-late 2022, which is when I retrieved all the data and performed the analysis described in the following sections.

4.2.1 All-Sky Automated Survey for Supernovae

ASASN-SN scans the whole sky every night down to 18th magnitude (5σ detection limit, Kochanek et al., 2017). It is composed of twenty-four telescopes distributed in five observatories, two in the north (Hawaii and Texas) and three in the south (Chile and South Africa) hemisphere. In addition to supernovae, AGN are one of the most studied kinds of objects by means of ASAS-SN data, as demonstrated by

Shappee et al. (2014) at the very beginning of the project. The data are easily accessible through the Sky Patrol tool[1], which processes in real-time the raw observations using several aperture photometry options. In my case, I retrieved data using the image subtraction photometry with reference flux added, to have a deeper flux limit and magnitude calibration available, making ASAS-SN LCs comparable with those of other surveys. Due to the faintness of the sources, several observations are flagged as non-detections. The Johnson V-band filter (λ_c=5510Å, FWHM=880Å) was the first filter used, sensitive down to ∼17.5 magnitude, from 2013 to ∼2018, and the Sloan g-band filter (λ_c=4800Å, FWHM=1410Å), sensitive up to ∼18.5 magnitude, since 2017 is the filter still operative. Because of this change in the set-up, the LCs have almost simultaneous points of both bands for a bit more than one year. Among the sources, on average, the LCs last from early 2013 to late 2022 (see the starting and ending modified Julian day (MJD) in Tab. 4.2). Moreover, the number of detections goes from about a few tens up to almost 500 (Tab. 4.1). An exception is J1029+5556 with only 2 and 9 points for its ASAS-SN LCs in V- and g-filter, respectively. For this reason, I decided not to use such LCs in the analysis. Flagged points and bad points, such as unreliable outliers, were removed through automatic processes and a visual inspection. As for all the long LCs of non-circumpolar sources, seasonal gaps are present.

4.2.2 Zwicky Transient Facility

ZTF is a time-domain survey using a wide-field camera mounted on the Palomar 48-inch Schmidt telescope. Since March 2018, it has been one of the most used and suited facilities for LC analysis of the northern sky (Masci et al., 2019; Bellm et al., 2019; Graham et al., 2019). It is widely used in variability searching thanks to the high observing cadence of 3 days in covering a specific portion of the sky and the rapidity with which the data is released. Moreover, the available Time-Series Tool[2] enables getting a first look at an LC and making simple period searching. Three filters are used: g (λ_c=4783.50Å), r (λ_c=6417.10Å) and i (λ_c=7867.41Å), with widths from ∼150Å to ∼310Å (Dekany et al., 2020). It is important to notice that even though both ASAS-SN and ZTF use the g-filter, the ASAS-SN filter is roughly ten times wider than the ZTF one. All the LCs analyzed have been retrieved from the DR18, with all the filters available and last from the beginning of the survey to mid-late 2022 (Tab. 4.2). Even in this case, the only exception is J1029+5556 for which the i-filter LC is missing. The most-crowded LCs are those observed using r-filter, with 584 points in the worst case and 946 in the best one, almost equal to g-filter, and approximately four times more than i-filter (Tab. 4.1). As for ASAS-SN data, flagged points and outliers were removed, and unavoidable seasonal gaps are present.

4.3 Optical light curves analysis

The first step of the analysis was to check if the radio flares had an optical counterpart. Considering the available optical filters, correlated radio-optical flares would give us more information on the flares' origin, given both intensity and delay at different wavelengths. To do so, I compared all the available radio and optical LCs for each object, as visible in Fig. 4.1.

[1] https://asas-sn.osu.edu/
[2] https://irsa.ipac.caltech.edu/irsaviewer/timeseries

Table 4.1: Number of data points in the sources LCs.

SDSS name	Alias	ASAS-SN V	ASAS-SN g	ZTF g	ZTF r	ZTF i
(1)	(2)	(3)	(4)	(5)	(6)	(7)
J102906.69+555625.2	J1029	2	9	437	691	–
J122844.81+501751.2	J1228	119	216	521	584	179
J123220.11+495721.8	J1232	110	261	528	584	179
J150916.18+613716.7	J1509	18	70	760	832	301
J151020.06+554722.0	J1510	32	46	903	944	318
J152205.41+393441.3	J1522	24	478	812	822	162
J164100.10+345452.7	J1641	268	322	959	946	149

Columns: (1) SDSS source name; (2) short name; (3) ASAS-SN V-filter LC points; (4) ASAS-SN g-filter LC points; (5) ZTF g-filter LC points; (6) ZTF r-filter LC points; (7) ZTF i-filter LC points.

Table 4.2: Starting-ending time of the sources LCs.

Source	ASAS-SN V	ASAS-SN g	ZTF g	ZTF r	ZTF i
(1)	(2)	(3)	(4)	(5)	(6)
J1029	56992-57163	58143-59605	58202-59731	58217-59739	–
J1228	56370-58447	58087-59806	58202-59755	58216-59751	58232-59339
J1232	56370-58303	58087-59806	58202-59755	58216-59751	58232-59339
J1509	56402-58310	58108-59817	58202-59789	58197-59791	58232-59341
J1510	56338-58328	58130-59792	58202-59824	58198-59806	58227-59341
J1522	56336-56535	58099-59848	58202-59824	58198-59824	58227-59341
J1641	56337-58391	58028-59856	58203-59828	58198-59828	58227-59341

Columns: (1) Source name; (2) starting-ending MJD of ASAS-SN V-filter LC; (3) starting-ending MJD of ASAS-SN g-filter LC; (4) starting-ending MJD of ZTF g-filter LC; (5) starting-ending MJD of ZTF r-filter LC; (6) starting-ending MJD of ZTF i-filter LC.

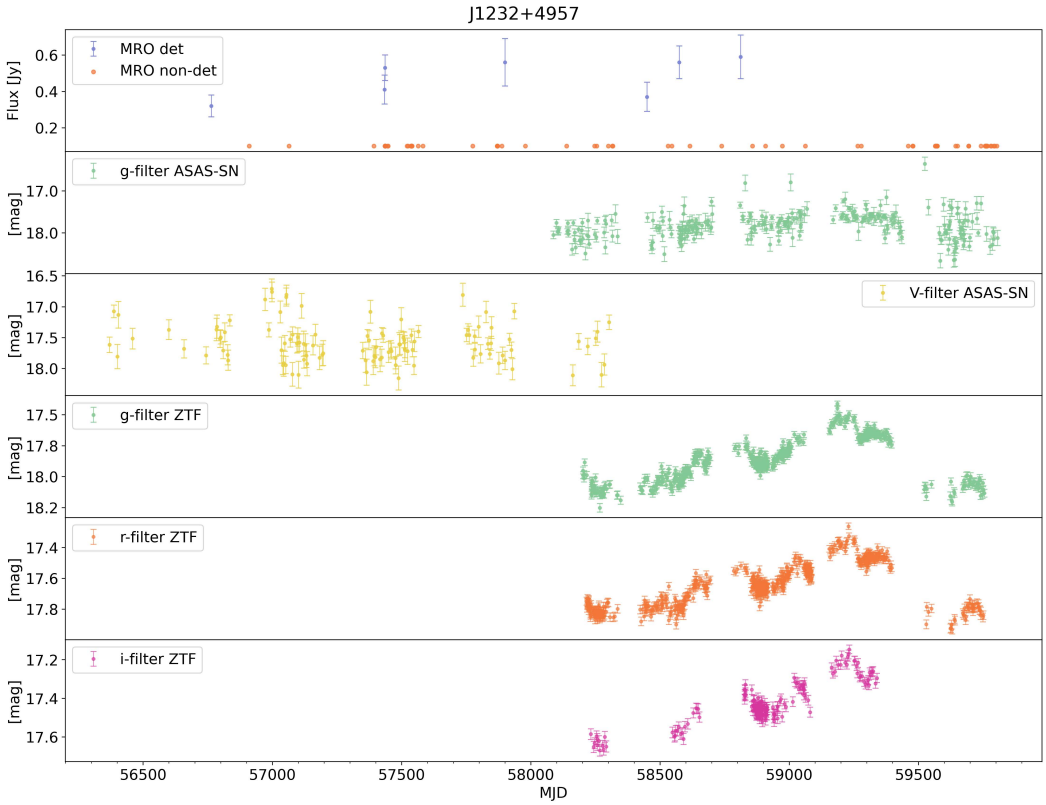

Figure 4.1: Radio and optical LCs of J1232.

The subsequent step was to evaluate the variability for all the LCs, since it is an important information of the time-series analysis as seen in Sec. 3, and even because the lack of variability excludes any periodicity in advance. To test the degree of variability of each LC, I used the reciprocal of the von Neumann ratio ($1/\eta$) as variability index.

4.3.1 Variability test

As described in Sec. 3, the von Neumann ratio is a correlation-based index (Neumann, 1941; Neumann, 1942; Sokolovsky et al., 2017). This means that, in comparison to the scatter-based indices which consider only the distribution of measured magnitudes, it examines the time information of the LC. It is the ratio of the mean square successive difference to the distribution variance, defined as

$$\frac{1}{\eta} = \frac{\sigma^2}{\delta^2} = \frac{\sum_{i=1}^{N} (m_i - \overline{m})^2/(N-1)}{\sum_{i=1}^{N-1} (m_{i+1} - m_i)^2/(N-1)}, \tag{4.1}$$

where m_i is the i-th magnitude, $\overline{m}$ the average magnitude, and N the total number of points in the LC. As already cited, Sokolovsky et al. (2017) tested $1/\eta$ index and several other variability indices using real and simulated data, comparing their performances. They found that $1/\eta$ appears to be the best compromise index as it performs better than most of the other tested indices. They point out that this index is sensitive only to variability on time-scales longer than the sampling time. However, considering the separation time of the points in the analyzed LCs, the detectable

variability using $1/\eta$ index is short enough for my purposes. Faster variability, like INOV for instance, cannot be detected in any case using surveys as those used in this work, which is beyond the scope anyway.

While performing variability tests, the most challenging aspect is to properly define a threshold that tells us if an LC is variable or not. As I will describe in Section 4.4.3, the statistically appropriate way to set a threshold is by means of simulated LCs. That way, I defined the null hypothesis of "no intrinsic variability" using a Monte Carlo approach, which was compared with the real LC through the variability index. In the following, the steps I used to label the variability of each LC:

1. For each real LC, I calculated the related variability index;
2. I simulated N=1000 Gaussian noise LCs with mean equal to zero and standard deviations equal to the uncertainties of the real data points. This sets the null hypothesis of "no intrinsic variability";
3. I calculated the variability index $1/\eta$ for all simulated LCs;
4. I counted how often the simulated LCs give a variability index equal to or higher than the one estimated for the real LC, defining this number with P;
5. I divided P by the number of simulated LCs (N=1000), obtaining the p-value;
6. I finally set the threshold to reject the null hypothesis at a significance level of 5%. Therefore, if the p-value is lower than 0.05, the alternative hypothesis is true, i.e., the real LC shows intrinsic variability.

To perform an additional test, I calculated the fractional variability that provides insights into the degree of variability. For the calculation, I followed the prescription of Vaughan et al. (2003), described also in MAGIC Collaboration et al. (2023). The parameter is estimated as

$$F_{var} = \sqrt{\frac{\sigma^2 - \overline{\sigma_{err}^2}}{\overline{S}^2}} \,, \tag{4.2}$$

where σ^2 is the variance of the measured fluxes, and $\overline{\sigma_{err}^2}$ is the mean square error of the points. The uncertainty associated to F_{var} (Poutanen, Zdziarski, and Ibragimov, 2008; Aleksić et al., 2015) is estimated as follows

$$\Delta F_{var} = \sqrt{F_{var}^2 - \sigma_{NXS}^2} - F_{var} \,, \tag{4.3}$$

where σ_{NXV}^2 is the normalized excess variance calculated as

$$\sigma_{NXV}^2 = \sqrt{\left(\sqrt{\frac{2}{N}}\frac{\overline{\sigma_{err}^2}}{\overline{S}^2}\right)^2 + \left(\sqrt{\frac{\overline{\sigma_{err}^2}}{N}}\frac{2F_{var}}{\overline{S}}\right)^2} \,, \tag{4.4}$$

where N is the number of points in the LC.

4.3.2 PSD slope estimation

The investigation of the PSD shape is crucial both for the understanding of the variability origin and for the simulation of synthetic LCs comparable to the observed LC. As I described in Sec. 3.2, the intrinsic PSD can be estimated through the PSRESP

Table 4.3: Selected gap for the PSD slope estimation algorithm

Source	ASAS-SN V	ASAS-SN g	ZTF g	ZTF r	ZTF i
(1)	(2)	(3)	(4)	(5)	(6)
J1029	–	–	40	40	–
J1228	50	50	40	40	50
J1232	70	50	40	40	50
J1509	50	60	50	40	40
J1510	60	70	40	50	40
J1522	30	40	40	40	40
J1641	50	40	40	40	40

Columns: (1) Source name; (2)-(6) minimum seasonal gap for the LC cited in the head of each column.

method, which takes into account the uneven and finite sampling, observational errors, red noise leakage, and aliasing of an LC. The original PSRESP method of Uttley, McHardy, and Papadakis (2002) has been revised by Max-Moerbeck et al. (2014), and translated into a Python algorithm by Kiehlmann (2015) with some minor improvements. This algorithm is the one I used for this work. Operatively, it firstly simulates artificial LCs by means of the TK method in Sec. 3.3, assuming an underlying power-law PSD. At the beginning, the simulated LCs have an even sampling rate ten times shorter than the median sampling of the observed LC, and a total duration ten times longer. After the simulation, each LC is divided into ten separate LCs, obtaining ten simulations through one iteration. At this point, the variance and the uneven sampling of the original LC are applied to the simulations, and the noise is added to each point following the suggestion of Max-Moerbeck et al. (2014) as explained in Sec. 3.3. N simulated LCs are generated trough a range of spectral indices β, calculating the periodogram for each one. After this, the algorithm searches for the optimal model parameters. Following the PSRESP method, the χ^2_{obs} in Eq. 3.5 is minimized, through a fitting process of χ^2_{obs} with different β, to find the most suitable intrinsic β (see Kiehlmann (2015) for the full description).

The used algorithm also considers the seasonal gaps and the minimum number of points in the time-series. Both constraints can be decided by the user according to the data. I decide to leave the minimum number of points as set by default, i.e., equal to 10, and to select for each LC a gap slightly shorter than the shortest seasonal gap. The set gaps are reported in Tab. 4.3. The algorithm, when converging to a result, returns plots of the tested PSDs (bottom box of Fig. 3.2) and the fitting that brings to the best spectral index (Fig. 4.2).

4.4 Periodicity searching

Considering the randomness in the occurrence of the radio flares, I do not expect that such an effect in optical, if correlated, would have shown a periodic trend. However, a periodic pattern in the optical band suggests instabilities in the accretion disk, which may lead to flare production. Unlike the variability analysis, the idea at the basis of the periodicity analysis was indeed the search for possible causes that can lead to the production of the radio flares, more than to the investigation of observational periodic traits produced by the flare episodes. Besides a visual inspection of both the LCs in the time domain and the respective PSDs in the frequency domain, for each LC I computed a detailed GLS periodogram analysis (Lomb, 1976; Scargle,

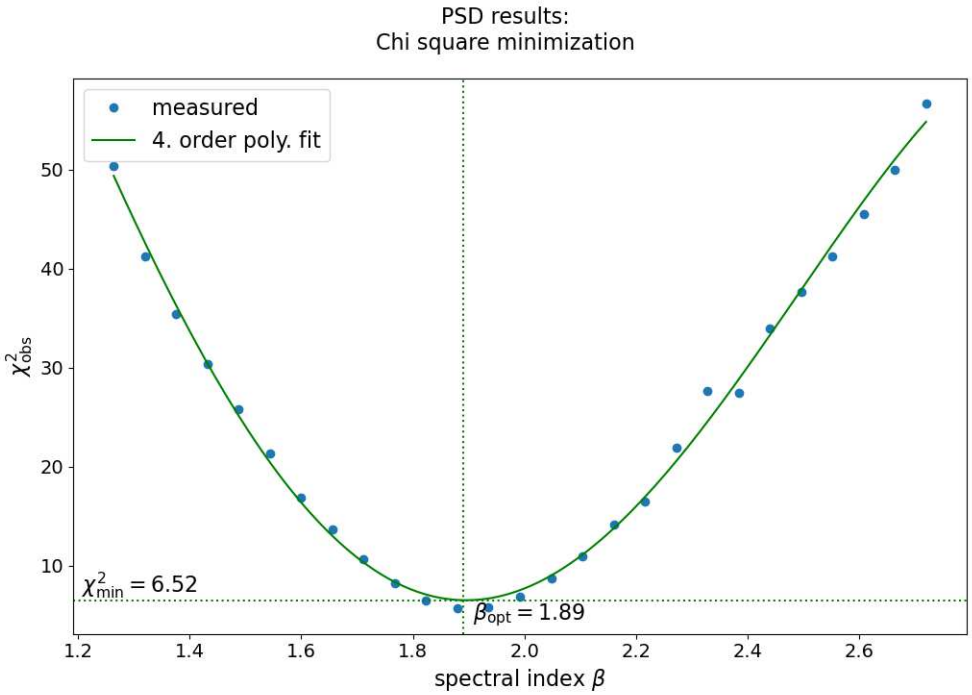

Figure 4.2: Fitting of the χ^2_{obs} calculated in the PSRESP method version of Kiehlmann (2015). The minimum χ^2_{min} corresponds to the most realistic intrinsic β.

1982) and a WWZ analysis (Foster, 1996a). For a periodicity searches would be beneficial joining multiple LCs to get a longer LC. However, I did not combine ASAS-SN and ZTF LCs because the characteristics of the respective observations (one above all is the different central wavelength of the filters) are not the same.

4.4.1 Generalized Lomb-Scargle periodogram

The GLS periodograms have been calculated using the version implemented in the pyAstronomy python package[3] (Czesla et al., 2019). I used the GLS instead of the simpler LS periodogram, given the much better performance for astronomical LCs. Moreover, I used a Hann function as a window function. The generated GLS periodograms have a frequency range between ν_{min} and ν_{Nyq}, which changes according to each LC. The frequency interval is uniformly sampled with steps of $\Delta\nu = 1/\zeta T$. I decided to use a $\zeta = 10$, enough for an adequate sampling. I derived the periodogram for all the LCs that have been found variable in Sec. 4.3.1 and for which the algorithm managed to measure the PSD slope. The latter is necessary for the significance levels estimation, which will be described in Sec. 4.4.3, since in that case the main step is the simulation of LCs with the same PSD as the observed LC.

4.4.2 weighted wavelet Z-transform

Unless the periodicity is very strong and lasts for a long enough time, the detection of a strong peak in the periodogram generated for the whole LC is not straightforward. The capability of the WWZ in the analysis of sub-portions of the whole LC is extremely useful in this case. For the WWZ calculation, I used the VARTOOLS Light Curve Analysis Program (Hartman and Bakos, 2016), a command-line utility that

[3] https://github.com/sczesla/PyAstronomy

provides tools for processing and analyzing astronomical time series data. Several parameters of the WWZ can be either set in advance or left free to vary. The one I chose in the software is a frequency range between 0 and 2 cycles per day, a step of 1/T for the frequency sampling, and a step of 5 days for the LC duration. Compared to the GLS periodogram, the additional constraints are necessary since the greatest complexity of the WWZ transform. This is evident even looking at Fig. 3.5, where the tree dimensions of the plot are related to the time, the frequency, and the power of the WWZ. As for the GLS, I calculated the WWZ only for the variable LCs with a measured, reliable PSD slope.

4.4.3 Significance levels estimation

I already pointed out that, as for AGN, also for NLS1s, the PSD red shape can deceive the detection of unreal periodicities. Especially for long timescales, even a quite strong peak related to the red noise can be confused with a periodicity. This possibility is reduced by means of analysis techniques that avoid such confusion, like the GLS periodogram and the WWZ, indeed. However, a dedicated analysis could not be enough to distinguish between real and fake peaks. Simulated LCs with preserved statistical and variational characteristics of the original AGN LC can be the answer. I therefore simulated 20000 LCs for all the sources in the sample, estimating the probability of chance occurrence of any feature present in the LCs. To do so, as already cited, I used a Python algorithm also included in Kiehlmann (2015), further divided into two main phases. As the first step, it produces simulated LCs with the same PSD and PDF of each observed LC, exploiting the EMP method described in Sec. 3.3. In this phase, the used PSDs are assumed to have a power-law shape, with the slopes retrieved in the Sec. 4.3.2. The second step consists of calculating the 1σ, 2σ, and 3σ significance levels for the GLS periodogram, following the last part of Sec. 3.3, extensively described in O'Neill et al. (2022). As p_{peak}, necessary for the calculation of the global p_{sim}, a value equal to 0.05 (5%) has been used. It is important to notice that even in the case where a peak has a power bigger than the 3σ significance level, the reliability of this peak cannot be taken for granted. This is because I am comparing simulated LCs with a real astronomical LC. In this case, the p-value of the peak can be very important (see O'Neill et al. (2022) for a detailed description). I did not calculate the significance levels for the WWZ since they require much longer computational time, and efficient dedicated algorithms are not present yet in the literature. Therefore, I used the WWZ to investigate the time information of the periodicities detected by the GLS periodogram and to compare the results obtained from the two methods.

4.5 Results

4.5.1 Radio-optical LCs comparison

Comparing the ASAS-SN and ZTF optical LCs with the radio LCs observed by MRO, the powerful flares at 37 GHz do not seem to be correlated to the optical variability. In all the optical LCs, indeed, there is neither a fast and strong increase of the flux as seen in radio nor particular variability close in time to the radio flares, which can suggest a multiwavelength correlation. Visually, the optical LCs have a constant stochastic variability, and the only points with a completely different flux compared to the mean value have been classified as outliers and so removed. As outliers, I

Table 4.4: Variability test.

Source	ASAS-SN V	ASAS-SN g	ZTF g	ZTF r	ZTF i
(1)	(2)	(3)	(4)	(5)	(6)
J1029	–	–	2.18, V	1.47, V	–
J1228	0.56, n-V	0.63, V	0.67, V	0.66, V	0.53, n-V
J1232	0.63, V	0.73, V	12.76, V	10.08, V	7.02, V
J1509	0.51, n-V	0.72, V	1.30, V	1.12, V	0.87, V
J1510	1.23, V	0.41, n-V	0.72, V	0.74, V	0.77, V
J1522	0.48, n-V	0.55, n-V	0.78, V	0.71, V	0.60, V
J1641	0.54, n-V	0.64, V	0.81, V	0.84, V	0.82, V

Columns: (1) Source name; (2)-(6) variability index described in Eq. 4.1 for the LC cited in the head of each column. n-V stands for non-Variable LC, while V stands for Variable LC.

Table 4.5: Fractional variability.

Source	ASAS-SN V	ASAS-SN g	ZTF g	ZTF r	ZTF i
(1)	(2)	(3)	(4)	(5)	(6)
J1029	–	–	0.90±0.02	0.70±0.02	–
J1228	1.21±0.10	1.39±0.05	0.19±0.01	0.17±0.01	0.16±0.02
J1232	1.53±0.09	1.57±0.05	0.93±0.01	0.76±0.01	0.61±0.01
J1509	4.04±0.27	1.29±0.14	0.58±0.02	0.36±0.01	0.26±0.01
J1510	2.41±0.20	1.13±0.21	0.48±0.01	0.44±0.01	0.43±0.01
J1522	0.45±0.07	0.65±0.02	0.51±0.01	0.52±0.01	0.52±0.01
J1641	1.09±0.05	1.28±0.04	0.46±0.01	0.42±0.01	0.39±0.01

Columns: (1) Source name; (2)-(6) fractional variability index described in Eq. 4.2 for the LC cited in the head of each column. All the values are multiplied by a value $\times 10^2$ only for readability purposes.

defined those isolated data points with unrealistic flux values. The radio and optical LCs of the sample are visible in Fig. 4.5, 4.6, 4.1, 4.7, 4.8, 4.9 and 4.10.

4.5.2 Variability

The results of the variability test, by means of the calculation of $1/\eta$ in Eq. 4.1, are reported in Tab. 4.4. 6 out of 14 ASAS-SN LCs and 19 out of 20 ZTF LCs have passed the test, and have been therefore classified as variable LCs. Moreover, in Tab. 4.5 I reported the fractional variability calculated following Eq. 4.2. This index is more useful for a comparison between fractional variability parameters of different LCs related to the same source rather than to identify if an LC is variable. For the LCs identified as variable, I estimated the intrinsic PSD slopes, which are listed in Tab. 4.6. The PSRESP method did not converge in all the cases, therefore, not for all the variable LCs I managed to calculate a proper estimation of the PSD slope. The results are between 0.74 for the minimum and 2.80 for the maximum, which are typical values for AGN.

4.5.3 GLS and WWZ

A first visual inspection of the optical LCs did not show long-lasting periodicities. Some LCs, as the J1232 g-filter ZTF LC in Fig 4.1, show a roughly sinusoidal trend,

Table 4.6: PSD slope.

Source	ASAS-SN V	ASAS-SN g	ZTF g	ZTF r	ZTF i
(1)	(2)	(3)	(4)	(5)	(6)
J1029	–	–	2.06	2.80	–
J1228	–	0.92	0.95	0.98	–
J1232	–	0.96	1.89	1.57	2.06
J1509	–	–	1.25	1.01	–
J1510	–	–	–	1.08	–
J1522	–	–	0.74	–	–
J1641	–	–	–	–	1.13

Columns: (1) Source name; (2)-(6) PSD slope for the LC cited in the head of each column.

even though a specific time-scale cannot be visually identified. For the sources with the PSD slope available in Tab. 4.6 I calculated the GLS with the relative significance levels and the WWZ. In three cases, J1029 g-filter and z-filter ZTF and J1232 i-filter ZTF LCs, the algorithm did not converge to reliable significance levels for the GLS. Therefore, I decided to remove these LCs from the analysis since there were no strong peaks visible, and the small peaks cannot be considered as reliable without proper significance levels. In the end, I performed a periodicity analysis for eleven LCs. The GLS and WWZ plots are reported in Fig. 4.3 and 4.4. In the GLS, one or more peaks with a power $>3\sigma$ are present only for the J1228 g-filter ZTF and J1510 r-filter ZTF LCs. In the first case, the detected periodicity has a time-scale of $\sim$7 days, which, looking at the WWZ, lasted for slightly more than 20 days. The p-value related to this peak is very high, confirming that the peak is due to an artifact on the LC, possibly caused by the aliasing, and not to a real periodic emission. For the ZTF LC of J1510 in r-filter, there are two peaks in the GLS, one related to a $\sim$29 days periodicity and one to a $\sim$27 days periodicity. Due to the similar time-scales, it is possible that both peaks are related to the same periodic trend. Considering the WWZ of this LC, there are two periods in which the periodic patterns have been detected. The first started at MJD58600 and lasted for $\sim$80 days, and the second started at MJD58950 and lasted for $\sim$90 days. Contrary to the previous case, the periodicities in J1510 have a low p-value, suggesting that they could be real periodic emissions. Interesting, right after the first period, the source has been detected in a flaring state by MRO (MJD58691). Unfortunately I could not investigate if this periodicity is visible also for the other filters since in those cases the PSD slope estimation failed, preventing the LCs simulations and then the periodicity analysis.

4.6 Discussion and conclusions

In this work, I performed a variability and a periodicity analysis of a sample of seven NLS1s, using publicly available optical LCs acquired by the ASAS-SN and ZTF surveys. The main goal was to identify if any possible pattern on the optical LC would be related to the radio flares detected at 37 GHz by MRO. According to what I found, there are no strong and unusual patterns on the optical LC, which might suggest a connection between the optical emission and the origin of the radio flares.

Low cadence in the optical observations could be one of the reasons why the radio flares have not been detected in the optical band. Assuming that all the radio flares have the same origin, and that they are visible at all wavelengths, I would

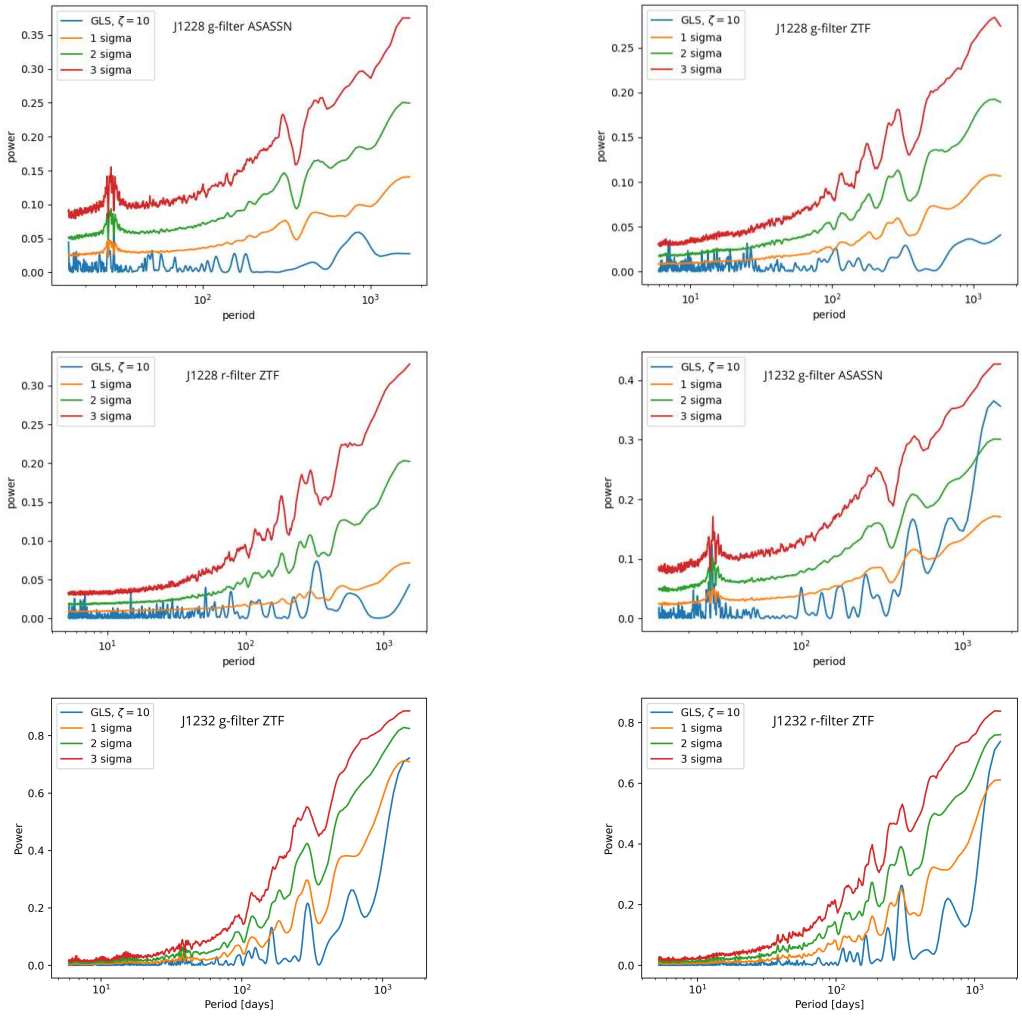

Figure 4.3: GLS with significance levels of the selected LCs.

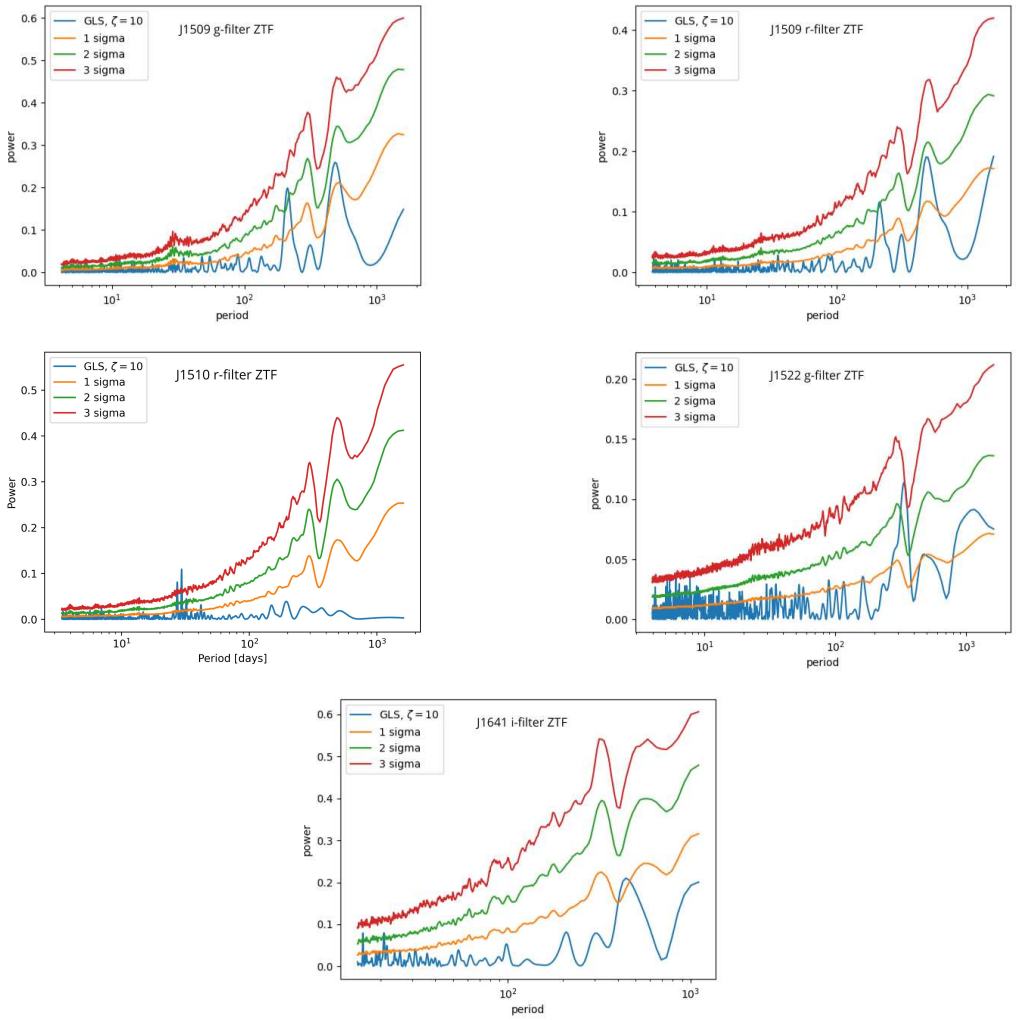

Figure 4.3: *continued*

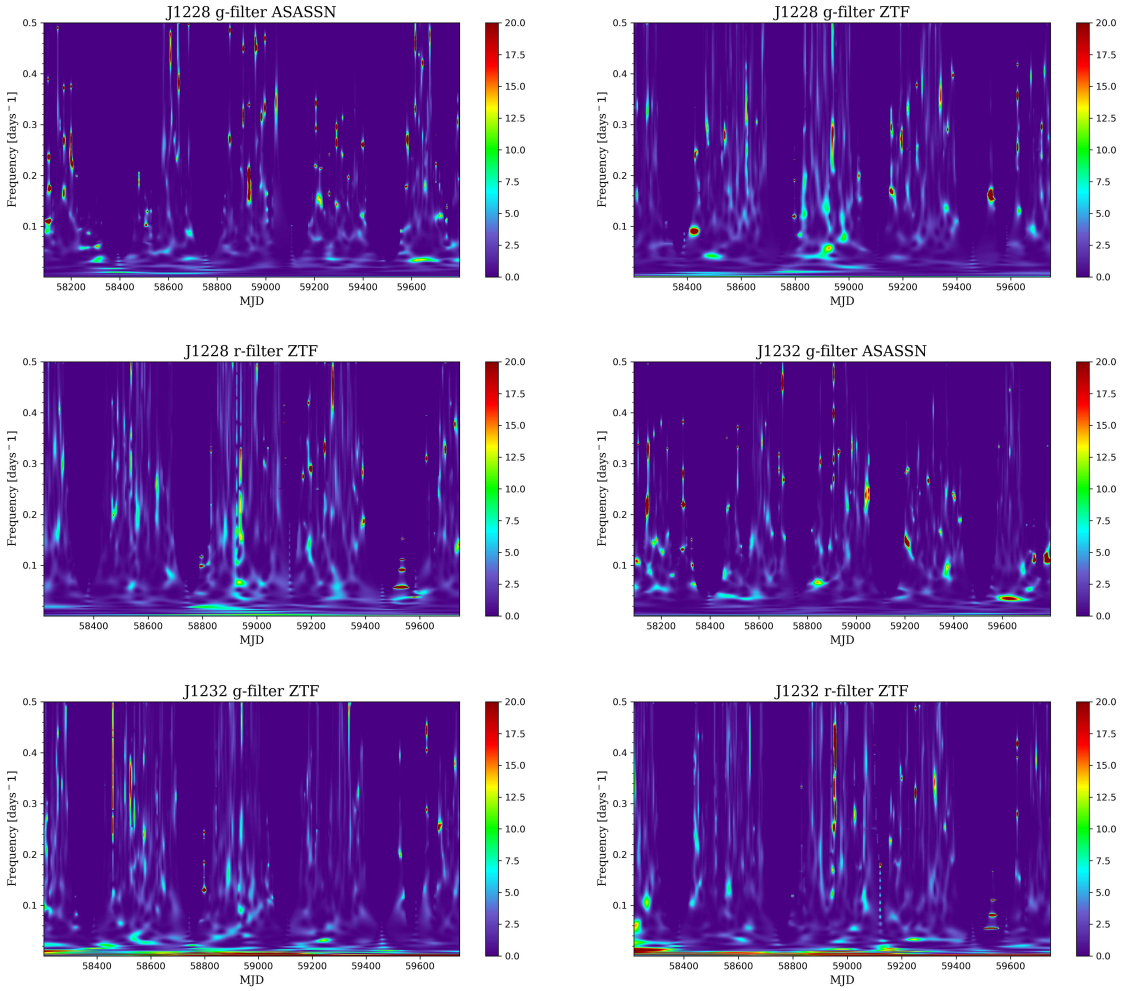

Figure 4.4: WWZ of the selected LCs.

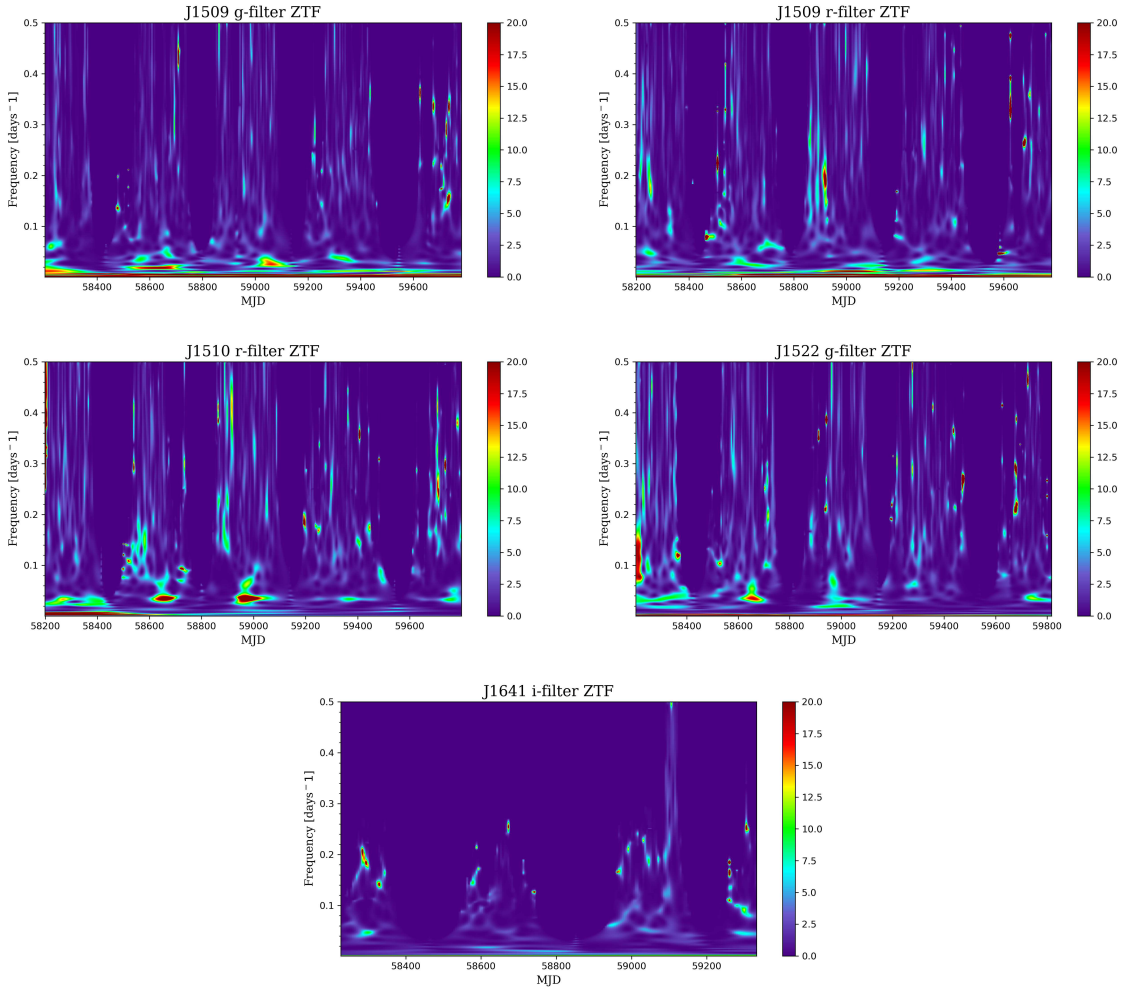

Figure 4.4: *continued*

expect a constant, positive or negative, time delay between the radio and the optical flux increasing. Since in the time covered by the optical LCs, several flares have been detected by MRO, it is quite improbable that absolutely no features of these flares have been seen in optical. Especially considering that, at least in a few cases, there are quasi-simultaneous radio-optical observations, at most a few days apart, as well as well-sampled optical LCs before and after the radio flares. Järvelä et al. (2024) stated that the detected radio flares had a duration of at least several hours. Under these conditions, if the episodes in the two frequencies had been correlated, the probability of detection of a flare in the optical LCs would have been quite high. However, as I will show in the next chapters, new radio observations are challenging this conclusion, showing much shorter flare time-scales. Assuming a correlation between the radio and the optical band, a flare duration even less than an hour makes the observation of the event in optical very hard, given the observational cadence of ASAS-SN and ZTF surveys. Therefore, although with a lower probability, an optical-radio correlation cannot be totally excluded.

The aim of the $1/\eta$ index is the calculation of the p-value, which uses simulated Gaussian noise LCs drawn relying on the uncertainties of the points in the real time-series. For this reason, in the literature, not great attention is given to the value of the variability index itself, as well as to its error estimation. A different derivation is used for the fractional variability index that includes the errors of the time-series points in Eq. 4.2, and for which the related uncertainty is provided as in Eq. 4.3. Because of the different derivation approach, a direct comparison between the values of the variability indexes is not very useful. In a similar manner, the absolute value of each index can be misleading. Indeed, it does not claim how variable an LC is in an absolute way, since it is strongly related to the general quality of the LC, such as sampling cadence, uncertainties, and so on. It is clear, even considering the analysis carried out here. Indeed, the ASAS-SN LCs used have a poorer density of points and larger uncertainties compared to the ZTF LCs. The results, for instance, for J1522 were that the two ASAS-SN LCs have been classified as non-variable, while the three ZTF LCs have been classified as variable. For this reason, the comparison with a p-value as described is the proper way in which a variability index must be used.

Beckmann and Shrader (2012) pointed out that, as in radio-quiet AGN, the continuum variability is color-dependent, namely, the blue bands have higher variability amplitude than red bands. This follows the hypothesis that the optical continuum emission is predominantly thermal emission from the accretion disk and that longer wavelength emission originates from larger radii where the disk is cooler, as represented in Fig. 1.2. Even if not all the sources are consistent with this scenario, the data analyzed in this work seem to be. Looking at the variability indexes in Tab. 4.4 and 4.5, for almost all the sources the resulting index is higher in the bluer band compared to the redder one, suggesting a higher amplitude of the variability at shorter wavelengths. It is important to notice that the comparison of the variability index, as I discussed before, can be misleading because it is strongly dependent on the quality of the LC. The only possible comparison can be done between the different filter LCs obtained for a source with the same telescope, since the observations with the available filters are performed simultaneously, which in this case supports the idea of color-dependent variability. Nevertheless, the direct comparison of the variability indexes must be used only as an indicator.

It is interesting that MRO detected a flare in J1510 close to the period when the optical emission in the r-band showed a periodic pattern. Even though a connection might be present, the probability is very low. The optical periodicity has a time-scale

∼28 days, while from the most recent radio data, the flares at 37 GHz have a time-scale of a few hours. This suggests that the emitting regions in the two frequencies are different, as well as the emission mechanism generating the amplitude variability. Moreover, this is the only case where a radio flare episode almost coincides with a detected optical periodicity in all the data I analyzed. The physical interpretation of the optical periodicity is not easy to address. The short duration of the two periodic patterns compared to the total LC duration obviously suggests a transient phenomenon. A TDE can safely be excluded, since this should have been visible also in other bands, and it usually shows a decrease in the time-scale with time, not present in this case. A likely interpretation is that the short-term periodicities are due to accretion instabilities in the disk, which occur in a specific layer and therefore are visible only in a limited wavelength range (Hameury, Viallet, and Lasota, 2009; Burke et al., 2021; Neustadt and Kochanek, 2022). Accretion instabilities might propagate into the relativistic jets, triggering flux variations of the jet emission. In this specific case, however, the viable hypotheses presented in Järvelä et al. (2024) to explain the radio flares' nature do not require any accretion instability. Considering what I discussed so far, even if it cannot be totally excluded, I can conclude that the radio flare and the optical periodicity are not related to each other.

Several authors found that the amplitude of the optical variability increases toward shorter wavelengths (Hawkins, 2002; Wilhite et al., 2008; Sun et al., 2014). Moreover, Wilhite et al. (2008) confirmed the presence of an anti-correlation between luminosity and optical variability, and a correlation between optical variability and black hole mass (Wold, Brotherton, and Shang, 2007; Sun et al., 2018). They tested it by means of the structure function defined in di Clemente et al. (1996). This function measures the variability amplitude as a function of the time-scale Δt. For strongly variable AGN, the structure function shows an increasing trend toward larger Δt (Wilhite et al., 2008). I calculated the structure function for all the LCs of the sample, possibly testing the correlations described before, using 200 days in the source rest-frame as the duration for each time bin. The results were totally variable, with a slope for the structure function from negative to positive without any rule. This is probably due to the small variability and the uneven distribution nature of the analyzed LCs (Kozłowski, 2017). Therefore, I did not manage to test the cited correlations with the physical parameters of the sample in the proper way.

The analyzed LCs have very uneven distributions, with some epochs with large gaps, usually due to the seasonal gaps, and others very crowded with observations. In general, for each filter, the available data had a duration of a couple of years. Even though it could be enough to reach the main goal of this work, namely the investigation of a possible correlation between radio flares and optical variabilities, longer-lasting LCs are necessary for a detailed analysis of the periodicities. For this reason, more sophisticated studies are necessary to spot even possible, relatively strong periodicities with longer time-scales. However it is important to notice that, given the possible very short time-scale of these events, a variability and correlation analysis like the one reported here would benefit most from a shorter cadence for the optical observations than from a longer LCs' duration. A monitoring using as many filters as possible, for at least a few months, and with a cadence of <1 hour during the night would be the best conditions for a deep and complete study. Romano et al. (2023) detected an X-ray brightening soon after an MRO detection, which suggests a possible connection between radio and X-ray frequencies. For instance an inverse Compton catastrophe event, coupled with the magnetic reconnection, produce a brightening at high-energies. Therefore, an interesting follow-up would be to apply the analysis I did in this work also at higher frequencies, e.g., X-ray, possibly

exploiting simultaneous observations.

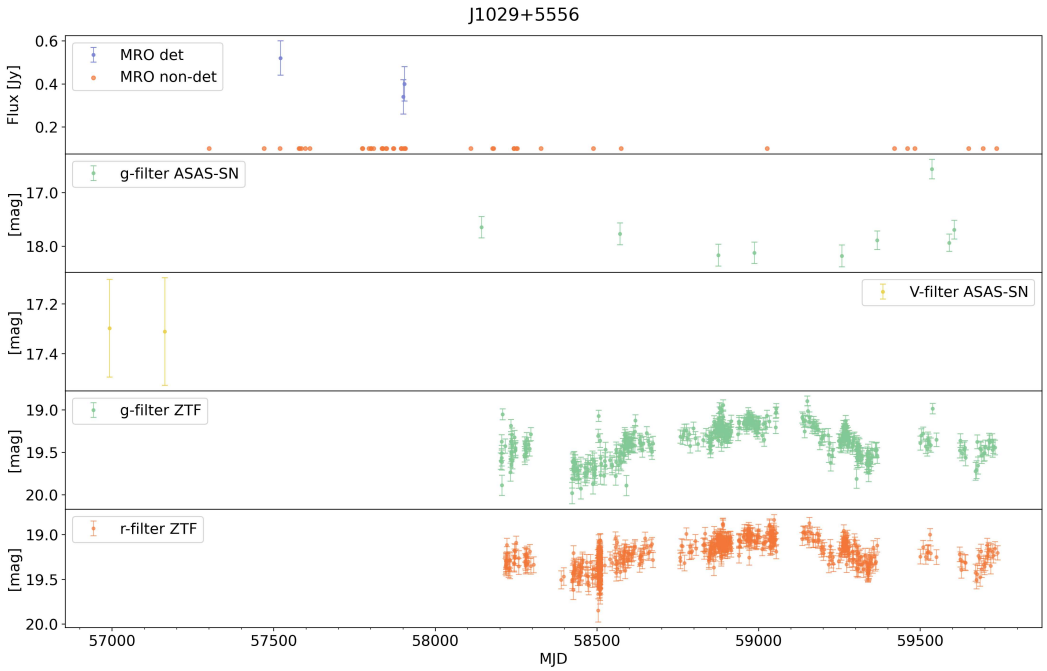

Figure 4.5: MRO and optical LCs of J1029.

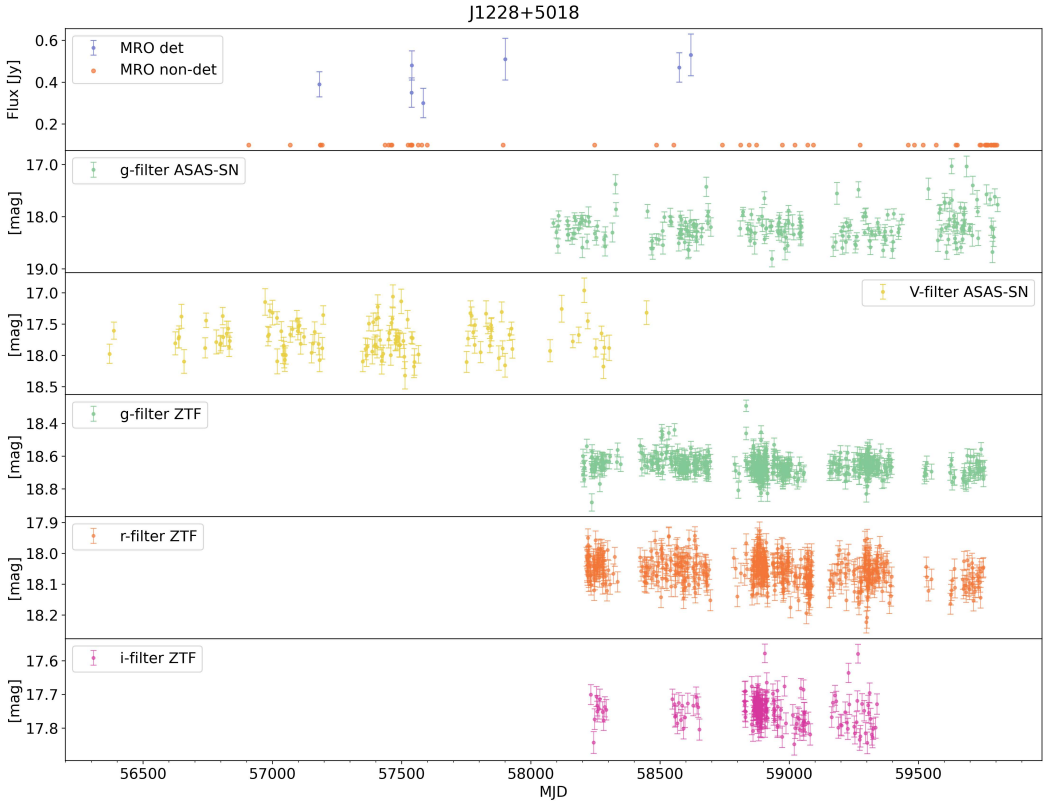

Figure 4.6: MRO and optical LCs of J1228.

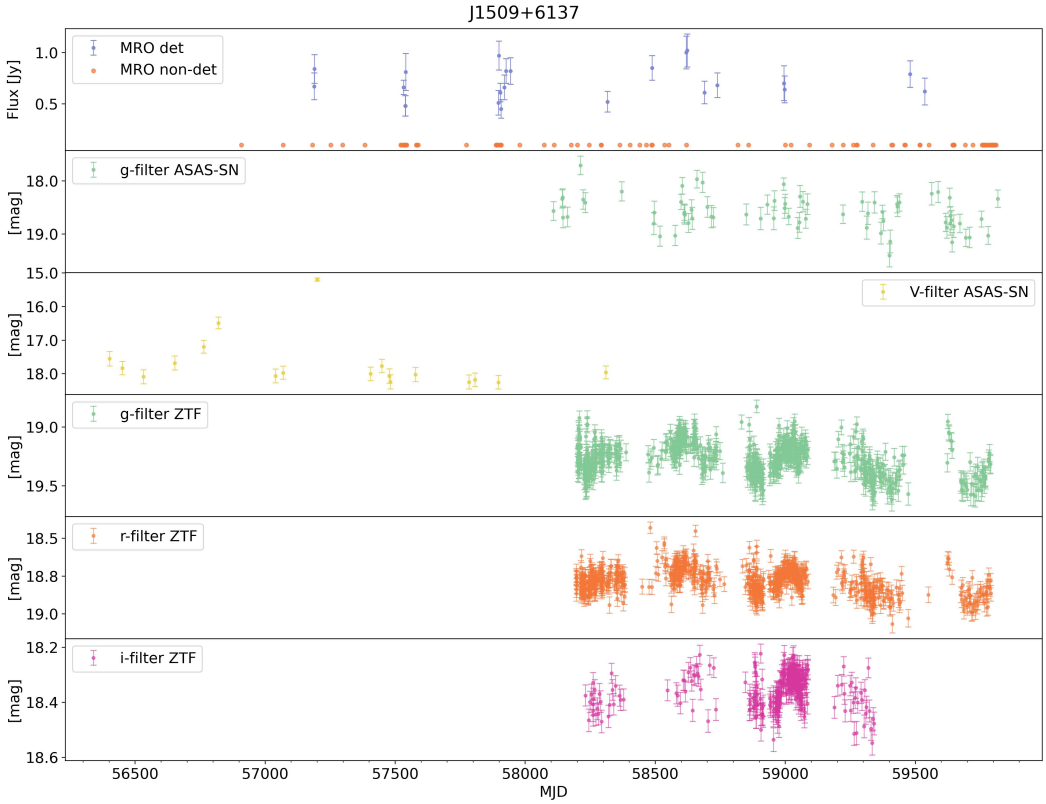

Figure 4.7: MRO and optical LCs of J1509.

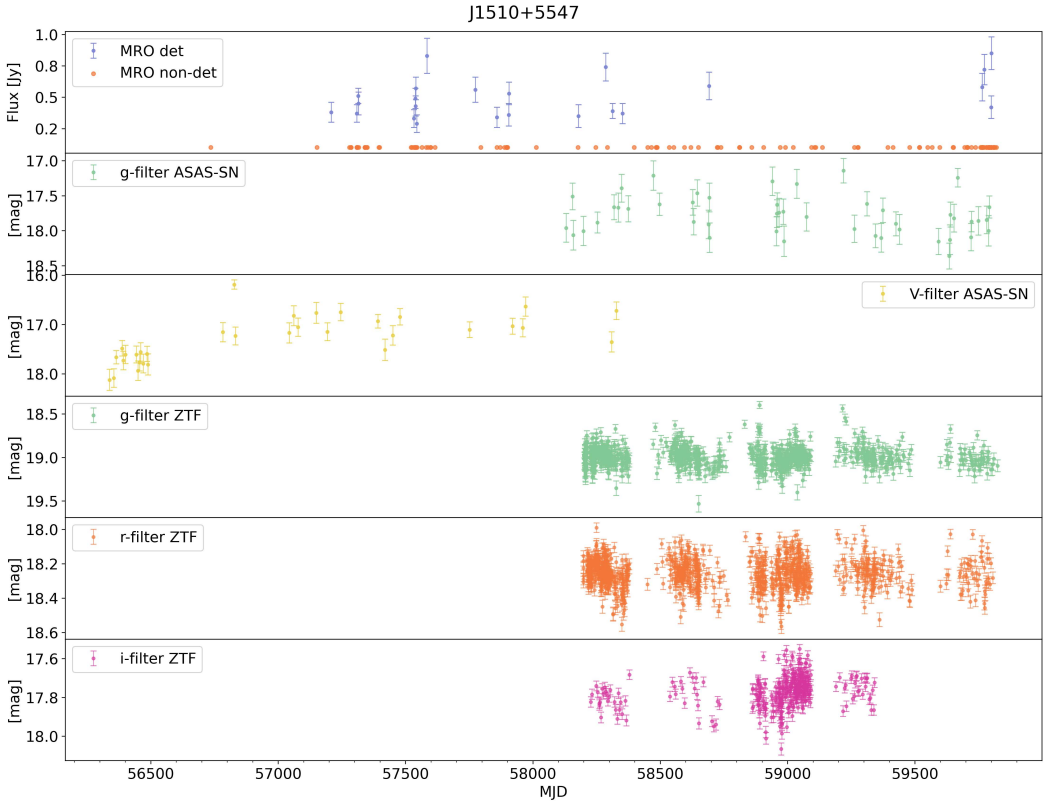

Figure 4.8: MRO and optical LCs of J1510.

Figure 4.9: MRO and optical LCs of J1522.

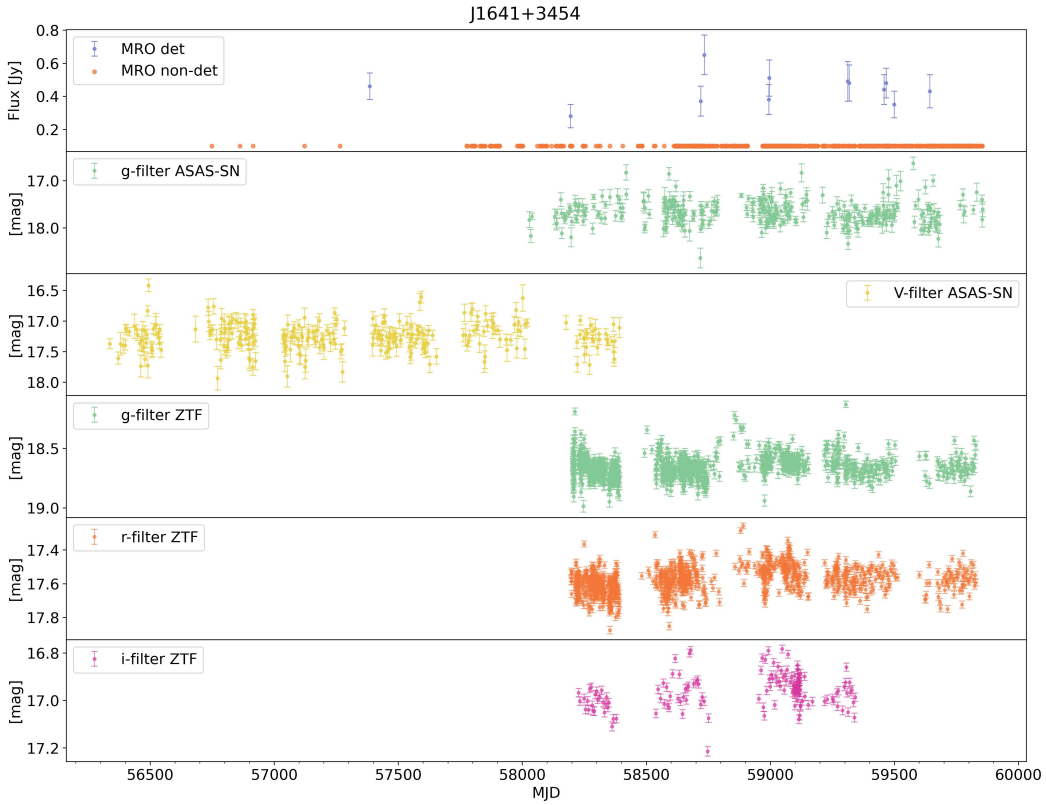

Figure 4.10: MRO and optical LCs of J1641.

Chapter 5

An optical perspective on early-stage AGN with extreme radio flares

Foreword: In the last decade of AGN monitoring programs, the MRO detected multiple times seven powerful flaring NLS1 galaxies at 37 GHz. Several hypotheses have been proposed, but the understanding of this unique phenomenon is still far. To look at the case from a different point of view, I performed an emission line analysis of the optical spectra, with the aim of identifying similarities among the sources, that can be, in turn, possibly tied to the radio behavior. The data used were obtained with the Gran Telescopio Canarias. The results I obtained show that six out of seven sources have typical properties for the NLS1 class, and one of them is an intermediate Seyfert galaxy. I found on average black hole masses above the median value for the class ($> 10^7$ $M_\odot$), and a strong Fe II emission, which could be a proxy for an intense ongoing accretion activity. Although interesting, the characteristics I found are not unusual for these kinds of AGN: the optical spectra of the sources do not relate to their unique radio properties. Therefore, further multi-wavelength studies will be necessary to narrow the field of hypotheses for this peculiar phenomenon.

Based on: Crepaldi et al., 2025

5.1 Introduction

Since the first identification of NLS1s in 1985 using their peculiar emission lines, the optical spectrum analysis is probably the most frequently used approach to investigate the physical properties of this class. As described in Sec. 2, two typical properties are the low black hole mass and the high Eddington ratio, which can be estimated using data from observations in the optical band. Especially the former is often debated, since the identification of NLS1s as jetted sources.

In this Chapter is described a study focused on the optical spectra of the seven flaring NLS1s described in Sec. 2.3, comparing each other and understanding if and how they differ from the spectra of the general NLS1s population. Moreover, I calculated in several ways some of the most important physical parameters for NLS1s such as the BLR radius, the black hole mass, the Eddington ratio, and the emission lines properties. This Chapter is organized as follows. In Sec. 5.2 I introduce the sample, in Sec. 5.3 I outline the observations performed and the data reduction techniques, in Sec. 5.4 I describe the emission lines analysis and how the physical parameters were calculated, in Sec. 5.5 I present the results, in Sec. 5.6 I discuss these results, and finally in Sec. 5.7 I provide a summary and the conclusions of this study.

Throughout this work, I adopt a standard ΛCDM cosmology, with a Hubble constant $H_0 = 70$ km s^{-1} Mpc^{-1}, and $\Omega_\Lambda = 0.73$ (Komatsu et al., 2011).

5.2 Sample

As described before, the sample is composed of seven NLS1s detected in a flaring state at 37 GHz by the MRO (Tab. 5.1). The sources span a redshift range from 0.0769 to 0.4511. The $\mathscr{R}$ parameter, has been calculated using the integrated radio fluxes at 5.2 GHz reported in Berton et al. (2020a), and the optical fluxes in the B band. The latter are measured from the optical spectra used in this work, using the Johnson-B filter response curve which is centered at λ_0=4500Å with a width of $\Delta\lambda$=1050Å. All the sources are radio-quiet (Tab. 5.1), even though as I already described they present strong flares which could suggest the presence of relativistic jets. Six sources are hosted in disk-like host galaxies, identified trough a photometric decomposition of their near-infrared images (Järvelä, Lähteenmäki, and Berton, 2018; Olguín-Iglesias, Kotilainen, and Chavushyan, 2020; Varglund et al., 2022), and in one case the host galaxy morphology is unknown. For a complete overview on the most recent radio properties of the sample, see Järvelä et al. (2024).

5.3 Observations and data reduction

The observations were performed with the long-slit spectrometer Optical System for Imaging and low-Intermediate-Resolution Integrated Spectroscopy (OSIRIS) mounted on the Gran Telescopio Canarias (GTC) as part of the programme GTC26-22B (P.I. E. Järvelä). The observations were performed using a 0.6 arcsec wide slit, and two different grisms, R1000B and R1000R, to widen the spectral range from 3630Å to 10'000Å. The two grisms have a spectral resolution of 1018 and 1122, respectively, and are thus sufficient to sample the main emission lines in the spectra properly. For all the observations, I carried out the standard data reduction using the software Image Reduction and Analysis Facility (IRAF), applying bias and flat-field corrections, and wavelength and flux calibrations. For each source I combined all the single spectra, to maximize the signal-to-noise ratio (S/N), and the final spectra of the two grisms, to obtain the final extended spectrum. However, I was not able to combine the spectra from the two grisms for all sources as in some cases one of the two spectra was too noisy or with bad features, decreasing the quality of the combined spectrum. In those cases, I decided to keep only the best spectrum for the analysis, acquired with either R1000B or R1000R grism.

I corrected the spectra for galactic absorption using the Cardelli, Clayton and Mathis extinction law with $R_v = 3.1$ (Cardelli, Clayton, and Mathis, 1989), which relies on the total extinction parameter, $A(V)$. Such parameter is proportional to the column density of neutral hydrogen atoms, N_H, by a factor 5.3×10^{-22}. I derived N_H by means of H I profiles templates[1] (Kalberla et al., 2005). The total extinction parameters are shown in Tab. 5.2.

I tried to apply the host galaxy subtraction by using a technique based on the principal component analysis (La Mura et al., 2007; Chen et al., 2018). However, the shape of the continuum is affected by the combination of the two grisms, and by the contamination of the second spectral order in the R1000R grism. This prevented from obtaining reliable models of the host spectra. Furthermore, the spectral range

[1] https://www.astro.uni-bonn.de/hisurvey/AllSky_profiles/index.php

Table 5.1: Properties of the sample.

SDSS name	Alias	RA	Dec	z	Sample	$\mathscr{R}$	Host
(1)	(2)	(3)	(4)	(5)	(6)	(7)	(8)
J102906.69+555625.2	J1029	10 29 06.69	+55 56 25.25	0.4511	D-env	–	–
J122844.81+501751.2	J1228	12 28 44.82	+50 17 51.24	0.2627	D-env	2.4	D[(3)]
J123220.11+495721.8	J1232	12 32 20.12	+49 57 21.82	0.2625	D-env	0.1	D[(3)]
J150916.18+613716.7	J1509	15 09 16.17	+61 37 16.80	0.2012	SED	–	D[(3)]
J151020.06+554722.0	J1510	15 10 20.05	+55 47 22.11	0.1497	SED	0.5	D,b[(1)]
J152205.41+393441.3	J1522	15 22 05.50	+39 34 40.45	0.0769	SED	1.7	D,b,PB[(1)],merger
J164100.10+345452.7	J1641	16 41 00.10	+34 54 52.67	0.1640	SED	8.0	D[(2)]

Columns: (1) SDSS source name; (2) short name; (3) right ascension [hh mm ss.s] (J2000); (4) declination [dd mm ss.s] (J2000); (5) spectroscopic redshift from the analyzed spectra; (6) sample of origin of the source. D-env: very dense Mpc-scale environment sample, SED: SED sample; (7) radio loudness parameter (Kellermann et al., 1989). The optical fluxes are measured from the spectra in this work, while the radio fluxes are taken from Berton et al. (2020a); (8) host galaxy morphology, composed by: D=disk, b=bar, PB=pseudo-bulge ([(1)]Järvelä, Lähteenmäki, and Berton, 2018, [(2)]Olguín-Iglesias, Kotilainen, and Chavushyan, 2020, and [(3)]Varglund et al., 2022).

covered by only one of the two grisms is also insufficient to perform accurate host modeling. Therefore, I decided to proceed without subtracting the host galaxy. It is worth noting that, in fact, the host contribution is relatively small in sources with z>0.1 (Letawe et al., 2007), and the analysis I carried out mostly focuses on emission lines, which are only marginally affected by the host contribution.

For the iron subtraction, I used the templates available on the Serbian Virtual Observatory[2] (Kovačević, Popović, and Dimitrijević, 2010; Shapovalova et al., 2012a). It produces a dedicated iron template with several Fe II lines between 4000Å and 5500Å, according to the source's spectral features. By means of this template, I computed the parameter $R4570=F(\text{Fe II}\lambda4570)/F(\text{H}\beta)$ which is shown in Tab. 5.2.

5.4 Spectral analysis

5.4.1 Line profiles

To extract the information from the spectra, I fitted the line profiles of the main emission lines with several models, using my own `Python3` code. The S/N of the spectra measured at 5100Å spans between 12 and 65 (Tab. 5.2). I analyzed the most prominent emission lines, such as Hβ, [O III]$\lambda\lambda$4959,5007, Hα+[N II]$\lambda\lambda$6548,6583 and, when visible, the [S II]$\lambda\lambda$6716,6731. I measured the spectroscopic redshift using all the forbidden lines present in the spectra, and I double-checked the results with the permitted lines. Even though low-ionization lines are usually less perturbed than high-ionization lines (Komossa et al., 2008), and thus more suitable for redshift measurements, the redshifts I obtained are comparable to those already reported in the literature.

The first lines I modeled were the [O III]$\lambda\lambda$4959,5007. Usually in NLS1s the [O III] lines show two main components. A core component, produced by the NLR gas which is at the same redshift as the host galaxy, and a wing component, associated with outflowing gas, on the blue side of the line core. Since the outflowing gas clouds can have different velocities, multiple components can be necessary to properly fit

[2]http://servo.aob.rs/FeII_AGN/

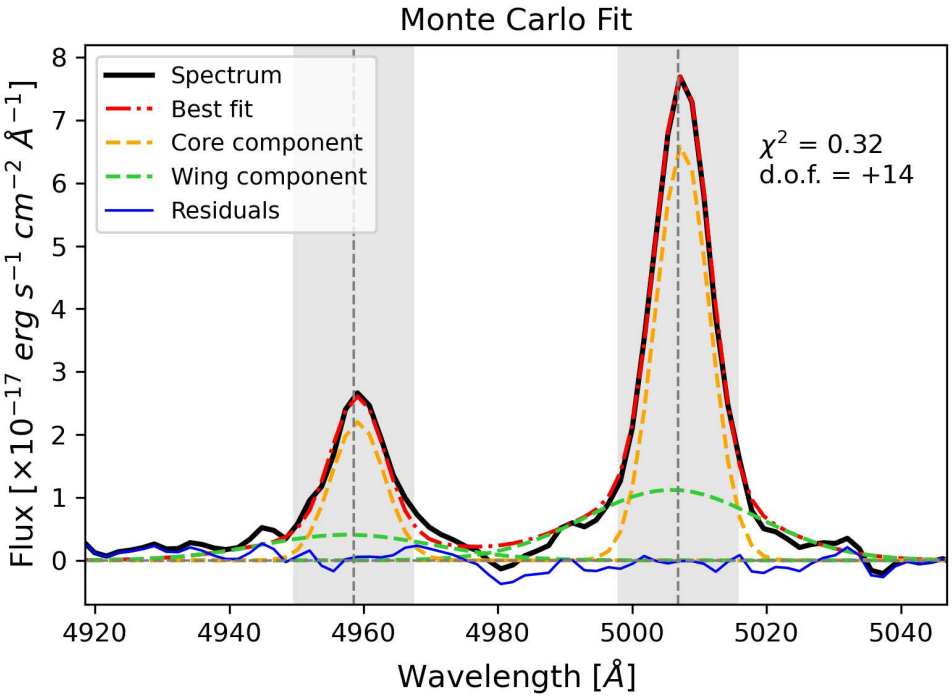

Figure 5.1: [O III]$\lambda\lambda$4959,5007 emission lines of J1641. The light gray shadows represent the ranges where the χ^2 is assessed.

their emission profile. Therefore, I fitted each [O III] with two or three Gaussians, one for the core component and one or two for the wing component. To reduce the number of free parameters, I tied certain parameters of the [O III]λ4959 with those of the [O III]λ5007. In particular, I constrained the central position to the rest frame wavelength and the FWHM, corrected for instrumental resolution, of all the components. Moreover, the flux ratio between the components of the two lines was fixed to the theoretical value of 1/3 (Dimitrijević et al., 2007). Due to the spectra being quite noisy, a goodness-of-fit test, such as the χ^2, needs particular attention to deliver reliable results, especially when multiple emission lines are fit simultaneously. For [O III] lines I set an interval around the rest frame position of the two lines, in which I computed the χ^2, avoiding the non-fitted region between the two lines that would inevitably increase the χ^2 value. Such intervals have been calculated as a multiple of the FWHM of the two [O III] lines, around the central wavelengths of both lines (Fig. 5.1). Since the outflow emission, when present, is on the blue side of the lines, the bluer side of the interval is often larger compared to the redder side (see Tab. 5.2). Finally, exploiting the [O III]λ5007 flux, I measured R5007=F([O III]λ5007)/F(Hβ) (Tab. 5.2).

To fit Hβ I tried several models for its line profile, with combinations of Gaussian and Lorentzian functions. Overall the best ones turned out to be the two Gaussians model (2G model), the three Gaussians model (3G model) and the Lorentzian + Gaussian model (LG model). One of the Gaussians in the 2G and 3G models and the only Gaussian in the LG model represent the narrow component of the Hβ. I constrained their central position to the Hβ rest frame wavelength and their FWHM, corrected for instrumental resolution, with the FWHM of the [O III]λ5007 core component, leaving the amplitude free to vary. I tied the FWHMs since the narrow

component of the Balmer lines is supposed to come from the same region, i.e. NLR, and thus with the same velocity dispersion, as the core component of the forbidden lines. Besides the narrow component, the Gaussians left, one in the 2G model and two in the 3G model, represent the broad emission of Hβ. In the 3G model, I had to adopt two Gaussians instead of one, due to the impossibility of properly fitting the wings of the line profile with only one function. For these, the resulting FWHM is the mean value of the FWHMs of the two Gaussians. In the LG model instead, the broad emission is represented by a Lorentzian function, which is often a good representation of the BLR in NLS1s (Cracco et al., 2016). For the fitting functions of the broad component of Hβ, I calculated the second-order moment, defined as

$$\sigma^2 = \frac{\int \lambda^2 F_{H\beta_b}(\lambda) d\lambda}{\int F_{H\beta_b}(\lambda) d\lambda} - \left(\frac{\int \lambda F_{H\beta_b}(\lambda) d\lambda}{\int F_{H\beta_b}(\lambda) d\lambda} \right)^2 . \tag{5.1}$$

This parameter has been calculated for models built using only Gaussian functions, since for a Lorentzian function it is, by definition, equal to infinite.

When visible I also modeled the [S II]$\lambda\lambda$6716,6731. I fitted each [S II] profile with a Gaussian function. To reduce the number of free parameters, I constrained the FWHM and the shift, with respect to the rest frame position, of the Gaussian for [S II]λ6716 with those retrieved with the Gaussian for [S II]λ6731, leaving the flux free to vary.

Finally, I fitted the complex line profile of Hα+[N II]$\lambda\lambda$6548,6583, which, as stated before, are blended together. For the Hα line profile, I applied the same model that was used for Hβ (2G, 3G or LG model), with the same FWHM, corrected for instrumental resolution, and the respective shifts for all the components. For the [N II]$\lambda\lambda$6548,6583 I adopted a 2G model, in which I constrained the position to the rest frame wavelength, and the FWHM using [S II] or [O III] width. This is particularly important since the [N II] are completely blended with Hα, and therefore impossible to model without any priors. I preferred [S II] over [O III], when possible, as a reference for [N II], because they are always observed with the same grism, and they are both low-ionization lines. I also fixed the flux ratio of the two Gaussians to the value 1/3.049 (Dojčinović, Kovačević-Dojčinović, and Popović, 2023). To investigate the internal extinction, I exploited the Balmer decrement calculating the $\mathcal{R}$ ratio, defined as the ratio between the Hα and Hβ narrow component fluxes. Following Cardelli, Clayton, and Mathis (1989), and assuming a theoretical ratio of 2.86, the internal extinction can be expressed as

$$A(V) = 7.215 \log \left(\frac{\mathcal{R}}{2.86} \right) . \tag{5.2}$$

Once the best-fit model has been selected for all the lines, based on the χ^2 and on a visual inspection, I performed a Monte Carlo method, repeating the fit one thousand times. For each iteration, I added a Gaussian noise to the line profile, proportional to the standard deviation of the signal in the continuum between 5050Å and 5150Å. Using a high number of iterations, for each parameter I measured the mean value $\overline{X}$ and the standard error $err_{\overline{X}}$ (Ahn and Fessler, 2003) defined as

$$\overline{X} \pm err_{\overline{X}} = \frac{1}{N} \sum_{i=1}^{N} X_i \pm \sqrt{\frac{\sigma_N^2}{N}} , \tag{5.3}$$

where N is the number of Monte Carlo iterations, X_i the i-th value of the parameter, and σ_N^2 the variance of the parameter expressed as

$$\sigma_N^2 = \frac{\sum_{i=1}^{N}(X_i - \overline{X})^2}{N-1} \,. \tag{5.4}$$

5.4.2 BLR radius estimation

It is possible to reasonably assume that the BLR is in a photoionization equilibrium state. The photoionization degree depends on the intensity of the photoionizing radiation, which is proportional to the intensity of all the radiation produced, for AGN, by the accretion flow. Likewise, for the equilibrium assumption, this translates into the intensity of the emission lines produced in the BLR. Furthermore, there is an empirical relation which binds the BLR radius with the luminosity of the accretion disk, such as the 5100Å continuum, or with the luminosity of emission lines that come from the BLR, such as Hβ. Exploiting Hβ emission, Greene et al. (2010) derived a relation for the BLR radius, expressed as

$$\log\left(\frac{R_{\rm BLR}}{\rm l.d.}\right) = (1.85 \pm 0.05) + (0.53 \pm 0.04)\log\left(\frac{L(\mathrm{H}\beta)}{10^{43}\ \mathrm{erg\ s^{-1}}}\right) \,, \tag{5.5}$$

where $L(\mathrm{H}\beta)$ is the integrated luminosity of the line profile, and the BLR radius is expressed in light days. A similar relation has been found by Bentz et al. (2013) using the continuum emission at 5100Å. As mentioned before, the continuum has a small contribution coming from the host galaxy, but I expect it to be inside the flux calibration error and therefore negligible. Bentz et al. (2013) derived the coefficients of such relation, relying on reverberation mapping data, which is expressed as

$$\log\left(\frac{R_{\rm BLR}}{\rm l.d.}\right) = (1.53 \pm 0.03) + (0.53 \pm 0.03)\log\left(\frac{\lambda L_\lambda(5100\text{Å})}{10^{44}\ \mathrm{erg\ s^{-1}}}\right) \,, \tag{5.6}$$

with the BLR radius expressed in light days. Recently, an implementation of Eq. 5.6, for AGN with high Eddington ratios, such as NLS1s, has been derived (Du and Wang, 2019; Paliya et al., 2024). Indeed, Du and Wang (2019) found that the $R_{\rm Hfi}$-L_{5100} relationship (Kaspi et al., 2000; Bentz et al., 2009; Bentz et al., 2013) diverges from the more precise results obtained through the most recent reverberation mapping data. By means of the sample analyzed, they found a strong dependence on Fe IIλ4570 emission, modifying Eq. 5.6 as

$$\log\left(\frac{R_{\rm BLR}}{\rm l.d.}\right) = (1.65 \pm 0.06) + (0.45 \pm 0.03)\log\left(\frac{\lambda L_\lambda(5100\text{Å})}{10^{44}\ \mathrm{erg\ s^{-1}}}\right) - (0.35 \pm 0.08)\, R4570 \,, \tag{5.7}$$

where $R4570$ is the ratio described in Sec. 5.3. Therefore I calculated the BLR radius through Eq. 5.7 whenever the $R4570$ was available. Only for one source the Fe IIλ4570 emission was not measurable. In this case I calculated the BLR radius using Eq. 5.5 and 5.6. For all the formulas described I performed an error propagation for the uncertainties estimation. It is important to remember that, even though all the cited equations for the BLR radius calculation were derived using sources with similar characteristics like the one analyzed here, they used real data. Therefore, they are never free from biases.

5.4.3 Black hole mass

Assuming virialized gas orbiting the black hole, as described in Sec. 2.1.1, the virial theorem (Eq. 2.1) can be used to express the black hole mass. In Eq. 2.1, the two main unknowns are the BLR radius and the velocity. These quantities can be derived in many different ways. In the case of the BLR radius, I already described in the previous section the three types of relations that can be used starting from different observables, namely Hβ luminosity (Eq. 5.5), 5100Å continuum luminosity (Eq. 5.6), and 5100Å continuum luminosity and $R4570$ (Eq. 5.7). Two independent parameters can also be used as a proxy for the rotational velocity v. The first is the FWHM of the Hβ broad component. I derived it using the functions in the line fitting process, which modeled only the broad emission of Hβ. In particular, the cited functions were a Gaussian for the 2G model, two Gaussians for the 3G model, and a Lorentzian for the LG model. Alternatively, I adopted the second-order moment (Eq. 5.1) as a proxy for v. As mentioned before, I did not calculate such a parameter for the LG model, as it is equal to infinite for the Lorentzian function. Several studies emphasized how the second-order moment is more reliable than the FWHM(Hβ_b) as a proxy for the rotational velocity, being less affected by inclination effects and the BLR geometry (Peterson et al., 2004; Peterson, 2011; Peterson and Dalla Bontà, 2018). Nevertheless, I decided to use both methods, reducing the probability of systematics and biases that each single assumption can have.

The parameter v represents the rotational velocity of the gas in the BLR, while the FWHM(Hβ_b) is instead an observable of the velocity dispersion. Such difference is included in Eq. 2.1 by the f factor. The black hole mass formula defined before is a theoretical relation for a completely virialized gas in a perfect Keplerian motion, a case that basically never occurs in AGN. The main sources of uncertainty are the BLR geometry and its inclination. It is clear that the measurable velocities for a flat BLR, seen face-on or edge-on, are different. In the former, as already described, the rotational velocity can even be close to zero, leading to an underestimation of the black hole mass (Decarli et al., 2008). However, although not negligible, in NLS1s the inclination effect might be not so significant (Vietri et al., 2018; Berton et al., 2020b), since a significant vertical structure in the BLR can be present (Kollatschny and Zetzl, 2011; Kollatschny and Zetzl, 2013b). On the other hand, a spherical BLR geometry is even harder to handle with just a relatively simple formula. The f factor accounts for the differences between the theoretical formula and the actual black hole mass, by correcting the rotational velocity observables. The most recent knowledge shows that a Keplerian motion of the BLR clouds is present (Peterson and Wandel, 1999; GRAVITY Collaboration et al., 2018), with possibly additional components such as turbulent vertical motions originating in a disk wind (Gaskell, 2009; Kollatschny and Zetzl, 2013b). Moreover, it has been found that f is inversely proportional to the FWHM(Hβ) (Shen and Ho, 2014). Mandal et al. (2021) estimated a typical range for the f factor between 0.8 and 5, mostly derived from a comparison with reverberation mapping observations. For this study, I decided to use the f factors estimated by Collin et al. (2006), frequently used for NLS1s studies, which are f_σ=3.93 and f_{FWHM}=2.12, for the rotational velocity obtained by the second-order moment and the FWHM(Hβ_b), respectively.

Summarizing, when the Hβ profile was modeled by either the 2G or the 3G model, I got two different black hole mass estimates, using Eq. 5.7 for the BLR radius, and considering the ways in which I calculated the v parameter. When I applied the LG model instead, I got the two black hole mass estimates using only the FWHM(Hβ_b) as a proxy for the rotational velocity, and Eq. 5.5 and 5.6 for the BLR

radius. In all cases to retrieve the associated error for each black hole mass, I applied a standard error propagation.

5.4.4 Eddington ratio

For AGN, the Eddington ratio is defined as

$$\epsilon = \frac{L_{\rm bol}}{L_{\rm Edd}} = \frac{L_{\rm bol}}{1.3 \times 10^{38} M_{\rm BH}/M_{\odot}} \,, \tag{5.8}$$

Objects with high ϵ, even higher than 1, usually show strong Fe II multiplets and narrow Hβ, while low Eddington objects show broader Hβ and a weak Fe II emission. At this point it is clear that NLS1s usually show Eddington between 0.1 and 1 (Boroson and Green, 1992; Williams, Pogge, and Mathur, 2002; Williams, Mathur, and Pogge, 2004; Grupe et al., 2010; Xu et al., 2012), but sometimes even super-Eddington accretion(Chen et al., 2018; Tortosa et al., 2022). The bolometric luminosity can be derived by exploiting simple relations with observables, such as the 5100Å continuum luminosity formula (Netzer, 2019) expressed as

$$L_{\rm bol} = k_{bol} \times \lambda L_{\lambda}(5100\text{Å}) \,, \tag{5.9}$$

where k_{bol} is the bolometric correction factor defined as

$$k_{bol} = 40 \left[\frac{\lambda L_{\lambda}(5100\text{Å})}{10^{42}\ \text{erg s}^{-1}} \right]^{-0.2} \,. \tag{5.10}$$

The main uncertainty of k_{bol} comes from the inclination of the AGN accretion disk with respect to the line of sight. Netzer (2019) estimated that for type-1 AGN the bolometric correction factor decreases by a factor of ~ 1.4 on average, and by a factor of ~ 2.5 for face-on accretion disks. Since the inclination of the analyzed sources is unknown, and consequently to account for all the possible inclinations, I decided to take $\frac{k_{bol}}{2}$ as bolometric correction factor, and $\Delta k_{bol} = \frac{k_{bol}}{2} - \frac{k_{bol}}{2.5}$ as its uncertainty. In general, Eq. 5.9 and 5.10 are particularly affected by the jet presence and can be partially affected by the host galaxy contribution, since both these components can contribute to the continuum luminosity. However, in my case, the presence of the jet is still debated, and the host component is only marginal, therefore I decided to keep such relation to estimate ϵ. Alternatively, I also used an approach less affected by non-nuclear contributions. I retrieved the 5100Å continuum luminosity for Eq. 5.9 and 5.10 using the $L_{\lambda}(5100\text{Å})$-$L(\text{H}\beta_b)$ relation (Ilić et al., 2017; Dalla Bontà et al., 2020) defined as

$$\log(\lambda L_{\lambda}(5100\text{Å})) = (43.396 \pm 0.018) + (1.003 \pm 0.022) \times [\log(L(\text{H}\beta_b)) - 41.746] \,. \tag{5.11}$$

This approach allowed me to indirectly calculate the continuum luminosity, and consequently the bolometric luminosity, exploiting the Hβ properties. Its flux is directly proportional to the ionizing continuum of the AGN, which is free from jet and host contamination. For the Eddington ratio calculation I averaged the black hole mass of each source. Also in this case I applied a proper error propagation for the error calculation through all the described steps.

Table 5.2: Observational parameters derived from the optical spectra.

Source	S/N	[O III] χ^2_{range}	FWHM(Hβ)	FWHM(Hβ_b)	σ	F(Hβ)	F(Hβ_b)	F_{cont}	F_{SDSS}	$R4570$	A(V)
(1)	(2)	(3)	(4)	(5)	(6)	(7)	(8)	(9)	(10)	(11)	(12)
J1029	12	-2/+1	2132	2320	2856	1.39	1.38	2.74	4.85	1.34	–
J1228	65	-3/+2	971	1360	1807	1.97	1.88	13.96	14.66	2.81	3.590
J1232	33	-2/+1	1518	1700	1631	8.14	8.01	17.67	15.95	1.58	1.826
J1509	26	-2/+1	1744	1861	2193	2.20	2.18	5.77	8.19	1.06	3.067
J1510	14	-3/+2	1031	1193	2307	1.99	1.87	8.09	12.97	2.37	3.764
J1522	42	-2/+1	886	1181	–	1.34	1.13	17.48	33.87	–	3.285
J1641	25	-1/+1	1140	4050	1767	0.90	0.79	10.48	21.23	2.58	–

Columns: (1) Source name; (2) S/N measured in the 5100Å continuum; (3) values multiplied to the FWHMs of [O III]$\lambda\lambda$4959,5007 for the χ^2 calculation; (4) FWHM of the Hβ profile [km s^{-1}]; (5) FWHM of the Hβ broad component [km s^{-1}]; (6) square root of the second-order moment as in Eq. 5.1 [km s^{-1}]; (7) Hβ flux [$\times10^{-15}$ erg s^{-1} cm^{-2}]; (8) Hβ broad flux [$\times10^{-15}$ erg s^{-1} cm^{-2}]; (9) flux density at 5100Å [$\times10^{-17}$ erg s^{-1} cm^{-2} Å^{-1}]; (10) flux density at 5100Å on SDSS spectra [$\times10^{-17}$ erg s^{-1} cm^{-2} Å^{-1}]; (11) flux ratio between Fe IIλ4570 multiplets and Hβ; (12) internal extinction as in Eq. 5.2.

5.5 Results

5.5.1 SDSS J102906.69+555625.2

J1029, with a redshift of 0.4511, is the farthest source of the sample. Due to its distance, the Hα and [S II] region is inside the portion of the spectrum contaminated by the sky emission. Therefore, in this case, I only managed to analyze Hβ and [O III]$\lambda\lambda$4959,5007 emission lines. Moreover, due to a bad feature on the bluer part of the spectrum, probably of instrumental origin, I kept only the R1000R grism spectrum. The fitting models I adopted were the 3G model for Hβ and the four Gaussians model for the [O III]$\lambda\lambda$4959,5007 since these last do not show any asymmetric shape. This source, with values of 2132 km s^{-1} and 2856 km s^{-1} , has the highest FWHM(Hβ) and σ respectively. Its FWHM(Hβ_b) is 2320 km s^{-1} , which means that it is not formally an NLS1 but it still shares all the properties of Population A sources. In turn, averaging the results in Table 5.3, it has the highest black hole mass in the sample, equal to (6.63$\pm$1.88) $\times10^7$ M$_\odot$. Such characteristics, coupled with a moderate Eddington ratio of 0.07 on average (Table 5.3), could be traits of an NLS1 in an evolved stage, possibly transitioning into a classical broad-line AGN.

5.5.2 SDSS J122844.81+501751.2

Also in this case I kept only the R1000R grism spectrum, since the R1000B grism spectrum had a much worst S/N, making difficult, among all, the modeling of the continuum. For the emission lines the applied fitting models were the 3G model, for Hβ and Hα, and the six Gaussians model, for the [O III]$\lambda\lambda$4959,5007. Thanks to an S/N of 65, the highest of the sample, the asymmetric profiles on the two [O III] emission lines are well visible (Fig. 5.2). Therefore, six Gaussian functions were necessary to properly fit such profiles. In NLS1s, classified as high-accretion sources, the [O III] blue wing is associated with powerful outflows that can be generated by the radiation pressure coming from the accretion disk or a jet (Proga, Stone, and Kallman, 2000; Greene and Ho, 2005). The wing components, usually broader than the core component, are likely produced in the innermost part of the NLR (Berton et al., 2016b). In my case, the two Gaussians used to model the wing components are shifted of -163 and -371 km s^{-1} toward the blue side. The average mass of the black hole is (9.21$\pm$4.96) $\times10^6$ M$_\odot$, and the calculated Eddington ratios are 0.94$\pm$0.19

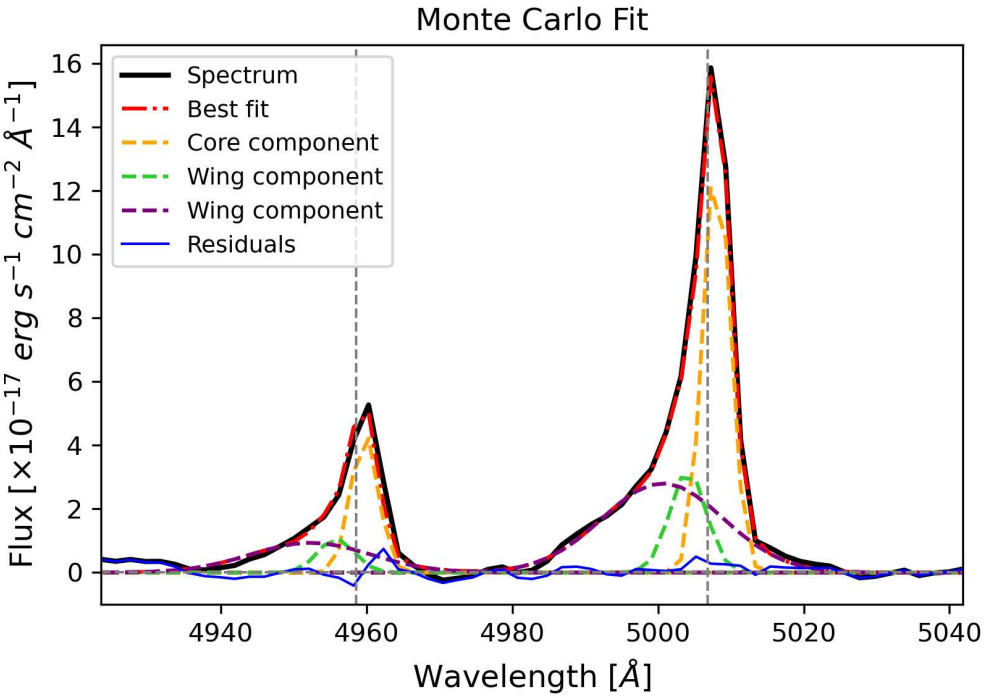

Figure 5.2: [O III]$\lambda\lambda$4959,5007 line profiles of J1228.

and 0.11±0.02. In agreement with these values (see Sec. 5.6.3 for the discussion) the $R4570$ is the highest in the sample (2.81), suggesting strong Fe II multiplets emission.

5.5.3 SDSS J123220.11+495721.8

The emission line parameters for J1232 have been derived using the 3G fitting model for the Hβ and Hα lines, and the six Gaussians model for the [O III]$\lambda\lambda$4959,5007. Along the whole spectrum, the permitted lines are much stronger than the forbidden lines (Fig. 5.3). Moreover, the [O III]$\lambda\lambda$4959,5007 profile shows core components fainter compared to the wing components (Fig. 5.4). The two Gaussians used to model the blue side of the [O III] lines are shifted about -411 km s^{-1} and -596 km s^{-1} . According to these, I can classify this source as a blue outlier (Marziani et al., 2003; Komossa et al., 2008; Berton et al., 2016b; Schmidt et al., 2018), following the criterion adopted by Zamanov et al. (2002) ([O III] wing component with a shift <-250 km s^{-1}). The origin of blue outliers could be due to a jet interacting with the NLR, as they correlate with the radio emission (Berton et al., 2021), but also due to winds produced by strong radiation pressure-driven outflows in a high-Eddington source (Komossa et al., 2008; Marziani et al., 2016). The latter is likely the case here since this is the source with the second highest Eddington ratio I found ($\sim$0.27). Also in this case the $R4570$=1.58 suggests strong Fe II multiplets emission, especially considering the high flux of the Hβ (8.14×10^{-15} erg s^{-1} cm^{-2}), placing J1232 in the A4 population region of the quasar main sequence (Sulentic and Marziani, 2015). The mean black hole mass of (2.73±0.88) $\times10^7$ M$_\odot$ is well inside the range for NLS1s.

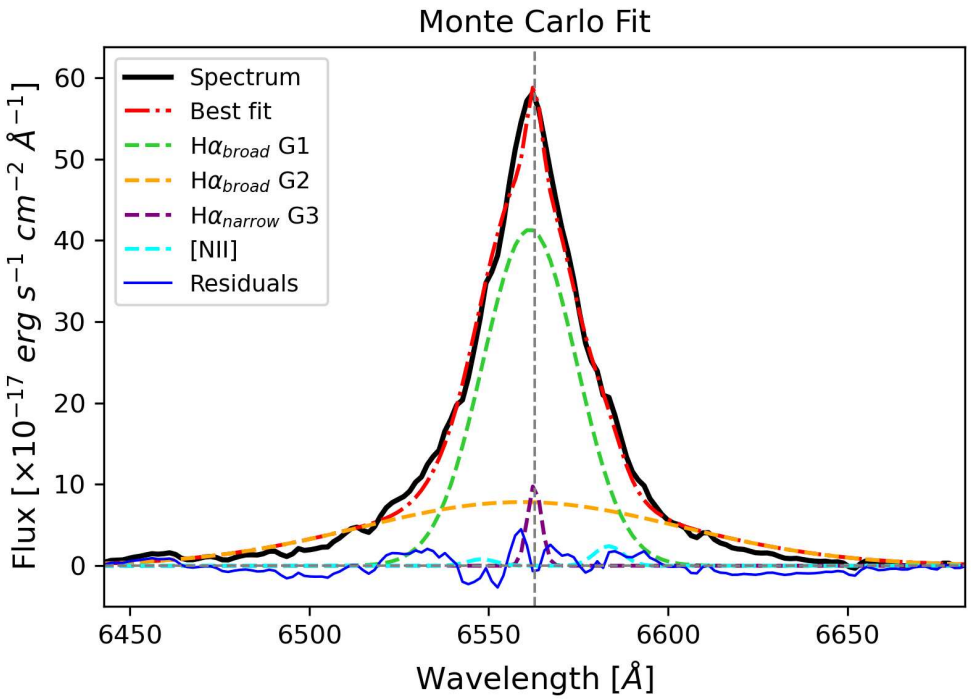

Figure 5.3: Hα+[N II]$\lambda\lambda$6548,6583 lines profile of J1232. The cyan dashed line represents the [N II] line profiles, which are much fainter than the Hα emission.

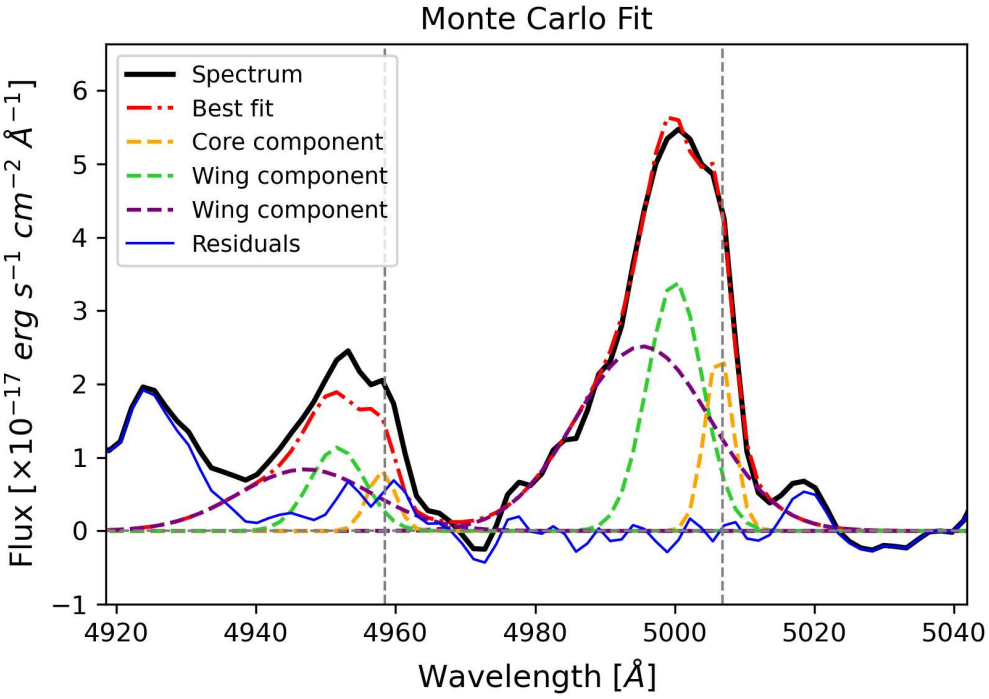

Figure 5.4: [O III]$\lambda\lambda$4959,5007 line profiles of J1232, which show wing components stronger than the core components.

5.5.4 SDSS J150916.18+613716.7

For this source I used the 3G model for the fitting of the Hβ and Hα lines, and the six Gaussians model for the fitting of the [O III]$\lambda\lambda$4959,5007 lines. Even thought the six Gaussians model was necessary to fit the [O III] lines, they did not show strong asymmetric wings. The Hβ line has a FWHM of 1744 km s^{-1} , inside the range for NLS1s. The mean black hole mass I obtained is (3.02$\pm$0.73) $\times10^7$ M$_\odot$ and the Eddington ratio is around 0.06. The R4570 of 1.06 and the Hβ flux of 2.20 $\times10^{-15}$ erg s^{-1} cm^{-2}, lowest and second highest values in the sample respectively, suggest faint Fe II emission. It is worth noting that the faint iron emission in this case is only in comparison to the other sources in the sample, since all the sources for which I manage to measure the R4570 belong to populations A3 and A4 of the quasar main sequence.

5.5.5 SDSS J151020.06+554722.0

With a black hole mass on average equal to (8.03$\pm$3.83) $\times10^6$ M$_\odot$, J1510 has the second least massive black hole in the sample, and an average Eddington ratio of 0.15. The applied fitting models to the spectrum were the 3G model for the Hβ and Hα lines, and the four Gaussians model for the [O III]$\lambda\lambda$4959,5007. Even in this case, the [O III] emission lines are quite symmetric, without strong evidence of outflows. A defect, possibly due to uncontrolled reflections inside the instrument, affected the blue side of the Hβ profile. Therefore, the measured FWHM(Hβ) of 1031 km s^{-1} , despite already quite narrow, might have been slightly overestimated, causing an overestimation of the black hole mass. The second-order moment of the line, equal to 2307 km s^{-1} , is roughly twice the FWHM(Hβ), which can be explained by the overestimated width of the line.

5.5.6 SDSS J152205.41+393441.3

J1522 is the closest source, with a redshift of 0.0769. As for J1228, I used only the R1000R grism spectrum, because in comparison, the R1000B grism spectrum had an 8 to 10 times worse S/N. Here the [S II] lines were too faint to be distinguished from the noise, therefore I used the FWHM of [O III]λ5007 core component as a reference for the FWHM of [N II] lines. The best fitting models turned out to be the four Gaussians model for the [O III]$\lambda\lambda$4959,5007, and the LG model for the Hβ and Hα lines. Since I used a Lorentzian to fit the broad components of the emission lines, I did not calculate the second-order moment for this source. Using only the FWHM(Hβ_b) as a proxy for the velocity parameter, I got the lowest value for the black hole mass of the whole sample, on average equal to (3.14$\pm$0.54) $\times10^6$ M$_\odot$. Considering that J1522 has the second highest Eddington ratio derived from the measured continuum luminosity at 5100Å, I could classify it as an NLS1 in an early evolutionary stage. However, the resulting lower ϵ using the derived continuum luminosity, as described in Sec. 5.4.4, suggests an overestimation of the former Eddington ratio likely due to contamination by the host galaxy. Such a hypothesis derives from the vicinity of the source, and from the presence of absorption lines in the spectrum, which can be produced only by the host galaxy. This contamination cannot be estimated since a proper host galaxy modeling was not possible, due to the unusable bluer spectrum.

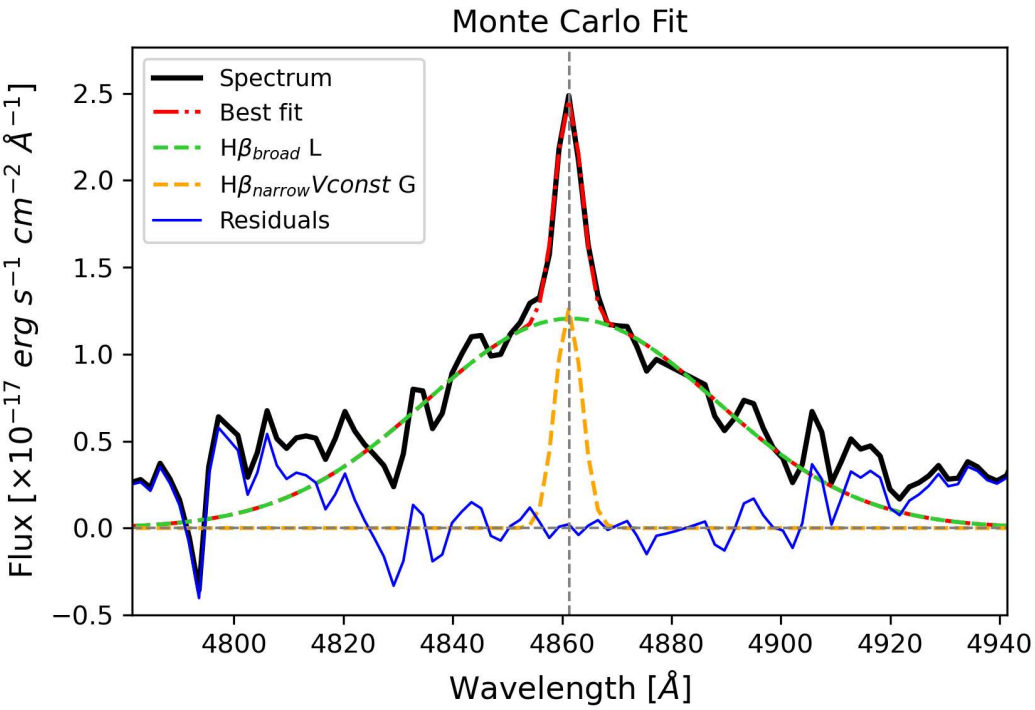

Figure 5.5: Hβ line profile of J1641. The broad and narrow components have a FWHM of 4050 km s^{-1} and 493 km s^{-1} , respectively.

5.5.7 SDSS J164100.10+345452.7

J1641 shows peculiar line profiles compared to the rest of the sample. The broad components of the Hβ line, with an FWHM of 4050 km s^{-1} is the broadest among the analyzed sources. This value, coupled with the FWHM of the narrow component of 493 km s^{-1} translates to a line profile (Fig.5.5) typical for intermediate Seyfert galaxies (Osterbrock, 1991; Dalla Barba et al., 2023). To properly fit the Hβ shape I used a 2G model. A four Gaussians model was used for the [O III]$\lambda\lambda$4959,5007 lines. Two Gaussians for each [O III] line were enough to achieve a good fit since no evidence of outflows was present. I did not perform a fitting of the Hα profile since it was strongly contaminated by the sky emission, impossible to remove despite several attempts. According to the results, J1641 turned out to be one of the sources with the lowest Eddington ratio, equal to 0.17$\pm$0.04 and 0.01$\pm$0.01. This source was found to be the only γ-ray emitter of the sample, hinting at the presence of a relativistic beamed jet (Lähteenmäki et al., 2018). Such a feature, coupled with the relatively low Eddington ratio and high FWHM(Hβ), might suggest an advanced evolutionary stage (Foschini, 2017).

5.6 Discussion

In this study, I analyzed the optical spectra of seven NLS1s with extreme radio features. I did so by performing a model fitting of the main emission lines. The goal was to investigate for similar characteristics among these sources by comparing their physical properties, such as black hole mass and Eddington ratio, and the emission lines profiles.

Table 5.3: Black hole mass and Eddington ratio results.

Source	$R_{\rm BLR}$	ν	$M_{\rm BH}$	ϵ_m	ϵ_d
(1)	(2)	(3)	(4)	(5)	(6)
J1029	15.60±4.43	FWHM(Hβ_b)	(3.48±0.99) $\times10^7$	0.10±0.02	0.04±0.01
		σ(Hβ)	(9.77±2.77) $\times10^7$		
J1228	5.63±3.02	FWHM(Hβ_b)	(4.32±2.31) $\times10^6$	0.94±0.19	0.11±0.02
		σ(Hβ)	(1.41±0.76) $\times10^7$		
J1232	16.84±5.44	FWHM(Hβ_b)	(2.02±0.65) $\times10^7$	0.38±0.08	0.16±0.03
		σ(Hβ)	(3.43±1.11) $\times10^7$		
J1509	11.77±2.85	FWHM(Hβ_b)	(1.69±0.41) $\times10^7$	0.09±0.02	0.03±0.01
		σ(Hβ)	(4.34±1.05) $\times10^7$		
J1510	3.56±1.64	FWHM(Hβ_b)	(2.10±0.96) $\times10^6$	0.25±0.05	0.05±0.01
		σ(Hβ)	(1.45±0.67) $\times10^7$		
J1522	11.53±1.12$^{(1)}$	FWHM(Hβ_b)	(5.09±0.50) $\times10^6$	0.38±0.08	0.02±0.01
	2.70±1.31$^{(2)}$	FWHM(Hβ_b)	(1.19±0.58) $\times10^6$		
J1641	3.70±1.86	FWHM(Hβ_b)	(2.51±1.26) $\times10^7$	0.17±0.04	0.01±0.01
		σ(Hβ)	(8.86±4.45) $\times10^6$		

Columns: (1) Source name; (2) BLR radius derived using Eq. 5.7, $^{(1)}$ BLR radius derived using Eq. 5.6, $^{(2)}$ BLR radius derived using Eq. 5.5; (3) proxy of the rotational velocity, either FWHM(Hβ_{broad}) or σ(Hβ); (4) black hole mass [$M_\odot$]; (5) Eddington ratio calculated using the measured L_{bol}; (6) Eddington ratio calculated using the derived L_{bol}, exploiting Eq. 5.11.

5.6.1 Black hole mass comparison

From Table 5.3, the black hole mass calculated using the second-order moment turned out to be on average larger than that obtained with the FWHM(Hβ_b). It is due to the fact that the σ I measured is systematically larger than the FWHM(Hβ). This is not uncommon in NLS1, as σ and FWHM(Hβ) can be different from each other, yielding significantly different results (e.g., see Foschini et al., 2015). The physical meaning of such a discrepancy is not easy to address. The FWHM(Hβ_b) is, by definition, a directly measurable geometric property of the line, which is the reason why most studies tend to use this simple parameter (e.g. see the large surveys by Rakshit et al., 2017; Paliya et al., 2024). However, even a small difference in line width drives a large variability in the output, i.e. the black hole mass, because of its quadratic dependence shown in Eq. 2.2. The way the line width is measured, for instance, the FWHM, has several limitations. This becomes particularly evident when an emission line presents a complex line profile. As described in Sec. 5.5, in all the cases but two the resulting broad profile in the Hβ line is no longer represented by a single function, but it is instead a composition of two functions. However, the measured FWHM comes mostly only from one of the two, according to the amplitude of each component. It leads to overestimation of the mass when lines are broader and underestimation when lines are narrower (Peterson and Dalla Bontà, 2018). This means that two different Hβ lines can yield the same black hole mass estimate, in all those cases where the main broad component is described by the same function. On the other hand, the second-order moment is more sensitive to the whole broad profile. This issue has already been widely discussed (Peterson et al., 2004; Peterson, 2011), and σ is likely the most reliable proxy for the gas velocity.

In two cases, however, I modeled the Hβ broad component using only one function, namely in J1522 and J1641. According to what I discussed until this point, in those two cases, the black hole masses derived with the FWHM(Hβ_b) and the second-order moment should be comparable. However, for J1522, the broad component in the Hβ line was modeled using a Lorentzian profile, therefore a comparison between the two methods is literally impossible since the second-order moment of a Lorentzian function cannot be measured. However, since it shows all the typical traits of NLS1s, I believe that the estimated black hole mass calculated with the FWHM of the Lorentzian profile is reliable. J1641, instead, turned out to be an intermediate Seyfert galaxy (Osterbrock and Koski, 1976; Osterbrock, 1977), and not an NLS1. The same classification can be retrieved by looking at the Sloan Digital Sky Survey (SDSS) spectrum. The main characteristic that distinguishes the two classes is the ratio between the narrow and the broad component, which is much larger in the intermediate Seyfert galaxies. The intermediate Seyfert galaxies are further subdivided according to the prominence of the broad component of the emission lines compared to the narrow component (Dalla Barba et al., 2023). The origin of these objects is widely discussed, spanning from inclination effects to intrinsic processes (Barquín-González et al., 2024). In the inclination hypothesis, the optical features visible in the spectra of intermediate Seyfert galaxies are due to the partial obscuration of the BLR (Malkan, Gorjian, and Tam, 1998; Guainazzi, Matt, and Perola, 2005). In this case, there would be an underestimation of the real width of the broad components in the emission lines. As a consequence, it can affect the calculation of the black hole mass and the Eddington ratio. In particular, an underestimation of the line width yields an underestimation of the black hole mass, and consequently an overestimation of the Eddington ratio. In my case, this means that J1641 may have a more massive black hole than the estimated. Considering that J1641 was found to be a γ-ray source, a more massive black hole would strengthen the hypothesis about its advanced stage of evolution.

The results I found through this work are systematically larger than previously estimated (Järvelä, Lähteenmäki, and León-Tavares, 2015). This is most likely due to the fact that past calculations adopted a totally different approach, that led to lower mass values. To further investigate the reliability of the results I obtained with Eq. 2.2, I additionally measured the black hole masses using a recent scaling law derived by Shen et al. (2024). They derived a relation comparing the masses of single epoch spectra with the ones obtained with the reverberation mapping technique, exploiting the $L_\lambda(5100\text{Å})$ and the FWHM(Hβ), with a scatter of $\sim$0.32 dex. The black hole masses I measured using such relation are listed in Tab. 5.5. Comparing the results obtained with this scaling law and the virial theorem, I found very similar values, confirming the reliability of the main approach used. Shen et al. (2024) derived similar scaling laws also for Mg II and C IV emission lines. Nevertheless, these two relations cannot be used in my case, since both Mg II and C IV are not visible in the spectra analyzed because of spectral coverage.

On average, the black hole masses derived for the whole sample are well within the typical range of NLS1s population (Peterson, 2011). Basically all of them, though, lie above the median value for the class ($M_{BH} = 1{\times}10^7$, Cracco et al., 2016), except for J1522. This is in agreement with the typical values in jetted NLS1s. Indeed, jetted NLS1s tend to have larger black hole masses than what is usually observed in non-jetted NLS1s (Foschini et al., 2015; Berton et al., 2015). Nevertheless, only based on the results obtained in this study, I cannot prove the presence of relativistic jets. It is worth noting, however, that the mass difference observed between jetted and non-jetted sources may be due to an observational bias. Since the power of relativistic

jets scales nonlinearly with the black hole mass (Heinz and Sunyaev, 2003; Foschini, 2014), more massive black holes have brighter relativistic jets, which in turn are easier to detect. Therefore, the population of jetted NLS1s of lower mass may still be missing. J1522 could fall exactly into this population. The Lorentzian profile for the broad Hβ suggests a source in an early stage of evolution (Berton et al., 2020b), indicating that the relatively low black hole mass does not derive from an underestimation.

5.6.2 Eddington ratio comparison

Regardless of the method used, the Eddington ratio of the sources is also consistent with typical NLS1 values, that is above 1% and up to super-Eddington (Boroson and Green, 1992; Sulentic et al., 2000). In particular, the results show ϵ closer to the lower limit of the range instead of high values of accretion. This, coupled with the black hole masses retrieved, suggests sources in a middle-advanced stage of evolution. However, an exception is present, which is J1522. Indeed, in this case, as described before, the low black hole mass and the Lorentzian profile used for the broad Hβ component are characteristics usually visible in unevolved sources, namely in an early stage of evolution.

Focusing on the approaches I used to calculate the Eddington ratios, there is a clear difference in the obtained results. The ϵ calculated using the derived continuum luminosity at 5100Å are always smaller compared to the ϵ obtained with the measured continuum luminosity. As stated in Sec. 5.4.4, the continuum at 5100Å can be contaminated mainly by the jet (Foschini et al., 2015) or by the host galaxy contribution, which is more likely in this case. Therefore, the difference in the Eddington ratio using the measured and derived continuum luminosity allows to quantify them. I can analyze at this point the differences in the Eddington ratios. The smallest difference is 0.06 for J1029 and J1509, and the largest is 0.83 for the J1228. Considering the associated errors, and excluding J1228 and J1522, a weak decreasing trend related to the redshift seems to be present (Fig. 5.6). Indeed J1510 is the source with the largest difference for the Eddington ratios but it has the lowest redshift, among the first five sources in Fig. 5.6. On the other hand, J1029 has the lowest difference for the Eddington ratios, but it has the highest redshift of the whole sample. However, given the contaminants that I will discuss in a moment, I cannot test such a possible correlation with the redshift for the whole sample. Therefore with only few sources, a conclusion on this may not be reliable. This has led me to focus more on the difference of each source separately. Although not formally compatible, five sources out of seven show similar Eddington ratios regardless of the calculation method used. J1228 and J1522 are exceptions. For J1228 the resulting Eddington ratios are 0.11 and 0.94. Carefully looking at the spectrum, there are no signs of possible contamination by the host galaxy. Considering the redshift of 0.2627, the second highest in the sample, a very bright host galaxy would be necessary to produce such a difference in the Eddington ratio results. This would lead to very intense absorption lines which are totally missing. A more reasonable explanation may come from a relativistic jet contamination, which is less affected by the redshift due to its strength. Nevertheless, it might not produce recognizable features in the optical spectrum, increasing the difficulty of recognizing it. It is worth noting that J1228 is the source with the highest $R4570$, proxy which suggests strong Fe II multiplets emission. Such behavior is associated with an intense ionizing continuum, which is produced by the accretion disk in a high accretion state (Gaskell et al., 2022). In J1522 I found the second largest Eddington ratios difference (0.36). This is the closest source in the sample

(z=0.0769). Contrarily to the previous case, the optical spectrum of J1522 shows a slight increase in the continuum level toward red wavelengths and multiple absorption lines. This behavior suggests contamination of the continuum luminosity by the host galaxy emission, resulting in an increase of the Eddington ratio calculated with the measured continuum luminosity at 5100Å. Behaviors that cannot be proven by a host galaxy modeling, since such modeling was not possible using the only available R1000R grism spectrum.

Two important conclusions can be drawn from such results. The former is that even without a strict host galaxy modeling, it is possible to evaluate if the host galaxy contaminates the continuum emission by analyzing the Eddington ratios calculated with the measured and derived continuum luminosity at 5100Å. In the end, only J1522 showed a non-negligible host galaxy contamination. The latter is the demonstration that the Eddington ratio obtained using the derived continuum luminosity is more reliable compared to the measured continuum luminosity approach, being less contaminated by relativistic jets and host galaxy emission. However, it is worth noting that the relations I used have a rather large standard deviation. This means that while they work for large samples, they may be misleading for a single source.

Even considering different sources of uncertainty in Eq. 5.9 and Eq. 5.10, I have to keep in mind that I am estimating a bolometric luminosity only using a luminosity in a small range of wavelength. This connection is based on the strong assumption that each value of $L_\lambda(5100\text{Å})$ corresponds to a specific SED shape. To this purpose, Ferland et al. (2020) found that similar spectral features are not always related to the same SED shape. Some authors also found a positive correlation between the bolometric correction in Eq. 5.10 and the Eddington ratio (Vasudevan and Fabian, 2007; Jin, Ward, and Done, 2012). Correlation disproved by Cheng et al. (2019), who also showed that the bolometric correction factor changes greatly according to the disk model assumed. The different Eddington ratios that can be obtained depending on the assumption made for the bolometric luminosity derivation, i.e. the scaling laws used, is clearly demonstrated for instance by comparing Berton et al. (2015) and Tortosa et al. (2023). The former derived the Eddington ratio from optical spectra, using scaling laws similar to those used in this work, while the latter derived the Eddington ratio from X-ray data. Looking at sources analyzed in both papers, the ϵ found in Tortosa et al. (2023) are three to four order of magnitude larger than those found in Berton et al. (2015). Such huge difference cannot be entirely due to a variation of the accretion of the sources, especially in a timescale of few years, but more likely on the approach used by the two papers. It is clear how the bolometric correction, and then the Eddington ratio among all, are just an estimation without precise knowledge of the SED shape. Therefore, the obtained results should be taken with a grain of salt and likely as a lower limit.

5.6.3 *R*4570-Eddington ratio discrepancy

An interesting parameter I can focus on is the *R*4570. The sources I analyzed turned out to belong to the populations A3 and A4 of the quasar main sequence, therefore with a strong Fe II emission. Gaskell, Klimek, and Nazarova (2007) with the Gaskell, Klimek & Nazarova BLR model showed that the Fe II emission comes from the outer part of the BLR, predominantly emitted at a radius twice that of Hβ. Moreover, Gaskell et al. (2022) stated that the Fe II emission is produced by photoionization, ruling out other possible hypotheses. They also found a positive correlation between the Fe II strength and the Eddington ratio (see also Boroson and Green, 1992; Wandel and Boller, 1998; Sulentic et al., 2000; Marziani et al., 2001). The sources of this study

Table 5.4: Pearson correlation coefficients.

Parameters	corr. coeff.	p-value
L(Hα)-L(5100Å)	0.89	0.04
L(Hβ)-L(5100Å)	0.82	0.04
L([O III]λ5007)-L(5100Å)	0.88	0.02
FWHM(Hβ_b)-R4570	-0.75	0.15
FWHM(Hα)-R4570	-0.96	0.04
R5007-R4570	0.90	0.02
R5007-L(Hβ)	-0.70	0.12
ϵ L_m(5100Å)-Δ[O III]$_c$	0.48	0.28
ϵ L_m(5100Å)-Δ[O III]$_w$	-0.26	0.57
ϵ L_d(5100Å)-Δ[O III]$_c$	0.09	0.85
ϵ L_d(5100Å)-Δ[O III]$_w$	-0.2	0.96

however seem to disagree with such a relation, except for J1228. As I described, despite all of them belonging to A3 and A4 populations, the resulting Eddington ratios are close to the lower boundary for the NLS1s class. Considering also the discussed biases which could affect the Eddington ratio calculation, the high R4570 parameters might indicate higher Eddington ratios than what I estimated. A higher Eddington ratio means a soft X-ray excess, which is not present in low-Eddington ratio sources. Soft X-ray radiation breaks down the dust grains in the outer BLR, thus releasing the iron that then gets photoionized by the photons coming from the accretion disk (Gaskell et al., 2022). Abramowicz and Fragile (2013) described that for a typical Shakura–Sunyaev disk, the viscous heating is balanced by radiative cooling. In high-Eddington ratio sources instead, the accretion disk does not have enough time to cool down only by the radiation losses, therefore an advective cooling is established. This forms the so-called slim disk, in which the efficiency of transforming gravitational energy into radiative flux decreases with increasing accretion rate. A slim disk shows a moderate luminosity despite super-Eddington accretion. If this is the case, the analyzed sources could have higher Eddington ratios than what I measured. This shows that the Eddington ratio estimate obtained via optical spectroscopy may be, at least in some cases, misleading. The R4570 parameter may thus be a very important, and more reliable, indicator of the real Eddington ratios of some AGN. Unfortunately, no other data of this sample are available for an independent measurement of ϵ. It is important to notice that the selection of the Fe II template might affect the measurement of the continuum luminosity, and then the resulting Eddington ratio, as well as for the investigation of the emission lines characteristics. Nevertheless, most of the Fe II emission is at wavelength shorter than that of Hβ. Therefore the main emission lines, like Hβ and [O III]$\lambda\lambda$4959,5007, and the continuum emission at 5100Å are not deeply dependent on the Fe II model used.

5.6.4 SDSS-GTC spectral continuum comparison

Looking at the available SDSS spectra of the sample, I measured and compared the continuum flux densities only, and not the emission lines properties, due to the much lower S/N compared to the GTC spectra, on average less than half. Computing the ratio of the flux densities at 5100Å in Tab 5.2, I found values between 0.90 for J1232 and 2.03 for J1641, the lowest and the highest respectively. For J1232 the SDSS

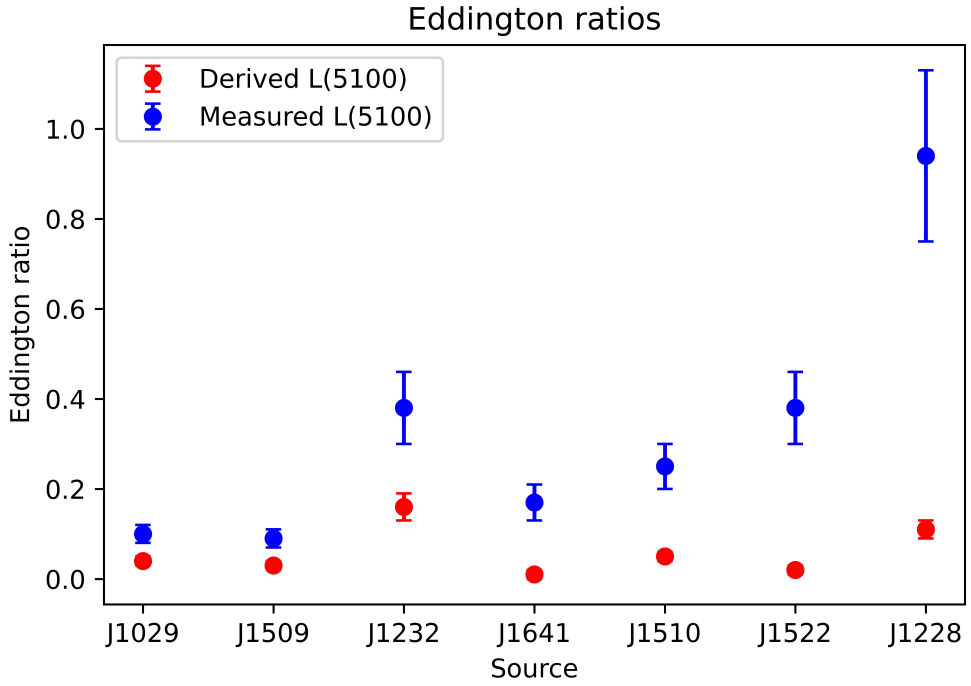

Figure 5.6: Eddington ratios calculated using the measured continuum luminosity at 5100Å (blue dots), and the derived continuum luminosity (red dots). The not visible error bars, due to their small values, are inside the size of the dots.

continuum is lower than the GTC continuum. In the remaining cases, however, the SDSS flux density is higher. In Seyfert galaxies, a variability of the flux density at 5100Å, sometimes even much larger than 2, has been found in several studies (Zastrocky et al., 2024; Shapovalova et al., 2012b; Grier et al., 2012). With a difference in the acquisition time of more than ten years between SDSS and GTC spectra, such values are in agreement with the well known long-term stochastic variability which characterize all the AGN.

5.6.5 Comparison of the NLS1s properties

In Tab. 5.4 are reported the Pearson correlation coefficients I computed for several couples of parameters, setting 0.05 as threshold for the significance of the correlation analysis. I compared the obtained results with the statistical analyses on large NLS1s samples available in the literature (Zhang et al., 2011; Rakshit et al., 2017; Paliya et al., 2024). The most significant correlations are those between Hα, Hβ and [O III]λ5007 luminosity and the continuum luminosity at 5100Å, with Pearson coefficients around 0.8-0.9. This is in agreement to what was found by Rakshit et al. (2017) and Paliya et al. (2024). The same authors found, even though with a quite large scatter, a weak anti-correlation in the couples of parameters of FWHM(Hβ_b)-R4570, FWHM(Hα)-R4570 and R5007-R4570, and a moderately strong anti-correlation between R5007 and L(Hβ). I found instead three strong correlations and one strong anti-correlation for the same couples of parameters. Nevertheless, the FWHM(Hβ_b)-R4570 and R5007-L(Hβ) correlation coefficients are not statistically significant, due to the p-values of 0.15 and 0.12, respectively. It is important to note that I did not consider the source J1641 in the FWHM(Hβ_b)-R4570 correlation test, since the

FWHM(Hβ_b) is much broader for intermediate Seyfert galaxies compared to NLS1s. Finally, I investigated the correlation between the Eddington ratios and the velocity shifts, with respect to the rest frame wavelength, of the core and the strongest wing components in the [O III]λ5007, as found by Zhang et al. (2011). Nothing can be said in this case due to the large p-values. Even though all the correlation coefficients are on average in agreement with the most recent literature, the extremely small number of sources I analyzed, cannot represent a statistically valid sample. Nevertheless, the lacking of noticeable peculiarities in the correlation analysis prove, once again, that these sources do not show deviations from the NLS1s class properties.

5.7 Conclusions

In this study I derived the physical parameters of seven NLS1s, performing an analysis of the main emission lines in optical spectra observed with the GTC. The goal was to identify any common optical property of the sources in the sample, which could explain why they show similar extreme features in the radio band. Investigating the most significant parameters, I did not find strong similarities between the sources. All but one showed classical behavior for the NLS1s class. Only J1641 turned out to be an intermediate Seyfert, but with physical properties that are common for this population. There are instead some shared traits. On average the black holes are more massive than the median value for the class (M_{BH} = 1×10^7, Cracco et al., 2016), with Eddington ratios much closer to the lower boundary for NLS1s. On the other hand, according to the $R4570$ parameter, the A3 and A4 nature of the sources (Sulentic and Marziani, 2015) suggests an underestimation of the actual Eddington ratio, which could be much higher than what I measured. High Eddington ratios for NLS1s could mean sources in an early stage of evolution, with an ongoing intense accretion activity. Though only the early evolutionary stage is not enough to explain why these sources show extreme flares in radio, it is an environment where the phenomena described by the hypotheses in Järvelä et al. (2024) can take place.

In particular AGN with a recently started activity, as NLS1s, can have regions with large amounts of gas, which is necessary to sustain a high Eddington ratio accretion (Mathur, 2000). A gas-rich nuclear environment, coupled with the relatively massive black holes which might suggest the possible presence of relativistic jets, is in agreement with scenarios such as jet-cloud/star interaction, relativistic jet and free-free absorption with moving clouds and magnetic reconnection in the jet (Järvelä et al., 2024). Nevertheless, with the results I obtained, nothing more can be said to support or rule out some of the cited hypotheses.

To better strengthen the obtained results in this study, optical spectra with wider wavelength ranges and higher S/N would be necessary. However, I would not expect much different results from those I obtained here since almost all the main emission lines were visible and I did not find substantial changes from the SDSS spectra. The only significant improvement I could get is spectra in which an host galaxy estimation can be done. In that case I could better constrain the Eddington ratio calculations. The similarities between the sources can be investigated more deeply with an analysis of the light curves, both in optical (Crepaldi et al., in prep.) and in radio frequencies. From the radio point of view, more observations at frequencies above 37 GHz would help to better understand all the ongoing physical processes on these sources. Moreover trigger observations, for example at high radio frequencies with the upgraded detectors of the Sardinia Radio Telescope or with other facilities such

as the Square Kilometer Array, can add more constraints to the viable hypotheses I already mentioned.

5.8 Appendix: tables, spectra and line profiles

Table 5.5: Observational and physical parameters derived from the optical spectra.

Source	L^{m}_{bol}	L^{d}_{bol}	$L_{[\mathrm{O\ III}]\tilde{}5007}$	$R5007$	R_{sub}	R_{out}	R_{NLR}	M^{*}_{BH}
(1)	(2)	(3)	(4)	(5)	(6)	(7)	(8)	(9)
J1029	8.39×10^{44}	3.81×10^{44}	1.23×10^{41}	0.12	0.25	7.50	906.05	9.32×10^{7}
J1228	1.12×10^{45}	1.35×10^{44}	3.08×10^{41}	0.72	0.16	4.79	1459.28	2.23×10^{7}
J1232	1.35×10^{45}	5.51×10^{44}	2.34×10^{41}	0.13	0.32	9.63	1263.67	5.99×10^{7}
J1509	3.40×10^{44}	1.15×10^{44}	4.86×10^{40}	0.19	0.13	3.74	558.36	3.97×10^{7}
J1510	2.64×10^{44}	5.45×10^{43}	8.61×10^{40}	0.71	0.09	2.55	751.76	1.22×10^{7}
J1522	1.56×10^{44}	9.08×10^{42}	1.02×10^{40}	0.52	0.04	1.05	248.59	6.94×10^{6}
J1641	3.81×10^{44}	2.57×10^{43}	7.33×10^{40}	1.12	0.06	1.89	691.75	1.80×10^{7}

Columns: (1) Source name; (2) bolometric luminosity calculated using the measured 5100Å continuum luminosity [erg s^{-1}] (Eq. 5.9); (3) bolometric luminosity calculated using the derived 5100Å continuum luminosity [erg s^{-1}] (Eq. 5.9 and Eq. 5.11); (4) [O III]λ5007 luminosity [erg s^{-1}]; (5) flux ratio between [O III]λ5007 line and Hβ; (6) dust sublimation radius (i.e. boundary between the BLR and the molecular torus) [pc] (Foschini et al., 2019); (7) outer radius of the molecular torus [pc] (Foschini et al., 2019); (8) maximum extension of the NLR [pc] (Foschini et al., 2019); (9) black hole mass [$M_{\odot}$] calculated using Eq. 2 in Shen et al., 2024.

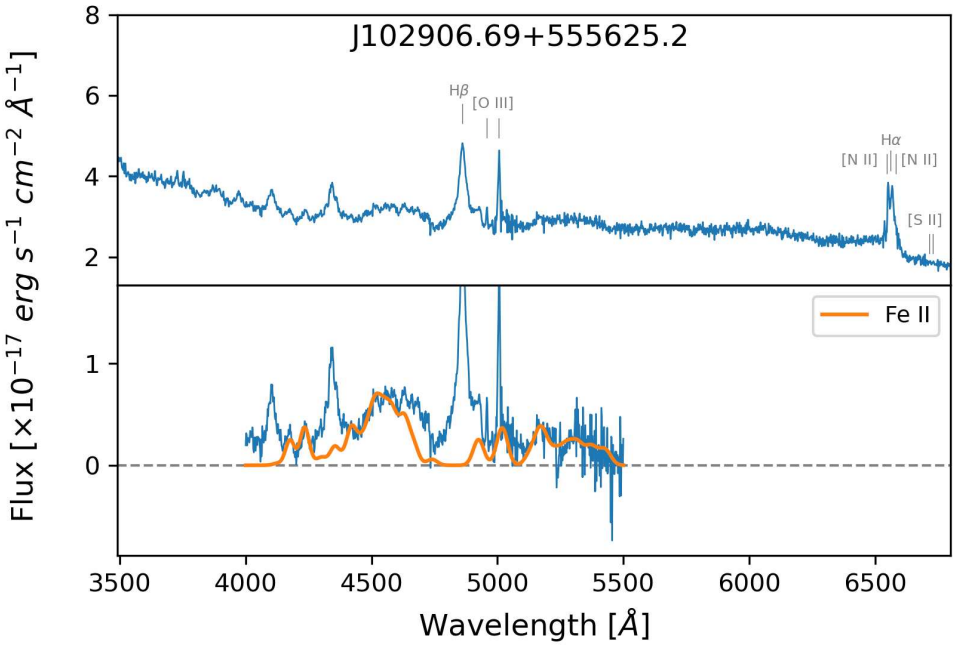

Figure 5.7: Spectrum of J1029.

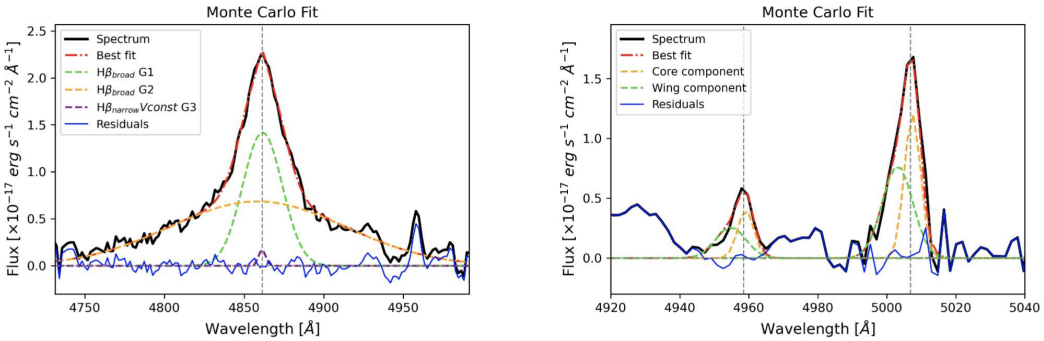

Figure 5.8: Hβ and [O III]$\lambda\lambda$4959,5007 line profiles of J1029.

Table 5.6: [O III]$\lambda\lambda$4959,5007 model parameters.

Param	J1029	J1228	J1232	J1509	J1510	J1522	J1641
(1) Model	4G	6G	6G	6G	4G	4G	4G
(2) f_{c5007}	1.25±0.30	13.23±0.66	2.35±0.42	2.84±0.53	16.80±0.34	4.14±0.87	6.61±0.22
(3) f_{c4959}	0.42±0.10	4.41±0.22	0.78±0.14	0.54±0.09	5.60±0.11	1.38±0.29	2.20±0.07
(4) Δc_c	31.14±34.73	71.25±4.49	-37.72±30.54	-60.48±29.94	1.20±2.99	98.20±77.84	38.32±4.19
(5) w_c	145.21±44.91	110.69±14.37	117.09±35.93	144.50±34.73	137.64±6.59	239.41±116.16	239.30±8.98
(6) f_{w5007}	0.72±0.30	3.21±0.44	3.02±0.38	0.83±0.55	2.23±0.35	2.12±0.80	1.22±0.22
(7) f_{w4959}	0.24±0.10	1.07±0.15	1.01±0.13	0.28±0.18	0.74±0.12	0.71±0.27	0.41±0.08
(8) Δc_{w1}	-288.01±266.45	-162.86±32.33	-411.35±42.51	-361.06±135.32	-252.68±50.30	-648.46±316.15	-58.08±55.69
(9) w_{w1}	343.85±247.29	149.58±44.31	221.68±37.72	153.96±116.76	606.28±95.20	326.89±283.22	770.93±83.83
(10) f_{w5007}		2.80±0.25	2.79±0.37	0.54±0.09			
(11) f_{w4959}		0.93±0.08	0.93±0.12	0.18±0.03			
(12) Δc_{w2}		-371.24±35.33	-595.77±10.78	-192.80±264.06			
(13) w_{w2}		497.35±25.15	587.48±46.11	895.15±16.17			

Rows: (1) Fitting model; (2) peak flux density of the [O III]λ5007 core component [$\times10^{-17}$ erg s^{-1} cm^{-2} $^{-1}$]; (3) peak flux density of the [O III]λ4959 core component [$\times10^{-17}$ erg s^{-1} cm^{-2} $^{-1}$]; (4) shift of the core component [km s^{-1}]; (5) width of the core component [km s^{-1}]; (6) peak flux density of the first [O III]λ5007 wing component [$\times10^{-17}$ erg s^{-1} cm^{-2} $^{-1}$]; (7) peak flux density of the first [O III]λ4959 wing component [$\times10^{-17}$ erg s^{-1} cm^{-2} $^{-1}$]; (8) shift of the first wing component [km s^{-1}]; (9) width of the first wing component [km s^{-1}]; (10) peak flux density of the second [O III]λ5007 wing component [$\times10^{-17}$ erg s^{-1} cm^{-2} $^{-1}$]; (11) peak flux density of the second [O III]λ4959 wing component [$\times10^{-17}$ erg s^{-1} cm^{-2} $^{-1}$]; (12) shift of the second wing component [km s^{-1}]; (13) width of the second wing component [km s^{-1}].

Table 5.7: Hβ model parameters.

Param	J1029	J1228	J1232	J1509	J1510	J1522	J1641
(1) Model	3G	3G	3G	3G	3G	LG	2G
(2) f_{b1}	1.42±0.07	4.23±0.15	13.23±0.27	3.85±0.08	2.64±0.19	3.35±0.42	1.11±0.05
(3) Δc_{b1}	15.23±25.28	-117.36±15.42	-79.74±7.40	41.75±10.48	-397.95±49.34	-285.09±70.92	23.25±76.47
(4) w_{b1}	773.06±48.72	541.14±28.98	601.43±18.50	737.35±20.35	395.13±48.72	685.14±109.15	1767.11±117.17
(5) f_{b2}	0.68±0.06	0.96±0.14	5.74±0.32	0.82±0.07	1.37±0.12		
(6) Δc_{b2}	-187.66±131.35	-596.52±160.34	-216.64±31.45	440.74±148.62	9.68±156.64		
(7) w_{b2}	3426.33±317.59	2465.03±297.24	2055.15±74.00	3091.26±254.69	2609.44±289.84		
(8) f_n	0.18±0.10	2.02±0.26	2.65±0.38	0.45±0.13	2.12±0.48	2.13±0.31	1.08±0.10
(9) w_n	145.21	110.69	117.09	144.50	137.64	239.41	239.30

Rows: (1) fitting model; (2) peak flux density of the first broad component [$\times10^{-17}$ erg s^{-1} cm^{-2} $^{-1}$]; (3) shift of the first broad component [km s^{-1}]; (4) width of the first broad component [km s^{-1}]; (5) peak flux density of the second broad component) [$\times10^{-17}$ erg s^{-1} cm^{-2} $^{-1}$]; (6) shift of the second broad component [km s^{-1}]; (7) width of the second broad component [km s^{-1}]; (8) peak flux density of the narrow component [$\times10^{-17}$ erg s^{-1} cm^{-2} $^{-1}$]; (9) width of the narrow component constrained with the width of the [O III]λ5007 core component [km s^{-1}].

Table 5.8: Hα+[N II]$\lambda\lambda$6548,6583 and [S II]$\lambda\lambda$6716,6731 model parameters.

Param	J1029	J1228	J1232	J1509	J1510	J1522	J1641
(1) f_{b1}		16.19±0.11	41.33±0.16	9.61±0.06	6.11±0.15	5.61±0.57	
(2) f_{b2}		1.35±0.05	7.82±0.07	0.90±0.03	2.40±0.06		
(3) f_n		14.42±0.19	10.03±0.26	2.50±0.10	14.83±0.23	13.56±0.70	
(4) f_{6583}		8.17±0.13	2.42±0.16	1.50±0.08	8.19±0.17	4.65±0.23	
(5) f_{6716}		1.93±0.13	1.28±0.17	0.51±0.08	2.54±0.18		1.69±0.09
(6) f_{6731}		1.77±0.13	1.02±0.17	0.49±0.08	2.33±0.17		1.67±0.10
(7) Δc_{6731}		22.49±12.03	-30.51±35.63	-24.72±21.83	22.94±11.14		-51.89±17.82
(8) w_{6731}		152.59±13.36	180.35±31.62	97.20±41.86	135.08±15.59		217.67±12.47

Rows: (1) Peak flux density of the first Hα broad component [$\times 10^{-17}$ erg s^{-1} cm^{-2} $^{-1}$]; (2) peak flux density of the second Hα broad component [$\times 10^{-17}$ erg s^{-1} cm^{-2} $^{-1}$]; (3) peak flux density of the first Hα narrow component [$\times 10^{-17}$ erg s^{-1} cm^{-2} $^{-1}$]; (4) peak flux density of the [N II]λ6583 [$\times 10^{-17}$ erg s^{-1} cm^{-2} $^{-1}$]; (5) peak flux density of the [S II]λ6716 [$\times 10^{-17}$ erg s^{-1} cm^{-2} $^{-1}$]; (6) peak flux density of the [S II]λ6731 [$\times 10^{-17}$ erg s^{-1} cm^{-2} $^{-1}$]; (7) shift of the [S II]λ6731 [km s^{-1}]; (8) width of the [S II]λ6731 [km s^{-1}].

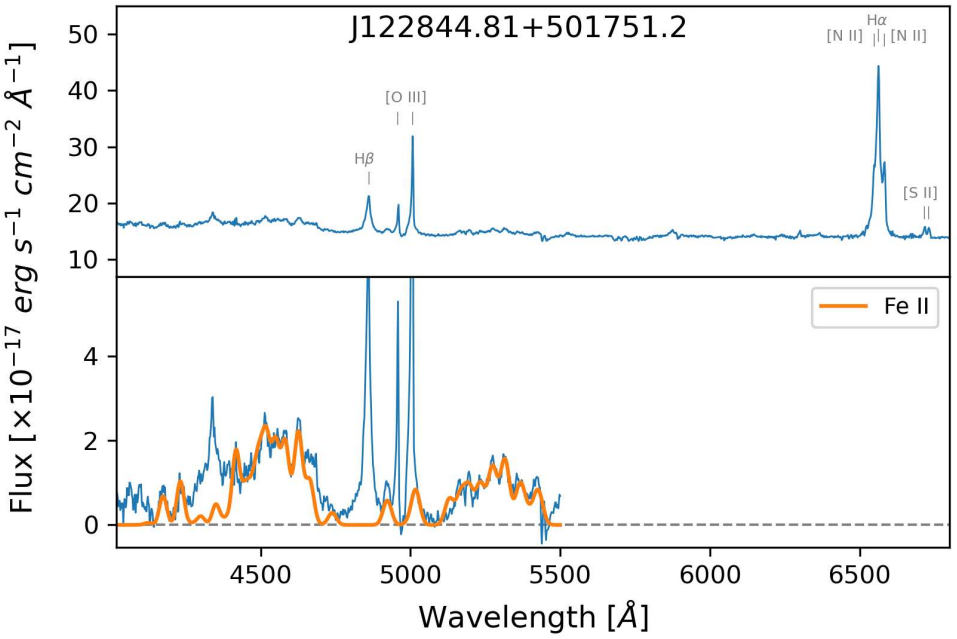

Figure 5.9: Spectrum of J1228.

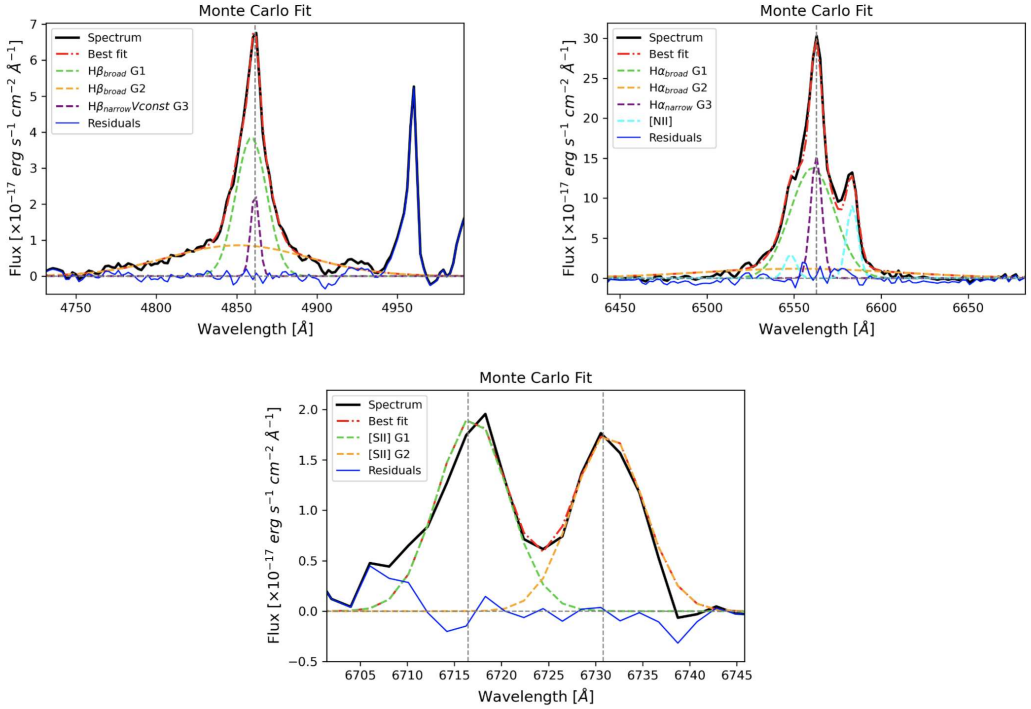

Figure 5.10: Hβ, Hα+[N II]$\lambda\lambda$6548,6583 and [S II]$\lambda\lambda$6716,6731 line profiles of J1228.

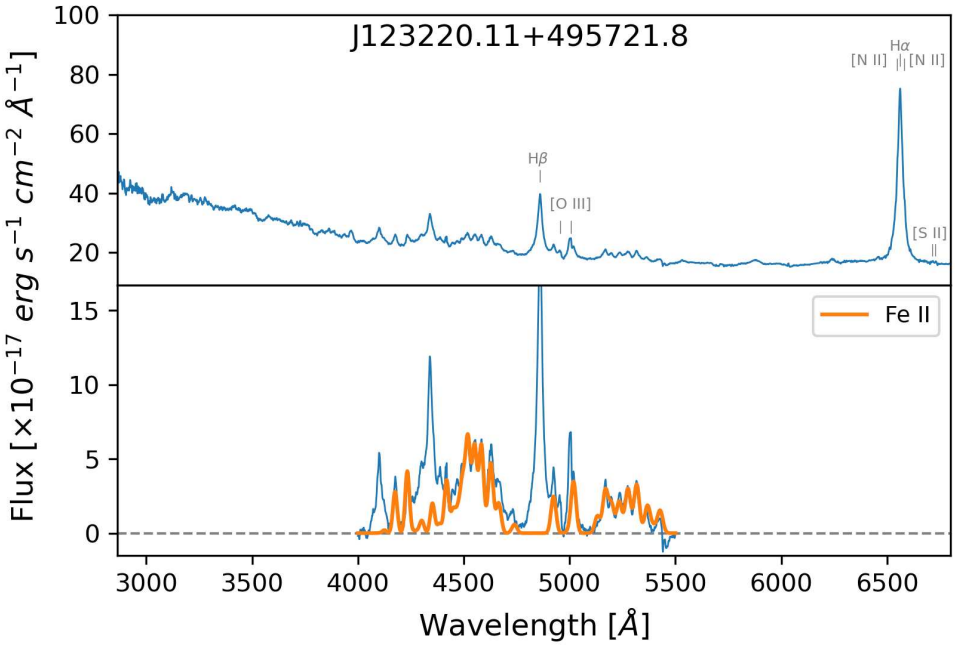

Figure 5.11: Spectrum of J1232.

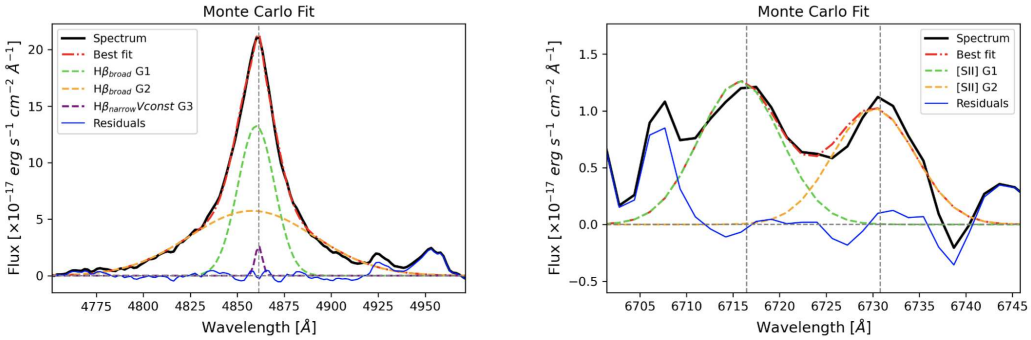

Figure 5.12: Hβ and [S II]$\lambda\lambda$6716,6731 line profiles of J1232.

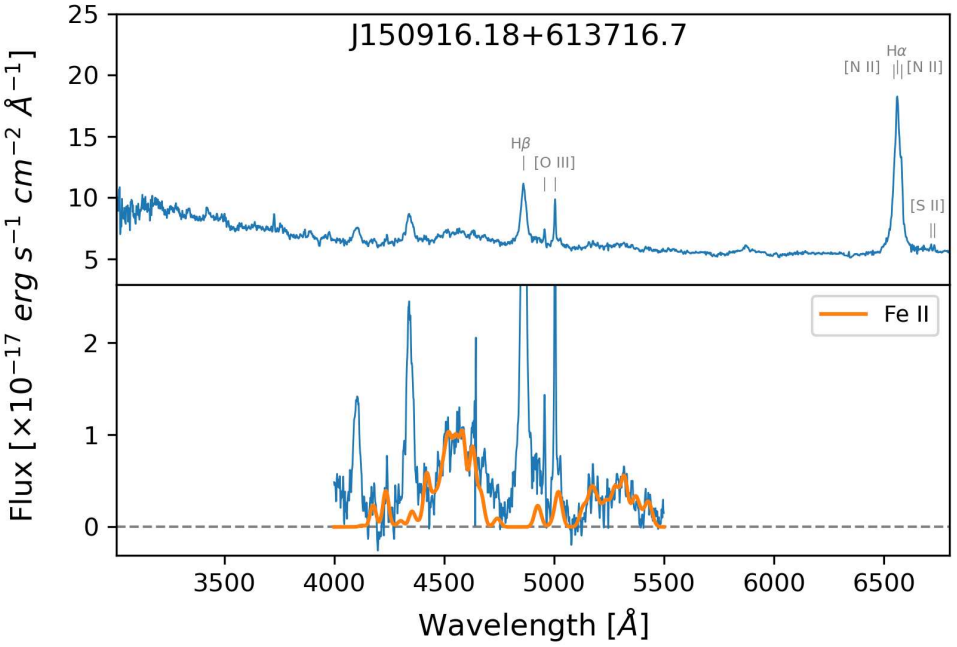

Figure 5.13: Spectrum of J1509.

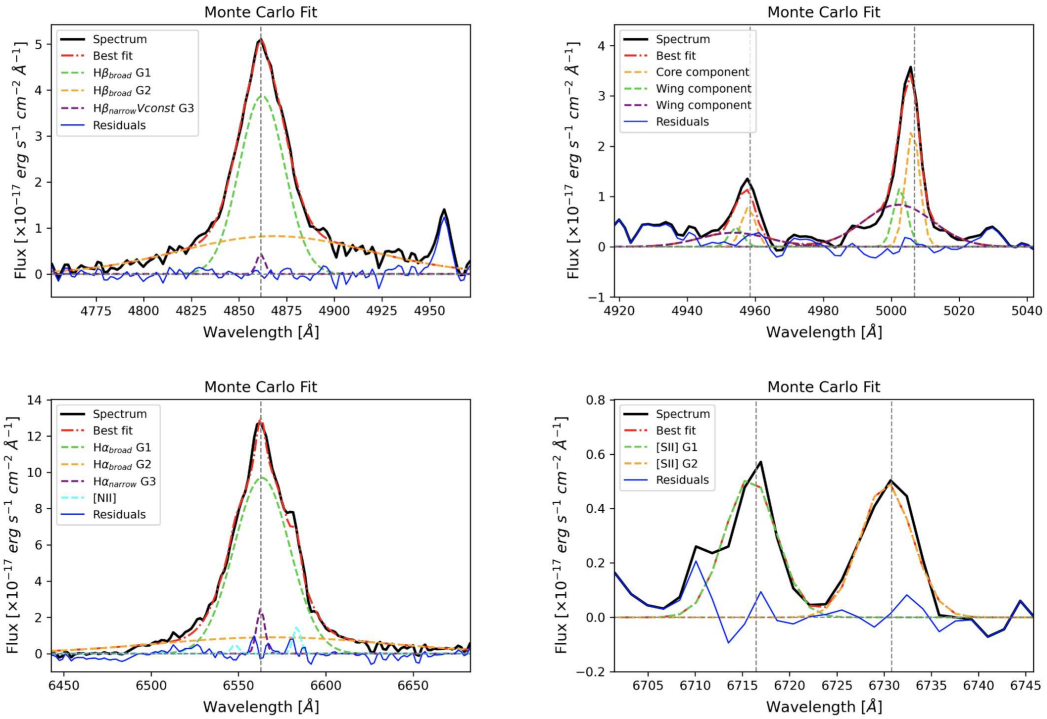

Figure 5.14: Hβ, [O III]$\lambda\lambda$4959,5007, Hα+[N II]$\lambda\lambda$6548,6583 and [S II]$\lambda\lambda$6716,6731 line profiles of J1509.

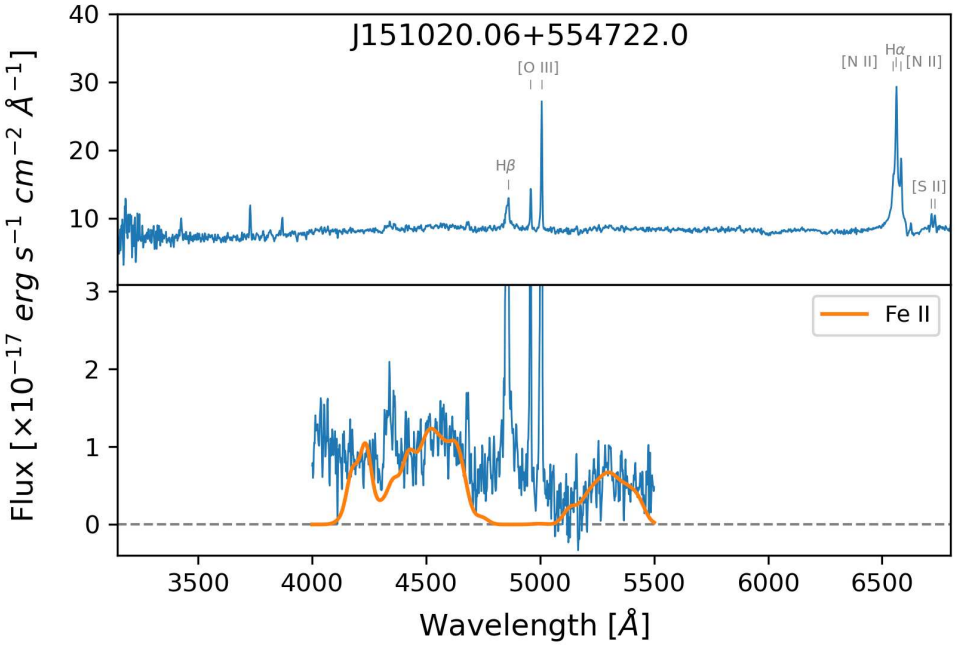

Figure 5.15: Spectrum of J1510.

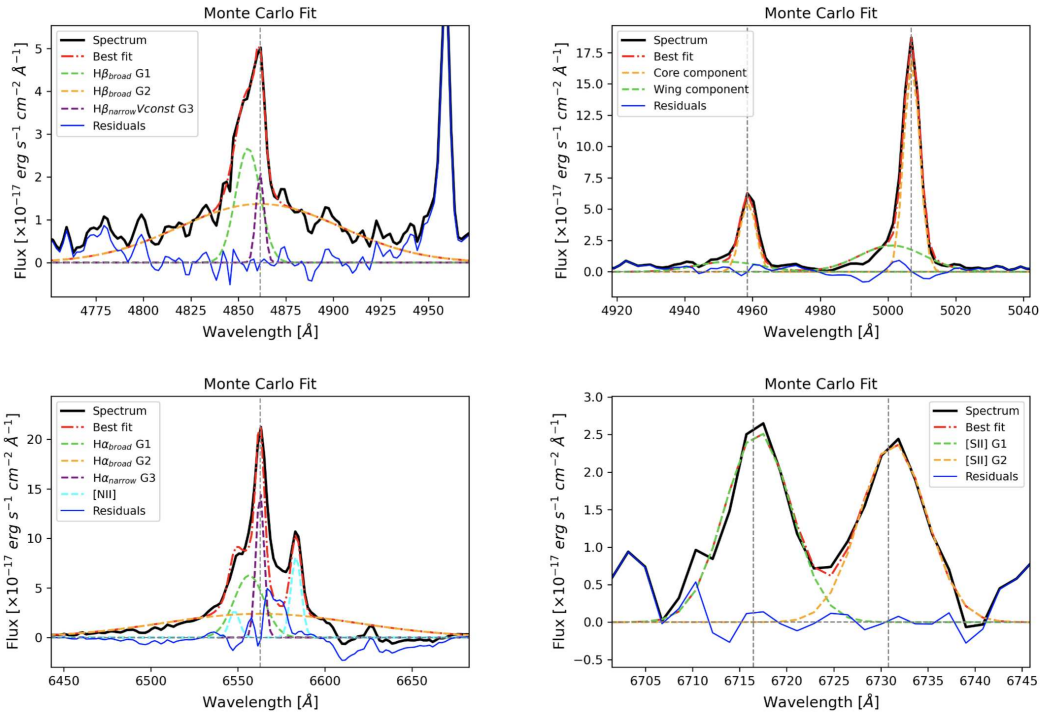

Figure 5.16: Hβ, [O III]$\lambda\lambda$4959,5007, Hα+[N II]$\lambda\lambda$6548,6583 and [S II]$\lambda\lambda$6716,6731 line profiles of J1510.

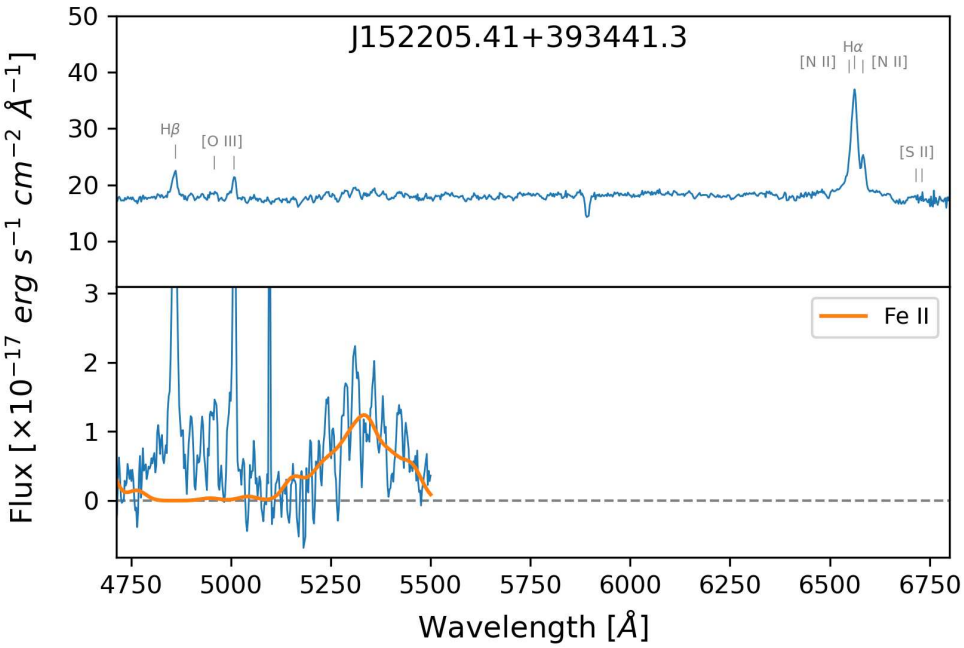

Figure 5.17: Spectrum of J1522.

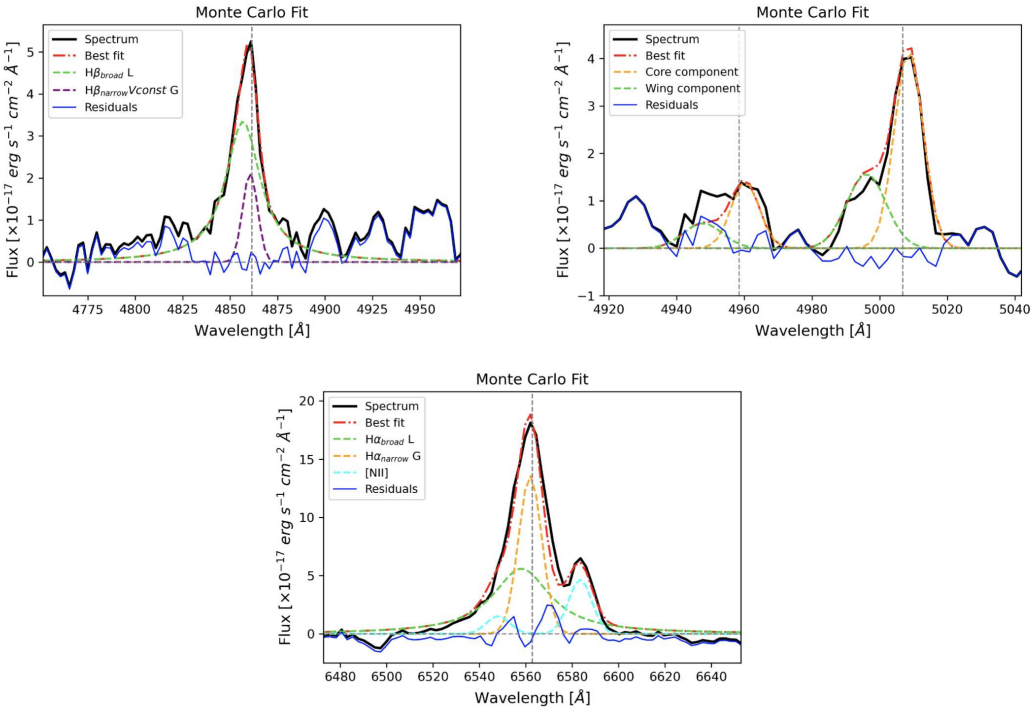

Figure 5.18: Hβ, [O III]$\lambda\lambda$4959,5007, Hα+[N II]$\lambda\lambda$6548,6583 and line profiles of J1522.

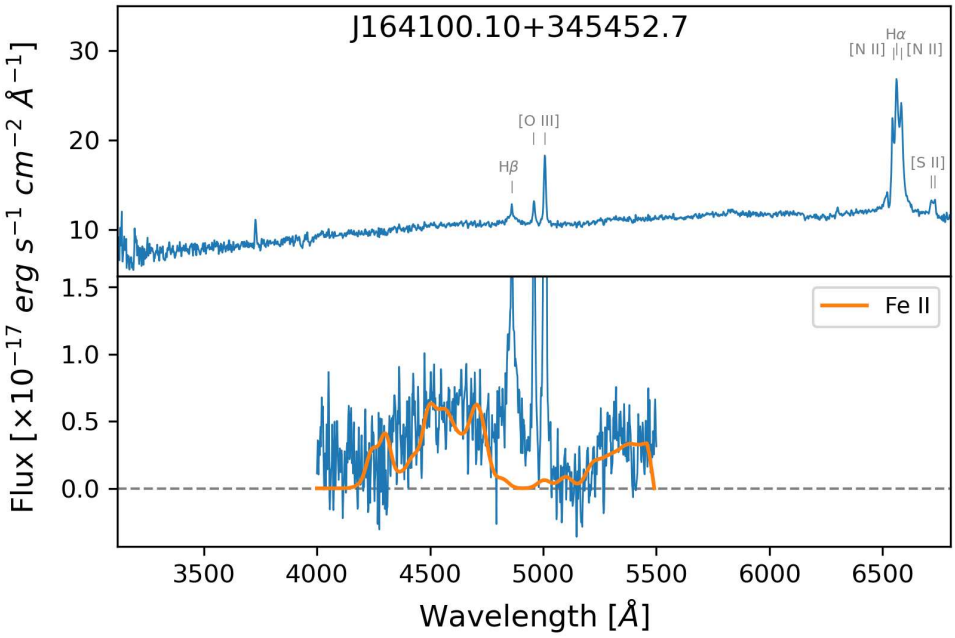

Figure 5.19: Spectrum of J1641.

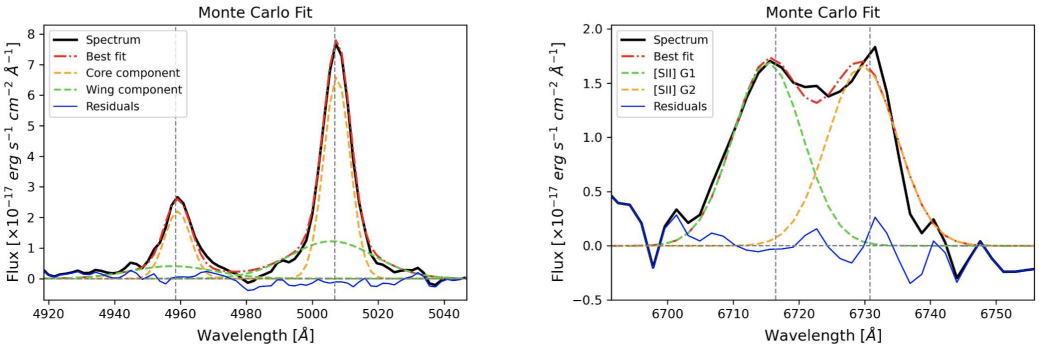

Figure 5.20: [O III]$\lambda\lambda$4959,5007, Hα+[N II]$\lambda\lambda$6548,6583 and line profiles of J1641.

Chapter 6

Investigation on the fastest radio variability in AGN

Foreword: MRO has been detecting for more than ten years extreme radio flares at 37 GHz from a sample of seven sources, six NLS1s and one intermediate Seyfert. The random time cadence and the short duration of the events make any deep investigation extremely challenging. Here I analyzed all the available radio data of the last three years at multiple frequencies, with the aim of estimating the main physical properties of the flares like the *e*-folding time-scale, the variability brightness temperature, and the variability Doppler factor. In the few cases where these measurements have been possible, I estimated time-scales down to a few tens of minutes and variability brightness temperatures $>10^{15}$, up to $\sim 10^{20}$. Among the presented hypotheses, the magnetic reconnection in the black hole magnetosphere seems to be the most suitable one. The extreme results I found suggest a coupling between magnetic reconnection and either an inverse Compton catastrophe or a coherent emission. Further follow-up observations, especially in radio and X-ray, will be fundamental to shed light on the possible scenarios.

Based on: Crepaldi et al. in prep.

6.1 Introduction

In recent years, the use of the radio-loudness parameter as a proxy for the presence of relativistic jets in AGN has decreased, and classification into jetted and non-jetted sources is now preferred (Padovani, 2017; Järvelä et al., 2017; Berton and Järvelä, 2021b). This is particularly relevant in sources as NLS1 galaxies, where relativistic jets have been found in radio-quiet objects (Caccianiga et al., 2015). It is clear that the classification of a source as radio-quite at a certain moment in time does not imply that such a source always presents a weak radio emission. The sample analyzed in this thesis is a clear example of this statement.

As described in the previous Chapters, multiple hypotheses might explain the behavior seen in radio. In the following work, I analyzed new data of the sample in several radio bands, with the aim of strengthening or discarding some of these hypotheses, possibly adding new ones. I used both single-dish data acquired by MRO, OVRO, Effelsberg, and Institut de Radioastronomie Millimétrique (IRAM) telescopes and interferometric data acquired with the JVLA. Previous radio data were published in Lähteenmäki et al., 2018, Berton et al., 2020a, and Järvelä, Berton, and Crepaldi, 2021; Järvelä et al., 2024. This Chapter is organized as follows. In Sec. 6.2 I introduce the sample and report the observations and data reduction, in Sec. 6.3 I describe the analysis of the data and the results, in Sec. 6.4 I discuss the results, and provide conclusions in Sec. 6.5. Throughout this work, I adopt a standard

ΛCDM cosmology, with a Hubble constant $H_0 = 72$ km s^{-1} Mpc^{-1}, and $\Omega_\Lambda = 0.73$ (Komatsu et al., 2011).

6.2 Sample and data reduction

As described in the previous chapters, the sample is composed of six radio-weak NLS1s and one radio-weak intermediate Seyfert. Some physical and observational properties of the sources are reported in Tab. 5.1.

6.2.1 Metsähovi Radio Observatory

The observations used in this work have been carried out as part of the large AGN monitoring programme at 37 GHz started in 2012 with the 13.7 m radio telescope at MRO. A detailed description of the programme is reported in Lähteenmäki et al. (2017). The measurements are made with a 1 GHz dual-beam receiver centered at 36.8 GHz. The beam full-width at half power is 144 arcsec, and the observations are performed in on-on mode, meaning that the source and the sky are alternated in each feed horn. The integration time adopted to obtain one flux density data point is between 1600 and 1800 s, which has been experimentally found to be enough to reach a good sensitivity, the latter being limited mainly by the sky noise. The detection limit of this telescope is around 200 mJy at 37 GHz under optimal conditions. The quality and reliability of the MRO data are constantly monitored by means of semi-automatic and manual checks, paying particular attention to the influence of weather conditions. An observed data point is labeled as a detection for an S/N higher than four. The flux density scale is set by observations of DR21. NGC 7027, 3C 274, and 3C 84 are sources used as secondary calibrators. A detailed description of the data reduction and analysis phase is provided in Teräsranta et al. (1998). The error associated with the flux density includes both the contribution from the measurement rms and the uncertainty of the absolute calibration, set to 3%. The observational period related to the MRO data used in this work goes between June 2022 and January 2024. See Järvelä et al. (2024) for further details about the observations of the sample by MRO.

6.2.2 Owens Valley Radio Observatory

The sample is part of the OVRO AGN monitoring programme, which performs observations at 15 GHz. The telescope is composed of an off-axis dual-beam optics and a cryogenic receiver centered at 15 GHz and with 3 GHz bandwidth, and the beam full-width at half power is 157 arcsec. The observations use an on-on fashion to remove atmospheric and ground contamination. The up-to-date pseudo-correlation receiver corrects the fast grain variations using a 180 deg phase switch. The calibrations are carried out using a temperature-stable diode noise source to remove the receiver gain drifts, and 3C 286 is used as a calibrator for the flux density scale, assuming a value of 3.44 Jy at 15 GHz (Baars et al., 1977). An additional 5% of the flux density is included in quadrature to the flux density error, and a detection is considered when the S/N $\geq$ 4. Richards et al. (2011) provided a full description of the data reduction and calibration procedure, and Järvelä et al. (2024) reported the details of OVRO observations of the sample. Here, I used OVRO data between June 2022 and October 2024.

6.2.3 Effelsberg 100-m telescope

The observations with the Effelsberg 100-m telescope were carried out in three epochs, between December 2021 and June 2023. The initial epoch of observations took place on December 16, 2021, the second on April 20-21, 2022, and the last epoch between May 31 and June 1, 2023. Not all the sample was observed with Effelsberg. J1232+4957, J1522+3934, and J1641+3454 were included in the first epoch, J1029+5556, J1228+5017, J1232+4957, J1509+6137, J1522+3934, and J1641+3454 were included in the second, and only J1228+5017 was part of the third epoch. The receivers used were: S45 (simultaneous measurements at 4.8, 5.3, 6.7, 6.8 GHz, with a beam full-width at half power of 147, 135, 113, 111 arcsec, respectively), S28 at 10.45 GHz with a beam full-width at half power of 68 arcsec, S14 (simultaneous measurements at 19.3, 21.2, 23, 24.8 GHz, with a beam full-width at half power of 39, 36, 35, 30 arcsec, respectively), and S7 low frequency configuration (simultaneous measurements at 35.8 and 38.3 GHz, with a beam full-width at half power of 25 and 22 arcsec). For the third epoch observations, the receiver S20 (simultaneous measurements at 14.3 and 16.8 GHz, with a beam full-width at half power of 50 and 45 arcsec) was also used. Each observation was made of cross-scans without pointing auto correction. The exposure time was 8 minutes for the receivers S45, S28, S14, and S7, and 6 minutes for the receiver S20. The data are listed in Tab. 6.8.

6.2.4 Institut de Radioastronomie Millimétrique

Additional observations were taken for this sample with the 30-m telescope at IRAM, a single-dish parabolic antenna on an alt-azimuthal mount. The telescope makes wide-angle observations with three receivers on frequencies from 80 to 370 GHz. The observations were carried out using the dual-band New IRAM KID Array 2 (NIKA2) camera, which observes at 150 and 260 GHz simultaneously. The observations were on-the-fly maps, using both the A1 and A3 receivers for 260 GHz and A2 for 150 GHz. Using the AGN 1637+574 as a pointing source, the sample was obtained on scattered days from October 28, 2022, to January 23, 2023. Only a portion of the sample was observed, including J1228+5017 only on October 28, J1509+6137 from October 28 to November 20, J1510+5547 from November 14 to January 29, J1522+3934 from November 14 to January 29, and J1641+3454 from October 28 to November 20. The data were reduced using the Pointing and Imaging In Continuum pipeline (Zylka, 2013; Berta and Zylka, 2019-2025) for observations on each NIKA2 band, using parameters for weak positive sources and a half-power beam width of 11 arcsec for the observations at 260 GHz and 17 arcsec for 150 GHz.

6.2.5 Karl G. Jansky Very Large Array

I exploited a strict JVLA monitoring of one source, J1522+3934, being one of the most active in the sample (Project VLA/23A-061, PI: Berton). The programme consisted of 38 observations in A- (8), BnA- (3), and B-configuration (27), in the period between January 19th and September 29th 2023. Only one observation in the B-configuration was flagged as bad quality data and then removed in the analysis. The two bands used were the *X*, centered at 10 GHz with a total bandwidth of 4 GHz, and the *K*, centered at 22 GHz with a total bandwidth of 8 GHz. Each band is divided into 128 MHz sub-bands, consisting of 64 channels of 2 MHz each. Since the duty cycle of all the sources is still unknown, an as long as possible short cadence monitoring fully dedicated to one source would have increased the chances of observations of a flare episode. For this reason, the observations of this programme have a cadence

Table 6.1: MRO 37 GHz detections.

Source	Date	S	N_{det}/N_{obs}
(1)	(2)	(3)	(4)
J1029+5556			0/43
J1228+5017	2023.405411	0.78±0.12	12/148
	2023.427261	0.44±0.08	
	2023.432697	0.50±0.11	
	2023.442703	0.87±0.17	
	2023.443627	0.61±0.12	
	2023.450887	0.63±0.15	
	2023.454555	0.60±0.13	
	2023.476434	0.49±0.09	
	2023.506495	0.48±0.09	
	2023.528383	0.36±0.09	
	2023.531103	0.59±0.10	
	2023.672204	0.66±0.14	
J1232+4957			0/55
J1509+6137	2023.479418	0.54±0.13	4/91
	2023.531236	0.96±0.20	
	2023.594168	0.71±0.15	
	2023.605128	0.92±0.18	
J1510+5547	2022.504126	0.58±0.11	4/83
	2022.525973	0.72±0.12	
	2022.599658	0.42±0.09	
	2022.602486	0.85±0.13	
J1522+3934	2022.523215	0.46±0.10	2/65
	2023.430322	0.42±0.10	
J1641+3454	2023.501381	0.50±0.11	1/276

Columns: (1) source; (2) time of detection [decimal year]; (3) flux density and its error [Jy]; (4) number of detections and observations.

of three days on average in both bands. For each band, 3 minutes of integration time have been spent on the source. 3C 286 (Berton et al., 2017) was used as main calibrator, and the source SDSS J152059.21+433535.1 as phase calibrator. In addition to the flux density error, derived from the fitting of the source in the radio map, I summed in quadrature the calibration uncertainty. This additional error is equal to 5% of the flux density for *X* band, and 10% for *K* band.

6.3 Analysis and results

Since the flaring episodes I am focusing on are so short (at most a few hours from the most recent estimations), I have failed thus far to make observations of the same flare at multiple frequencies. Moreover, no very close observations in time (e.g., with time-scales of a few hours) of a flare are available either, which would be useful to recover the flare shape. This is because the flares have been detected only by MRO, which cannot observe at multiple frequencies simultaneously, but requires receiver changes. Nevertheless, I can use consecutive MRO detections to derive some properties of the radio emission at 37 GHz. Two detections are defined as consecutive if there are no non-detections between them, and when they are observed less than seven days apart. Considering the typical dimension of an NLS1s, this choice safely include a large fraction of the possible mechanisms that produce flares, since the

Table 6.2: Flare properties at 37 GHz from the MRO detection.

Source	t_1	t_2	S_1	S_2	τ	$T_{b,var}$	δ_{var}
(1)	(2)	(3)	(4)	(5)	(6)	(7)	(8)
J1228+5017	2023.528383	2023.531103	0.36±0.09	0.59±0.10	$2.08^{+13.30}_{-1.01}$	$19.40^{+40.82}_{-18.98}$	$33.85^{+15.53}_{-24.45}$
J1510+5547	2022.599658	2022.602486	0.42±0.09	0.85±0.13	$1.49^{+1.63}_{-0.53}$	$17.09^{+17.86}_{-12.60}$	$32.45^{+8.74}_{-11.66}$

Columns: (1) source; (2) time of first detection [decimal year]; (3) time of second detection [decimal year]; (4) flux density of first detection [Jy]; (5) flux density of second detection [Jy]; (6) time-scale [days]; (7) variability brightness temperature [$\times 10^{14}$ K]; (8) variability Doppler factor.

right time-scale is unknown. In addition, a flare is defined if the flux density between one detection and the next is not the same within the error bars. If the second detection has the higher flux density, we are clearly looking at the rising phase of the flare. In the inverse case, we are looking at the decaying phase. Only two pairs of observations show clear flares, and they are both in the rising phase. I reported these in Tab. 6.2. Valtaoja et al. (1999) and Hovatta et al. (2009) calculated the flare rise and decay *e*-folding time-scales, variability brightness temperatures, and variability Doppler factors, and I carried out the same calculations in this case. For the rising phase of a flare, the equation of the flux density at the epoch t is expressed as

$$\Delta S(t) = \Delta S_{\rm max} e^{(t-t_{\rm max})/\tau} \quad [\rm Jy] \,, \tag{6.1}$$

where $\Delta S_{\rm max}$ is the maximum amplitude of the flare in Jy, with the subtracted baseline flux density level, S_b, $t_{\rm max}$ is the epoch of the peak of the flare, and τ is the rise time of the flare in days, also called *e*-folding time-scale. Since no other detections by single-dish telescopes are available to determine the quiescent flux density level, I used the one adopted in Järvelä et al. (2024) and derived from OVRO observations, which corresponds to ∼10 mJy. I cannot be sure, even considering the described constraints, that the two detections used in this formula come from the same flare. But were this not the case, the variability would be even faster. I also considered the detection with the higher flux density as the peak of the flare. So these values represent the minimum amplitude change and the maximum time-scale for the change.

I calculated the variability brightness temperature in the source proper frame, $T_{b,var}$, which is necessary to estimate the variability Doppler factor, through the equation

$$T_{b,var} = 1.548 \times 10^{-32} \frac{\Delta S_{\rm max} d_L^2}{\nu^2 \tau^2 (1+z)} \quad [\rm K] \,, \tag{6.2}$$

where ν is the observed frequency in GHz, d_L is the luminosity distance in meters, and $\Delta S_{\rm max}$ and τ are the quantities in Eq. 6.1. The numerical factor corresponds to using $H_0 = 72$ km s^{-1} Mpc^{-1}, and $\Omega_\Lambda = 0.73$, and assuming that the source is a homogeneous sphere. It is important to remember that the estimation of the brightness temperature from the flux density variability is based on a causality argument. Therefore, the values must be considered as lower limits.

At this point, I calculated the variability Doppler factor, expressed as

$$\delta_{var} = \left(\frac{T_{b,var}}{T_{b,int}} \right)^{1/3} \,, \tag{6.3}$$

where $T_{b,int}$ is the intrinsic brightness temperature, which I assumed to be equal to 5×10^{10} K (Readhead, 1994; Lähteenmäki and Valtaoja, 1999; Homan et al., 2021), for equipartition between the energy densities of the magnetic field and the radiating particles. It is not trivial to know if the sources are in equipartition, therefore, the variability Doppler factor in Eq. 6.3 might not be accurate. However, the large error bars reasonably include the real Doppler factor if the intrinsic brightness temperature deviates from the equipartition one.

The results are reported in Tab. 6.2. The two cases that respect the chosen criteria derive from the sources J1228+5017 and J1510+5547, related to flares that occurred respectively in 2023 and 2022. I found *e*-folding time-scales of the order of one/two days, up to a few weeks, considering the errors. The variability brightness temperatures are around 10^{14}-10^{15} K, and the variability Doppler factors are between 10 and 50. All the results but the time-scales are comparable to the ones seen in FSRQs (Hovatta et al., 2009). Following Raiteri (2024) I estimated the dimension of the emitting region r. It is derived from causality arguments based on the light travel time, exploiting τ to set an upper limit. This size is $r < c\tau\delta/(1+z)$ where c is the speed of light. Using the two available flare properties, I found that r must be smaller than $\sim$50 milliparsecs. This means that the emitting region is small enough to be well within the BLR, close to the black hole, or from small regions inside the jet.

6.3.1 MRO-JVLA quasi-simultaneous observations

During the monitoring period of J1522+3934 with the JVLA, MRO detected the source only once (see Tab. 6.4 and 6.1 for the data). Close to the MRO detection, the JVLA was in BnA-configuration, and observed the source one day apart. It should be clear that the emission resolved out by the JVLA cannot explain the difference in the flux density of these flare episodes (Järvelä et al., 2024). On these time-scales the change has to occur in a compact component.

Considering the derived $\tau > 1$ in Tab. 6.2, I can assume that both the telescopes were looking at the source during the same flare episode. If this is true, at least the *K*-band would have followed a flux density increasing as measured at 37 GHz. The MRO detection (second detection for J1522+3934 in Tab. 6.1) occurred on 2023.430322 with a flux density of 0.42$\pm$0.10 Jy, while the closest JVLA observation has been done on 2023.427586 (Tab. 6.4), with a flux density of 0.217$\pm$0.034 mJy/beam and 0.127$\pm$0.028 mJy/beam respectively in *X* and *K* band. For the JVLA observations before and after this date, there have been no strong variations of the peak flux density, suggesting no influence of this specific flare below 22 GHz. Assuming a power law trend for the spectrum as $S(\nu) = A \times \nu^{\alpha}$, with A equal to a constant value, the spectral index formula is expressed as

$$\alpha = \frac{log\left(\frac{S_1}{S_2}\right)}{log\left(\frac{\nu_1}{\nu_2}\right)}, \tag{6.4}$$

where S_1 and S_2 are the measured flux densities at the frequencies ν_1 and ν_2. I calculated the error for α using error propagation. The spectral index between the two JVLA observations is $\alpha_{22-10GHz} = -0.68 \pm 0.34$, with a spectral shape inverted compared to the spectrum at higher frequencies (Fig. 6.1). Using this spectral index, I extrapolated a 37 GHz flux density of 0.089$\pm$0.030 mJy and combined it with the MRO detection, calculating the same flare properties I derived from the pairs of MRO detections in Tab. 6.2. In this way, I am assuming that the JVLA was not observing the

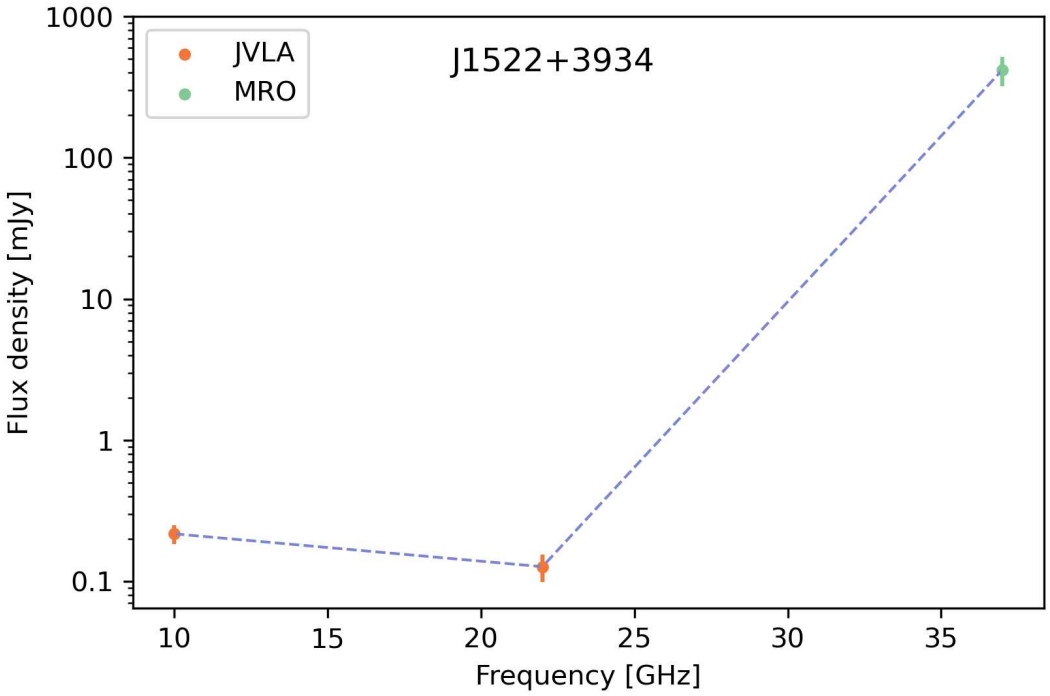

Figure 6.1: Quasi-simultaneous radio spectrum of J1522+3934. Note the very steep rise between 22 GHz and 37 GHz with $\alpha \simeq 16$. This is unphysical and indicates that the source varied between these two measurements, so they cannot be treated as simultaneous for the purposes of spectral analysis.

flare detected by MRO one day apart, but it was instead looking at the low state activity. Performing the calculations I found an e-folding time-scale of $0.12^{+0.01}_{-0.01}$ days, a variability brightness temperature of $33.68^{+14.70}_{-11.54} \times 10^{15}$ K, and a variability Doppler factor of $87.66^{+11.25}_{-11.44}$.

6.3.2 MRO-OVRO quasi-simultaneous observations

The closest observations from different telescopes are those between MRO and OVRO: MRO detected J1228+5017 on 2023.454555, and OVRO observed the source, without detecting it, on 2023.454719, namely just 1.44 hours after the MRO observation. Since OVRO did not detect the source, I can only derive upper and lower limits of the possible flare properties through its upper limit flux and assuming that the MRO detection coincides with the peak of the flare. Similarly to what I did in Sec. 6.3.1 I calculated these properties estimating the 15 GHz flux using the 37 GHz one (= 0.60 Jy). I considered different spectral shapes assuming three scenarios: $\alpha = 4$ for FFA, $\alpha = 2.5$ for SSA, and $\alpha = 0$ for a flat spectrum. The results are reported in Tab. 6.3. In this case, all the observations are performed using single-dish telescopes, removing possible biases compared to the MRO-JVLA quasi-simultaneous observations.

In the following, I summarized the results for the individual sources. The MRO detections of the sample are listed in Tab. 6.1 and visually reported in Figure 6.3.

Table 6.3: Flare properties at 15 GHz from the MRO-OVRO quasi-simultaneous observations of J1228+5017.

α	S_{upp}	S_{der}	τ	$T_{b,var}$	δ_{var}
(1)	(2)	(3)	(4)	(5)	(6)
4	0.011	0.016	$\leq$0.099	$\geq 5.41\times10^{16}$	$\geq$102.67
2.5	0.011	0.063	$\leq$0.038	$\geq 3.22\times10^{18}$	$\geq$400.70
0	0.011	0.60	$\leq$0.015	$\geq 2.30\times10^{20}$	$\geq$1662.36

Columns: (1) spectral index in Eq. 6.4; (2) upper limit flux of OVRO observation [Jy]; (3) derived flux at 15 GHz [Jy]; (4) time-scale [days]; (5) variability brightness temperature [K]; (6) variability Doppler factor.

6.3.3 J1029+5556

J1029+5556, with a redshift of 0.4511, is the farthest source in the sample. For this reason, it is the only object with a missing host galaxy classification. Varglund et al. (2022) tried to model the host galaxy morphology by means of near-infrared images obtained with the Nordic Optical Telescope without success, due to the impossibility of properly spatially resolving the object. During the investigated time, it has been detected neither by MRO nor by Effelsberg. These upper limits, coupled with the high black hole mass, suggest a source in an evolved phase of evolution, possibly with a smoother variability compared to the rest of the sample. However, it is important to note that the missing detections by MRO may also be due to the few observations focused on it.

6.3.4 J1228+5017

J1228+5017 has a detection rate at 37 GHz of 8.1%, the highest of the sample. MRO registered two consecutive detections of a flare around mid-2023 with an *e*-folding time-scale $\sim$2 days, a variability brightness temperature $\sim 19 \times 10^{14}$ K, and a variability Doppler factor $\sim$34 (Tab. 6.2). The MRO and OVRO quasi-simultaneous observations suggest a completely different scenario. By means of the calculations described in Sec. 6.3.2 and reported in Tab. 6.3, I derived a $\tau \leq 2.4$ hours, down to 22 minutes, a $T_{b,var} \geq 5.41 \times 10^{16}$ K and a $\delta_{var} \geq 102.67$. Since I used the OVRO upper limit flux in the calculations, the *e*-folding time-scale is an upper limit. Under these conditions, the two consecutive MRO detections may not be related to the same flare. No detections with the Effelsberg and IRAM telescopes are present in the investigated period.

6.3.5 J1232+4957

As in the case of J1029+5556, this source has not been detected by MRO between June 2022 and December 2023. However, also for this source, the low number of observations might have led to the zero detection rate. It has been classified in Sec. 5 as blue outlier (Marziani et al., 2003; Komossa et al., 2008; Berton et al., 2016b; Schmidt et al., 2018), namely the wing component of the [O III] emission lines has a blueshift $>$250 km s^{-1}. The origin could be due to a jet interacting with the narrow-line region as they correlate with the radio emission (Berton et al., 2021; Dalla Barba et al., 2025), but also due to winds produced by strong radiation pressure-driven outflows in a

high-Eddington source (Komossa et al., 2008; Marziani et al., 2016). Crepaldi et al. (2025) stated that this source is likely produced by the second hypothesis, since it has the second-highest Eddington ratio in the sample (∼0.27). The absence of flare detections for a long time might be in agreement with that hypothesis. Indeed, the jet may have greatly decreased its power or even turned off. No detections with the Effelsberg telescope are present in this case in the investigated period.

6.3.6 J1509+6137

J1509+6137 was the source with the highest MRO detection rate in Järvelä et al. (2024), equal to 25.3%, with flares exceeding 1 Jy of amplitude. In my case, it has been detected 4.4% of the time, sometimes with a flux density at the Jy level. During the investigated time, it showed the highest flux density detections compared to the rest of the sample. Unfortunately, two consecutive detections have comparable amplitudes considering the error bars, so they are not usable for a flare properties analysis. However, what has been found here and in previous studies confirms the intriguing nature of this source. The Effelsberg telescope did not detect this source in any of the three epochs. At first glance, J1509+6137 was detected at $\sim 7\sigma$ by the IRAM telescope at 260 GHz, with a peak flux density of 7.62±0.56 mJy/beam. It is undetected at 150 GHz, but the upper limit at this frequency is 0.75 mJy/beam. Nevertheless, a deep analysis of the radio map revealed that the actual detection occurred at an angular distance of ∼27.62 arcsec with respect to the AGN coordinates (Fig. 6.2). Assuming that this event is at the same redshift as J1509+6137, the spatial distance is ∼92.25 kpc, well outside the host galaxy. Searching in several catalogs (like Pan-STARRS, ASAS-SN, and ZTF), no signs of a possible source are present in the location of the event, neither in optical nor in radio.

6.3.7 J1510+5547

Even if the MRO detection rate is not so high, 4.8%, two detections of J1510+5547 in mid-2022 respect the constraints to be related to a single flare episode. The results I found are comparable to the ones obtained for the J1228+5017 flare. Also in this case, the *e*-folding time-scale is ∼2 days, the variability brightness temperature is $\sim 17 \times 10^{14}$ K, and the variability Doppler factor is ∼33 (Tab. 6.2). No detections with the Effelsberg and the IRAM telescopes are present in the investigated period.

6.3.8 J1522+3934

J1522+3934, with a redshift of 0.0769, is the closest source in the sample, and the one with the lowest black hole mass, suggesting an NLS1 in the first phases of evolution. The MRO detection rate is 3.1%, and as described before, a dedicated monitoring with the JVLA has been carried out. Along all the monitoring programme, neither large amplitude variabilities nor 10-22 GHz spectral index variations have been measured (Fig. 6.7). It is important to notice that the flux density remains constant regardless of the antennas' configurations (Tab. 6.4). This suggests that the resold-out structures do not contribute significantly to the measured flux density. As described in Sec. 6.3.1, the detected flare by MRO did not influence the JVLA observations at 10 and 22 GHz taken one day apart, which is comparable with the *e*-folding time-scales derived in Tab. 6.3. Also in this case no Effelsberg and IRAM detections are present.

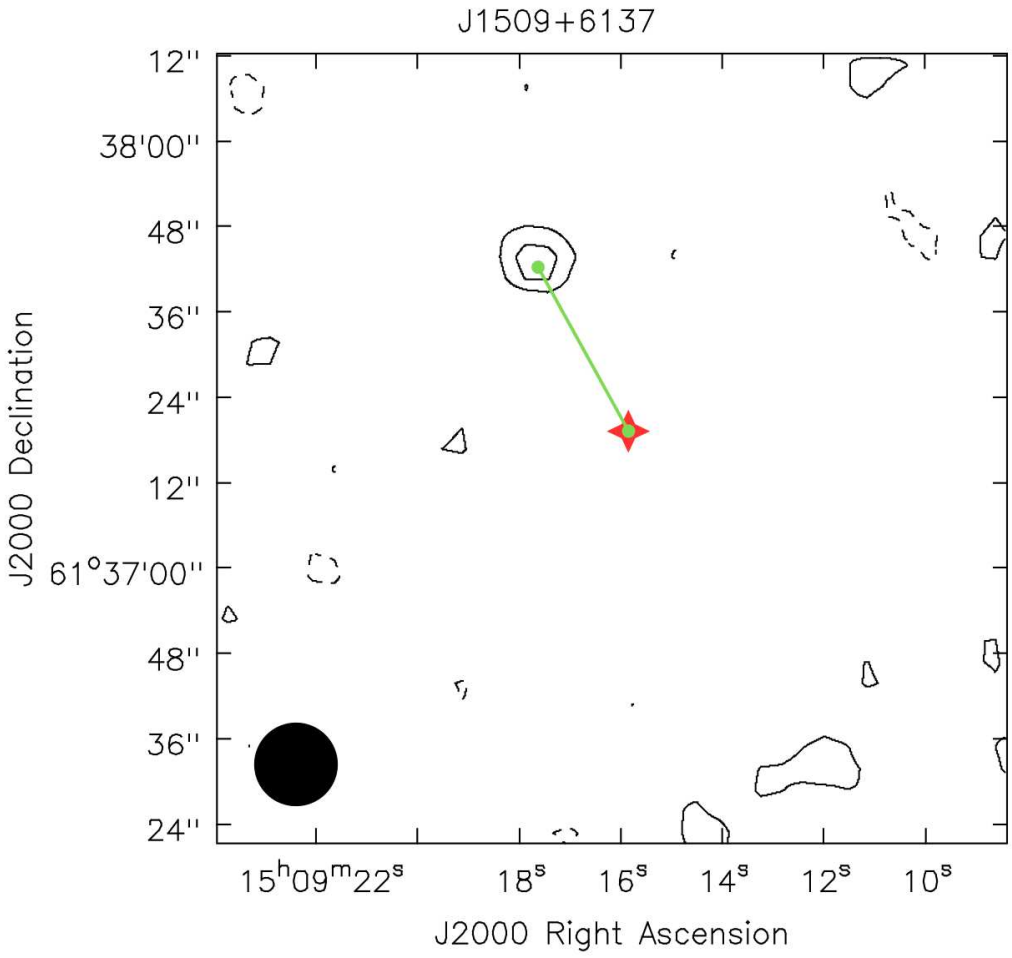

Figure 6.2: IRAM radio map at 260 GHz of J1509+6137. The contours are related to the uncatalogued source, while the red symbol is located in the actual position of J1509+6137.

6.3.9 J1641+3454

Even if J1641+3454 is the most observed source, with 276 observations in the investigated period by MRO, it has been detected only once with a flux density of 0.50 ± 0.11 Jy. Indeed, the few detections found here and in past works, usually at sub-Jy levels, indicate a modest activity. Interestingly Romano et al. (2023) observed a brightening in X-ray soon after an MRO-detected flare, suggesting a connection between radio and X-ray. No detections with the Effelsberg and the IRAM telescopes are present.

6.4 Discussion

The interpretation of the measured flare properties can be attributed to either a short time-scale of the flare episode or an extremely narrow frequency range of emission. The estimated time-scale from the closest MRO-JVLA observations is $\sim$ 0.12 days, while the one from the closest MRO-OVRO observations is between 0.015 and 0.099 days. In both cases, only MRO detected the sources with a flux level well above the median value. Considering the estimated brightness temperatures $T_{b,var} > 10^{16}$, such a rapid variability might be explained through inverse Compton catastrophe events (Longair, 2011; Beckmann and Shrader, 2012). In a typical region composed of electrons immersed in a magnetic field, the energy of the electrons is partially converted into incoherent synchrotron radiation. If $T_{b,var} > 10^{12}$, the intense radiation field produced is so high that the low-energy radio photons are up-scattered to X-ray and γ-rays, via multiple IC, by the same relativistic electrons. The result is a great energy loss by the electrons and an intense brightening in radio and high-energy bands. Since this is a sort of cascade process, the time-scale of the event is extremely short. Such an event can take place only in extreme regions, with a high density of electrons, like in AGN or X-ray binaries for instance. Once the electrons have lost all their energy, the inverse Compton catastrophe cannot occur again unless there is a source of energy that re-charges them. The magnetic reconnection can provide the necessary energy in the region where the flare takes place. Indeed, the break and reconnection of the magnetic field lines convert magnetic energy into kinetic energy for the electrons. Even if this scenario is physically possible, an inverse Compton catastrophe has never been recorded. Some sources slightly exceeding the brightness temperature limit have been seen, but the short variability time-scale and the high brightness temperature were due to the beamed radiation emitted by a region with a relativistic bulk motion. For relativistic velocities, the Lorentz factor can be $\gg 1$, and since $t_{var} = \gamma\tau$, the variability time-scale in the source frame can be much longer compared to the measured one (Frank, King, and Raine, 2002). However, Lorentz factors of the order of $10^2 - 10^3$ are necessary to explain the variability time-scales and brightness temperatures I estimated, which is quite unrealistic.

Assuming that the flare emission has a narrow frequency range, it would be detected only at a specific frequency regardless of the time-scale of the event. The only telescope that detected multiple times the same sources in a short time range is MRO at 37 GHz. As shown in Tab. 6.2, the measured time-scale is of a few days on average. The brightness temperature is still above the inverse Compton catastrophe limit, even though not as extreme as in the estimations from MRO-JVLA and MRO-OVRO observations. Nevertheless, high values of brightness temperature and a narrow frequency range of emission are the characteristics of coherent emission (Lyutikov, 2021). There are a few mechanisms that produce coherent emission, which are still under investigation (Melrose, 2017). From a physical point of view, coherent

emission refers to the process where many radiating particles, like electrons, emit radiation with a fixed phase relationship. Because the emitted electromagnetic waves are phase-correlated, their electric fields add constructively, leading to an intensity that scales as the square of the number of emitters, instead of linearly as for incoherent emission. This phase correlation is induced by a strong magnetic field, and the rotationally driven paradigm has been first suggested (Ruderman and Sutherland, 1975; Fawley, Arons, and Scharlemann, 1977; Arons and Scharlemann, 1979; Hibschman and Arons, 2001). Here, the rotating magnetic field generates parallel electric fields that accelerate charged particles with an unstable distribution function, eventually leading to the production of coherent emission. Recently, Lyutikov (2021) suggested that the coherent radio emission is reconnection-driven instead of rotationally driven. Magnetic reconnection has been suggested as the source of coherent emission in radio pulsars (Istomin, 2004), magnetars (Lyutikov, 2002; Lyutikov, 2006), and fast radio bursts (Popov and Postnov, 2013; Lyutikov, 2017; Lyubarsky, 2020; Lyutikov and Popov, 2020), and it might be the source also in the analyzed case here. All the described scenarios have never been observed in an astrophysical sources, precluding any possible comparison. Therefore, only with these knowledge. it is not possible to understand if NLS1s might be more suitable for this kind of events compared to other AGN classes or not.

6.5 Conclusions

In this work I estimated the flares' properties at radio frequencies using close observations in time from multiple telescopes of a sample of six NLS1s and one intermediate Seyfert galaxy. Due to the few detections, I managed to calculate the flares' properties only for some sources. In particular, for J1228+5017 and J1510+5547 at 37 GHz with MRO detections, for J1522+3934 at 37 GHz with MRO-JVLA observations, and for J1228+5017 at 15 GHz with MRO-OVRO observations. The results showed very short *e*-folding time-scale, from a couple of days down to $\sim$20 minutes, extremely high variability brightness temperatures $>10^{15}$ K, as well as for the variability Doppler factors, from $\sim$30 up to more than 10^3. Considering these results, the magnetic reconnection hypothesis in the SMBH magnetosphere suggested in Järvelä et al. (2024) seems to be the most suitable. As described in Sec. 6.4, magnetic reconnection should be coupled with either an inverse Compton catastrophe or a coherent emission. None of these last two phenomena has ever been observed in AGN, making a comparison with other sources not possible. To better constrain both hypotheses, follow-up observations are fundamental. An inverse Compton catastrophe implies a fast and extremely intense emission at multiple frequencies in radio, followed by an intense brightening at high energies. Triggered observations at different radio frequencies soon after a radio detection would help to estimate more precisely the *e*-folding time-scale of the flare. Moreover, the detection of a correlated X-ray emission, similarly to what has been measured by Romano et al. (2023), would strongly support this hypothesis. If multi-frequency radio observations did not detect a flare shortly after a detection at a specific radio frequency, the coherent emission scenario would be more plausible. The narrow bandwidth of the emission in this case makes the observations of a flare episode more challenging. Indeed, after having discovered the emission frequency, multiple short-cadence observations at that frequency are the only way to investigate the flare properties. In my case, MRO was the only one to detect 37 GHz multiple flare episodes so far. Therefore, assuming true the coherent emission hypothesis, quick repeated observations at 37 GHz

are the right approach. Since a new 37 GHz receiver will be mounted at MRO soon, the next years will be fundamental to further investigate the cited hypothesis.

6.6 Appendix: lists and light curves of observations

Table 6.4: J1522+3934 JVLA observations.

Config.	Date	S^X_{peak}	rms^X	S^K_{peak}	rms^K
(1)	(2)	(3)	(4)	(5)	(6)
B	2023.051068	0.212±0.056	0.016	0.106±0.031	0.025
B	2023.081183	0.256±0.024	0.019	0.183±0.025	0.019
B	2023.100421	0.244±0.036	0.019	0.202±0.021	0.021
B	2023.127560	0.247±0.030	0.020	0.135±0.025	0.029
B	2023.135935	0.207±0.046	0.018	0.154±0.041	0.026
B	2023.239114	0.223±0.051	0.018	0.150±0.035	0.024
B	2023.247964	0.227±0.051	0.018	0.187±0.047	0.023
B	2023.286076	0.236±0.056	0.020	0.160±0.028	0.022
B	2023.288046	0.247±0.049	0.021	–	0.024
B	2023.299853	0.220±0.043	0.018	0.176±0.034	0.022
B	2023.307177	0.269±0.036	0.019	0.148±0.038	0.026
B	2023.316061	0.246±0.063	0.018	0.144±0.023	0.022
B	2023.321083	0.246±0.053	0.021	0.173±0.039	0.023
B	2023.329256	0.223±0.043	0.018	0.202±0.043	0.026
B	2023.335201	0.214±0.037	0.024	0.176±0.039	0.026
B	2023.342950	0.224±0.060	0.020	0.201±0.050	0.022
B	2023.343446	0.259±0.066	0.019	0.172±0.038	0.021
B	2023.351714	0.223±0.058	0.018	0.149±0.037	0.022
B	2023.359194	0.269±0.089	0.018	0.162±0.045	0.023
B	2023.362529	0.230±0.055	0.018	0.142±0.028	0.024
B	2023.370724	0.241±0.059	0.019	0.117±0.030	0.029
B	2023.383686	0.259±0.078	0.019	0.093±0.020	0.033
B	2023.389912	0.213±0.062	0.021	0.155±0.045	0.023
B	2023.398170	0.252±0.071	0.019	0.182±0.050	0.022
B	2023.405577	0.291±0.088	0.019	0.136±0.024	0.026
B	2023.409063	0.224±0.073	0.022	0.162±0.039	0.024
BnA	2023.417212	0.207±0.041	0.017	0.148±0.044	0.024
BnA	2023.427586	0.217±0.034	0.016	0.127±0.028	0.026
BnA	2023.449970	0.217±0.053	0.017	0.144±0.024	0.021
A	2023.592115	0.209±0.062	0.016	0.086±0.032	0.026
A	2023.613974	0.205±0.037	0.016	0.122±0.043	0.030
A	2023.622117	0.180±0.038	0.015	0.095±0.026	0.029
A	2023.654333	0.199±0.042	0.017	–	0.034
A	2023.665981	0.234±0.061	0.015	–	0.024
A	2023.728652	0.181±0.059	0.015	0.164±0.050	0.028
A	2023.739722	0.196±0.045	0.015	0.126±0.032	0.024
A	2023.744334	0.177±0.023	0.015	–	0.031

Columns: (1) telescope array configuration; (2) time of the observation [decimal year]; (3) peak flux density and its error [mJy/beam] in X band; (4) rms level of the observation [mJy/beam] in X band; (5) peak flux density and its error [mJy/beam] in K band; (6) rms level of the observation [mJy/beam] in K band.

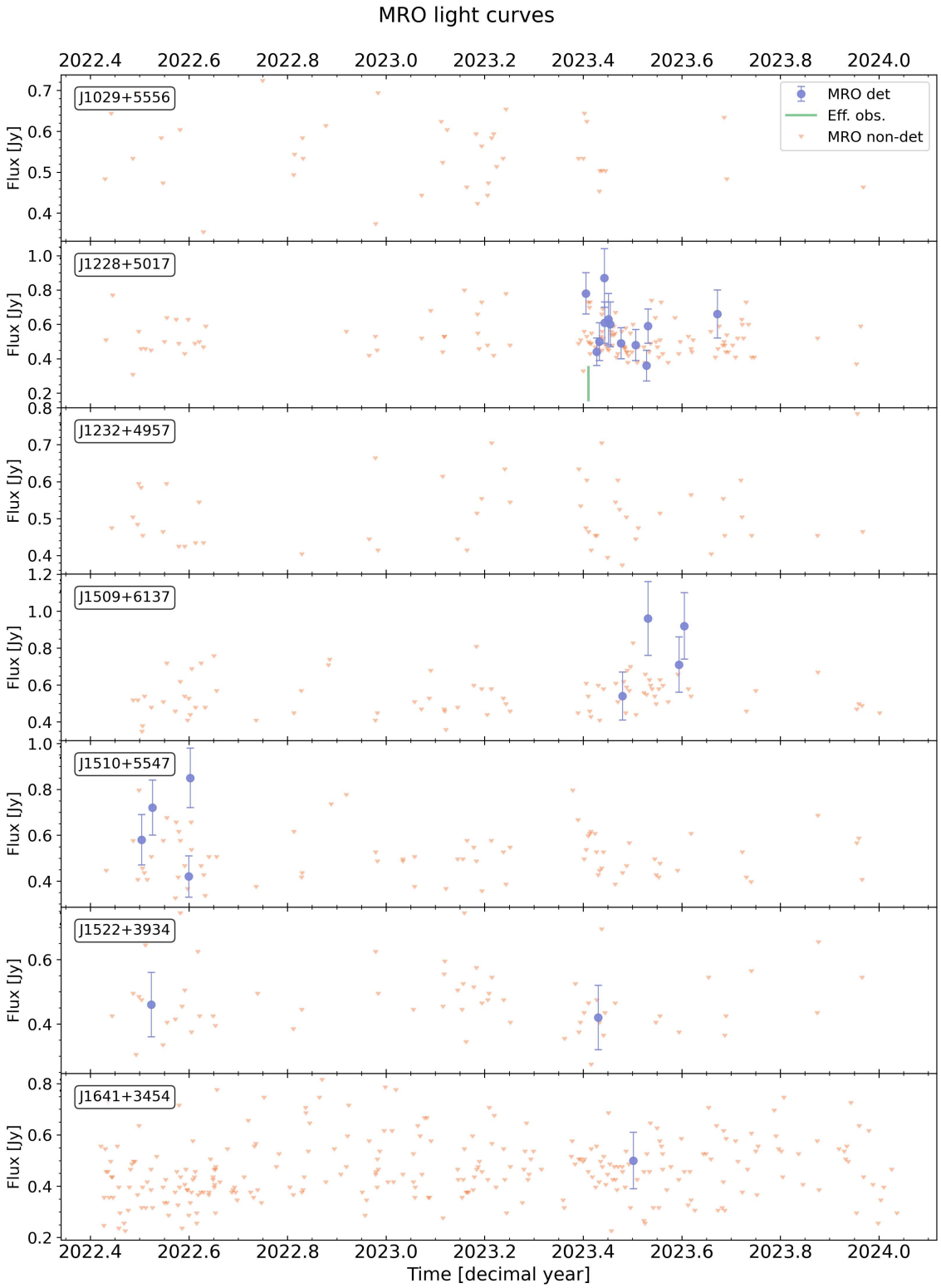

Figure 6.3: MRO light curves of the sample between June 2022 and January 2024. The blue dots are detections, with the relative flux densities and errors. The orange triangles are the upper limits of non-detections. The green line is related to the date of Effelsberg epoch 3 observations, with an arbitrary flux.

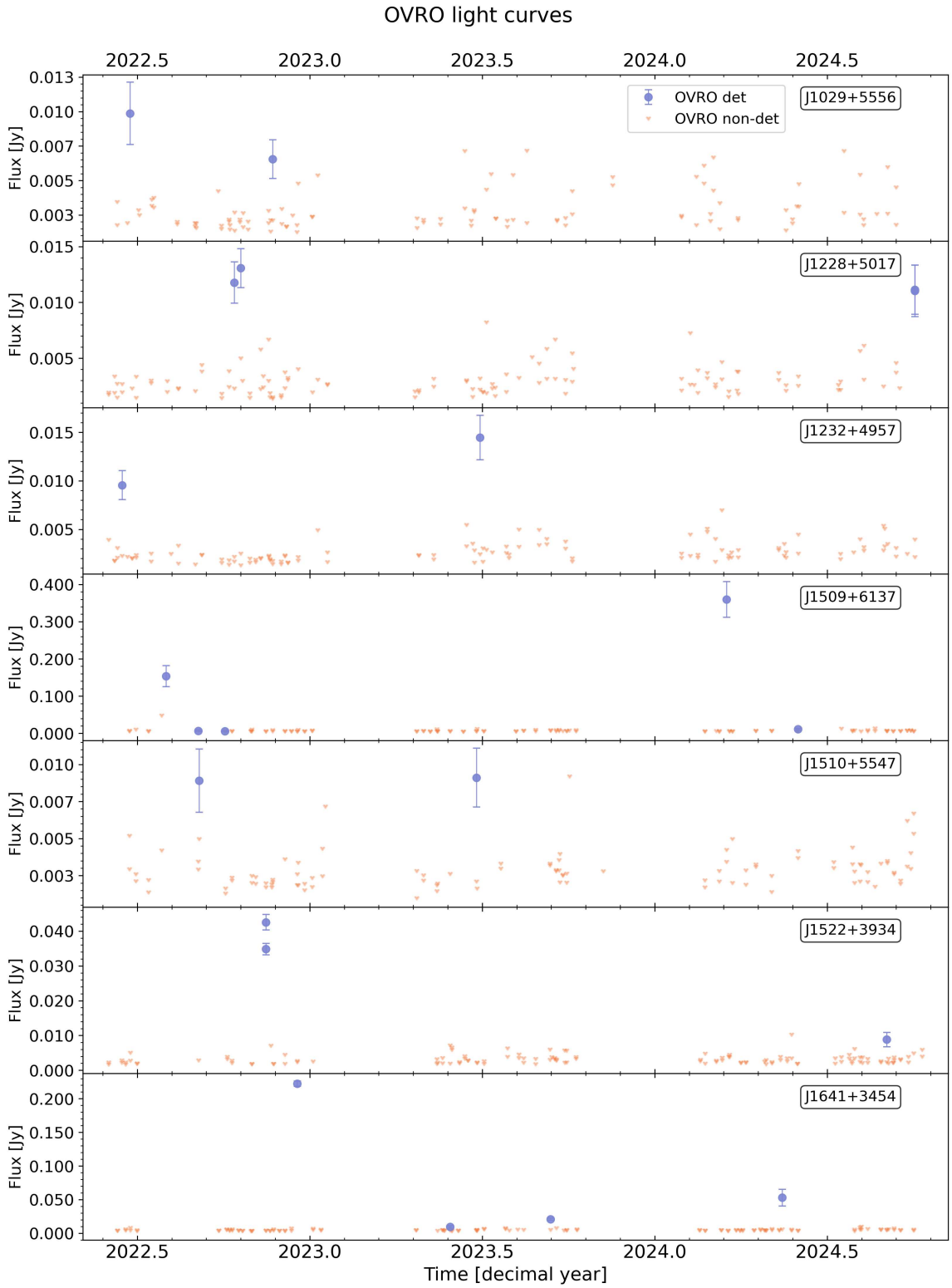

Figure 6.4: OVRO light curves of the sample between June 2022 and October 2024. The blue dots are detections, with the relative flux densities and errors, while the orange triangles are the upper limits of non-detections. The error bars that are not visible, due to their small values, are within the size of the dots.

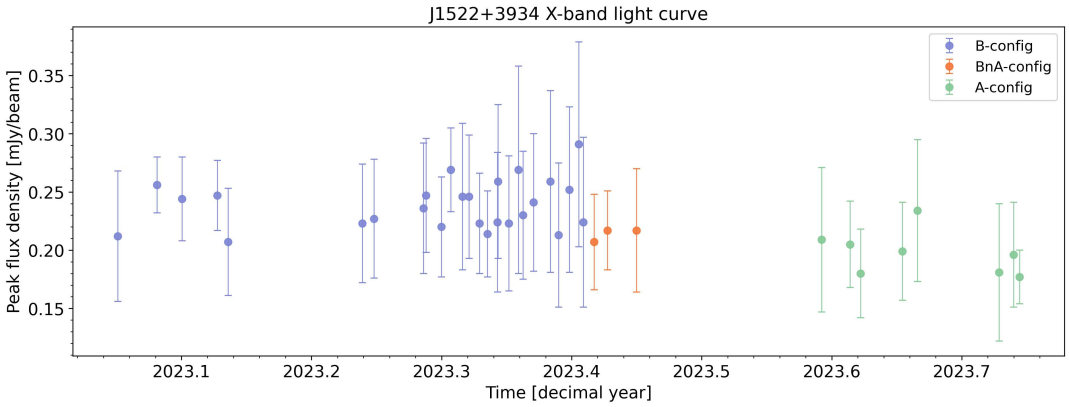

Figure 6.5: J1522+3934 light curve of JVLA X-band observations.

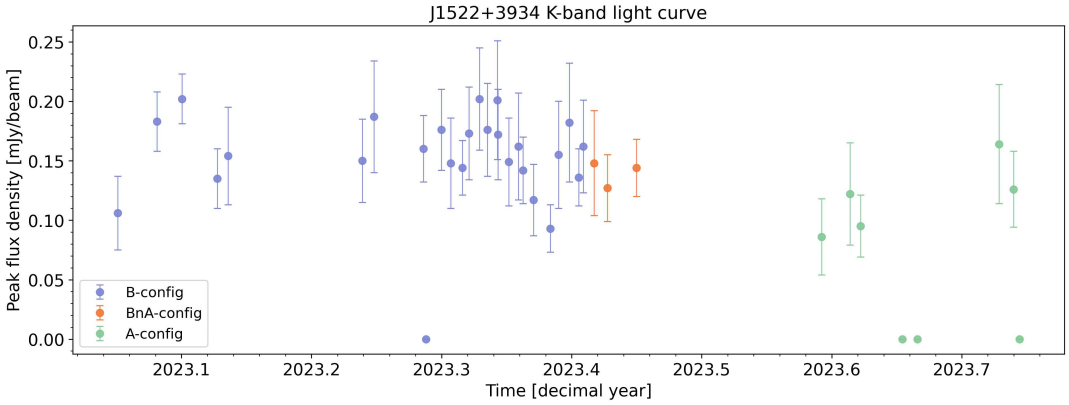

Figure 6.6: J1522+3934 light curve of JVLA K-band observations. The dots at the bottom are related to non-detections.

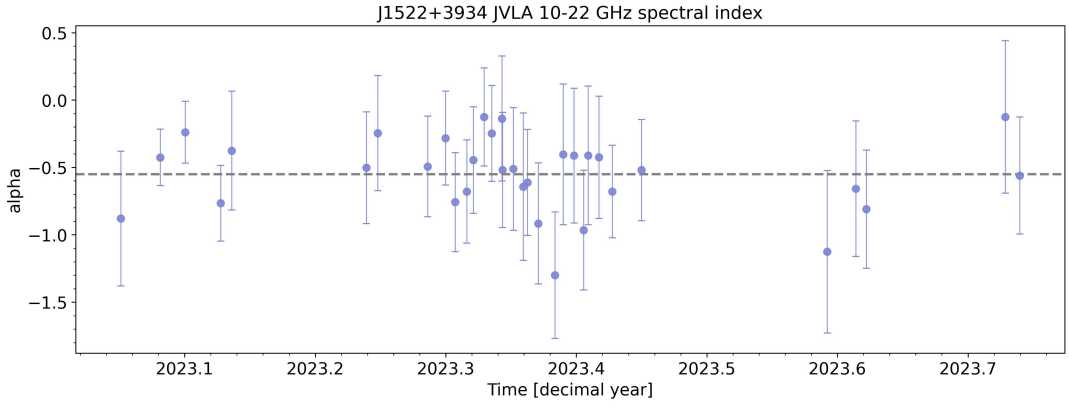

Figure 6.7: 10-22 GHz spectral index for the J1522+3934 JVLA observations. The grey dashed line represents the mean value.

Table 6.5: OVRO detections.

Source	Date	S
(1)	(2)	(3)
J1029+5556	2022.479144	0.01±0.002
	2022.892543	0.007±0.001
J1228+5017	2022.780789	0.012±0.002
	2022.799807	0.013±0.002
	2024.754022	0.011±0.002
	2024.754025	0.011±0.002
J1232+4957	2022.455644	0.010±0.001
	2023.493042	0.014±0.002
J1509+6137	2022.583406	0.154±0.028
	2022.677108	0.007±0.002
	2022.753641	0.006±0.001
	2024.208494	0.360±0.048
	2024.415663	0.011±0.003
J1510+5547	2022.679043	0.009±0.002
	2023.483077	0.009±0.002
J1522+3934	2022.873085	0.043±0.002
	2022.873087	0.035±0.002
	2024.672553	0.009±0.002
J1641+3454	2022.964080	0.222±0.004
	2023.406719	0.009±0.002
	2023.698411	0.021±0.002
	2024.369413	0.053±0.012

Columns: (1) source; (2) time of the observation [decimal year]; (3) flux density and its error [Jy].

Table 6.6: Effelsberg observations.

Source	Receiver	Freq.	Date	rms
(1)	(2)	(3)	(4)	(5)
		Epoch 1		
J1232+4957	S45	4.8	2021.956525	1.6
	S45	5.3	2021.956525	2.6
	S45	6.7	2021.956525	5.8
	S45	6.8	2021.956525	4.2
	S28	10.45	2021.956580	1.8
	S14	19.3	2021.956621	6.9
	S14	21.2	2021.956621	10.2
	S14	23.0	2021.956621	26.3
	S14	24.8	2021.956621	12.5
	S7	35.8	2021.956682	33.9
	S7	38.3	2021.956682	38.9
J1522+3934	S45	4.8	2021.956775	1.6
	S45	5.3	2021.956775	259.3
	S45	6.7	2021.956775	4.0
	S45	6.8	2021.956775	5.4
	S28	10.45	2021.956817	1.6
	S14	19.3	2021.956862	8.0
	S14	21.2	2021.956862	7.1
	S14	23.0	2021.956862	24.5
	S14	24.8	2021.956862	5.3
	S7	35.8	2021.956911	31.3
	S7	38.3	2021.956911	41.9
J1641+3454	S45	4.8	2021.957009	1.9
	S45	5.3	2021.957009	58.6
	S45	6.7	2021.957009	8.4
	S45	6.8	2021.957009	5.2
	S28	10.45	2021.957048	1.8
	S14	19.3	2021.957087	4.8
	S14	21.2	2021.957087	5.7
	S14	23.0	2021.957087	27.6
	S14	24.8	2021.957087	6.0
	S7	35.8	2021.957125	35.2
	S7	38.3	2021.957125	36.4
		Epoch 2		
J1029+5556	S45	4.8	2022.300494	1.9
	S45	5.3	2022.300494	3.5
	S45	6.7	2022.300494	14.2
	S45	6.8	2022.300494	5.2
	S28	10.45	2022.300538	1.7
	S14	19.3	2022.300585	6.9
	S14	21.2	2022.300585	5.8
	S14	23.0	2022.300585	17.5
	S14	24.8	2022.300585	5.3
	S7	35.8	2022.300632	35.4
	S7	38.3	2022.300632	36.4

Table 6.7: Effelsberg observations - *continued*

Source	Receiver	Freq.	Date	rms
(1)	(2)	(3)	(4)	(5)
J1232+4957	S45	4.8	2022.300684	1.9
	S45	5.3	2022.300684	28.1
	S45	6.7	2022.300684	6.4
	S45	6.8	2022.300684	3.4
	S28	10.45	2022.300727	1.7
	S14	19.3	2022.300769	5.6
	S14	21.2	2022.300769	5.2
	S14	23.0	2022.300769	16.1
	S14	24.8	2022.300769	5.1
	S7	35.8	2022.300811	35.2
	S7	38.3	2022.300811	39.0
J1228+5017	S45	4.8	2022.300853	1.9
	S45	5.3	2022.300853	8.5
	S45	6.7	2022.300853	13.9
	S45	6.8	2022.300853	5.1
	S28	10.45	2022.300895	1.7
	S14	19.3	2022.300938	5.5
	S14	21.2	2022.300938	5.1
	S14	23.0	2022.300938	15.0
	S14	24.8	2022.300938	4.8
	S7	35.8	2022.300982	31.8
	S7	38.3	2022.300982	34.0
J1522+3934	S45	4.8	2022.301100	1.8
	S45	5.3	2022.301100	3.4
	S45	6.7	2022.301100	9.6
	S45	6.8	2022.301100	3.6
	S28	10.45	2022.301142	1.7
	S14	19.3	2022.301185	6.9
	S14	21.2	2022.301185	6.1
	S14	23.0	2022.301185	16.5
	S14	24.8	2022.301185	5.8
	S7	35.8	2022.301227	29.8
	S7	38.3	2022.301227	32.9
J1641+3454	S45	4.8	2022.301268	1.6
	S45	5.3	2022.301268	1.9
	S45	6.7	2022.301268	10.1
	S45	6.8	2022.301268	3.4
	S28	10.45	2022.301307	1.6
	S14	19.3	2022.301347	7.1
	S14	21.2	2022.301347	5.9
	S14	23.0	2022.301347	16.3
	S14	24.8	2022.301347	5.0
	S7	35.8	2022.301387	29.4
	S7	38.3	2022.301387	34.1
J1509+6137	S45	4.8	2022.301479	2.3
	S45	5.3	2022.301479	5.9
	S45	6.7	2022.301479	18.0
	S45	6.8	2022.301479	5.9
	S28	10.45	2022.301511	2.2
	S7	35.8	2022.301529	52.8
	S7	38.3	2022.301529	55.0

Table 6.8: Effelsberg observations - *continued*

Source	Receiver	Freq.	Date	rms
(1)	(2)	(3)	(4)	(5)
		Epoch 3		
J1228+5017	S45	4.8	2023.412477	6.3
	S45	4.8	2023.412477	2.5
	S45	5.3	2023.412477	9.0
	S45	6.7	2023.412477	13.6
	S45	6.7	2023.412477	3.3
	S45	6.8	2023.412477	9.1
	S45	4.8	2023.412481	8.8
	S45	4.8	2023.412481	3.9
	S28	10.45	2023.412498	2.5
	S14	21.2	2023.412538	7.3
	S14	23.0	2023.412538	13.3
	S14	24.8	2023.412538	14.9
	S7	35.8	2023.412554	46.0
	S7	38.3	2023.412554	53.4
	S20	14.3	2023.413453	1.5
	S20	14.3	2023.413453	1.8
	S20	16.8	2023.413453	4.0
	S20	16.8	2023.413453	1.7
	S20	16.8	2023.415318	4.6

Columns: (1) source; (2) receiver; (3) frequency [GHz]; (4) time of the observation [decimal year]; (5) rms [mJy].

Chapter 7

Conclusions

The common thread of the single works' goals in this thesis is the study of peculiar NLS1s with radio behavior never seen before, demonstrating once again the importance of NLS1s as natural astrophysical laboratories for different phenomena. Given the uniqueness of the flaring events shown by the sample, characterizing their origin and properties proved very challenging. Therefore, the present work is the starting point of a long road. I decided to perform a variety of analyses in optical and radio regimes, trying to add step-by-step more constraints on the most plausible hypotheses presented recently (Järvelä et al., 2024). As I described in Sec. 2.3, the three main viable hypotheses are: jet-cloud/star interaction, relativistic jet and FFA with moving clouds, and magnetic reconnection. I performed two works at optical wavelengths. In the first one, I investigated time-series in multiple bands in a window of $\sim$10 years, performing a variability and a periodicity analysis. In the second one, I analyzed the optical spectra of the seven currently known sources, deriving their main physical properties by means of the detected emission lines. In the radio regime, I focused on the flares randomly observed in the sample. Here, I estimated the main flares' properties using all the available radio data of the last three years, both from single-dish telescopes and interferometers.

The two optical works I carried out had the aim to investigate possible peculiarities and similarities among the sources in the sample, and to search for the optical counterpart of the radio flare episodes. This last did not bring any relevant results, since neither in the time-series analysis nor in the spectra analysis were present traits coming from the flares. On average, the stochastic variability measured as well as the PSD shape had typical values for this class of AGN. The same conclusions were drawn from the spectral analysis. One source revealed to be an intermediate Seyfert, however, this and the other six NLS1s showed behaviors fully aligned with their respective classes. I can conclude that the extreme phenomena seen in radio are likely not related to the general properties of the sources, but more to specific circumstances that arise close to the nucleus, given the timescale. It is interesting to notice that the seven sources analyzed here were part of a larger sample of NLS1s, which was selected by MRO following defined criteria. Also other sources not included in the first sample might show the peculiar radio behaviors of this sample, also not necessarily classified as NLS1s. However, since the results of the optical analyses did not reveal deviations from the typical characteristics of the NLS1s class, the optical band is certainly not suitable for selecting new candidates. The radio work led to more interesting results. Indeed, even though only MRO detected the high state activity in a few cases, the estimation I carried out showed flares with extremely short time-scales, down to a few tens of minutes, and high variability brightness temperatures $>10^{15}$ K. Flux variations such rapid must come from very small regions and have to be related to very powerful phenomena.

Considering the results, I found the magnetic reconnection seems to be the most

likely hypothesis among those described. Since there is no strong evidence for the presence of relativistic jets, the magnetic reconnection in the black hole magnetosphere is preferred compared to the jet-in-jet one. In that case, the reconnection of the magnetic field lines of the SMBH converts magnetic energy into kinetic energy that is gained by the surrounding particles. If the particles are free electrons, considering the high variability brightness temperature estimated, either an inverse Compton catastrophe or a coherent emission might be the actual process that produces the flare emission with the measured behaviors. An inverse Compton catastrophe generates an intense emission at multiple frequencies in radio, followed by a brightening at high energies similar to what has been detected by Romano et al. (2023). On the other hand, the narrow emission bandwidth of a coherent emission might explain why the flares are detected only at 37 GHz by MRO. Neither phenomenon has ever been seen in AGN, making the study very interesting and challenging at the same time.

If the magnetic reconnection coupled with either inverse Compton catastrophe or coherent emission were confirmed, it would be a discovery with groundbreaking implication, since such a scenario has basically never been seen in an astrophysical source. To this aim, non-trivial efforts must be made, especially from the observational point of view. To reduce the uncertainties in the *e*-folding time-scale measurements, triggered observations able to detect the same flare events are necessary, both in a specific and in multiple frequencies. With an estimated time-scale of even less than an hour, such a goal is very challenging. It can be done with a tight collaboration between MRO, for which the monitoring of the sample is still ongoing, and other single-dish antennas, like the Sardinia Radio Telescope, OVRO, and Effelsberg, for instance. Moreover, multiple close and rapid monitoring of the same source with the same telescope will be possible soon at MRO with the installation of the new 37 GHz receiver. Triggered observations would also be fundamental in X-ray, to better investigate a possible brightening at high energies connected to the radio emission. All these efforts are necessary not only to disentangle between the two possible scenarios, but also to open up new possible hypotheses which might lead closer to the understanding of this singular and extreme phenomenon. The analyses presented in this thesis could be taken as reference and applied to eventual new candidates similar to those studied here. Enlarging in this way the knowledge of a possible new class of AGN. New facilities like the incoming Large Synoptic Survey Telescope at the Vera C. Rubin Observatory, with long lasting monitoring projects, might be extremely useful on the selection and monitoring of new candidates.

References

Abdo, A. A. et al. (July 2009a). "Fermi/Large Area Telescope Discovery of Gamma-Ray Emission from a Relativistic Jet in the Narrow-Line Quasar PMN J0948+0022". In: 699, pp. 976–984. DOI: 10.1088/0004-637X/699/2/976. arXiv: 0905.4558 [astro-ph.HE].

Abdo, A. A. et al. (Dec. 2009b). "Multiwavelength Monitoring of the Enigmatic Narrow-Line Seyfert 1 PMN J0948+0022 in 2009 March-July". In: 707, pp. 727–737. DOI: 10.1088/0004-637X/707/1/727. arXiv: 0910.4540 [astro-ph.HE].

Abramowicz, M. A. et al. (Sept. 1988). "Slim Accretion Disks". In: 332, p. 646. DOI: 10.1086/166683.

Abramowicz, Marek A. and P. Chris Fragile (Jan. 2013). "Foundations of Black Hole Accretion Disk Theory". In: *Living Reviews in Relativity* 16.1, 1, p. 1. DOI: 10.12942/lrr-2013-1. arXiv: 1104.5499 [astro-ph.HE].

Abramowicz, Marek A. et al. (July 2004). "The Importance of Discovering a 3:2 Twin-Peak Quasi-periodic Oscillation in an Ultraluminous X-Ray Source, or How to Solve the Puzzle of Intermediate-Mass Black Holes". In: 609.2, pp. L63–L65. DOI: 10.1086/422810. arXiv: astro-ph/0402012 [astro-ph].

Ackermann, M. et al. (Sept. 2015). "The Third Catalog of Active Galactic Nuclei Detected by the Fermi Large Area Telescope". In: 810, 14, p. 14. DOI: 10.1088/0004-637X/810/1/14. arXiv: 1501.06054 [astro-ph.HE].

Ahn, S. and J. A. Fessler (July 2003). *Standard errors of mean, variance, and standard deviation estimators*. Tech. rep. 413. Univ. of Michigan, Ann Arbor, MI, 48109-2122: Comm. and Sign. Proc. Lab., Dept. of EECS. URL: http://web.eecs.umich.edu/~fessler/papers/files/tr/stderr.pdf.

Akylas, A., I. Papadakis, and A. Georgakakis (Oct. 2022). "Black hole mass estimation using X-ray variability measurements in Seyfert galaxies". In: 666, A127, A127. DOI: 10.1051/0004-6361/202244162. arXiv: 2208.12490 [astro-ph.HE].

Aleksić, J. et al. (Apr. 2015). "The 2009 multiwavelength campaign on Mrk 421: Variability and correlation studies". In: 576, A126, A126. DOI: 10.1051/0004-6361/201424216. arXiv: 1502.02650 [astro-ph.HE].

Alfvén, H. and N. Herlofson (June 1950). "Cosmic Radiation and Radio Stars". In: *Physical Review* 78.5, pp. 616–616. DOI: 10.1103/PhysRev.78.616.

Almeida, Andrés et al. (Aug. 2023). "The Eighteenth Data Release of the Sloan Digital Sky Surveys: Targeting and First Spectra from SDSS-V". In: 267.2, 44, p. 44. DOI: 10.3847/1538-4365/acda98. arXiv: 2301.07688 [astro-ph.GA].

Alston, W. N. et al. (Nov. 2014). "Detection of a QPO in five XMM-Newton observations of RE J1034+396." In: 445, pp. L16–L20. DOI: 10.1093/mnrasl/slu127. arXiv: 1407.7657 [astro-ph.HE].

Angelakis, E. et al. (Mar. 2015). "Radio jet emission from GeV-emitting narrow-line Seyfert 1 galaxies". In: 575, A55, A55. DOI: 10.1051/0004-6361/201425081. arXiv: 1501.02158 [astro-ph.HE].

Antonucci, R. (1993). "Unified models for active galactic nuclei and quasars". In: *ARA&A* 31, pp. 473–521. DOI: 10.1146/annurev.aa.31.090193.002353.

Antonucci, R. R. J. and J. S. Miller (Oct. 1985). "Spectropolarimetry and the nature of NGC 1068". In: 297, pp. 621–632. DOI: 10.1086/163559.

Antonucci, Robert and Richard Barvainis (1988). "Excess 2 Centimeter Emission: A New Continuum Component in the Spectra of Radio-quiet Quasars". In: 332, p. L13. DOI: 10.1086/185256.

Arnaud, K. A. et al. (Nov. 1985). "EXOSAT observations of a strong soft X-ray excess in MKN 841." In: 217, pp. 105–113. DOI: 10.1093/mnras/217.1.105.

Arons, J. and E. T. Scharlemann (Aug. 1979). "Pair formation above pulsar polar caps: structure of the low altitude acceleration zone." In: 231, pp. 854–879. DOI: 10.1086/157250.

Baars, J. W. M. et al. (Oct. 1977). "Reprint of 1977A&A....61...99B. The absolute spectrum of Cas A; an accurate flux density scale and a set of secondary calibrators." In: 500, pp. 135–142.

Bade, N., S. Komossa, and M. Dahlem (May 1996). "Detection of an extremely soft X-ray outburst in the HII-like nucleus of NGC 5905." In: 309, pp. L35–L38.

Bagchi, Joydeep et al. (June 2014). "Megaparsec Relativistic Jets Launched from an Accreting Supermassive Black Hole in an Extreme Spiral Galaxy". In: 788.2, 174, p. 174. DOI: 10.1088/0004-637X/788/2/174. arXiv: 1404.6889 [astro-ph.GA].

Bahcall, John N. et al. (Apr. 1997). "Hubble Space Telescope Images of a Sample of 20 Nearby Luminous Quasars". In: 479.2, pp. 642–658. DOI: 10.1086/303926. arXiv: astro-ph/9611163 [astro-ph].

Baldi, Ranieri D. et al. (May 2016). "Radio-loud Narrow Line Seyfert 1 under a different perspective: a revised black hole mass estimate from optical spectropolarimetry". In: 458.1, pp. L69–L73. DOI: 10.1093/mnrasl/slw019. arXiv: 1602.02783 [astro-ph.GA].

Barnes, Joshua E. and Lars Hernquist (Jan. 1992). "Dynamics of interacting galaxies." In: 30, pp. 705–742. DOI: 10.1146/annurev.aa.30.090192.003421.

Barquín-González, L. et al. (Apr. 2024). "Extinction and AGN over host galaxy contrast effects on the optical spectroscopic classification of AGN". In: *arXiv e-prints*, arXiv:2404.19544, arXiv:2404.19544. DOI: 10.48550/arXiv.2404.19544. arXiv: 2404.19544 [astro-ph.GA].

Baskin, Alexei and Ari Laor (Apr. 2005). "What controls the [OIII]λ5007 line strength in active galactic nuclei?" In: 358.3, pp. 1043–1054. DOI: 10.1111/j.1365-2966.2005.08841.x. arXiv: astro-ph/0501436 [astro-ph].

Becker, R. H., R. L. White, and D. J. Helfand (Sept. 1995). "The FIRST Survey: Faint Images of the Radio Sky at Twenty Centimeters". In: 450, p. 559. DOI: 10.1086/176166.

Beckmann, V. and C. R. Shrader (Aug. 2012). *Active Galactic Nuclei*.

Begelman, M. C., R. D. Blandford, and M. J. Rees (Sept. 1980). "Massive black hole binaries in active galactic nuclei". In: 287.5780, pp. 307–309. DOI: 10.1038/287307a0.

Bellm, Eric C. et al. (Jan. 2019). "The Zwicky Transient Facility: System Overview, Performance, and First Results". In: 131.995, p. 018002. DOI: 10.1088/1538-3873/aaecbe. arXiv: 1902.01932 [astro-ph.IM].

Bentz, Misty C. et al. (May 2009). "The Radius-Luminosity Relationship for Active Galactic Nuclei: The Effect of Host-Galaxy Starlight on Luminosity Measurements. II. The Full Sample of Reverberation-Mapped AGNs". In: 697.1, pp. 160–181. DOI: 10.1088/0004-637X/697/1/160. arXiv: 0812.2283 [astro-ph].

Bentz, Misty C. et al. (2013). "The Low-luminosity End of the Radius-Luminosity Relationship for Active Galactic Nuclei". In: 767.2, 149, p. 149. DOI: 10.1088/0004-637X/767/2/149. arXiv: 1303.1742 [astro-ph.CO].

Berkley, Andrew J., Demosthenes Kazanas, and Jonathan Ozik (June 2000). "Modeling the X-Ray-Ultraviolet Correlations in NGC 7469". In: 535.2, pp. 712–720. DOI: 10.1086/308880. arXiv: astro-ph/0001239 [astro-ph].

Berta, Stefano and Robert Zylka (2019-2025). *Welcome to the PIIC Pipelines (Pointing and Imaging In Continuum, as code by Robert Zylka)*.

Berton, M. et al. (June 2015). "Parent population of flat-spectrum radio-loud narrow-Line Seyfert 1 galaxies". In: 578, A28.

Berton, M. et al. (June 2016a). "Compact steep-spectrum sources as the parent population of flat-spectrum radio-loud narrow-line Seyfert 1 galaxies". In: 591, A98, A98. DOI: 10.1051/0004-6361/201628171. arXiv: 1601.06165.

Berton, M. et al. (June 2016b). "[O III] line properties in two samples of radio-emitting narrow-line Seyfert 1 galaxies". In: 591, A88, A88. DOI: 10.1051/0004-6361/201527056. arXiv: 1506.05800.

Berton, M. et al. (Jan. 2016c). "Unveiling the submerged part of the iceberg: radio-loud narrow-line Seyfert 1s with SKA". In: *ArXiv e-prints*. arXiv: 1601.05791.

Berton, M. et al. (July 2017). "An orientation-based unification of young jetted active galactic nuclei: the case of 3C 286". In: *Frontiers in Astronomy and Space Sciences* 4, 8, p. 8. DOI: 10.3389/fspas.2017.00008. arXiv: 1705.07905.

Berton, M. et al. (June 2018). "Radio-emitting narrow-line Seyfert 1 galaxies in the JVLA perspective". In: 614, A87, A87. DOI: 10.1051/0004-6361/201832612. arXiv: 1801.03519.

Berton, M. et al. (Apr. 2020a). "Absorbed relativistic jets in radio-quiet narrow-line Seyfert 1 galaxies". In: 636, A64, A64. DOI: 10.1051/0004-6361/202037793. arXiv: 2003.02654 [astro-ph.GA].

Berton, M. et al. (2020b). "Line shapes in narrow-line Seyfert 1 galaxies: a tracer of physical properties?" In: *Contributions of the Astronomical Observatory Skalnate Pleso* 50.1, pp. 270–292. DOI: 10.31577/caosp.2020.50.1.270. arXiv: 1909.12343 [astro-ph.GA].

Berton, M. et al. (Oct. 2021). "Hunting for the nature of the enigmatic narrow-line Seyfert 1 galaxy PKS 2004-447". In: 654, A125, A125. DOI: 10.1051/0004-6361/202141409. arXiv: 2106.12536 [astro-ph.HE].

Berton, Marco and Emilia Järvelä (June 2021a). "Jet-Induced Feedback in the [O III] Lines of Early Evolution Stage Active Galactic Nuclei". In: *Universe* 7.6, p. 188. DOI: 10.3390/universe7060188. arXiv: 2106.01076 [astro-ph.GA].

— (Nov. 2021b). "Peaked sources and narrow-line Seyfert 1s: A love story". In: *Astronomische Nachrichten* 342.1066, pp. 1066–1070. DOI: 10.1002/asna.20210036. arXiv: 2110.02973 [astro-ph.GA].

Bhatta, Gopal and Niraj Dhital (Mar. 2020). "The Nature of γ-Ray Variability in Blazars". In: 891.2, 120, p. 120. DOI: 10.3847/1538-4357/ab7455. arXiv: 1911.08198 [astro-ph.HE].

Bianchi, S. et al. (July 2009). "CAIXA: a catalogue of AGN in the XMM-Newton archive. II. Multiwavelength correlations". In: 501, pp. 915–924. DOI: 10.1051/0004-6361/200911905. arXiv: 0905.0267.

Bicknell, Geoffrey V., Michael A. Dopita, and Christopher P. O. O'Dea (1997). "Unification of the Radio and Optical Properties of Gigahertz Peak Spectrum and Compact Steep-Spectrum Radio Sources". In: 485.1, pp. 112–124. DOI: 10.1086/304400.

Bisnovatyi-Kogan, G. S. and A. A. Ruzmaikin (May 1974). "The Accretion of Matter by a Collapsing Star in the Presence of a Magnetic Field". In: 28.1, pp. 45–59. DOI: 10.1007/BF00642237.

Blandford, R. D. and C. F. McKee (Apr. 1982). "Reverberation mapping of the emission line regions of Seyfert galaxies and quasars". In: 255, pp. 419–439. DOI: 10.1086/159843.

Blandford, R. D. and M. J. Rees (1978). "Some comments on radiation mechanisms in Lacertids". In: *BL Lac Objects*. Ed. by A. M. Wolfe, pp. 328–341.

Blandford, R. D. and R. L. Znajek (May 1977). "Electromagnetic extraction of energy from Kerr black holes". In: 179, pp. 433–456.

Blandford, Roger, David Meier, and Anthony Readhead (Aug. 2019). "Relativistic Jets from Active Galactic Nuclei". In: 57, pp. 467–509. DOI: 10.1146/annurev-astro-081817-051948. arXiv: 1812.06025 [astro-ph.HE].

Boissay, Rozenn, Claudio Ricci, and Stéphane Paltani (Apr. 2016). "A hard X-ray view of the soft excess in AGN". In: 588, A70, A70. DOI: 10.1051/0004-6361/201526982. arXiv: 1511.08168 [astro-ph.HE].

Boller, T. (Sept. 2000). "X-ray observations of AGN". In: *New Vistas in Astrophysics*. Ed. by M. M. Shapiro et al., pp. 143–171. DOI: 10.1142/9789812793997_0009.

Boller, T., W. N. Brandt, and H. Fink (Jan. 1996). "Soft X-ray properties of narrow-line Seyfert 1 galaxies." In: 305, p. 53. eprint: astro-ph/9504093.

Boller, Th. et al. (Aug. 1997). "ROSAT monitoring of persistent giant and rapid variability in the narrow-line Seyfert 1 galaxy IRAS 13224-3809". In: 289.2, pp. 393–405. DOI: 10.1093/mnras/289.2.393. arXiv: astro-ph/9703114 [astro-ph].

Boroson, T. (Aug. 2005). "Blueshifted [O III] Emission: Indications of a Dynamic Narrow-Line Region". In: 130, pp. 381–386. DOI: 10.1086/431722. eprint: astro-ph/0505127.

Boroson, T. A. (July 2011). "A New Orientation Indicator for Radio-quiet Quasars". In: 735, L14, p. L14. DOI: 10.1088/2041-8205/735/1/L14. arXiv: 1105.5161.

Boroson, T. A. and R. F. Green (May 1992). "The emission-line properties of low-redshift quasi-stellar objects". In: 80, pp. 109–135. DOI: 10.1086/191661.

Borucki, William J. et al. (Feb. 2010). "Kepler Planet-Detection Mission: Introduction and First Results". In: *Science* 327.5968, p. 977. DOI: 10.1126/science.1185402.

Burke, Colin J. et al. (Aug. 2021). "A characteristic optical variability time scale in astrophysical accretion disks". In: *Science* 373.6556, pp. 789–792. DOI: 10.1126/science.abg9933. arXiv: 2108.05389 [astro-ph.GA].

Caccianiga, A. et al. (Aug. 2015). "WISE colours and star formation in the host galaxies of radio-loud narrow-line Seyfert 1". In: 451, pp. 1795–1805. DOI: 10.1093/mnras/stv939. arXiv: 1504.07068.

Cackett, Edward M., Misty C. Bentz, and Erin Kara (June 2021). "Reverberation mapping of active galactic nuclei: from X-ray corona to dusty torus". In: *iScience* 24.6, p. 102557. DOI: 10.1016/j.isci.2021.102557. arXiv: 2105.06926 [astro-ph.GA].

Cackett, Edward M., Keith Horne, and Hartmut Winkler (Sept. 2007). "Testing thermal reprocessing in active galactic nuclei accretion discs". In: 380.2, pp. 669–682. DOI: 10.1111/j.1365-2966.2007.12098.x. arXiv: 0706.1464 [astro-ph].

Calderone, G. et al. (May 2013). "Black hole mass estimate for a sample of radio-loud narrow-line Seyfert 1 galaxies". In: 431, pp. 210–239. DOI: 10.1093/mnras/stt157. arXiv: 1212.1181 [astro-ph.CO].

Camenzind, M. and M. Krockenberger (Feb. 1992). "The lighthouse effect of relativistic jets in blazars. A geometric originof intraday variability." In: 255, pp. 59–62.

Campitiello, Samuele et al. (Dec. 2021). "The disk-torus system in active galactic nuclei: possible evidence of highly spinning black holes". In: 656, A96, A96. DOI: 10.1051/0004-6361/202141602. arXiv: 2110.00010 [astro-ph.HE].

Capetti, A., F. Massaro, and R. D. Baldi (Feb. 2017a). "FRICAT: A FIRST catalog of FR I radio galaxies". In: 598, A49, A49. DOI: 10.1051/0004-6361/201629287. arXiv: 1610.09376 [astro-ph.HE].

— (May 2017b). "FRIICAT: A FIRST catalog of FR II radio galaxies". In: 601, A81, A81. DOI: 10.1051/0004-6361/201630247. arXiv: 1703.03427 [astro-ph.HE].

Capetti, A. et al. (May 1999). "The Origin of the Narrow-Line Region of Markarian 3: An Overpressured Jet Cocoon". In: 516.1, pp. 187–194. DOI: 10.1086/307099. arXiv: astro-ph/9811381 [astro-ph].

Caproni, A., Z. Abraham, and H. Monteiro (Jan. 2013). "Parsec-scale jet precession in BL Lacertae (2200+420)". In: 428.1, pp. 280–290. DOI: 10.1093/mnras/sts014. arXiv: 1210.2286 [astro-ph.HE].

Cardelli, J. A., G. C. Clayton, and J. S. Mathis (Oct. 1989). "The relationship between infrared, optical, and ultraviolet extinction". In: 345, pp. 245–256. DOI: 10.1086/167900.

Chakrabarti, Sandip K. and Paul J. Wiita (July 1993). "Spiral Shocks in Accretion Disks As a Contributor to Variability in Active Galactic Nuclei". In: 411, p. 602. DOI: 10.1086/172862.

Chamani, Wara et al. (Aug. 2021). "Testing the magnetic flux paradigm for AGN radio loudness with a radio-intermediate quasar". In: 652, A14, A14. DOI: 10.1051/0004-6361/202140676. arXiv: 2106.01089 [astro-ph.HE].

Chambers, K. C. et al. (Dec. 2016). "The Pan-STARRS1 Surveys". In: *arXiv e-prints*, arXiv:1612.05560, arXiv:1612.05560. DOI: 10.48550/arXiv.1612.05560. arXiv: 1612.05560 [astro-ph.IM].

Chan, James Hung-Hsu et al. (Jan. 2025). "Reverberation Mapping of Lamppost and Wind Structures in Accretion Thin Disks". In: 978.1, 54, p. 54. DOI: 10.3847/1538-4357/ad93af. arXiv: 2409.15669 [astro-ph.GA].

Chen, S. et al. (Aug. 2018). "Probing narrow-line Seyfert 1 galaxies in the southern hemisphere". In: 615, A167, A167. DOI: 10.1051/0004-6361/201832678. arXiv: 1801.07234.

Chen, S. et al. (Aug. 2020). "Radio morphology of southern narrow-line Seyfert 1 galaxies with Very Large Array observations". In: 498.1, pp. 1278–1297. DOI: 10.1093/mnras/staa2373. arXiv: 2006.01700 [astro-ph.GA].

Chen, Sina et al. (May 2022). "Radio spectra of narrow-line Seyfert 1 galaxies observed with Australia Telescope Compact Array and Very Large Array Sky Survey". In: 512.1, pp. 471–489. DOI: 10.1093/mnras/stac530. arXiv: 2202.11065 [astro-ph.GA].

Chen, Sina et al. (Oct. 2023). "The radio emission in radio-quiet quasars: the VLBA perspective". In: 525.1, pp. 164–182. DOI: 10.1093/mnras/stad2289. arXiv: 2307.13599 [astro-ph.GA].

Cheng, Huaqing et al. (Aug. 2019). "Modelling accretion disc emission with generalized temperature profile and its effect on AGN spectral energy distribution". In: 487.3, pp. 3884–3903. DOI: 10.1093/mnras/stz1532. arXiv: 1906.00157 [astro-ph.HE].

Chiu, Hong-Yee (May 1964). "Gravitational collapse". In: *Physics Today* 17.5, pp. 21–34. ISSN: 0031-9228. DOI: 10.1063/1.3051610. eprint: https://pubs.aip.org/physicstoday/article-pdf/17/5/21/8261856/21_1_online.pdf. URL: https://doi.org/10.1063/1.3051610.

Collier, Stefan et al. (Jan. 1999). "A new direct method for measuring the Hubble constant from reverberating accretion discs in active galaxies". In: 302.1, pp. L24–L28. DOI: 10.1046/j.1365-8711.1999.02250.x. arXiv: astro-ph/9811278 [astro-ph].

Collin, S. et al. (Sept. 2006). "Systematic effects in measurement of black hole masses by emission-line reverberation of active galactic nuclei: Eddington ratio and inclination". In: 456, pp. 75–90. DOI: 10.1051/0004-6361:20064878. eprint: astro-ph/0603460.

Collinson, James S. et al. (Feb. 2017). "Reaching the peak of the quasar spectral energy distribution - II. Exploring the accretion disc, dusty torus and host galaxy". In: 465.1, pp. 358–382. DOI: 10.1093/mnras/stw2666. arXiv: 1610.04221 [astro-ph.HE].

Collmar, W. et al. (Nov. 2010). "The multifrequency campaign on 3C 279 in January 2006". In: 522, A66, A66. DOI: 10.1051/0004-6361/201014823. arXiv: 1008.1010 [astro-ph.HE].

Condon, J. J. et al. (May 1998a). "The NRAO VLA Sky Survey". In: 115, pp. 1693–1716. DOI: 10.1086/300337.

— (May 1998b). "The NRAO VLA Sky Survey". In: 115.5, pp. 1693–1716. DOI: 10.1086/300337.

Condon, James J. and Scott M. Ransom (2016). *Essential Radio Astronomy*.

Congiu, E. et al. (July 2017). "Kiloparsec-scale emission in the narrow-line Seyfert 1 galaxy Mrk 783". In: 603, A32, A32. DOI: 10.1051/0004-6361/201730616. arXiv: 1704.03881.

Constantin, Anca and Joseph C. Shields (May 2003). "Ultraviolet and Optical Properties of Narrow-Line Seyfert 1 Galaxies". In: 115.807, pp. 592–608. DOI: 10.1086/374724. arXiv: astro-ph/0302369 [astro-ph].

Conway, J. E. and D. W. Murphy (July 1993). "Helical Jets and the Misalignment Distribution for Core-dominated Radio Sources". In: 411, p. 89. DOI: 10.1086/172809.

Cracco, V. et al. (Dec. 2011). "The origin of gas in extended narrow-line regions of nearby Seyfert galaxies - I. NGC 7212". In: 418.4, pp. 2630–2641. DOI: 10.1111/j.1365-2966.2011.19654.x. arXiv: 1109.1195 [astro-ph.CO].

Cracco, V. et al. (Oct. 2016). "A spectroscopic analysis of a sample of narrow-line Seyfert 1 galaxies selected from the Sloan Digital Sky Survey". In: 462, pp. 1256–1280. DOI: 10.1093/mnras/stw1689. arXiv: 1607.03438.

Crenshaw, D. M., S. B. Kraemer, and J. R. Gabel (Oct. 2003). "The Host Galaxies of Narrow-Line Seyfert 1 Galaxies: Evidence for Bar-Driven Fueling". In: 126, pp. 1690–1698. DOI: 10.1086/377625. eprint: astro-ph/0306404.

Crepaldi, L. et al. (Apr. 2025). "An optical perspective on early-stage active galactic nuclei with extreme radio flares". In: 696, A74, A74. DOI: 10.1051/0004-6361/202451512. arXiv: 2502.13214 [astro-ph.GA].

Curtis, H. D. (1918). "Descriptions of 762 Nebulae and Clusters Photographed with the Crossley Reflector". In: *Publications of Lick Observatory* 13, pp. 9–42.

Czesla, Stefan et al. (2019). *PyA: Python astronomy-related packages*. ascl: 1906.010.

Dalla Barba, B. et al. (June 2025). "Interaction of the relativistic jet and the narrow-line region of PMN J0948+0022". In: 698, A320, A320. DOI: 10.1051/0004-6361/202452421. arXiv: 2505.14776 [astro-ph.GA].

Dalla Barba, Benedetta et al. (Nov. 2023). "Optical Properties of Two Complementary Samples of Intermediate Seyfert Galaxies". In: *Physics* 5.4, pp. 1061–1080. DOI: 10.3390/physics5040069. arXiv: 2311.01510 [astro-ph.GA].

Dalla Bontà, Elena et al. (Nov. 2020). "The Sloan Digital Sky Survey Reverberation Mapping Project: Estimating Masses of Black Holes in Quasars with Single-epoch Spectroscopy". In: 903.2, 112, p. 112. DOI: 10.3847/1538-4357/abbc1c. arXiv: 2007.02963 [astro-ph.GA].

Davidson, K. and T. D. Kinman (Nov. 1978). "On the possible importance of Markarian 359". In: 225, pp. 776–779. DOI: 10.1086/156541.

Decarli, R. et al. (May 2008). "Are the black hole masses in narrow-line Seyfert 1 galaxies actually small?" In: 386, pp. L15–L19. DOI: 10.1111/j.1745-3933.2008.00451.x. arXiv: 0801.4560.

Deeming, T. J. (Aug. 1975). "Fourier Analysis with Unequally-Spaced Data". In: 36.1, pp. 137–158. DOI: 10.1007/BF00681947.

Dekany, Richard et al. (Mar. 2020). "The Zwicky Transient Facility: Observing System". In: 132.1009, 038001, p. 038001. DOI: 10.1088/1538-3873/ab4ca2. arXiv: 2008.04923 [astro-ph.IM].

Deo, R. P., D. M. Crenshaw, and S. B. Kraemer (July 2006). "The Host Galaxies of Narrow-Line Seyfert 1 Galaxies: Nuclear Dust Morphology and Starburst Rings". In: 132, pp. 321–346. DOI: 10.1086/504894. eprint: astro-ph/0603806.

Dexter, Jason et al. (Nov. 2019). "The Sloan Digital Sky Survey Reverberation Mapping Project: Accretion and Broad Emission Line Physics from a Hypervariable Quasar". In: 885.1, 44, p. 44. DOI: 10.3847/1538-4357/ab4354. arXiv: 1906.10138 [astro-ph.GA].

di Clemente, A. et al. (June 1996). "The Variability of Quasars. II. Frequency Dependence". In: 463, p. 466. DOI: 10.1086/177261. arXiv: astro-ph/9512159 [astro-ph].

Di Gesu, Laura et al. (Oct. 2023). "Discovery of X-ray polarization angle rotation in the jet from blazar Mrk 421." In: *Nature Astronomy* 7, pp. 1245–1258. DOI: 10.1038/s41550-023-02032-7. arXiv: 2305.13497 [astro-ph.HE].

Dimitrijević, M. S. et al. (Jan. 2007). "The flux ratio of the [OIII] $\lambda\lambda$5007, 4959 lines in AGN: comparison with theoretical calculations". In: 374.3, pp. 1181–1184. DOI: 10.1111/j.1365-2966.2006.11238.x. arXiv: astro-ph/0610848 [astro-ph].

Dobrotka, A., H. Negoro, and S. Mineshige (Nov. 2019). "Similar shot profile morphology of fast variability in a cataclysmic variable, X-ray binary, and blazar: The MV Lyrae case". In: 631, A134, A134. DOI: 10.1051/0004-6361/201935198. arXiv: 1908.11745 [astro-ph.SR].

Dojčinović, Ivan, Jelena Kovačević-Dojčinović, and Luka Č. Popović (Jan. 2023). "The flux ratio of the [N II] $\lambda\lambda$ 6548, 6583 Å lines in sample of Active Galactic Nuclei Type 2". In: *Advances in Space Research* 71.2, pp. 1219–1226. DOI: 10.1016/j.asr.2022.04.041. arXiv: 2204.10036 [astro-ph.GA].

Donato, D. (July 2010). "Fermi LAT detection of a GeV flare from the radio-loud NL Sy1 PMN J0948+0022". In: *The Astronomer's Telegram* 2733, p. 1.

Done, C. et al. (Nov. 1992). "The X-Ray Variability of NGC 6814: Power Spectrum". In: 400, p. 138. DOI: 10.1086/171979.

Dotti, M. et al. (Jan. 2013). "On the Orientation and Magnitude of the Black Hole Spin in Galactic Nuclei". In: 762.2, 68, p. 68. DOI: 10.1088/0004-637X/762/2/68. arXiv: 1211.4871 [astro-ph.CO].

Drewes, Farin et al. (Jan. 2025). "I Zw 1 and H0557-385: The dusty tori of two high Eddington AGNs observed in the MATISSE LM-Bands". In: DOI: 10.1093/mnras/staf110.

Du, Pu and Jian-Min Wang (Nov. 2019). "The Radius-Luminosity Relationship Depends on Optical Spectra in Active Galactic Nuclei". In: 886.1, 42, p. 42. DOI: 10.3847/1538-4357/ab4908. arXiv: 1909.06735 [astro-ph.GA].

Du, Pu et al. (Dec. 2018). "Monitoring AGNs with Hβ Asymmetry. I. First Results: Velocity-resolved Reverberation Mapping". In: 869.2, 142, p. 142. DOI: 10.3847/1538-4357/aaed2c. arXiv: 1810.11996 [astro-ph.GA].

Eddington, A. S. (1926). *The Internal Constitution of the Stars*.

Edelson, R. et al. (Jan. 2019). "The First Swift Intensive AGN Accretion Disk Reverberation Mapping Survey". In: 870.2, 123, p. 123. DOI: 10.3847/1538-4357/aaf3b4. arXiv: 1811.07956 [astro-ph.HE].

Edelson, R. A. (Feb. 1987). "Broad-band properties of the CfA Seyfert galaxies. I - Radio properties". In: 313, pp. 651–661. DOI: 10.1086/165004.

Edge, D. O. et al. (Jan. 1959). "A survey of radio sources at a frequency of 159 Mc/s." In: 68, pp. 37–60.

Elitzur, Moshe (Aug. 2008). "The toroidal obscuration of active galactic nuclei". In: 52.6, pp. 274–288. DOI: 10.1016/j.newar.2008.06.010. arXiv: 0805.3699 [astro-ph].

Emmanoulopoulos, D., I. M. McHardy, and I. E. Papadakis (Aug. 2013). "Generating artificial light curves: revisited and updated". In: 433.2, pp. 907–927. DOI: 10.1093/mnras/stt764. arXiv: 1305.0304 [astro-ph.IM].

Fabian, A. C. (Nov. 1989). "The origin of the continuum of AGN and the X-ray background." In: *Two Topics in X-Ray Astronomy, Volume 1: X Ray Binaries. Volume 2: AGN and the X Ray Background*. Ed. by J. Hunt and B. Battrick. Vol. 296. ESA Special Publication, pp. 1097–1104.

Fabian, A. C. et al. (Mar. 2013). "Long XMM observation of the narrow-line Seyfert 1 galaxy IRAS 13224-3809: rapid variability, high spin and a soft lag". In: 429, pp. 2917–2923. DOI: 10.1093/mnras/sts504. arXiv: 1208.5898 [astro-ph.HE].

Fabian, A. C. et al. (May 2017). "Properties of AGN coronae in the NuSTAR era - II. Hybrid plasma". In: 467.3, pp. 2566–2570. DOI: 10.1093/mnras/stx221. arXiv: 1701.06774 [astro-ph.HE].

Fabian, Andrew C. and Anthony N. Lasenby (Nov. 2019). "Astrophysical Black Holes". In: *arXiv e-prints*, arXiv:1911.04305, arXiv:1911.04305. arXiv: 1911.04305 [astro-ph.HE].

Falcke, H., E. Körding, and S. Markoff (Feb. 2004). "A scheme to unify low-power accreting black holes. Jet-dominated accretion flows and the radio/X-ray correlation". In: 414, pp. 895–903. DOI: 10.1051/0004-6361:20031683. arXiv: astro-ph/0305335 [astro-ph].

Fath, E. A. (1909). "The spectra of some spiral nebulae and globular star clusters". In: *Lick Observatory Bulletin* 5, pp. 71–77. DOI: 10.5479/ADS/bib/1909LicOB.5.71F.

Fawley, W. M., J. Arons, and E. T. Scharlemann (Oct. 1977). "Potential drops above pulsar polar caps: acceleration of nonneutral beams from the stellar surface." In: 217, pp. 227–243. DOI: 10.1086/155573.

Ferland, G. J. and R. F. Mushotzky (Nov. 1982). "Broad line region clouds and the absorbing material in NGC 4151". In: 262, pp. 564–577. DOI: 10.1086/160448.

Ferland, G. J. et al. (June 2020). "State-of-the-art AGN SEDs for photoionization models: BLR predictions confront the observations". In: 494.4, pp. 5917–5922. DOI: 10.1093/mnras/staa1207. arXiv: 2004.11873 [astro-ph.HE].

Fernández-Ontiveros, Juan Antonio et al. (Dec. 2013). "The nature of the IR emission in LLAGN at parsec scales. Does the jet dominate at low-luminosities?" In: *European Physical Journal Web of Conferences*. Vol. 61. European Physical Journal Web of Conferences, 04005, p. 04005. DOI: 10.1051/epjconf/20136104005.

Ferrarese, L. and D. Merritt (Aug. 2000). "A Fundamental Relation between Supermassive Black Holes and Their Host Galaxies". In: 539, pp. L9–L12. DOI: 10.1086/312838. eprint: astro-ph/0006053.

Ferrarese, Laura and Holland Ford (Feb. 2005). "Supermassive Black Holes in Galactic Nuclei: Past, Present and Future Research". In: 116.3-4, pp. 523–624. DOI: 10.1007/s11214-005-3947-6. arXiv: astro-ph/0411247 [astro-ph].

Foschini, L. (Nov. 2011a). "Accretion and jet power in active galactic nuclei". In: *Research in Astronomy and Astrophysics* 11, pp. 1266–1278. DOI: 10.1088/1674-4527/11/11/003. arXiv: 1106.5532 [astro-ph.HE].

— (2011b). "Evidence of powerful relativistic jets in narrow-line Seyfert 1 galaxies". In: *Narrow-Line Seyfert 1 Galaxies and their Place in the Universe, Proc. of Science*. Vol. NLS1, id. 24, 24, p. 24. arXiv: 1105.0772 [astro-ph.HE].

— (2012). "Powerful relativistic jets in narrow-line Seyfert 1 glaxies (review)". In: *Proceedings of Nuclei of Seyfert galaxies and QSOs - Central engine & conditions of star formation, Proc. of Science*. Vol. Seyfert 2012, id. 10.

— (Mar. 2014). "The Unification of Relativistic Jets". In: *International Journal of Modern Physics Conference Series* 28, 1460188, p. 1460188. DOI: 10.1142/S2010194514601884. arXiv: 1310.5822 [astro-ph.HE].

— (July 2017). "What we talk about when we talk about blazars?" In: *Frontiers in Astronomy and Space Sciences* 4, 6, p. 6. DOI: 10.3389/fspas.2017.00006. arXiv: 1705.10166 [astro-ph.HE].

Foschini, L. et al. (Oct. 2010). "Fermi/LAT Discovery of Gamma-Ray Emission from a Relativistic Jet in the Narrow-Line Seyfert 1 Quasar PMN J0948+0022". In: *Accretion and Ejection in AGN: a Global View*. Ed. by L. Maraschi et al. Vol. 427. Astronomical Society of the Pacific Conference Series, pp. 243–248. arXiv: 0908.3313 [astro-ph.CO].

Foschini, L. et al. (Oct. 2011). "Short time scale variability at gamma rays in FSRQs and implications on the current models". In: *ArXiv e-prints*. arXiv: 1110.4471 [astro-ph.HE].

Foschini, L. et al. (Mar. 2015). "Properties of flat-spectrum radio-loud narrow-line Seyfert 1 galaxies". In: 575, A13, A13. DOI: 10.1051/0004-6361/201424972. arXiv: 1409.3716 [astro-ph.HE].

Foschini, Luigi (Aug. 2020). "Jetted Narrow-Line Seyfert 1 Galaxies & Co.: Where Do We Stand?" In: *Universe* 6.9, p. 136. DOI: 10.3390/universe6090136. arXiv: 2008.13383 [astro-ph.HE].

Foschini, Luigi et al. (Sept. 2019). "Mapping the Narrow-Line Seyfert 1 Galaxy 1H 0323+342". In: *Universe* 5.9, p. 199. DOI: 10.3390/universe5090199. arXiv: 1909.05525 [astro-ph.GA].

Foschini, Luigi et al. (Oct. 2021). "A New Sample of Gamma-Ray Emitting Jetted Active Galactic Nuclei—Preliminary Results". In: *Universe* 7.10, p. 372. DOI: 10.3390/universe7100372. arXiv: 2110.01995 [astro-ph.HE].

Foschini, Luigi et al. (Nov. 2022). "A New Sample of Gamma-Ray Emitting Jetted Active Galactic Nuclei". In: *Universe* 8.11, p. 587. DOI: 10.3390/universe8110587. arXiv: 2211.03400 [astro-ph.HE].

Foster, Grant (Jan. 1996a). "Time Series Analysis by Projection. I. Statistical Properties of Fourier Analysis". In: 111, p. 541. DOI: 10.1086/117805.

— (Oct. 1996b). "Wavelets for period analysis of unevenly sampled time series". In: 112, pp. 1709–1729. DOI: 10.1086/118137.

Frank, Juhan, Andrew King, and Derek J. Raine (2002). *Accretion Power in Astrophysics: Third Edition*.

Gallo, L. C. (May 2006). "Investigating the nature of narrow-line Seyfert 1 galaxies with high-energy spectral complexity". In: 368, pp. 479–486. DOI: 10.1111/j.1365-2966.2006.10137.x. eprint: astro-ph/0602145.

Gardner, Emma and Chris Done (Apr. 2015). "Complex narrow-line Seyfert 1s: high spin or high inclination?" In: 448.3, pp. 2245–2259. DOI: 10.1093/mnras/stv168. arXiv: 1411.6425 [astro-ph.HE].

Gaskell, C. M. (July 2009). "What broad emission lines tell us about how active galactic nuclei work". In: *NewAR* 53, pp. 140–148. DOI: 10.1016/j.newar.2009.09.006. arXiv: 0908.0386.

Gaskell, C. M. and R. W. Goosmann (May 2013). "Line Shifts, Broad-line Region Inflow, and the Feeding of Active Galactic Nuclei". In: 769, 30, p. 30. DOI: 10.1088/0004-637X/769/1/30. arXiv: 0805.4258.

Gaskell, C. M. and E. S. Klimek (Aug. 2003). "Variability of Active Galactic Nuclei from Optical to X-ray Regions". In: *Astronomical and Astrophysical Transactions* 22.4-5, pp. 661–680. DOI: 10.1080/1055679031000153851. arXiv: 0907.1415 [astro-ph.CO].

Gaskell, C. M., E. S. Klimek, and L. S. Nazarova (Dec. 2007). "The Structure of the Torus and Broad-line Region Of AGNs". In: *American Astronomical Society Meeting Abstracts*. Vol. 39. Bulletin of the American Astronomical Society, 118.02, p. 947.

Gaskell, Martin et al. (Jan. 2022). "Fe II emission in active galactic nuclei". In: *Astronomische Nachrichten* 343.1-2, e210112, e210112. DOI: 10.1002/asna.20210112. arXiv: 2112.06559 [astro-ph.GA].

Gebhardt, K. et al. (Aug. 2000). "A Relationship between Nuclear Black Hole Mass and Galaxy Velocity Dispersion". In: 539, pp. L13–L16. DOI: 10.1086/312840. eprint: astro-ph/0006289.

Gebhardt, Karl et al. (Jan. 2003). "Axisymmetric Dynamical Models of the Central Regions of Galaxies". In: 583.1, pp. 92–115. DOI: 10.1086/345081. arXiv: astro-ph/0209483 [astro-ph].

George, I. M. and A. C. Fabian (Mar. 1991). "X-ray reflection from cold matter in Active Galactic Nuclei and X-ray binaries." In: 249, p. 352. DOI: 10.1093/mnras/249.2.352.

Gezari, S. et al. (Dec. 2006). "Ultraviolet Detection of the Tidal Disruption of a Star by a Supermassive Black Hole". In: 653.1, pp. L25–L28. DOI: 10.1086/509918. arXiv: astro-ph/0612069 [astro-ph].

Gezari, S. et al. (Apr. 2008). "UV/Optical Detections of Candidate Tidal Disruption Events by GALEX and CFHTLS". In: 676.2, pp. 944–969. DOI: 10.1086/529008. arXiv: 0712.4149 [astro-ph].

Ghisellini, G. et al. (May 2013). "The red blazar PMN J2345-1555 becomes blue". In: 432, p. L66. DOI: 10.1093/mnrasl/slt041. arXiv: 1302.4444 [astro-ph.HE].

Gierliński, Marek et al. (Sept. 2008). "A periodicity of ~1hour in X-ray emission from the active galaxy RE J1034+396". In: 455.7211, pp. 369–371. DOI: 10.1038/nature07277.

Gilliland, Ronald L. and Sallie L. Baliunas (Mar. 1987). "Objective Characterization of Stellar Activity Cycles. I. Methods and Solar Cycle Analyses". In: 314, p. 766. DOI: 10.1086/165103.

Gliozzi, M. et al. (July 2011). "Testing a Scale-independent Method to Measure the Mass of Black Holes". In: 735.1, 16, p. 16. DOI: 10.1088/0004-637X/735/1/16. arXiv: 1104.2758 [astro-ph.HE].

Gliozzi, M. et al. (Feb. 2024). "Comparing indirect methods for black hole masses in AGN: the good, the bad, and the ugly". In: 528.2, pp. 3417–3432. DOI: 10.1093/mnras/stad3974. arXiv: 2312.14098 [astro-ph.HE].

González-Martín, O. and S. Vaughan (Aug. 2012). "X-ray variability of 104 active galactic nuclei. XMM-Newton power-spectrum density profiles". In: 544, A80, A80. DOI: 10.1051/0004-6361/201219008. arXiv: 1205.4255 [astro-ph.HE].

Goodrich, R. W. (July 1989). "Spectropolarimetry of 'narrow-line' Seyfert 1 galaxies". In: 342, pp. 224–234. DOI: 10.1086/167586.

Gopal-Krishna, Ram Sagar, and Paul J. Wiita (June 1995). "Intranight optical variability in optically selected QSOs". In: 274.3, pp. 701–710. DOI: 10.1093/mnras/274.3.701.

Gopal-Krishna et al. (Mar. 2003). "Clear Evidence for Intranight Optical Variability in Radio-quiet Quasars". In: 586.1, pp. L25–L28. DOI: 10.1086/374655. arXiv: astro-ph/0302188 [astro-ph].

Goyal, A. et al. (Aug. 2012). "Intra-night optical variability of core dominated radio quasars: the role of optical polarization". In: 544, A37, A37. DOI: 10.1051/0004-6361/201218888. arXiv: 1205.2324 [astro-ph.HE].

Graham, Matthew J. et al. (Feb. 2015). "A possible close supermassive black-hole binary in a quasar with optical periodicity". In: 518.7537, pp. 74–76. DOI: 10.1038/nature14143. arXiv: 1501.01375 [astro-ph.GA].

Graham, Matthew J. et al. (July 2019). "The Zwicky Transient Facility: Science Objectives". In: 131.1001, p. 078001. DOI: 10.1088/1538-3873/ab006c. arXiv: 1902.01945 [astro-ph.IM].

GRAVITY Collaboration et al. (Nov. 2018). "Spatially resolved rotation of the broad-line region of a quasar at sub-parsec scale". In: 563.7733, pp. 657–660. DOI: 10.1038/s41586-018-0731-9. arXiv: 1811.11195 [astro-ph.GA].

GRAVITY Collaboration et al. (Nov. 2020). "The spatially resolved broad line region of IRAS 09149-6206". In: 643, A154, A154. DOI: 10.1051/0004-6361/202039067. arXiv: 2009.08463 [astro-ph.GA].

GRAVITY Collaboration et al. (Apr. 2021). "The central parsec of NGC 3783: a rotating broad emission line region, asymmetric hot dust structure, and compact coronal line region". In: 648, A117, A117. DOI: 10.1051/0004-6361/202040061. arXiv: 2102.00068 [astro-ph.GA].

GRAVITY Collaboration et al. (Apr. 2024). "The size-luminosity relation of local active galactic nuclei from interferometric observations of the broad-line region". In: 684, A167, A167. DOI: 10.1051/0004-6361/202348167. arXiv: 2401.07676 [astro-ph.GA].

GRAVITY+ Collaboration et al. (Sept. 2025). "Spatially resolved broad line region in a quasar at z=4: Dynamical black hole mass and prominent outflow". In: *arXiv e-prints*, arXiv:2509.13911, arXiv:2509.13911. DOI: 10.48550/arXiv.2509.13911. arXiv: 2509.13911 [astro-ph.GA].

Green, A. R., I. M. McHardy, and C. Done (Apr. 1999). "The discovery of non-linear X-ray variability in NGC 4051". In: 305.2, pp. 309–318. DOI: 10.1046/j.1365-8711.1999.02370.x.

Green, A. R., I. M. McHardy, and H. J. Lehto (Dec. 1993). "On the nature of rapid X-ray variability in active galactic nuclei." In: 265, pp. 664–680. DOI: 10.1093/mnras/265.3.664.

Greene, J. E. and L. C. Ho (July 2005). "A Comparison of Stellar and Gaseous Kinematics in the Nuclei of Active Galaxies". In: 627, pp. 721–732. DOI: 10.1086/430590. eprint: astro-ph/0503675.

Greene, J. E. et al. (Nov. 2010). "The Lick AGN Monitoring Project: Alternate Routes to a Broad-line Region Radius". In: 723, pp. 409–416. DOI: 10.1088/0004-637X/723/1/409. arXiv: 1009.0532 [astro-ph.CO].

Greenhill, L. J. et al. (Jan. 2003). "The Discovery of H_2O Maser Emission in Seven Active Galactic Nuclei and at High Velocities in the Circinus Galaxy". In: 582.1, pp. L11–L14. DOI: 10.1086/367602. arXiv: astro-ph/0212038 [astro-ph].

Grier, C. J. et al. (Aug. 2012). "Reverberation Mapping Results for Five Seyfert 1 Galaxies". In: 755, 60, p. 60. DOI: 10.1088/0004-637X/755/1/60. arXiv: 1206.6523.

Grossmann, A., R. Kronland-Martinet, and J. Morlet (Jan. 1989). "Reading and Understanding Continuous Wavelet Transforms". In: *Wavelets. Time-Frequency Methods and Phase Space*. Ed. by Jean-Michel Combes, Alexander Grossmann, and Philippe Tchamitchian, p. 2.

Grossmann, A. and J. Morlet (1984). "Decomposition of Hardy Functions into Square Integrable Wavelets of Constant Shape". In: *SIAM Journal on Mathematical Analysis* 15.4, pp. 723–736. DOI: 10.1137/0515056. eprint: https://doi.org/10.1137/0515056. URL: https://doi.org/10.1137/0515056.

Grünwald, G. et al. (Jan. 2023). "The first look at narrow-line Seyfert 1 galaxies with eROSITA". In: 669, A37, A37. DOI: 10.1051/0004-6361/202244620. arXiv: 2211.06184 [astro-ph.HE].

Grupe, D. (Sept. 2000). "Statistical properties of narrow-line Seyfert 1 galaxies". In: *New Astron. Rev.* 44, pp. 455–460. DOI: 10.1016/S1387-6473(00)00080-4. eprint: astro-ph/0005139.

Grupe, D. et al. (Mar. 2010). "The Simultaneous Optical-to-X-Ray Spectral Energy Distribution of Soft X-Ray Selected Active Galactic Nuclei Observed by Swift". In: 187, pp. 64–106. DOI: 10.1088/0067-0049/187/1/64. arXiv: 1001.3140.

Guainazzi, M., G. Matt, and G. C. Perola (Dec. 2005). "X-ray obscuration and obscured AGN in the local universe". In: 444.1, pp. 119–132. DOI: 10.1051/0004-6361:20053643. arXiv: astro-ph/0508265 [astro-ph].

Guilbert, P. W. and M. J. Rees (July 1988). "'Cold' material in non-thermal sources." In: 233, pp. 475–484. DOI: 10.1093/mnras/233.2.475.

Haardt, F. and L. Maraschi (Oct. 1991). "A Two-Phase Model for the X-Ray Emission from Seyfert Galaxies". In: 380, p. L51. DOI: 10.1086/186171.

Haardt, Francesco and Laura Maraschi (Aug. 1993). "X-Ray Spectra from Two-Phase Accretion Disks". In: 413, p. 507. DOI: 10.1086/173020.

Hagino, Kouichi et al. (Oct. 2016). "A disc wind interpretation of the strong Fe Kα features in 1H 0707-495". In: 461.4, pp. 3954–3963. DOI: 10.1093/mnras/stw1579. arXiv: 1509.05645 [astro-ph.HE].

Hameury, J. M., M. Viallet, and J. P. Lasota (Mar. 2009). "The thermal-viscous disk instability model in the AGN context". In: 496.2, pp. 413–421. DOI: 10.1051/0004-6361/200810928. arXiv: 0901.1229 [astro-ph.GA].

Hancock, S., A. J. Young, and P. Chainakun (Mar. 2023). "Extended corona models of X-ray reverberation in the AGN 1H 0707-495 and IRAS 13224-3809". In: 520.1, pp. 180–192. DOI: 10.1093/mnras/stad144. arXiv: 2301.04731 [astro-ph.HE].

Hardcastle, M. J., D. A. Evans, and J. H. Croston (Aug. 2006). "The X-ray nuclei of intermediate-redshift radio sources". In: 370.4, pp. 1893–1904. DOI: 10.1111/j.1365-2966.2006.10615.x. arXiv: astro-ph/0603090 [astro-ph].

Hardee, Philip E. and Alexander Rosen (Oct. 1999). "On the Dynamics and Structure of Three-dimensional Trans-Alfvénic Jets". In: 524.2, pp. 650–666. DOI: 10.1086/307833. arXiv: astro-ph/9906490 [astro-ph].

Harrison, C. M. et al. (July 2014). "Kiloparsec-scale outflows are prevalent among luminous AGN: outflows and feedback in the context of the overall AGN population". In: 441.4, pp. 3306–3347. DOI: 10.1093/mnras/stu515. arXiv: 1403.3086 [astro-ph.GA].

Hartman, J. D. and G. Á. Bakos (Oct. 2016). "VARTOOLS: A program for analyzing astronomical time-series data". In: *Astronomy and Computing* 17, pp. 1–72. DOI: 10.1016/j.ascom.2016.05.006. arXiv: 1605.06811 [astro-ph.IM].

Hawking, S. W. (Mar. 1974). "Black hole explosions?" In: 248.5443, pp. 30–31. DOI: 10.1038/248030a0.

Hawkins, M. R. S. (Jan. 2002). "Variability in active galactic nuclei: confrontation of models with observations". In: 329.1, pp. 76–86. DOI: 10.1046/j.1365-8711.2002.04939.x. arXiv: astro-ph/0110707 [astro-ph].

Heckman, T. M. and P. N. Best (Aug. 2014). "The Coevolution of Galaxies and Supermassive Black Holes: Insights from Surveys of the Contemporary Universe". In: 52, pp. 589–660. DOI: 10.1146/annurev-astro-081913-035722. arXiv: 1403.4620.

Heinz, S. and R. A. Sunyaev (Aug. 2003). "The non-linear dependence of flux on black hole mass and accretion rate in core-dominated jets". In: 343, pp. L59–L64. DOI: 10.1046/j.1365-8711.2003.06918.x. eprint: astro-ph/0305252.

Helfand, David J., Richard L. White, and Robert H. Becker (Mar. 2015). "The Last of FIRST: The Final Catalog and Source Identifications". In: 801.1, 26, p. 26. DOI: 10.1088/0004-637X/801/1/26. arXiv: 1501.01555 [astro-ph.GA].

Henri, G. and P. O. Petrucci (Oct. 1997). "Anisotropic illumination of AGN's accretion disk by a non thermal source. I. General theory and application to the Newtonian geometry." In: 326, pp. 87–98. DOI: 10.48550/arXiv.astro-ph/9705233. arXiv: astro-ph/9705233 [astro-ph].

Hibschman, Johann A. and Jonathan Arons (Oct. 2001). "Pair Production Multiplicities in Rotation-powered Pulsars". In: 560.2, pp. 871–884. DOI: 10.1086/323069. arXiv: astro-ph/0107209 [astro-ph].

Ho, L. C. and C. Y. Peng (July 2001). "Nuclear Luminosities and Radio Loudness of Seyfert Nuclei". In: 555, pp. 650–662. DOI: 10.1086/321524. eprint: astro-ph/0102502.

Hogg, J. Drew and Christopher S. Reynolds (July 2016). "Testing the Propagating Fluctuations Model with a Long, Global Accretion Disk Simulation". In: 826.1, 40, p. 40. DOI: 10.3847/0004-637X/826/1/40. arXiv: 1512.05350 [astro-ph.HE].

Homan, D. C. et al. (Dec. 2021). "MOJAVE. XIX. Brightness Temperatures and Intrinsic Properties of Blazar Jets". In: 923.1, 67, p. 67. DOI: 10.3847/1538-4357/ac27af. arXiv: 2109.04977 [astro-ph.HE].

Hönig, S. F. and M. Kishimoto (Oct. 2011). "Constraining properties of dusty environments by infrared variability". In: 534, A121, A121. DOI: 10.1051/0004-6361/201117750. arXiv: 1109.3465 [astro-ph.CO].

Hota, A. et al. (Oct. 2011). "Discovery of a spiral-host episodic radio galaxy". In: 417, pp. L36–L40. DOI: 10.1111/j.1745-3933.2011.01115.x. arXiv: 1107.4742.

Hovatta, T. et al. (July 2008). "Long-term radio variability of AGN: flare characteristics". In: 485.1, pp. 51–61. DOI: 10.1051/0004-6361:200809806. arXiv: 0805.1283 [astro-ph].

Hovatta, T. et al. (Feb. 2009). "Doppler factors, Lorentz factors and viewing angles for quasars, BL Lacertae objects and radio galaxies". In: 494.2, pp. 527–537. DOI: 10.1051/0004-6361:200811150. arXiv: 0811.4278 [astro-ph].

Howell, Steve B. et al. (Apr. 2014). "The K2 Mission: Characterization and Early Results". In: 126.938, p. 398. DOI: 10.1086/676406. arXiv: 1402.5163 [astro-ph.IM].

Hoyle, F. and W. A. Fowler (Jan. 1963). "On the nature of strong radio sources". In: 125, p. 169. DOI: 10.1093/mnras/125.2.169.

Hu, C. et al. (May 2015). "Supermassive Black Holes with High Accretion Rates in Active Galactic Nuclei. III. Detection of Fe II Reverberation in Nine Narrow-line Seyfert 1 Galaxies". In: 804, 138, p. 138. DOI: 10.1088/0004-637X/804/2/138. arXiv: 1503.03611.

Hu, Chin-Ping et al. (June 2014). "Tracking the Evolution of Quasi-periodic Oscillation in RE J1034+396 Using the Hilbert-Huang Transform". In: 788.1, 31, p. 31. DOI: 10.1088/0004-637X/788/1/31. arXiv: 1404.5108 [astro-ph.HE].

Hubble, E. P. (Dec. 1926). "Extragalactic nebulae." In: 64. DOI: 10.1086/143018.
Hughes, P. A., H. D. Aller, and M. F. Aller (Nov. 1985). "Polarized radio outbursts in BL Lacertae. II. The flux and polarization of a piston-driven shock." In: 298, pp. 301–315. DOI: 10.1086/163611.
— (June 1989). "Synchrotron Emission from Shocked Relativistic Jets. II. A Model for the Centimeter Wave Band Quiescent and Burst Emission from BL Lacertae". In: 341, p. 68. DOI: 10.1086/167472.
Hutchings, J. B., T. Janson, and S. G. Neff (July 1989). "What Is the Difference between Radio-loud and Radio-quiet Objects?" In: 342, p. 660. DOI: 10.1086/167626.
Ichimaru, S. (June 1977). "Bimodal behavior of accretion disks: theory and application to Cygnus X-1 transitions." In: 214, pp. 840–855. DOI: 10.1086/155314.
Ilić, D. et al. (Dec. 2015). "Line Shape Variability in a Sample of AGN with Broad Lines". In: *Journal of Astrophysics and Astronomy* 36.4, pp. 433–445. DOI: 10.1007/s12036-015-9360-y. arXiv: 1510.02162 [astro-ph.GA].
Ilić, Dragana et al. (Sept. 2017). "Long-Term Monitoring of the Broad-Line Region Properties in a Selected Sample of AGN". In: *Frontiers in Astronomy and Space Sciences* 4, 12, p. 12. DOI: 10.3389/fspas.2017.00012. arXiv: 1803.10860 [astro-ph.GA].
Impey, C. D. and G. Neugebauer (Feb. 1988). "Energy Distributions of Blazars". In: 95, p. 307. DOI: 10.1086/114638.
Impey, Christopher D. et al. (Dec. 2011). "AGN and Host Galaxies in the COSMOS Survey". In: *Tracing the Ancestry of Galaxies*. Ed. by Claude Carignan, Françoise Combes, and Ken C. Freeman. Vol. 277. IAU Symposium, pp. 21–25. DOI: 10.1017/S1743921311022381.
Irwin, Alan W. et al. (Feb. 1989). "Long-Period Radial-Velocity Variations of Arcturus". In: 101, p. 147. DOI: 10.1086/132415.
Istomin, Y. N. (Jan. 2004). "Origin of Giant Radio Pulses". In: *Young Neutron Stars and Their Environments*. Ed. by Fernando Camilo and Bryan M. Gaensler. Vol. 218. IAU Symposium, p. 369.
Ivezić, Željko et al. (Mar. 2019). "LSST: From Science Drivers to Reference Design and Anticipated Data Products". In: 873.2, 111, p. 111. DOI: 10.3847/1538-4357/ab042c. arXiv: 0805.2366 [astro-ph].
Järvelä, E., A. Lähteenmäki, and M. Berton (Nov. 2018). "Near-infrared morphologies of the host galaxies of narrow-line Seyfert 1 galaxies". In: 619, A69, A69. DOI: 10.1051/0004-6361/201832876. arXiv: 1807.02970.
Järvelä, E., A. Lähteenmäki, and J. León-Tavares (Jan. 2015). "Statistical multifrequency study of narrow-line Seyfert 1 galaxies". In: 573, A76, A76. DOI: 10.1051/0004-6361/201424694. arXiv: 1410.2743.
Järvelä, E., A. Lähteenmäki, and H. Lietzen (Nov. 2017). "Large-Scale Environment Properties of Narrow-Line Seyfert 1 Galaxies at z 0.4". In: *Frontiers in Astronomy and Space Sciences* 4, 54, p. 54. DOI: 10.3389/fspas.2017.00054.
Järvelä, E. et al. (Sept. 2017). "Large-scale environments of narrow-line Seyfert 1 galaxies". In: 606, A9, A9. DOI: 10.1051/0004-6361/201731318. arXiv: 1707.01411 [astro-ph.GA].
Järvelä, E. et al. (Feb. 2022). "Unravelling the origin of extended radio emission in narrow-line Seyfert 1 galaxies with the JVLA". In: 658, A12, A12. DOI: 10.1051/0004-6361/202141698. arXiv: 2109.07841 [astro-ph.GA].
Järvelä, E. et al. (July 2024). "Unprecedented extreme high-frequency radio variability in early-stage active galactic nuclei". In: DOI: 10.1093/mnras/stae1701.

Järvelä, Emilia, Marco Berton, and Luca Crepaldi (Sept. 2021). "Narrow-line Seyfert 1 galaxies with absorbed jets -insights from radio spectral index maps". In: *Frontiers in Astronomy and Space Sciences* 8, 147, p. 147. DOI: 10.3389/fspas.2021.735310. arXiv: 2108.08521 [astro-ph.GA].

Javadi, Atefeh et al. (Mar. 2015). "The UK Infrared Telescope M33 monitoring project - IV. Variable red giant stars across the galactic disc". In: 447.4, pp. 3973–3991. DOI: 10.1093/mnras/stu2637. arXiv: 1412.3840 [astro-ph.SR].

Jin, C. et al. (Oct. 2017). "Super-Eddington QSO RX J0439.6-5311 - II. Multiwavelength constraints on the global structure of the accretion flow". In: 471, pp. 706–721. DOI: 10.1093/mnras/stx1634. arXiv: 1706.08125 [astro-ph.HE].

Jin, Chichuan, Martin Ward, and Chris Done (Sept. 2012). "A combined optical and X-ray study of unobscured type 1 active galactic nuclei - III. Broad-band SED properties". In: 425.2, pp. 907–929. DOI: 10.1111/j.1365-2966.2012.21272.x. arXiv: 1205.1846 [astro-ph.HE].

Jones, T. W., S. L. O'Dell, and W. A. Stein (Mar. 1974). "Physics of Compact Nonthermal Sources. I. Theory of Radiation Processes". In: 188, pp. 353–368. DOI: 10.1086/152724.

Kalberla, P. M. W. et al. (Sept. 2005). "The Leiden/Argentine/Bonn (LAB) Survey of Galactic HI. Final data release of the combined LDS and IAR surveys with improved stray-radiation corrections". In: 440.2, pp. 775–782. DOI: 10.1051/0004-6361:20041864. arXiv: astro-ph/0504140 [astro-ph].

Kammoun, E. S. et al. (Jan. 2021). "UV/Optical Disk Thermal Reverberation in Active Galactic Nuclei: An In-depth Study with an Analytic Prescription for Time-lag Spectra". In: 907.1, 20, p. 20. DOI: 10.3847/1538-4357/abcb93. arXiv: 2011.08563 [astro-ph.HE].

Kankkunen, S., M. Tornikoski, and T. Hovatta (Jan. 2025). "Active galactic nucleus time-variability analysis and its caveats". In: 693, A319, A319. DOI: 10.1051/0004-6361/202450562. arXiv: 2412.08192 [astro-ph.GA].

Kara, E. et al. (July 2017). "The high-Eddington NLS1 Ark 564 has the coolest corona". In: 468.3, pp. 3489–3498. DOI: 10.1093/mnras/stx792. arXiv: 1703.09815 [astro-ph.HE].

Kaspi, Shai et al. (Apr. 2000). "Reverberation Measurements for 17 Quasars and the Size-Mass-Luminosity Relations in Active Galactic Nuclei". In: 533.2, pp. 631–649. DOI: 10.1086/308704. arXiv: astro-ph/9911476 [astro-ph].

Katz, J. I. (Mar. 1997). "A Precessing Disk in OJ 287?" In: 478.2, pp. 527–529. DOI: 10.1086/303811.

Kaviraj, Sugata et al. (Dec. 2015). "Radio AGN in spiral galaxies". In: 454.2, pp. 1595–1604. DOI: 10.1093/mnras/stv1957. arXiv: 1412.5602 [astro-ph.GA].

Kazanas, Demosthenes and Sergei Nayakshin (Apr. 2001). "Modeling the X-Ray-Optical Correlations in NGC 3516". In: 550.2, pp. 655–667. DOI: 10.1086/319786. arXiv: astro-ph/0007421 [astro-ph].

Kellermann, K. I. et al. (Oct. 1989). "VLA observations of objects in the Palomar Bright Quasar Survey". In: 98, pp. 1195–1207. DOI: 10.1086/115207.

Kelly, Brandon C., Jill Bechtold, and Aneta Siemiginowska (June 2009). "Are the Variations in Quasar Optical Flux Driven by Thermal Fluctuations?" In: 698.1, pp. 895–910. DOI: 10.1088/0004-637X/698/1/895. arXiv: 0903.5315 [astro-ph.CO].

Khachikian, E. Y. and D. W. Weedman (Sept. 1974). "An atlas of Seyfert galaxies". In: 192, pp. 581–589. DOI: 10.1086/153093.

Kharb, P. et al. (Nov. 2006). "A Radio Study of the Seyfert Galaxy Markarian 6: Implications for Seyfert Life Cycles". In: 652.1, pp. 177–188. DOI: 10.1086/507945. arXiv: astro-ph/0607603 [astro-ph].

Kiehlmann, Sebastian (May 2015). "Origin of the gamma-ray emission in AGN jets - A multi-wavelength photometry and polarimetry data analysis of the quasar 3C 279". PhD thesis. Andreas Eckart University of Cologne, Germany.

Kim, Dae-Won et al. (July 2011). "Quasi-stellar Object Selection Algorithm Using Time Variability and Machine Learning: Selection of 1620 Quasi-stellar Object Candidates from MACHO Large Magellanic Cloud Database". In: 735.2, 68, p. 68. DOI: 10.1088/0004-637X/735/2/68. arXiv: 1101.3316 [astro-ph.IM].

Kim, Dae-Won et al. (June 2014). "The EPOCH Project. I. Periodic variable stars in the EROS-2 LMC database". In: 566, A43, A43. DOI: 10.1051/0004-6361/201323252. arXiv: 1403.6131 [astro-ph.IM].

Kinney, A. L. et al. (July 2000). "Jet Directions in Seyfert Galaxies". In: 537, pp. 152–177. DOI: 10.1086/309016. eprint: astro-ph/0002131.

Kochanek, C. S. (Apr. 2004). "Quantitative Interpretation of Quasar Microlensing Light Curves". In: 605.1, pp. 58–77. DOI: 10.1086/382180. arXiv: astro-ph/0307422 [astro-ph].

Kochanek, C. S. et al. (Oct. 2017). "The All-Sky Automated Survey for Supernovae (ASAS-SN) Light Curve Server v1.0". In: 129.980, p. 104502. DOI: 10.1088/1538-3873/aa80d9. arXiv: 1706.07060 [astro-ph.SR].

Kollatschny, W. and M. Zetzl (Feb. 2011). "Broad-line active galactic nuclei rotate faster than narrow-line ones". In: 470, pp. 366–368. DOI: 10.1038/nature09761.

— (Jan. 2013a). "The shape of broad-line profiles in active galactic nuclei". In: 549, A100, A100. DOI: 10.1051/0004-6361/201219411. arXiv: 1211.3065.

— (2013b). "Vertical broad-line region structure in nearby active galactic nuclei". In: 558, A26, A26. DOI: 10.1051/0004-6361/201321685. arXiv: 1308.1902 [astro-ph.CO].

Komatsu, E. et al. (Feb. 2011). "Seven-year Wilkinson Microwave Anisotropy Probe (WMAP) Observations: Cosmological Interpretation". In: 192, 18, p. 18. DOI: 10.1088/0067-0049/192/2/18. arXiv: 1001.4538 [astro-ph.CO].

Komossa, S. (Apr. 2018). "Multi-wavelength properties of radio-loud Narrow-line Seyfert 1 galaxies". In: *Proceedings of Science, vol. Revisiting narrow-line Seyfert 1 galaxies and their place in the Universe*, 15, p. 15. arXiv: 1807.03666.

Komossa, S. and J. Meerschweinchen (Feb. 2000). "X-ray emission/absorption mechanisms of 4 NLSy-1-like AGN and a radio quasar. QSO 0117-2837, RX J0134.3-4258, NGC 4051, Mrk 1298, 4C +74.26". In: 354, pp. 411–422. eprint: astro-ph/9911429.

Komossa, S. et al. (Aug. 2006). "Radio-loud Narrow-Line Type 1 Quasars". In: 132, pp. 531–545. DOI: 10.1086/505043. eprint: astro-ph/0603680.

Komossa, S. et al. (June 2008). "On the Nature of Seyfert Galaxies with High [O III] λ5007 Blueshifts". In: 680, pp. 926–938. DOI: 10.1086/587932. arXiv: 0803.0240.

Komossa, S. et al. (July 2024). "The extremes of AGN variability: outbursts, deep fades, changing looks, exceptional spectral states, and semi-periodicities". In: *arXiv e-prints*, arXiv:2408.00089, arXiv:2408.00089. DOI: 10.48550/arXiv.2408.00089. arXiv: 2408.00089 [astro-ph.HE].

Komossa, Stefanie and Norbert Bade (Mar. 1999). "The giant X-ray outbursts in NGC 5905 and IC 3599:() hfill Follow-up observations and outburst scenarios". In: 343, pp. 775–787. DOI: 10.48550/arXiv.astro-ph/9901141. arXiv: astro-ph/9901141 [astro-ph].

Kormendy, J. and L. C. Ho (Aug. 2013). "Coevolution (Or Not) of Supermassive Black Holes and Host Galaxies". In: 51, pp. 511–653. DOI: 10.1146/annurev-astro-082708-101811. arXiv: 1304.7762.

Kovačević, J., L. Č. Popović, and M. S. Dimitrijević (July 2010). "Analysis of Optical Fe II Emission in a Sample of Active Galactic Nucleus Spectra". In: 189, pp. 15–36. DOI: 10.1088/0067-0049/189/1/15. arXiv: 1004.2212 [astro-ph.CO].

Kovačević, Jelena, Luka Č. Popović, and Milan S. Dimitrijević (July 2010). "Analysis of Optical Fe II Emission in a Sample of Active Galactic Nucleus Spectra". In: 189.1, pp. 15–36. DOI: 10.1088/0067-0049/189/1/15. arXiv: 1004.2212 [astro-ph.CO].

Kozłowski, Szymon (Feb. 2017). "A Method to Measure the Unbiased Decorrelation Timescale of the AGN Variable Signal from Structure Functions". In: 835.2, 250, p. 250. DOI: 10.3847/1538-4357/aa56c0. arXiv: 1701.00005 [astro-ph.GA].

Kozłowski, Szymon et al. (Jan. 2010). "Quantifying Quasar Variability as Part of a General Approach to Classifying Continuously Varying Sources". In: 708.2, pp. 927–945. DOI: 10.1088/0004-637X/708/2/927. arXiv: 0909.1326 [astro-ph.CO].

Krongold, Y., D. Dultzin-Hacyan, and P. Marziani (Feb. 2001). "Host Galaxies and Circumgalactic Environment of "Narrow Line" Seyfert 1 Nuclei". In: 121, pp. 702–709. DOI: 10.1086/318768.

Kuo, C. Y. et al. (Jan. 2011). "The Megamaser Cosmology Project. III. Accurate Masses of Seven Supermassive Black Holes in Active Galaxies with Circumnuclear Megamaser Disks". In: 727.1, 20, p. 20. DOI: 10.1088/0004-637X/727/1/20. arXiv: 1008.2146 [astro-ph.CO].

La Mura, G. et al. (Dec. 2007). "Detailed Analysis of Balmer Lines in a Sloan Digital Sky Survey Sample of 90 Broad-Line Active Galactic Nuclei". In: 671.1, pp. 104–117. DOI: 10.1086/522821.

Lähteenmäki, A. and E. Valtaoja (Aug. 1999). "Total Flux Density Variations in Extragalactic Radio Sources. III. Doppler Boosting Factors, Lorentz Factors, and Viewing Angles for Active Galactic Nuclei". In: 521.2, pp. 493–501. DOI: 10.1086/307587.

Lähteenmäki, A. et al. (July 2017). "37 GHz observations of narrow-line Seyfert 1 galaxies". In: 603, A100, A100. DOI: 10.1051/0004-6361/201630257. arXiv: 1703.10365.

Lähteenmäki, A. et al. (June 2018). "Radio jets and gamma-ray emission in radio-silent narrow-line Seyfert 1 galaxies". In: 614, L1, p. L1. DOI: 10.1051/0004-6361/201833378. arXiv: 1806.02058.

LaMassa, Stephanie M. et al. (Feb. 2015). "The Discovery of the First "Changing Look" Quasar: New Insights Into the Physics and Phenomenology of Active Galactic Nucleus". In: 800.2, 144, p. 144. DOI: 10.1088/0004-637X/800/2/144. arXiv: 1412.2136 [astro-ph.GA].

Lanzuisi, G. et al. (May 2016). "NuSTAR reveals the extreme properties of the super-Eddington accreting supermassive black hole in PG 1247+267". In: 590, A77, A77. DOI: 10.1051/0004-6361/201628325. arXiv: 1604.02462 [astro-ph.HE].

Laor, A. (Nov. 2000). "On Black Hole Masses and Radio Loudness in Active Galactic Nuclei". In: 543, pp. L111–L114. DOI: 10.1086/317280. eprint: astro-ph/0009192.

Larson, S. et al. (May 2003). "The CSS and SSS NEO surveys". In: *AAS/Division for Planetary Sciences Meeting Abstracts #35*. Vol. 35. AAS/Division for Planetary Sciences Meeting Abstracts, 36.04, p. 36.04.

Lawrence, A. et al. (Nov. 1988). "Extreme Fe II emission from an IRAS quasar." In: 235, pp. 261–268. DOI: 10.1093/mnras/235.1.261.

Letawe, G. et al. (June 2007). "On-axis spectroscopy of the host galaxies of 20 optically luminous quasars at z ~ 0.3". In: 378, pp. 83–108. DOI: 10.1111/j.1365-2966.2007.11741.x. eprint: astro-ph/0605288.

Liang, E. P. T. (Aug. 1979). "On the hard X-ray emission mechanism of active galactic nuclei sources." In: 231, pp. L111–L114. DOI: 10.1086/183015.

Liodakis, I. et al. (June 2017). "Bimodal radio variability in OVRO-40 m-monitored blazars". In: 467.4, pp. 4565–4576. DOI: 10.1093/mnras/stx432. arXiv: 1702.05493 [astro-ph.HE].

Lisakov, M. M. et al. (July 2017). "A connection between γ-ray and parsec-scale radio flares in the blazar 3C 273". In: 468.4, pp. 4478–4493. DOI: 10.1093/mnras/stx710. arXiv: 1703.07976 [astro-ph.GA].

Liska, M. T. P. et al. (Aug. 2022). "Formation of Magnetically Truncated Accretion Disks in 3D Radiation-transport Two-temperature GRMHD Simulations". In: 935.1, L1, p. L1. DOI: 10.3847/2041-8213/ac84db. arXiv: 2201.03526 [astro-ph.HE].

Lister, M. L. et al. (July 2016). "MOJAVE: XIII. Parsec-scale AGN Jet Kinematics Analysis Based on 19 years of VLBA Observations at 15 GHz". In: 152, 12, p. 12. DOI: 10.3847/0004-6256/152/1/12. arXiv: 1603.03882.

Liu, X. et al. (2016). "Properties of the Narrow Line Seyfert 1 Galaxies Revisited". In: *International Journal of Astronomy and Astrophysics* 6, pp. 166–174. DOI: 10.4236/ijaa.2016.62014. arXiv: 1605.01553.

Lohfink, A. M. et al. (Jan. 2013). "Tackling the soft X-ray excess in AGN with variability studies ." In: 84, p. 699. DOI: 10.48550/arXiv.1301.4997. arXiv: 1301.4997 [astro-ph.HE].

Lomb, N. R. (Feb. 1976). "Least-Squares Frequency Analysis of Unequally Spaced Data". In: 39.2, pp. 447–462. DOI: 10.1007/BF00648343.

Longair, Malcolm S. (2011). *High Energy Astrophysics*.

Lyubarskii, Yu. E. (Dec. 1997). "Flicker noise in accretion discs". In: 292.3, pp. 679–685. DOI: 10.1093/mnras/292.3.679.

Lyubarsky, Yuri (July 2020). "Fast Radio Bursts from Reconnection in a Magnetar Magnetosphere". In: 897.1, 1, p. 1. DOI: 10.3847/1538-4357/ab97b5. arXiv: 2001.02007 [astro-ph.HE].

Lyutikov, Maxim (Nov. 2002). "Radio Emission from Magnetars". In: 580.1, pp. L65–L68. DOI: 10.1086/345493. arXiv: astro-ph/0206439 [astro-ph].

— (Apr. 2006). "Magnetar giant flares and afterglows as relativistic magnetized explosions". In: 367.4, pp. 1594–1602. DOI: 10.1111/j.1365-2966.2006.10069.x. arXiv: astro-ph/0511711 [astro-ph].

— (Mar. 2017). "Fast Radio Bursts' Emission Mechanism: Implication from Localization". In: 838.1, L13, p. L13. DOI: 10.3847/2041-8213/aa62fa. arXiv: 1701.02003 [astro-ph.HE].

— (Dec. 2021). "Coherent Emission in Pulsars, Magnetars, and Fast Radio Bursts: Reconnection-driven Free Electron Laser". In: 922.2, 166, p. 166. DOI: 10.3847/1538-4357/ac1b32. arXiv: 2102.07010 [astro-ph.HE].

Lyutikov, Maxim and Sergey Popov (May 2020). "Fast Radio Bursts from reconnection events in magnetar magnetospheres". In: *arXiv e-prints*, arXiv:2005.05093, arXiv:2005.05093. DOI: 10.48550/arXiv.2005.05093. arXiv: 2005.05093 [astro-ph.HE].

Macchetto, F. et al. (Nov. 1997). "The Supermassive Black Hole of M87 and the Kinematics of Its Associated Gaseous Disk". In: 489.2, pp. 579–600. DOI: 10.1086/304823. arXiv: astro-ph/9706252 [astro-ph].

MacLeod, C. L. et al. (Oct. 2010). "Modeling the Time Variability of SDSS Stripe 82 Quasars as a Damped Random Walk". In: 721.2, pp. 1014–1033. DOI: 10.1088/0004-637X/721/2/1014. arXiv: 1004.0276 [astro-ph.CO].

Maehara, H. (2014). "The Unanticipated Phenomenology of the Blazar PKS 2131-021: A Unique Supermassive Black Hole Binary Candidate". In: *JAXA Research and Development Report JAXA-RR-13-010*.

MAGIC Collaboration et al. (Feb. 2023). "Long-term multi-wavelength study of 1ES 0647+250". In: 670, A49, A49. DOI: 10.1051/0004-6361/202244477. arXiv: 2211.13268 [astro-ph.HE].

Malkan, Matthew A., Varoujan Gorjian, and Raymond Tam (July 1998). "A Hubble Space Telescope Imaging Survey of Nearby Active Galactic Nuclei". In: 117.1, pp. 25–88. DOI: 10.1086/313110. arXiv: astro-ph/9803123 [astro-ph].

Mandal, Amit Kumar et al. (Jan. 2021). "Estimation of the size and structure of the broad line region using Bayesian approach". In: DOI: 10.1093/mnras/stab012. arXiv: 2101.00802 [astro-ph.GA].

Marinello, M. et al. (Apr. 2016). "The Fe II Emission in Active Galactic Nuclei: Excitation Mechanisms and Location of the Emitting Region". In: 820, 116, p. 116. DOI: 10.3847/0004-637X/820/2/116.

Marinucci, A. et al. (Nov. 2022). "Polarization constraints on the X-ray corona in Seyfert Galaxies: MCG-05-23-16". In: 516.4, pp. 5907–5913. DOI: 10.1093/mnras/stac2634. arXiv: 2207.09338 [astro-ph.HE].

Markoff, Sera et al. (Oct. 2015). "As Above, So Below: Exploiting Mass Scaling in Black Hole Accretion to Break Degeneracies in Spectral Interpretation". In: 812.2, L25, p. L25. DOI: 10.1088/2041-8205/812/2/L25. arXiv: 1510.02244 [astro-ph.HE].

Marscher, A. P. and W. K. Gear (Nov. 1985). "Models for high-frequency radio outbursts in extragalactic sources, with application to the early 1983 millimeter-to-infrared flare of 3C 273." In: 298, pp. 114–127. DOI: 10.1086/163592.

Martocchia, A., V. Karas, and G. Matt (Mar. 2000). "Effects of Kerr space-time on spectral features from X-ray illuminated accretion discs". In: 312.4, pp. 817–826. DOI: 10.1046/j.1365-8711.2000.03205.x. arXiv: astro-ph/9910562 [astro-ph].

Martocchia, Andrea and Giorgio Matt (Oct. 1996). "Iron Kalpha line intensity from accretion discs around rotating black holes". In: 282.4, pp. L53–L57. DOI: 10.1093/mnras/282.4.L53.

Marziani, P. et al. (2001). "Searching for the Physical Drivers of the Eigenvector 1 Correlation Space". In: 558.2, pp. 553–560. DOI: 10.1086/322286. arXiv: astro-ph/0105343 [astro-ph].

Marziani, P. et al. (Nov. 2003). "Searching for the physical drivers of eigenvector 1: influence of black hole mass and Eddington ratio". In: 345, pp. 1133–1144. DOI: 10.1046/j.1365-2966.2003.07033.x. eprint: astro-ph/0307367.

Marziani, P. et al. (Jan. 2016). "The most powerful quasar outflows as revealed by the Civ λ1549 resonance line". In: 361, 29, p. 29. DOI: 10.1007/s10509-015-2611-1. arXiv: 1512.00381 [astro-ph.GA].

Marziani, P. et al. (Mar. 2018a). "A main sequence for quasars". In: *Frontiers in Astronomy and Space Sciences* 5, 6, p. 6. DOI: 10.3389/fspas.2018.00006. arXiv: 1802.05575.

Marziani, P. et al. (Apr. 2018b). "Narrow-line Seyfert 1s: what is wrong in a name?" In: *Proceedings of Science, vol. Revisiting narrow-line Seyfert 1 galaxies and their place in the Universe*, 2, p. 2. arXiv: 1807.03003.

Marziani, Paola, Deborah Dultzin-Hacyan, and Jack W. Sulentic (2006). "Accretion onto Supermassive Black Holes in Quasars: Learning from Optical/UV Observations". In: *New Developments in Black Hole Research*. Ed. by Paul V. Kreitler, p. 123. DOI: 10.48550/arXiv.astro-ph/0606678.

Marziani, Paola et al. (Dec. 2021). "Optical Singly-Ionized Iron Emission in Radio-Quiet and Relativistically Jetted Active Galactic Nuclei". In: *Universe* 7.12, p. 484. DOI: 10.3390/universe7120484. arXiv: 2112.02632 [astro-ph.GA].

Masci, Frank J. et al. (Jan. 2019). "The Zwicky Transient Facility: Data Processing, Products, and Archive". In: 131.995, p. 018003. DOI: 10.1088/1538-3873/aae8ac. arXiv: 1902.01872 [astro-ph.IM].

Mathur, S. (June 2000). "Narrow-line Seyfert 1 galaxies and the evolution of galaxies and active galaxies". In: 314, pp. L17–L20. DOI: 10.1046/j.1365-8711.2000.03530.x. eprint: astro-ph/0003111.

Mathur, S. et al. (Aug. 2012). "Supermassive Black Holes, Pseudobulges, and the Narrow-line Seyfert 1 Galaxies". In: 754, 146, p. 146. DOI: 10.1088/0004-637X/754/2/146. arXiv: 1102.0537 [astro-ph.CO].

Matt, G., A. C. Fabian, and R. R. Ross (May 1993). "Iron K-alpha lines from X-ray photoionized accretion discs." In: 262, pp. 179–186. DOI: 10.1093/mnras/262.1.179.

Matt, G., G. C. Perola, and L. Piro (July 1991). "The iron line and high energy bump as X-ray signatures of cold matter in Seyfert 1 galaxies." In: 247, p. 25.

Matthews, Thomas A. and Allan R. Sandage (July 1963). "Optical Identification of 3C 48, 3C 196, and 3C 286 with Stellar Objects." In: 138, p. 30. DOI: 10.1086/147615.

Max-Moerbeck, W. et al. (Nov. 2014). "A method for the estimation of the significance of cross-correlations in unevenly sampled red-noise time series". In: 445.1, pp. 437–459. DOI: 10.1093/mnras/stu1707. arXiv: 1408.6265 [astro-ph.IM].

McHardy, I. (2010). "X-Ray Variability of AGN and Relationship to Galactic Black Hole Binary Systems". In: *Lecture Notes in Physics, Berlin Springer Verlag*. Ed. by Tomaso Belloni. Vol. 794, p. 203. DOI: 10.1007/978-3-540-76937-8_8.

McKinney, Jonathan C., Alexander Tchekhovskoy, and Roger D. Blandford (July 2012). "General relativistic magnetohydrodynamic simulations of magnetically choked accretion flows around black holes". In: 423.4, pp. 3083–3117. DOI: 10.1111/j.1365-2966.2012.21074.x. arXiv: 1201.4163 [astro-ph.HE].

McKinney, Jonathan C. et al. (May 2017). "Double Compton and Cyclo-Synchrotron in Super-Eddington Discs, Magnetized Coronae, and Jets". In: 467.2, pp. 2241–2265. DOI: 10.1093/mnras/stx227. arXiv: 1608.08627 [astro-ph.HE].

McLure, R. J. et al. (Sept. 1999). "A comparative HST imaging study of the host galaxies of radio-quiet quasars, radio-loud quasars and radio galaxies - I". In: 308.2, pp. 377–404. DOI: 10.1046/j.1365-8711.1999.02676.x. arXiv: astro-ph/9809030 [astro-ph].

Mejía-Restrepo, Julian E. et al. (July 2022). "BASS. XXV. DR2 Broad-line-based Black Hole Mass Estimates and Biases from Obscuration". In: 261.1, 5, p. 5. DOI: 10.3847/1538-4365/ac6602. arXiv: 2204.05321 [astro-ph.GA].

Melrose, D. B. (Dec. 2017). "Coherent emission mechanisms in astrophysical plasmas". In: *Reviews of Modern Plasma Physics* 1.1, 5, p. 5. DOI: 10.1007/s41614-017-0007-0. arXiv: 1707.02009 [physics.plasm-ph].

Merloni, A., S. Heinz, and T. di Matteo (Nov. 2003). "A Fundamental Plane of black hole activity". In: 345, pp. 1057–1076. DOI: 10.1046/j.1365-2966.2003.07017.x. eprint: astro-ph/0305261.

Middei, R. et al. (Mar. 2017). "A long-term study of AGN X-ray variability . Structure function analysis on a ROSAT-XMM quasar sample". In: 599, A82, A82. DOI: 10.1051/0004-6361/201629940. arXiv: 1612.08547 [astro-ph.HE].

Miller, L., T. J. Turner, and J. N. Reeves (May 2008). "An absorption origin for the X-ray spectral variability of MCG-6-30-15". In: 483.2, pp. 437–452. DOI: 10.1051/0004-6361:200809590. arXiv: 0803.2680 [astro-ph].

Mineshige, Shin et al. (June 2000). "Slim-Disk Model for Soft X-Ray Excess and Variability of Narrow-Line Seyfert 1 Galaxies". In: 52, pp. 499–508. DOI: 10.1093/pasj/52.3.499. arXiv: astro-ph/0003017 [astro-ph].

Mingaliev, M. G. et al. (July 2015). "A study of the synchrotron component in the blazar spectral energy distributions". In: *Astrophysical Bulletin* 70.3, pp. 264–272. DOI: 10.1134/S1990341315030037. arXiv: 1508.01109 [astro-ph.GA].

Miniutti, G. and A. C. Fabian (Apr. 2004). "A light bending model for the X-ray temporal and spectral properties of accreting black holes". In: 349.4, pp. 1435–1448. DOI: 10.1111/j.1365-2966.2004.07611.x. arXiv: astro-ph/0309064 [astro-ph].

Mohan, P. and A. Mangalam (June 2015). "Kinematics of and Emission from Helically Orbiting Blobs in a Relativistic Magnetized Jet". In: 805.2, 91, p. 91. DOI: 10.1088/0004-637X/805/2/91. arXiv: 1503.06551 [astro-ph.HE].

Morgan, Christopher W. et al. (Aug. 2006). "Microlensing of the Lensed Quasar SDSS 0924+0219". In: 647.2, pp. 874–885. DOI: 10.1086/505569. arXiv: astro-ph/0601523 [astro-ph].

— (Apr. 2010). "The Quasar Accretion Disk Size-Black Hole Mass Relation". In: 712.2, pp. 1129–1136. DOI: 10.1088/0004-637X/712/2/1129. arXiv: 1002.4160 [astro-ph.CO].

Morganti, R. (Nov. 2017). "The many routes to AGN feedback". In: *Frontiers in Astronomy and Space Sciences* 4, 42, p. 42. DOI: 10.3389/fspas.2017.00042. arXiv: 1712.05301.

Munari, Ulisse et al. (Dec. 2014). "APASS discovery and characterization of 180 variable stars in Aquarius". In: *Journal of Astronomical Data* 20, p. 4.

Narayan, R. and I. Yi (Oct. 1995). "Advection-dominated Accretion: Underfed Black Holes and Neutron Stars". In: 452, p. 710. DOI: 10.1086/176343. eprint: astro-ph/9411059.

Narayan, Ramesh, Igor V. Igumenshchev, and Marek A. Abramowicz (Dec. 2003). "Magnetically Arrested Disk: an Energetically Efficient Accretion Flow". In: 55, pp. L69–L72. DOI: 10.1093/pasj/55.6.L69. arXiv: astro-ph/0305029 [astro-ph].

Narayan, Ramesh et al. (Nov. 2012). "GRMHD simulations of magnetized advection-dominated accretion on a non-spinning black hole: role of outflows". In: 426.4, pp. 3241–3259. DOI: 10.1111/j.1365-2966.2012.22002.x. arXiv: 1206.1213 [astro-ph.HE].

Nardini, E. et al. (Jan. 2011). "A reflection origin for the soft and hard X-ray excess of Ark 120". In: 410.2, pp. 1251–1261. DOI: 10.1111/j.1365-2966.2010.17518.x. arXiv: 1008.2157 [astro-ph.HE].

Nelson, C. H. and M. Whittle (July 1996). "Stellar and Gaseous Kinematics of Seyfert Galaxies. II. The Role of the Bulge". In: 465, p. 96. DOI: 10.1086/177405.

Nenkova, M. et al. (Sept. 2008a). "AGN Dusty Tori. I. Handling of Clumpy Media". In: 685, pp. 147–159. DOI: 10.1086/590482. arXiv: 0806.0511.

Nenkova, M. et al. (Sept. 2008b). "AGN Dusty Tori. II. Observational Implications of Clumpiness". In: 685, pp. 160–180. DOI: 10.1086/590483. arXiv: 0806.0512.

Netzer, Hagai (Aug. 2015). "Revisiting the Unified Model of Active Galactic Nuclei". In: 53, pp. 365–408. DOI: 10.1146/annurev-astro-082214-122302. arXiv: 1505.00811 [astro-ph.GA].

— (Oct. 2019). "Bolometric correction factors for active galactic nuclei". In: 488.4, pp. 5185–5191. DOI: 10.1093/mnras/stz2016. arXiv: 1907.09534 [astro-ph.GA].

Netzer, Hagai et al. (Sept. 2007). "Spitzer Quasar and ULIRG Evolution Study (QUEST). II. The Spectral Energy Distributions of Palomar-Green Quasars". In: 666.2, pp. 806–816. DOI: 10.1086/520716. arXiv: 0706.0818 [astro-ph].

Neumann, John von (1941). "Distribution of the Ratio of the Mean Square Successive Difference to the Variance". In: *The Annals of Mathematical Statistics* 12.4, pp. 367

–395. DOI: 10.1214/aoms/1177731677. URL: https://doi.org/10.1214/aoms/1177731677.

Neumann, John von (1942). "A Further Remark Concerning the Distribution of the Ratio of the Mean Square Successive Difference to the Variance". In: *The Annals of Mathematical Statistics* 13.1, pp. 86 –88. DOI: 10.1214/aoms/1177731645. URL: https://doi.org/10.1214/aoms/1177731645.

Neustadt, J. M. M. and C. S. Kochanek (June 2022). "Using AGN light curves to map accretion disc temperature fluctuations". In: 513.1, pp. 1046–1062. DOI: 10.1093/mnras/stac888. arXiv: 2201.10565 [astro-ph.GA].

Olguín-Iglesias, Alejandro, Jari Kotilainen, and Vahram Chavushyan (Feb. 2020). "The disc-like host galaxies of radio-loud narrow-line Seyfert 1s". In: 492.1, pp. 1450–1464. DOI: 10.1093/mnras/stz3549. arXiv: 1912.02746 [astro-ph.GA].

O'Neill, S. et al. (Feb. 2022). "The Unanticipated Phenomenology of the Blazar PKS 2131-021: A Unique Supermassive Black Hole Binary Candidate". In: 926.2, L35, p. L35. DOI: 10.3847/2041-8213/ac504b. arXiv: 2111.02436 [astro-ph.HE].

Onori, F. et al. (June 2017). "Detection of faint broad emission lines in type 2 AGN - II. On the measurement of the black hole mass of type 2 AGN and the unified model". In: 468.1, pp. L97–L102. DOI: 10.1093/mnrasl/slx032. arXiv: 1703.05167 [astro-ph.GA].

Orban de Xivry, G. et al. (Nov. 2011). "The role of secular evolution in the black hole growth of narrow-line Seyfert 1 galaxies". In: 417, pp. 2721–2736. DOI: 10.1111/j.1365-2966.2011.19439.x. arXiv: 1104.5023.

Osterbrock, D. E. (Aug. 1977). "Spectrophotometry of Seyfert 1 galaxies". In: 215, pp. 733–745. DOI: 10.1086/155407.

— (Apr. 1991). "Active galactic nuclei". In: *Reports on Progress in Physics* 54, pp. 579–633. DOI: 10.1088/0034-4885/54/4/002.

Osterbrock, D. E. and A. T. Koski (Aug. 1976). "NGC 4151 and Markarian 6 - two intermediate-type Seyfert galaxies". In: 176, 61P–66P. DOI: 10.1093/mnras/176.1.61P.

Osterbrock, D. E. and R. W. Pogge (Oct. 1985). "The spectra of narrow-line Seyfert 1 galaxies". In: 297, pp. 166–176. DOI: 10.1086/163513.

Padovani, P. (Aug. 2017). "On the two main classes of active galactic nuclei". In: *Nature Astronomy* 1, 0194, p. 0194. DOI: 10.1038/s41550-017-0194. arXiv: 1707.08069.

Padovani, P. et al. (Aug. 2017). "Active galactic nuclei: what's in a name?" In: 25.1, 2, p. 2. DOI: 10.1007/s00159-017-0102-9. arXiv: 1707.07134 [astro-ph.GA].

Paliya, V. S. et al. (Jan. 2018). "Gamma-Ray-emitting Narrow-line Seyfert 1 Galaxies in the Sloan Digital Sky Survey". In: 853, L2, p. L2. DOI: 10.3847/2041-8213/aaa5ab. arXiv: 1801.01905 [astro-ph.HE].

Paliya, V. S. et al. (Feb. 2019). "General Physical Properties of Gamma-Ray-emitting Narrow-line Seyfert 1 Galaxies". In: 872, 169, p. 169. DOI: 10.3847/1538-4357/ab01ce. arXiv: 1901.07613 [astro-ph.HE].

Paliya, Vaidehi S. et al. (Jan. 2024). "Narrow-line Seyfert 1 galaxies in Sloan Digital Sky Survey: a new optical spectroscopic catalogue". In: 527.3, pp. 7055–7069. DOI: 10.1093/mnras/stad3650. arXiv: 2311.13818 [astro-ph.GA].

Pan, Hai-Wu et al. (Mar. 2016). "Detection of a Possible X-Ray Quasi-periodic Oscillation in the Active Galactic Nucleus 1H 0707-495". In: 819.2, L19, p. L19. DOI: 10.3847/2041-8205/819/2/L19. arXiv: 1601.07639 [astro-ph.HE].

Panagiotou, Christos et al. (Aug. 2022). "A Physical Model for the UV/Optical Power Spectra of AGN". In: 935.2, 93, p. 93. DOI: 10.3847/1538-4357/ac7e4d. arXiv: 2207.04917 [astro-ph.GA].

Panessa, Francesca et al. (2019). "The origin of radio emission from radio-quiet active galactic nuclei". In: *Nature Astronomy* 3, pp. 387–396. DOI: 10.1038/s41550-019-0765-4. arXiv: 1902.05917 [astro-ph.GA].

Papadakis, I. E. (Feb. 2004). "The scaling of the X-ray variability with black hole mass in active galactic nuclei". In: 348, pp. 207–213. DOI: 10.1111/j.1365-2966.2004.07351.x. eprint: astro-ph/0311016.

Penston, M. V. and E. Perez (Nov. 1984). "An evolutionary link between Seyfert I and II galaxies." In: 211, 33P–39. DOI: 10.1093/mnras/211.1.33P.

Peterson, B. and E. Dalla Bontà (Apr. 2018). "Reverberation Mapping and Implications for Narrow-Line Seyfert 1 Galaxies". In: *Proceedings of Science, vol. Revisiting narrow-line Seyfert 1 galaxies and their place in the Universe*, 8, p. 8.

Peterson, B. M. (Feb. 1997). *An Introduction to Active Galactic Nuclei*.

— (2011). "Masses of Black Holes in Active Galactic Nuclei: Implications for Narrow-Line Seyfert 1 Galaxies". In: *Narrow-Line Seyfert 1 Galaxies and their Place in the Universe*, 32, p. 32.

Peterson, B. M. et al. (Oct. 2004). "Central Masses and Broad-Line Region Sizes of Active Galactic Nuclei. II. A Homogeneous Analysis of a Large Reverberation-Mapping Database". In: 613, pp. 682–699. DOI: 10.1086/423269. eprint: astro-ph/0407299.

Peterson, Bradley M. (Mar. 1993). "Reverberation Mapping of Active Galactic Nuclei". In: 105, p. 247. DOI: 10.1086/133140.

Peterson, Bradley M. and Amri Wandel (Aug. 1999). "Keplerian Motion of Broad-Line Region Gas as Evidence for Supermassive Black Holes in Active Galactic Nuclei". In: 521.2, pp. L95–L98. DOI: 10.1086/312190. arXiv: astro-ph/9905382 [astro-ph].

Petrucci, P. O. and G. Henri (Oct. 1997). "Anisotropic illumination of AGN's accretion disk by a non thermal source. II. General relativistic effects." In: 326, pp. 99–107. DOI: 10.48550/arXiv.astro-ph/9705232. arXiv: astro-ph/9705232 [astro-ph].

Phillipson, R. A., P. T. Boyd, and A. P. Smale (July 2018). "The chaotic long-term X-ray variability of 4U 1705-44". In: 477.4, pp. 5220–5237. DOI: 10.1093/mnras/sty970. arXiv: 1809.06393 [astro-ph.HE].

Piconcelli, E. et al. (Mar. 2005). "The XMM-Newton view of PG quasars. I. X-ray continuum and absorption". In: 432.1, pp. 15–30. DOI: 10.1051/0004-6361:20041621. arXiv: astro-ph/0411051 [astro-ph].

Pollacco, D. L. et al. (Oct. 2006). "The WASP Project and the SuperWASP Cameras". In: 118.848, pp. 1407–1418. DOI: 10.1086/508556. arXiv: astro-ph/0608454 [astro-ph].

Ponti, G. et al. (June 2012). "CAIXA: a catalogue of AGN in the XMM-Newton archive. III. Excess variance analysis". In: 542, A83, A83. DOI: 10.1051/0004-6361/201118326. arXiv: 1112.2744 [astro-ph.HE].

Popov, S. B. and K. A. Postnov (July 2013). "Millisecond extragalactic radio bursts as magnetar flares". In: *arXiv e-prints*, arXiv:1307.4924, arXiv:1307.4924. DOI: 10.48550/arXiv.1307.4924. arXiv: 1307.4924 [astro-ph.HE].

Pounds, K. A., C. Done, and J. P. Osborne (Nov. 1995). "RE 1034+39: a high-state Seyfert galaxy?" In: 277, pp. L5–L10. DOI: 10.1093/mnras/277.1.L5.

Poutanen, Juri, Andrzej A. Zdziarski, and Askar Ibragimov (Sept. 2008). "Superorbital variability of X-ray and radio emission of Cyg X-1 - II. Dependence of the orbital modulation and spectral hardness on the superorbital phase". In: 389.3, pp. 1427–1438. DOI: 10.1111/j.1365-2966.2008.13666.x. arXiv: 0802.1391 [astro-ph].

Pozo Nuñez, F. et al. (Apr. 2013). "Size and disk-like shape of the broad-line region of ESO 399-IG20". In: 552, A1, A1. DOI: 10.1051/0004-6361/201321047. arXiv: 1303.3653 [astro-ph.CO].

Priestley, M. B. (Jan. 1997). "Application of Wavelet Analysis to the Study of Time-dependent Spectra". In: *Statistical Challenges in Modern Astronomy II*. Ed. by G. Jogesh Babu and Eric D. Feigelson, p. 283.

Proga, D., J. M. Stone, and T. R. Kallman (Nov. 2000). "Dynamics of Line-driven Disk Winds in Active Galactic Nuclei". In: 543, pp. 686–696. DOI: 10.1086/317154. eprint: astro-ph/0005315.

Raiteri, Claudia Maria (Dec. 2024). "Monitoring Blazar Variability to Understand Extragalactic Jets". In: *Publications de l'Observatoire Astronomique de Beograd* 104, pp. 29–38. DOI: 10.69646/aob104p029. arXiv: 2412.11565 [astro-ph.HE].

Rakshit, S. et al. (Apr. 2017). "A Catalog of Narrow Line Seyfert 1 Galaxies from the Sloan Digital Sky Survey Data Release 12". In: 229, 39, p. 39. DOI: 10.3847/1538-4365/aa6971. arXiv: 1704.07700.

Readhead, Anthony C. S. (May 1994). "Equipartition Brightness Temperature and the Inverse Compton Catastrophe". In: 426, p. 51. DOI: 10.1086/174038.

Reber, Grote (Nov. 1944). "Cosmic Static." In: 100, p. 279. DOI: 10.1086/144668.

Rees, M. J. (July 1966). "Appearance of Relativistically Expanding Radio Sources". In: 211, pp. 468–470. DOI: 10.1038/211468a0.

Remillard, R. A. et al. (Feb. 1986). "The discovery of eight bright active galactic nuclei observed with the HEAO 1 scanning modulation collimator". In: 301, pp. 742–752. DOI: 10.1086/163940.

Remillard, Ronald A. and Jeffrey E. McClintock (Sept. 2006). "X-Ray Properties of Black-Hole Binaries". In: 44.1, pp. 49–92. DOI: 10.1146/annurev.astro.44.051905.092532. arXiv: astro-ph/0606352 [astro-ph].

Remillard, Ronald A. et al. (Dec. 2002). "Evidence for Harmonic Relationships in the High-Frequency Quasi-periodic Oscillations of XTE J1550-564 and GRO J1655-40". In: 580.2, pp. 1030–1042. DOI: 10.1086/343791. arXiv: astro-ph/0202305 [astro-ph].

Ren, Chongyang, Sisi Sun, and Pengfei Zhang (Jan. 2024). "A Possible Optical Quasiperiodic Oscillation of 134 days in the Radio-loud Narrow-line Seyfert 1 Galaxy TXS 1206+549 at z = 1.34". In: 961.1, 38, p. 38. DOI: 10.3847/1538-4357/ad150c. arXiv: 2312.06917 [astro-ph.HE].

Rest, A. et al. (Nov. 2014). "Cosmological Constraints from Measurements of Type Ia Supernovae Discovered during the First 1.5 yr of the Pan-STARRS1 Survey". In: 795.1, 44, p. 44. DOI: 10.1088/0004-637X/795/1/44. arXiv: 1310.3828 [astro-ph.CO].

Ricci, F. et al. (Feb. 2017). "Novel calibrations of virial black hole mass estimators in active galaxies based on X-ray luminosity and optical/near-infrared emission lines". In: 598, A51, A51. DOI: 10.1051/0004-6361/201629380. arXiv: 1610.03490 [astro-ph.GA].

Ricci, L. et al. (Aug. 2022). "Exploring the disk-jet connection in NGC 315". In: 664, A166, A166. DOI: 10.1051/0004-6361/202243958. arXiv: 2206.12193 [astro-ph.HE].

Richards, J. L. and M. L. Lister (Feb. 2015). "Kiloparsec-Scale Jets in Three Radio-Loud Narrow-Line Seyfert 1 Galaxies". In: 800, L8, p. L8. DOI: 10.1088/2041-8205/800/1/L8. arXiv: 1501.05299.

Richards, J. L. et al. (June 2011). "Blazars in the Fermi Era: The OVRO 40 m Telescope Monitoring Program". In: 194, 29, p. 29. DOI: 10.1088/0067-0049/194/2/29. arXiv: 1011.3111 [astro-ph.CO].

Ricker, George R. et al. (Aug. 2014). "Transiting Exoplanet Survey Satellite (TESS)". In: *Space Telescopes and Instrumentation 2014: Optical, Infrared, and Millimeter Wave*. Ed. by Jacobus M. Oschmann Jr. et al. Vol. 9143. Society of Photo-Optical Instrumentation Engineers (SPIE) Conference Series, 914320, p. 914320. DOI: 10.1117/12.2063489. arXiv: 1406.0151 [astro-ph.EP].

Rieger, Frank M. (June 2007). "Supermassive binary black holes among cosmic gamma-ray sources". In: 309.1-4, pp. 271–275. DOI: 10.1007/s10509-007-9467-y. arXiv: astro-ph/0611224 [astro-ph].

Roland, J., R. Teyssier, and N. Roos (Oct. 1994). "On the origin of the variability of superluminal radio sources similar to 3C 273". In: 290, pp. 357–363.

Romano, P. et al. (Dec. 2018). "Prospects for gamma-ray observations of narrow-line Seyfert 1 galaxies with the Cherenkov Telescope Array". In: 481, pp. 5046–5061. DOI: 10.1093/mnras/sty2484. arXiv: 1809.03426 [astro-ph.HE].

Romano, P. et al. (May 2023). "Long-term Swift and Metsähovi monitoring of SDSS J164100.10+345452.7 reveals multi-wavelength correlated variability". In: 673, A85, A85. DOI: 10.1051/0004-6361/202345936. arXiv: 2303.05534 [astro-ph.HE].

Romero, G. E. et al. (Aug. 2000). "Beaming and precession in the inner jet of 3C 273 — II. The central engine". In: 360, pp. 57–64.

Ruderman, M. A. and P. G. Sutherland (Feb. 1975). "Theory of pulsars: polar gaps, sparks, and coherent microwave radiation." In: 196, pp. 51–72. DOI: 10.1086/153393.

Ryan, C. J. et al. (Jan. 2007). "The Central Engines of Narrow-Line Seyfert 1 Galaxies". In: 654.2, pp. 799–813. DOI: 10.1086/509313. arXiv: astro-ph/0609729 [astro-ph].

Salpeter, E. E. (Aug. 1964). "Accretion of Interstellar Matter by Massive Objects." In: 140, pp. 796–800. DOI: 10.1086/147973.

Sani, E. et al. (Apr. 2010). "Enhanced star formation in narrow-line Seyfert 1 active galactic nuclei revealed by Spitzer". In: 403, pp. 1246–1260. DOI: 10.1111/j.1365-2966.2009.16217.x. arXiv: 0908.0280.

Scargle, J. D. (Dec. 1982). "Studies in astronomical time series analysis. II. Statistical aspects of spectral analysis of unevenly spaced data." In: 263, pp. 835–853. DOI: 10.1086/160554.

Scargle, Jeffrey D. (Aug. 1989). "Studies in Astronomical Time Series Analysis. III. Fourier Transforms, Autocorrelation Functions, and Cross-Correlation Functions of Unevenly Spaced Data". In: 343, p. 874. DOI: 10.1086/167757.

— (1997). "Wavelet methods in astronomical time series analysis". In: *Applications of Time Series Analysis in Astronomy and Meteorology*. Ed. by T. Subba Rao, M. B. Priestley, and O. Lessi, p. 226.

— (June 2020). "Studies in Astronomical Time-series Analysis. VII. An Enquiry Concerning Nonlinearity, the rms-Mean Flux Relation, and Lognormal Flux Distributions". In: 895.2, 90, p. 90. DOI: 10.3847/1538-4357/ab8d38. arXiv: 2001.08314 [astro-ph.IM].

Scaringi, S. et al. (Oct. 2015). "Accretion-induced variability links young stellar objects, white dwarfs, and black holes". In: *Science Advances* 1.9, e1500686–e1500686. DOI: 10.1126/sciadv.1500686. arXiv: 1510.02471 [astro-ph.HE].

Schmidt, E. O. et al. (July 2018). "Asymmetric emission of the [OIII]λ5007 profile in narrow-line Seyfert 1 galaxies". In: 615, A13, A13. DOI: 10.1051/0004-6361/201731557. arXiv: 1802.00072 [astro-ph.GA].

Schmidt, M. (Mar. 1963). "3C 273 : A Star-Like Object with Large Red-Shift". In: 197, p. 1040. DOI: 10.1038/1971040a0.

Schmitt, H. R. et al. (Feb. 2001). "Jet Directions in Seyfert Galaxies: Radio Continuum Imaging Data". In: 132, pp. 199–209. DOI: 10.1086/318957. eprint: astro-ph/0012123.

Schulz, R. et al. (2016). "The gamma-ray emitting radio-loud narrow-line Seyfert 1 galaxy PKS 2004-447. II. The radio view". In: 588, A146, A146. DOI: 10.1051/0004-6361/201527404. arXiv: 1511.02631 [astro-ph.HE].

Seyfert, C. K. (Jan. 1943). "Nuclear Emission in Spiral Nebulae." In: 97, p. 28. DOI: 10.1086/144488.

Shakura, N. I. and R. A. Sunyaev (1973). "Black holes in binary systems. Observational appearance." In: 24, pp. 337–355.

Shaposhnikov, Nickolai and Lev Titarchuk (July 2009). "Determination of Black Hole Masses in Galactic Black Hole Binaries Using Scaling of Spectral and Variability Characteristics". In: 699.1, pp. 453–468. DOI: 10.1088/0004-637X/699/1/453. arXiv: 0902.2852 [astro-ph.HE].

Shapovalova, A. I. et al. (Sept. 2012a). "Spectral Optical Monitoring of the Narrow-line Seyfert 1 Galaxy Ark 564". In: 202.1, 10, p. 10. DOI: 10.1088/0067-0049/202/1/10. arXiv: 1207.1782 [astro-ph.CO].

Shapovalova, A. I. et al. (Sept. 2012b). "Spectral Optical Monitoring of the Narrow-line Seyfert 1 Galaxy Ark 564". In: 202, 10, p. 10. DOI: 10.1088/0067-0049/202/1/10. arXiv: 1207.1782 [astro-ph.CO].

Shappee, B. J. et al. (June 2014). "The Man behind the Curtain: X-Rays Drive the UV through NIR Variability in the 2013 Active Galactic Nucleus Outburst in NGC 2617". In: 788.1, 48, p. 48. DOI: 10.1088/0004-637X/788/1/48. arXiv: 1310.2241 [astro-ph.HE].

Shen, Y. and L. C. Ho (Sept. 2014). "The diversity of quasars unified by accretion and orientation". In: 513, pp. 210–213. DOI: 10.1038/nature13712. arXiv: 1409.2887.

Shen, Yue et al. (June 2024). "The Sloan Digital Sky Survey Reverberation Mapping Project: Key Results". In: 272.2, 26, p. 26. DOI: 10.3847/1538-4365/ad3936. arXiv: 2305.01014 [astro-ph.GA].

Sillanpaa, A. et al. (Feb. 1988). "OJ 287: Binary Pair of Supermassive Black Holes". In: 325, p. 628. DOI: 10.1086/166033.

Singh, Veeresh et al. (Dec. 2015). "Discovery of rare double-lobe radio galaxies hosted in spiral galaxies". In: 454.2, pp. 1556–1572. DOI: 10.1093/mnras/stv2071. arXiv: 1509.01559 [astro-ph.GA].

Sinha, Atreyee et al. (Oct. 2018). "The flux distribution of individual blazars as a key to understand the dynamics of particle acceleration". In: 480.1, pp. L116–L120. DOI: 10.1093/mnrasl/sly136. arXiv: 1807.09073 [astro-ph.HE].

Slipher, V. M. (1917). "The spectrum and velocity of the nebula N.G.C. 1068 (M 77)". In: *Lowell Observatory Bulletin* 3, pp. 59–62.

Sob'yanin, Denis Nikolaevich (Sept. 2018). "Black hole spin from wobbling and rotation of the M87 jet and a sign of a magnetically arrested disc". In: 479.1, pp. L65–L69. DOI: 10.1093/mnrasl/sly097. arXiv: 1807.06296 [astro-ph.HE].

Soifer, B. T., G. Helou, and M. Werner (Sept. 2008). "The Spitzer view of the extragalactic universe." In: 46, pp. 201–240. DOI: 10.1146/annurev.astro.46.060407.145144.

Sokolovsky, K. V. et al. (Jan. 2017). "Comparative performance of selected variability detection techniques in photometric time series data". In: 464.1, pp. 274–292. DOI: 10.1093/mnras/stw2262. arXiv: 1609.01716 [astro-ph.IM].

Soldi, S. et al. (Aug. 2008). "The multiwavelength variability of 3C 273". In: 486.2, pp. 411–425. DOI: 10.1051/0004-6361:200809947. arXiv: 0805.3411 [astro-ph].

Stalin, C. S. et al. (May 2004). "Intranight optical variability of radio-quiet and radio lobe-dominated quasars". In: 350.1, pp. 175–188. DOI: 10.1111/j.1365-2966.2004.07631.x. arXiv: astro-ph/0306394 [astro-ph].

Stevens, J. A. et al. (Dec. 1994). "Multifrequency Observations of Blazars. V. Long-Term Millimeter, Submillimeter, and Infrared Monitoring". In: 437, p. 91. DOI: 10.1086/174978.

Stirling, A. M. et al. (May 2003). "Discovery of a precessing jet nozzle in BL Lacertae". In: 341.2, pp. 405–422. DOI: 10.1046/j.1365-8711.2003.06448.x.

Strittmatter, P. A. et al. (July 1972). "Compact Extragalactic Nonthermal Sources". In: 175, p. L7. DOI: 10.1086/180974.

Sulentic, J. and P. Marziani (Oct. 2015). "Quasars in the 4D Eigenvector 1 Context: a stroll down memory lane". In: *Frontiers in Astronomy and Space Sciences* 2, 6, p. 6. DOI: 10.3389/fspas.2015.00006. arXiv: 1506.01276.

Sulentic, J. W., M. Calvani, and P. Marziani (June 2001). "Eigenvector 1: an H-R diagram for AGN?" In: *The Messenger* 104, pp. 25–28.

Sulentic, J. W., D. Dultzin-Hacyan, and P. Marziani (June 2007). "Eigenvector 1: Towards AGN Spectroscopic Unification". In: *Revista Mexicana de Astronomia y Astrofisica Conference Series*. Ed. by Stanley Kurtz. Vol. 28. Revista Mexicana de Astronomia y Astrofisica Conference Series, pp. 83–88.

Sulentic, J. W. et al. (June 2000). "Eigenvector 1: An Optimal Correlation Space for Active Galactic Nuclei". In: 536, pp. L5–L9. DOI: 10.1086/312717. eprint: astro-ph/0005177.

Sun, Mouyuan et al. (Oct. 2018). "Evolution of Quasar Stochastic Variability along Its Main Sequence". In: 866.1, 74, p. 74. DOI: 10.3847/1538-4357/aae208. arXiv: 1809.05655 [astro-ph.HE].

Sun, Yu-Han et al. (Sept. 2014). "The Discovery of Timescale-dependent Color Variability of Quasars". In: 792.1, 54, p. 54. DOI: 10.1088/0004-637X/792/1/54. arXiv: 1407.4230 [astro-ph.GA].

Sunyaev, R. A. and L. G. Titarchuk (June 1980). "Comptonization of X-Rays in Plasma Clouds - Typical Radiation Spectra". In: 86, p. 121.

Swingler, D. N. (Jan. 1989). "A comparison of the Fourier, Jurkevich, and Stellingwerf methods of period estimation". In: 97, pp. 280–287. DOI: 10.1086/114981.

Szuszkiewicz, Ewa, Matthew A. Malkan, and Marek A. Abramowicz (Feb. 1996). "The Observational Appearance of Slim Accretion Disks". In: 458, p. 474. DOI: 10.1086/176830. arXiv: astro-ph/9509037 [astro-ph].

Tadhunter, C. et al. (Oct. 2001). "Emission-line outflows in PKS1549-79: the effects of the early stages of radio-source evolution?" In: 327, pp. 227–232. DOI: 10.1046/j.1365-8711.2001.04708.x. eprint: astro-ph/0105146.

Tadhunter, Clive (June 2016). "Radio AGN in the local universe: unification, triggering and evolution". In: 24.1, 10, p. 10. DOI: 10.1007/s00159-016-0094-x. arXiv: 1605.08773 [astro-ph.GA].

Tarchi, A. et al. (Aug. 2011). "Narrow-line Seyfert 1 galaxies: an amasing class of AGN". In: 532, A125, A125. DOI: 10.1051/0004-6361/201117213. arXiv: 1107.5155 [astro-ph.CO].

Tatum, M. M. et al. (June 2012). "Modeling the Fe K Line Profiles in Type I Active Galactic Nuclei with a Compton-thick Disk Wind". In: 752.2, 94, p. 94. DOI: 10.1088/0004-637X/752/2/94. arXiv: 1204.2535 [astro-ph.CO].

Tchekhovskoy, Alexander, Ramesh Narayan, and Jonathan C. McKinney (Mar. 2010). "Black Hole Spin and The Radio Loud/Quiet Dichotomy of Active Galactic Nuclei". In: 711.1, pp. 50–63. DOI: 10.1088/0004-637X/711/1/50. arXiv: 0911.2228 [astro-ph.HE].

Tchekhovskoy, Alexander, Ramesh Narayan, and Jonathan C. McKinney (Nov. 2011). "Efficient generation of jets from magnetically arrested accretion on a rapidly spinning black hole". In: 418.1, pp. L79–L83. DOI: 10.1111/j.1745-3933.2011.01147.x. arXiv: 1108.0412 [astro-ph.HE].

Teräsranta, H. et al. (Nov. 1998). "Fifteen years monitoring of extragalactic radio sources at 22, 37 and 87 GHz". In: 132, pp. 305–331. DOI: 10.1051/aas:1998297.

Thorne, Jessica et al. (Mar. 2022). *AGN Unification Diagram*. DOI: 10.5281/zenodo.6381013. URL: https://doi.org/10.5281/zenodo.6381013.

Timmer, J. and M. König (Aug. 1995). "On generating power law noise." In: 300, p. 707.

Tornikoski, M. et al. (Sept. 1994). "Correlated radio and optical variations in a sample of active galactic nuclei." In: 289, pp. 673–710.

Tortosa, Alessia et al. (Jan. 2022). "The extreme properties of the nearby hyper-Eddington accreting active galactic nucleus in IRAS 04416+1215". In: 509.3, pp. 3599–3615. DOI: 10.1093/mnras/stab3152. arXiv: 2109.02573 [astro-ph.GA].

Tortosa, Alessia et al. (Mar. 2023). "Systematic broad-band X-ray study of super-Eddington accretion on to supermassive black holes - I. X-ray continuum". In: 519.4, pp. 6267–6283. DOI: 10.1093/mnras/stac3590. arXiv: 2212.06183 [astro-ph.HE].

Türler, M. (Jan. 2011). "Shock-in-jet model for quasars and microquasars". In: 82, p. 104. DOI: 10.48550/arXiv.1010.0907. arXiv: 1010.0907 [astro-ph.HE].

Türler, M., T. J.-L. Courvoisier, and S. Paltani (Sept. 2000). "Modelling 20 years of synchrotron flaring in the jet of 3C 273". In: 361, pp. 850–862. DOI: 10.48550/arXiv.astro-ph/0008480. arXiv: astro-ph/0008480 [astro-ph].

Turner, Martin J. L. (June 2007). "XEUS and the physics of the hot universe". In: *Astronomy and Geophysics* 48.3, pp. 3.34–3.36. DOI: 10.1111/j.1468-4004.2007.48334.x.

Uhlenbeck, G. E. and L. S. Ornstein (Sept. 1930). "On the Theory of the Brownian Motion". In: *Physical Review* 36.5, pp. 823–841. DOI: 10.1103/PhysRev.36.823.

Ulrich, Marie-Helene, Laura Maraschi, and C. Megan Urry (Jan. 1997). "Variability of Active Galactic Nuclei". In: 35, pp. 445–502. DOI: 10.1146/annurev.astro.35.1.445.

Urry, C. M. and P. Padovani (Sept. 1995). "Unified Schemes for Radio-Loud Active Galactic Nuclei". In: 107, p. 803. DOI: 10.1086/133630. eprint: astro-ph/9506063.

Uttley, P., I. M. McHardy, and I. E. Papadakis (May 2002). "Measuring the broad-band power spectra of active galactic nuclei with RXTE". In: 332.1, pp. 231–250. DOI: 10.1046/j.1365-8711.2002.05298.x. arXiv: astro-ph/0201134 [astro-ph].

Uttley, Philip and Ian M. McHardy (Oct. 2005). "X-ray variability of NGC 3227 and 5506 and the nature of active galactic nucleus 'states'". In: 363.2, pp. 586–596. DOI: 10.1111/j.1365-2966.2005.09475.x.

Valtaoja, E. et al. (Feb. 1992). "Five years monitoring of extragalactic radio sources. III. Generalized shock models and the dependence of variability on frequency." In: 254, pp. 71–79.

Valtaoja, E. et al. (Jan. 1999). "Total Flux Density Variations in Extragalactic Radio Sources. I. Decomposition of Variations into Exponential Flares". In: 120, pp. 95–99. DOI: 10.1086/313170.

van Velzen, Sjoert et al. (Nov. 2011). "Optical Discovery of Probable Stellar Tidal Disruption Flares". In: 741.2, 73, p. 73. DOI: 10.1088/0004-637X/741/2/73. arXiv: 1009.1627 [astro-ph.CO].

van Velzen, Sjoert et al. (June 2019). "Late-time UV Observations of Tidal Disruption Flares Reveal Unobscured, Compact Accretion Disks". In: 878.2, 82, p. 82. DOI: 10.3847/1538-4357/ab1844. arXiv: 1809.00003 [astro-ph.HE].

VanderPlas, Jacob T. (May 2018). "Understanding the Lomb-Scargle Periodogram". In: 236.1, 16, p. 16. DOI: 10.3847/1538-4365/aab766. arXiv: 1703.09824 [astro-ph.IM].

Varglund, I. et al. (Dec. 2022). "Jetted narrow-line Seyfert 1 galaxies breaking the jet paradigm: A comprehensive study of host-galaxy morphologies". In: 668, A91, A91. DOI: 10.1051/0004-6361/202244465. arXiv: 2209.09270 [astro-ph.GA].

Varglund, I. et al. (Nov. 2023). "A host galaxy study of southern narrow-line Seyfert 1 galaxies". In: 679, A32, A32. DOI: 10.1051/0004-6361/202346131. arXiv: 2309.03277 [astro-ph.GA].

Vasudevan, R. V. and A. C. Fabian (Nov. 2007). "Piecing together the X-ray background: bolometric corrections for active galactic nuclei". In: 381.3, pp. 1235–1251. DOI: 10.1111/j.1365-2966.2007.12328.x. arXiv: 0708.4308 [astro-ph].

Vaughan, S. et al. (Nov. 2003). "On characterizing the variability properties of X-ray light curves from active galaxies". In: 345.4, pp. 1271–1284. DOI: 10.1046/j.1365-2966.2003.07042.x. arXiv: astro-ph/0307420 [astro-ph].

Véron-Cetty, M.-P., P. Véron, and A. C. Gonçalves (June 2001). "A spectrophotometric atlas of Narrow-Line Seyfert 1 galaxies". In: 372, pp. 730–754. DOI: 10.1051/0004-6361:20010489. eprint: astro-ph/0104151.

Vietri, A. et al. (Apr. 2018). "The link between X-ray complexity and optical lines in NLS1s". In: *Proceedings of Science, vol. Revisiting narrow-line Seyfert 1 galaxies and their place in the Universe*, 47, p. 47. arXiv: 1809.09901.

Vignali, C. et al. (Nov. 2015). "The XMM deep survey in the CDF-S. IX. An X-ray outflow in a luminous obscured quasar at z $\approx$ 1.6". In: 583, A141, A141. DOI: 10.1051/0004-6361/201525852. arXiv: 1509.05413 [astro-ph.GA].

Villata, M. and C. M. Raiteri (July 1999). "Helical jets in blazars. I. The case of MKN 501". In: 347, pp. 30–36.

Viswanath, Gayathri et al. (Aug. 2019). "Are Narrow-line Seyfert 1 Galaxies Powered by Low-mass Black Holes?" In: 881.1, L24, p. L24. DOI: 10.3847/2041-8213/ab365e. arXiv: 1907.02683 [astro-ph.GA].

Vlahakis, N. and K. Tsinganos (Aug. 1998). "Systematic construction of exact magnetohydrodynamic models for astrophysical winds and jets". In: 298.3, pp. 777–789. DOI: 10.1046/j.1365-8711.1998.01660.x. arXiv: astro-ph/9812354 [astro-ph].

Volonteri, Marta et al. (Feb. 2005). "The Distribution and Cosmic Evolution of Massive Black Hole Spins". In: 620.1, pp. 69–77. DOI: 10.1086/426858. arXiv: astro-ph/0410342 [astro-ph].

Wandel, A. and Th. Boller (Mar. 1998). "BLR sizes and the X-ray spectrum in AGN". In: 331, pp. 884–890. DOI: 10.48550/arXiv.astro-ph/9711047. arXiv: astro-ph/9711047 [astro-ph].

Wang, Ailing et al. (June 2025). "A Relativistic Jet in the Radio Quiet AGN Mrk 110". In: *arXiv e-prints*, arXiv:2506.03970, arXiv:2506.03970. DOI: 10.48550/arXiv.2506.03970. arXiv: 2506.03970 [astro-ph.GA].

Wang, F. et al. (June 2016). "Reverberation Mapping of the Gamma-Ray Loud Narrow-line Seyfert 1 Galaxy 1H 0323+342". In: 824, 149, p. 149. DOI: 10.3847/0004-637X/824/2/149.

Webb, James R. et al. (Dec. 2021). "The Nature of Micro-Variability in Blazars". In: *Galaxies* 9.4, 114, p. 114. DOI: 10.3390/galaxies9040114.

Whipple, Fred L. and Jesse L. Greenstein (Mar. 1937). "On the Origin of Interstellar Radio Disturbances". In: *Proceedings of the National Academy of Science* 23.3, pp. 177–181. DOI: 10.1073/pnas.23.3.177.

Wilhite, Brian C. et al. (Jan. 2008). "On the variability of quasars: a link between the Eddington ratio and optical variability?" In: 383.3, pp. 1232–1240. DOI: 10.1111/j.1365-2966.2007.12655.x. arXiv: 0711.4844 [astro-ph].

Williams, James K. et al. (May 2023). "Assessing indirect methods to determine black hole masses using NGC 4151". In: 521.2, pp. 2897–2910. DOI: 10.1093/mnras/stad718. arXiv: 2303.03968 [astro-ph.GA].

Williams, R. J., S. Mathur, and R. W. Pogge (Aug. 2004). "Chandra Observations of X-Ray-weak Narrow-Line Seyfert 1 Galaxies". In: 610, pp. 737–744. DOI: 10.1086/421768. eprint: astro-ph/0402236.

Williams, R. J., R. W. Pogge, and S. Mathur (Dec. 2002). "Narrow-line Seyfert 1 Galaxies from the Sloan Digital Sky Survey Early Data Release". In: 124, pp. 3042–3049. DOI: 10.1086/344765. eprint: astro-ph/0208211.

Wilson, A. S. and E. J. M. Colbert (Jan. 1995). "The Difference between Radio-loud and Radio-quiet Active Galaxies". In: 438, p. 62. DOI: 10.1086/175054. arXiv: astro-ph/9408005 [astro-ph].

Winkel, N. et al. (Feb. 2023). "The Close AGN Reference Survey (CARS). A parsec-scale multi-phase outflow in the super-Eddington NLS1 Mrk 1044". In: 670, A3, A3. DOI: 10.1051/0004-6361/202244630. arXiv: 2211.00657 [astro-ph.GA].

Wold, M., M. S. Brotherton, and Zhaohui Shang (Mar. 2007). "The dependence of quasar variability on black hole mass". In: 375.3, pp. 989–999. DOI: 10.1111/j.1365-2966.2006.11364.x. arXiv: astro-ph/0612042 [astro-ph].

Woltjer, L. (July 1959). "Emission Nuclei in Galaxies." In: 130, p. 38. DOI: 10.1086/146694.

Woo, Jong-Hak and C. Megan Urry (Nov. 2002). "Active Galactic Nucleus Black Hole Masses and Bolometric Luminosities". In: 579.2, pp. 530–544. DOI: 10.1086/342878. arXiv: astro-ph/0207249 [astro-ph].

Xanthopoulos, E. (May 1996). "VRI CCD surface photometry of Seyfert 1, Seyfert 2 and intermediate Seyfert-type galaxies". In: 280.1, pp. 6–28. DOI: 10.1093/mnras/280.1.6.

Xu, D. et al. (Apr. 2012). "Correlation Analysis of a Large Sample of Narrow-line Seyfert 1 Galaxies: Linking Central Engine and Host Properties". In: 143, 83, p. 83. DOI: 10.1088/0004-6256/143/4/83. arXiv: 1201.2810.

Xu, D. W. et al. (Jan. 2024). "Changing-Look Narrow-Line Seyfert 1 Galaxies, their Detection with SVOM, and the Case of NGC 1566". In: *Universe* 10.2, 61, p. 61. DOI: 10.3390/universe10020061. arXiv: 2401.10600 [astro-ph.GA].

Yang, Hui et al. (July 2018). "SDSS J211852.96-073227.5: a new γ-ray flaring narrow-line Seyfert 1 galaxy". In: 477.4, pp. 5127–5138. DOI: 10.1093/mnras/sty904. arXiv: 1801.03963 [astro-ph.HE].

Yang, Qian et al. (Dec. 2017). "Quasar Photometric Redshifts and Candidate Selection: A New Algorithm Based on Optical and Mid-infrared Photometric Data". In: 154.6, 269, p. 269. DOI: 10.3847/1538-3881/aa943c. arXiv: 1710.09155 [astro-ph.GA].

Yang, Yujian, Bo Ma, and Chen Chen (Nov. 2024). "Studying Intra-Night Optical Variability of AGNs Using the TESS Survey Data". In: *Universe* 10.12, 434, p. 434. DOI: 10.3390/universe10120434.

Yao, S. et al. (Nov. 2015). "Identification of a new γ-ray-emitting narrow-line Seyfert 1 galaxy, at redshift

1". In: 454, pp. L16–L20. DOI: 10.1093/mnrasl/slv119. arXiv: 1509.03030 [astro-ph.HE].

Zamanov, R. et al. (Sept. 2002). "Kinematic Linkage between the Broad- and Narrow-Line-emitting Gas in Active Galactic Nuclei". In: 576, pp. L9–L13. DOI: 10.1086/342783. eprint: astro-ph/0207387.

Zastrocky, T. E. et al. (June 2024). "Monitoring AGNs with Hβ Asymmetry. IV. First Reverberation Mapping Results of 14 Active Galactic Nuclei". In: 272.2, 29, p. 29. DOI: 10.3847/1538-4365/ad3bad. arXiv: 2404.07343 [astro-ph.GA].

Zechmeister, M. and M. Kürster (Mar. 2009). "The generalised Lomb-Scargle periodogram. A new formalism for the floating-mean and Keplerian periodograms". In: 496.2, pp. 577–584. DOI: 10.1051/0004-6361:200811296. arXiv: 0901.2573 [astro-ph.IM].

Zel'dovich, Y. B. and I. D. Novikov (Oct. 1964). "The Radiation of Gravity Waves by Bodies Moving in the Field of a Collapsing Star". In: *Soviet Physics Doklady* 9, p. 246.

Zhang, K. et al. (Aug. 2011). "The Blueshifting and Baldwin Effects for the [O III] λ5007 Emission Line in Type 1 Active Galactic Nuclei". In: 737, 71, p. 71. DOI: 10.1088/0004-637X/737/2/71. arXiv: 1105.1094 [astro-ph.CO].

Zhang, L. and K. S. Cheng (Oct. 1997). "Gamma-Ray Production through Inverse Compton Scattering with Anisotropic Photon Field from Accretion Disk in AGNs". In: 488.1, pp. 94–108. DOI: 10.1086/304663.

Zhang, X. H. and G. Bao (June 1991). "The rotation of accretion disks and the power spectra of X-ray "flickering"." In: 246, p. 21.

Zhou, H. et al. (Sept. 2006). "A Comprehensive Study of 2000 Narrow Line Seyfert 1 Galaxies from the Sloan Digital Sky Survey. I. The Sample". In: 166, pp. 128–153. DOI: 10.1086/504869. eprint: astro-ph/0603759.

Zhou, Xin-Lin et al. (Jan. 2015). "Universal Scaling of the 3:2 Twin-peak Quasi-periodic Oscillation Frequencies With Black Hole Mass and Spin Revisited". In: 798.1, L5, p. L5. DOI: 10.1088/2041-8205/798/1/L5. arXiv: 1411.7731 [astro-ph.HE].

Zylka, Robert (Mar. 2013). *MOPSIC: Extended Version of MOPSI*. Astrophysics Source Code Library, record ascl:1303.011.